Studies on Intrinsic Defects and Doping Induced Tunable Optical and Magnetic Properties of TiO_2 Nanostructures

A Thesis Submitted to
Indian Institute of Technology Guwahati
For the Degree of
Doctor of Philosophy

By

Batakrushna Santara

Department of Physics
Indian Institute of Technology Guwahati
Guwahati-781039, India

May 2014

Dedicated to

..... My Beloved Parents

DEPARTMENT OF PHYSICS
Indian Institute of Technology Guwahati
Guwahati-781039, India

Date: May 27, 2014

STATEMENT

The work contained in the thesis entitled "***Studies on Intrinsic Defects and Doping Induced Tunable Optical and Magnetic Properties of TiO_2 Nanostructures***" has been carried out by me at Indian Institute of Technology Guwahati under the supervision of **Prof. P. K. Giri**, Professor, Department of Physics, Indian Institute of Technology Guwahati. This work has not been submitted elsewhere for the award of any degree.

Batakrushna Santara

Senior Research Fellow
Department of Physics
Indian Institute of Technology Guwahati
Guwahati-781039, India

Prof. P. K. Giri
Professor
Department of Physics
Indian Institute of Technology Guwahati
Guwahati-781039, India
Phone: +91 361 2582703, Fax: +91 361 2690762
Email: giri@iitg.ernet.in

Date: May 27, 2014

CERTIFICATE

This is to certify that the work contained in the thesis entitled "***Studies on Intrinsic Defects and Doping Induced Tunable Optical and Magnetic Properties of TiO_2 Nanostructures***" has been carried out by **Mr. Batakrushna Santara** at Indian Institute of Technology Guwahati under my supervision. This work has not been submitted elsewhere for the award of any degree.

Prof. P. K. Giri

Thesis supervisor

ACKNOWLEDGEMENT

At the time of writing the acknowledgement, I realize that nearly 5 years of Ph. D. life at IIT Guwahati is finally coming to an end and I am able to submit my thesis report. The research work reported in this thesis is the results of years of hard work with patience and would not have been possible without the help, support and encouragement of a number of people. It is my pleasure to take this opportunity to thank all of them who helped me in the way of my Ph.D. life.

First of all, I would like to express my sincere gratitude to my thesis supervisor, Prof. P. K. Giri for his excellent guidance, valuable discussion, kind support, constant encouragement and suggestion about independent thinking. I am thankful to him for giving me complete freedom in my work and providing the necessary arrangements, laboratory facilities and supports throughout my Ph. D. work to achieve the goal. I am really indebted to him for accepting me as a Ph. D. student into his research group. I would like to thank my doctoral committee members, Dr. P. K. Padmanabhan, Prof. Gopal Das and Dr. D. Pamu for regular review of my research work and their valuable suggestions.

I am thankful to our Head of the Department of Physics, other faculty members of Physics, members of the Central Instruments Facilities and Centre for Nanotechnology for providing me a research friendly environment with up-to-date research facilities. I am also thankful to Department of Chemistry to carry out the diffuse reflectance spectroscopy measurements. I am grateful to Indian Institute of Technology Guwahati for providing the fellowship, good accommodation in this beautiful campus and having enjoyable working environment. A special thanks to the scientific officers and technicians, Dr. Sidananda Sharma, Indrajit Talukdar, Kaustav Acharya, Dr. K. K. Senapati, Chandan Borgohain, Madhurya Bora, Dr. Babulal Das and Diganta Hira for their help and cooperation to complete my work.

I also express my special thanks to Dr. Perumal Alagarsamy, Bhagaban Kisan and Akhilesh Singh for their help to carry out Vibrating Sample Magnetometer measurements.

I express my sincere thanks to my seniors Dr. Soumen Dhara, Dr. Arindam Pal and Himanshu Jha for their help and good company. Thanks to my labmates Bappaditya, Ravi, Ramesh, Gone, Manjira and Larionette for a good and enjoyable company and their supports. They shared every success and problems in and out of the lab during my stay at IIT Guwahati.

I must thank my friends Ranjan, Bramha, Tikemani, Sunita, Bhagaban, Indrajeet, Himangsu, Basudev and Bigyan for their company and sharing success, problems, frustrations and, every kind of discussions throughout my stay at IIT Guwahati. I cannot repay the support and enjoyment which I received from Ranjan, Ajit, Amit and Manmatha bhai during my universities studies and preparation for examinations that helped me in various ways. I am happy to thank them.

I should acknowledge the supports received from my uncles (Badakaka, Sanakaka, Sanamamun and Tutukaka), cousin grandfather (U. C. Gochhayat), Kanhu bhai, Narayankaka, Sarat sir and well-wishers. They supported me in all possible ways during my early days of study by means of motivation, academic books, free tuitions and financial help. My beloved uncles (Badakaka, Sanakaka and Sanamamun) have been a great support of pillar behind my academic growth and their strong advice inspired me to pursue higher studies in science.

Finally, I would like to express my deepest sense of gratitude to my parents, Mr. Srustidhar Santara and Mrs. Sumitra Santara for their endless love, blessings and constant encouragement to pursue higher studies. Especially, my parents taught me the value of hard work, patience and to be honest. Their hard work and dedication in helping me to pursue higher studies is the strongest source of inspiration for me. I am wordless to thank my late grandfather with whom I spent my childhood days. His moral support and encouragement helped me to go ahead for higher studies. My lovely brother, Pranakrushna and lovely Lipi are always a source of love, support and affection in all walks of life. I must thank them.

Batakrushna Santara
IIT Guwahati

CONTENTS

Synopsis

Titanium dioxide (TiO_2) is a wide band gap semiconductor well-known for its outstanding physical and chemical properties. It can exist mainly in one of the four crystalline forms: anatase, rutile, brookite and TiO_2(B). Rutile is the most stable phase whereas anatase, brookite and TiO_2(B) are metastable phases and usually convert to rutile upon heating. Each of these forms has specific applications. Among the oxide semiconductors, TiO_2 has received widespread attention due to its unique properties such as nontoxicity, stability against photo and chemical corrosion, strong oxidizing and reducing ability, biocompatibility, low cost, excellent optical transmittance, photocatalyst, hydrophilicity etc. Further, TiO_2 has wide variety of potential applications such as, water purification, environmental cleaning, self cleaning, antifogging, cancer treatment, drug delivery, optoelectronic devices, hydrogen production and storage, gas sensors, dye sensitized solar cell (DSSC) and spintronic devices.

The one dimensional (1D) TiO_2 nanostructures such as nanotubes (NTs), nanorods (NRs), nanoribbons (NRbs) and nanowires (NWs) have a large surface area, with unique 1D morphology providing a direct path for electron transport with enhanced carrier collection. As a result, 1D nanostructures of TiO_2 have gained huge attention for several promising and high performance applications. The properties of nanocrystalline TiO_2 would be further improved if morphologies, size, compositions and texture of the material are modified. Considerable efforts have been made to explore novel approaches from vapor-phase technique to solution-growth process to grow TiO_2 nanostructures with tunable properties by controlling their size and morphology. The typical vapor-phase technique requires high temperature (> 1000 °C) and the control over morphology is challenging. After the first successful synthesis of titanate NTs by Kasuga et al. [*Langmuir* **14**, 3160, **1998**], extensive research has been carried out on the hydrothermal growth of titanate and TiO_2 NRs, NTs and NWs by adjusting various growth parameters within the hydrothermal system to determine their effects on the nanostructure formation and resultant morphology. These parameters include reaction temperature, alkaline concentration, reaction duration, precursor phase, and crystallite size. Moreover, systematic study of solvent and temperature controlled growth of

nanostructures and the exact growth mechanism of solvothermally synthesized titanate and TiO_2 NTs and NWs is still a topic debated extensively in the contemporary literature. Understanding the formation mechanism and tuning the properties of TiO_2 nanostructures by manipulation of intrinsic defects and doping remain a challenge for exploiting their applications in various fields. In this thesis, we have studied the formation mechanism of solvothermally synthesized 1D TiO_2 NTs, NRs, NWs and nanoporous NRbs by varying the reaction temperatures, solvents and post-growth calcinations. The growth mechanism of the as-prepared nanostructures is elucidated from the systematic studies of field emission scanning electron microscopy (FESEM) and transmission electron microscopy (TEM) imaging.

Anatase TiO_2 nanostructures having large surface area are used as a promising photocatalyst for the degradation of organic pollutants and for water splitting of hydrogen production. But due to its large band gap, the industrial application is limited to UV light only. Therefore, band gap engineering is essential to tune the band gap of TiO_2 into visible light so that it could be working using renewable solar light rather than using the cost effective, hazardous UV light. For this purpose, attempts have been made to dope metal or nonmetal impurities to optimize the band gap of TiO_2 to visible light. However, the introduction of dopants acts as charge carrier recombination centers, which reduce the chance of the carriers to reach the particle surface to participate in the desired reaction and becomes a major issue affecting the photocatalytic efficiency. So, there are lots of challenges and fundamental issues related to the band gap tuning, electron-hole recombination in undoped and doped TiO_2 nanostructures and the visible light photocatalytic applications, which need to be explored further. Recently, some approaches based on dopant-free, pure TiO_2 phase were proposed in order to overcome this limitation. The decisive role of surface disorder and point defects, such as oxygen vacancy (O_v) and Ti interstitial (Ti_i) in dictating the band gap narrowing and related application of TiO_2 has been emphasized in the recent literatures, mainly through computational studies. However, experimental understanding on the actual nature of defects such as O_v and Ti_i in reduced TiO_2 and its role in the visible light photocatalysis are still unclear. The concentration of the native defects typically depends on the growth conditions. However, the nature of band gap states induced by the Ti_i is yet to be identified experimentally. It is therefore imperative to understand the evolution of the native

defects in band gap engineered TiO_2 nanostructures with different growth/processing conditions and identify the defects responsible for extended visible absorption and visible to near infrared photoluminescence in such nanostructures. In this work, through careful *in-situ* photoluminescence studies under controlled environment coupled with optical absorption measurement, we attempt to identify the specific defect responsible for the red shift in the absorption edge, visible and near infrared (NIR) photoluminescence (PL) emission in undoped TiO_2 NRbs grown by a solvothermal technique. In particular, monitoring the time evolution of the visible and NIR PL emissions at low temperature, under high vacuum and oxygen environment, allows us to distinguish and unambiguously identify the defect states associated with O_v, oxygen interstitial (O_i) and Ti_i. Our studies also reveal that these native defects are the microscopic origin of lattice expansion and contraction in undoped rutile TiO_2 nanostructures by employing several structural and optical spectroscopic tools. The control of lattice parameters through the intrinsic defects may provide new routes to achieving novel functionalities in advanced materials that can be tailored for future technological applications.

In the recent decade, diluted magnetic semiconductors (DMSs), in particular the ferromagnetic oxides, have been at the forefront of research for spintronics and magneto-optic device materials. The discovery of ferromagnetism in Co doped TiO_2 with a Curie temperature (T_C) exceeding 300 K [Matsumoto et al., *Science* **291**, 854, **2001**] lead the expansion of the field of DMS to oxides, leading to a rapid development of new materials and phenomena arising from a synergy of semiconductor physics and strongly correlated systems. However, in spite of several studies reported on TiO_2-based DMS, there is no clear agreement about the nature and origin of the observed ferromagnetism (FM). It is being currently debated whether the observed FM in oxide DMS has anything to do with transition metal (TM) doping or might be solely related to intrinsic defects. Some reports suggested segregation and the formation of TM metal clusters as the origin of FM signal, while most recent results strongly support the intrinsic nature of FM mediated by carriers or defects. These controversial results among research groups suggest that the magnetic properties of DMS materials are critically dependent on fabrication, growth conditions, and doping agents. However, unambiguous determination of the nature of defects responsible for the observed FM remains a considerable challenge to the researchers. Till date, most of the reported FM in

undoped TiO_2 was for thin films and nanoparticles (NPs). The observed FM in undoped thin films and NPs are usually weak. Compared to thin films and nanoparticles, 1D TiO_2 nanostructures such as NWs, NRs and NRbs with high surface area can possess abundant surface defects, thus the intrinsic FM could be enhanced. Our present attempt in this work has been to enhance the magnetic moments which are solely due to intrinsic defects and explore a better understanding about the origin of observed ferromagnetism in undoped 1D TiO_2 system through systematic studies of magnetic, structural and optical properties. For further enhancement of the FM and to investigate the role of TM in the enhanced FM in TiO_2 system, we studied the optical and magnetic properties of Fe and Cr doped TiO_2 NRbs by a solvothermal method and Co doped TiO_2 NPs by ball milling method, and elucidate the mechanism of enhanced FM in TM (Fe, Cr and Co) doped and undoped TiO_2 systems. From the temperature dependence magnetization (M-T) measurement, we observed a high Curie temperature (T_c) of ~793 K, i.e., ferromagnetic to paramagnetic transition, for Co doped TiO_2 NPs and it is an important step for the development of practical commercial devices that can operate at and above RT.

We believe that the comprehensive study in this thesis on the controlled growth and tunable optical and magnetic properties of TiO_2 nanostructures through intrinsic defects and doping would further promote TiO_2-based research and development efforts to tackle the environmental and energy challenges which we are currently being faced by the humanity, and the technological applications of spintronic and magneto-optic devices. The complete works for this thesis are presented in nine chapters as described below.

Chapter 1 presents a glimpse of the important features of the TiO_2 nanostructures and their potential use in different technological applications ranging from the photocatalyst, nanoelectronics, spintronics to chemical sensors. The fundamental issues related to growth mechanism, understanding of native defects, and intrinsic and extrinsic origin of FM in TiO_2 nanostructures are discussed and the motivation for the present work is presented at the end of this chapter.

Chapter 2 provides brief information about the experimental techniques used for the present work and their working principles. Brief account of the growth techniques used for the preparation of various kinds of samples and the in-house development of the vacuum annealing system is presented in this chapter. Since several growth techniques have been adopted in this work, details of the growth conditions for each sample are presented in the

relevant chapters. The methodology adopted to analyze the data of the undoped and doped TiO_2 nanostructures is also discussed in brief.

Chapter 3 presents details of the three-step growth process of TiO_2 nanostructures and overall chemical processes. One dimensional TiO_2 and hybrid TiO_2/titanate nanostructures are synthesized by a simple low temperature solvothermal route followed by the Na^+/H^+ ion-exchange and final calcination process. We investigated the impact of reaction temperature, stirring condition and cosolvent on the morphologies of the as-prepared nanostructures. Growth mechanism is elucidated from the systematic studies of FESEM and TEM imaging. This work will be valuable for controlled growth of TiO_2 NTs, NRs, NWs and nanoporous NRbs, and understanding the formation mechanism of various nanostructured TiO_2 synthesized under different growth conditions.

Chapter 4 presents the critical role of intrinsic defects in the extended visible absorption, and visible and near infrared PL from undoped TiO_2 NRbs. TiO_2 nanoporous NRbs are grown by ethylene glycol mediated solvothermal method at different temperatures, reaction durations and calcinations. Through a careful *in-situ* PL studies under controlled environment, we identified the specific defect responsible for the red-shift in the absorption edge, visible and NIR PL emission in undoped TiO_2 NRbs grown by the solvothermal technique. In particular, monitoring the time evolution of the visible and NIR PL emissions at low temperature, under high vacuum and oxygen environment, allowed us to distinguish and unambiguously identify the associated defect states (e.g., O_v, O_i and Ti_i). Interestingly, we observed a wide range of visible absorption from these undoped TiO_2 NRbs fabricated under different growth conditions, and we demonstrate that Ti_i rich samples have higher red-shifts in the absorption edge, which is crucial for more efficient visible light photocatalysis in TiO_2-based materials. Based on our experimental observations, the origin of the tunable NIR PL from TiO_2 NRbs has been traced to surface Ti interstitials for the first time. The identification of Ti_i states in the band gap of undoped TiO_2 NRbs is considered an important step in further exploitation of defect engineered undoped TiO_2 nanostructures and is believed to be an important milestone in realizing improved visible light photocatalytic and photovoltaic applications of this novel material.

Chapter 5 presents the intrinsic defects induced room temperature ferromagnetism (RTFM) in undoped TiO_2 NRbs. We study the structural, optical and magnetic properties of the NRbs, and attempt to prove the origin of RTFM in the undoped TiO_2 NRbs grown by a solvothermal method. The samples exhibit strong visible PL associated with O_v and a clear ferromagnetic hysteresis loop, both of which dramatically enhanced after vacuum annealing. Direct evidence of oxygen vacancies and related Ti^{3+} in the as-prepared and vacuum annealed TiO_2 samples are provided through x-ray photoelectron spectroscopy (XPS) analysis. It is believed that a large concentration of oxygen vacancies with high thermal stability indeed results in stronger RTFM compared to those previously reported in undoped/ doped TiO_2 systems. The observed RTFM is explained on the basis of a bound magnetic polaron (BMP) model and extracted density of BMP is shown to directly scale with the integrated PL intensity that arises from oxygen vacancies. Thus, our results provide convincing evidence for oxygen vacancy induced strong FM at and above room temperature (RT) in the undoped TiO_2 nanoporous nanoribbons. These findings not only help to gain better insight into the defect engineering of RTFM in undoped TiO_2, but also constitute an important step for the development of practical nanospintronic devices which can be operated at and above RT.

In **Chapter 6,** we discuss the microscopic origin of lattice contraction and expansion in rutile TiO_2 nanostructures. Rutile TiO_2 nanostructures with a variety of well-defined morphologies such as NRs, nanopillars and nanoflowers, depending upon the growth conditions are synthesized by an acid-hydrothermal process. Depending on the growth conditions and post growth annealing, lattice contraction and expansion are observed in the nanostructures and it is found to correlate with the nature and density of intrinsic defects in rutile TiO_2. The change in lattice volume is correlated well with the optical band gap energy. We propose that the Ti^{4+} interstitial and F^{+} oxygen vacancy defects are primarily responsible for lattice expansion, whereas the electrostatic attraction between Ti^{4+} interstitial and O^{2-} interstitial defects causes the lattice contraction in the undoped TiO_2 nanostructures. The native defects in the nanostructures are confirmed from the PL and electron spin resonance (ESR) studies. The control of lattice parameters through the intrinsic defects may provide new routes to

achieving novel functionalities in advanced materials that can be tailored for future technological applications.

Chapter 7 presents structural, optical and magnetic properties of Fe and Cr doped TiO_2 NRbs. Fe (0.1 and 0.2 at.%) doped TiO_2 NRbs are grown by ethylene glycol mediated solvothermal method. XPS and ESR studies confirm the successful incorporation of Fe^{3+} into the TiO_2 crystal lattice. In 0.1% Fe doped TiO_2 (Fe:TiO_2) NRbs, the FM is enhanced by ~4.8 fold as compared to undoped NRbs grown under similar growth conditions. When TiO_2 is doped with low concentration of Fe, additional O_v defects are expected due to the substitution of Ti^{4+} by Fe^{3+} in TiO_2 lattice and thus, formation of Fe^{3+}-O_v defect complex resulting in enhanced FM in doped TiO_2 NRbs as compared to undoped NRbs. However, we observed that higher concentration of Fe doping decreases the FM, may be due to the Fe^{3+}-Fe^{3+} antiferromagnetic ordering in the absence of O_v in between two nearby Fe atoms. This result highlights that TM ion in the presence/ absence of O_v in host TiO_2 play a major role in DMS materials. This study brings out the role and impact of O_v defects and Fe dopant on the observed RTFM in our Fe:TiO_2 NRbs, which is supported by structural and optical measurements.

Next, Cr (0.3 and 0.7 at.%) doped TiO_2 NRbs are grown by hydrothermal method at two different reaction temperatures. We observed RTFM in Cr doped TiO_2 (Cr:TiO_2) NRbs. These samples exhibit O_v and Ti_i related visible and NIR PL, respectively. ESR and XPS studies reveal the presence of Cr in 3+ valence state, thus avoiding the formation of Cr metal clusters and CrO_2 secondary phases. Among the Cr oxides, CrO_2 only shows ferromagnetic ordering. ESR study also reveals the presence of oxygen vacancy related F^+ defect. Therefore, the observed FM is believed to arises due to the formations of Cr^{3+}-F^+ defects complexes in Cr:TiO_2 NRbs. After vacuum annealing, the FM is enhanced, indicating oxygen vacancy play a major role in ferromagnetic ordering. FM decreases with increase in Cr concentration; this may be due to antiferromagnetic ordering between Cr^{3+}-Cr^{3+} in the absence of oxygen vacancy.

Chapter 8 presents the results on high temperature ferromagnetism in Co doped TiO_2 NPs grown by a ball milling method. The structural and optical spectroscopic studies reveal the

incorporation of Co into TiO_2 crystal lattice. The observed RTFM is explained on the basis of BMP model which involves electrons locally trapped by oxygen vacancy, with the trapped electron occupying an orbital overlapping with the d shells of TM neighbors. The high temperature FM may be partly due to the presence of extended defects such as dislocations in TiO_2 NPs. In the ball milled NPs, lattice strain is usually caused by dislocations that develop during the milling process. Usually the dislocation density first goes up with milling time and then it reduces with further milling accompanied by particle size reduction. Thus, it is quite likely that strain/dislocations may have reasonable contributions to the observed high temperature FM.

Chapter 9 highlights the main contributions of the thesis and important conclusions of the work. Open questions and scope for future studies are also presented.

List of Publications

In peer-reviewed international journals:

1. **Batakrushna Santara**, Bappaditya Pal and P. K. Giri; *"Signature of Strong Ferromagnetism and Optical Properties of Co Doped TiO_2 Nanoparticles"* **Journal of Applied Physics 110, 114322 (2011).**
2. **Batakrushna Santara** and P. K. Giri; *"Impact of Solvent, Growth Temperature and Stirring on the Solvothermal Synthesis of Anatase TiO_2 and TiO_2/ Titanate Hybrid Nanostructures: Elucidating the Growth Mechanism"* **Materials Chemistry and Physics 137, 928 (2013).**
3. **Batakrushna Santara**, P. K. Giri, Kenji Imakita and Minoru Fujii; *"Evidence of Oxygen Vacancy Induced Room Temperature Ferromagnetism in Solvothermally Synthesized Undoped TiO_2 Nanoribbons"* **Nanoscale 5, 5476 (2013).**
4. **Batakrushna Santara**, P. K. Giri, Kenji Imakita and Minoru Fujii; "*Evidence of Ti Interstitials as the Origin of Visible Absorption and Near Infrared Emission from Undoped TiO_2 Nanoribbons: An In-Situ Photoluminescence Study"* **Journal of Physical Chemistry C 117, 23402 (2013).**
5. **Batakrushna Santara**, P. K. Giri, Kenji Imakita and Minoru Fujii; "*Microscopic origin of Lattice Contraction and Expansion in Undoped Rutile TiO_2 Nanostructures*" **Journal of Physics D: Applied Physics 47, 215302 (2014).**
6. **Batakrushna Santara**, P. K. Giri, Soumen Dhara, Kenji Imakita and Minoru Fujii; *"Oxygen Vacancy Mediated Enhanced Ferromagnetism in Undoped and Fe Doped TiO_2 Nanoribbons"* **Journal of Physics D: Applied Physics 47, 235304 (2014).**

Conference presentations:

1. **Batakrushna Santara**, Bappaditya Pal and P. K. Giri; *"High Temperature Ferromagnetism in Co Doped Anatase TiO_2 Nanoparticles Grown by a Ball Milling Method"* International Conference on Materials for Advanced Technology (**ICMAT 2011**), June 26-July 01, 2011, Suntec, Singapore.

2. **Batakrushna Santara** and P. K. Giri; *"Signature of Defect Induced Room Temperature Ferromagnetism in Co Doped Anatase TiO_2 Nanoparticles"*

International Conference on Advanced Nanomaterials and Nanotechnology (**ICANN 2011**), December 08-10, 2011, IIT Guwahati, India. **(Oral presentation)**

3. **Batakrushna Santara** and P. K. Giri; *"Effect of Growth Temperature on the Synthesis of TiO_2 Nanowires/ Nanorods and Nanotubes by a Hydrothermal Method"* International Conference on Advanced Nanomaterials and Nanotechnology (**ICANN 2011**), December 08-10, 2011, IIT Guwahati, India.

4. **Batakrushna Santara** and P. K. Giri; *"Hydrothermal Growth and Characterization of TiO_2 Nanowires on Ti Substrate"* International Conference on Nanoscience and Nanotechnology (**ICONSAT 2012**), January 20-23, 2012, ARCI Hyderabad, India.

5. **Batakrushna Santara** and P. K. Giri; *"Fabrication of Rutile TiO_2 Nanopillars by a Low Temperature Chemical Route"* International Conference on Advanced Nanomaterials (**ANM 2012**), October 17-19, 2012, IIT Madras, India.

6. **Batakrushna Santara** and P. K. Giri; *"Effect of Growth Temperature and Calcinations on Solvothermally Synthesized TiO_2 Nanoporous Nanoribbons"* International Symposium on Processing and Fabrication of Advanced Materials (**PFAM XII 2012**), December 10-13, 2012, IIT Guwahati, India.

7. **Batakrushna Santara** and P. K. Giri; *"Solvothermal Synthesis and Characterization of Ag Modified TiO_2 Nanostructures"* Indo-Singapore Joint Physics Symposium on Physics and Advanced Materials (**ISJPS 2013**), February 25-27, 2013, IIT Kharagpur, India.

8. **Batakrushna Santara**, Gone Rejender and P. K. Giri; *"Fabrication of 3D Flower Like Complex Structures of TiO_2 Nanotubes and Nanopillars with Tunable Architectures on Various Substrates"* Indo-Singapore Joint Physics Symposium on Physics and Advanced Materials (**ISJPS 2013**), February 25-27, 2013, IIT Kharagpur, India.

9. **Batakrushna Santara** and P. K. Giri; *"Native Defect Induced Strong Room Temperature Ferromagnetism in Chemically Synthesized Undoped and Reduced TiO_2 Nanoribbons"* International Conference on Magnetic Materials and Applications (**MagMA 2013**), December 05-07, 2013, IIT Guwahati, India.

10. **Batakrushna Santara** and P. K. Giri; "*Structural, Optical and Ferromagnetic Properties of Cr Doped TiO_2 Nanoribbons Synthesized by a Simple Hydrothermal Method"* International Conference on Nanoscience and Nanotechnology (**ICONSAT 2014**), March 03-05, 2014, INST Mohali, India.

School Attended

1. 5th DST Advanced School on **Nanoscience and Nanotechnology**, January 17 - 23, 2011, IISC Bangalore, India

List of Abbreviations

Abbreviation	Meaning
1D	One dimensional
DMS	Diluted Magnetic Semiconductor
DRS	Diffuse Reflectance Spectroscopy
EDX	Energy Dispersive X-ray
ESR	Electron Spin Resonance
F^+	Singly ionized oxygen vacancy
FESEM	Field Emission Scanning Electron Microscopy
FM	Ferromagnetism
FTIR	Fourier Transform Infrared
HRTEM	High Resolution Transmission Electron Microscopy
NIR	Near Infrared
NR	Nanorod
NRb	Nanoribbon
NP	Nanoparticle
NS	Nanostructures
NT	Nanotube
NW	Nanowire
O_v	Oxygen vacancy
O_i	Oxygen interstitial
PL	Photoluminescence
SAED	Selected Area Electron Diffraction

Abbreviation	Meaning
TEM	Transmission Electron Microscopy
Ti_i	Ti interstitial
TM	Transition Metal
TRPL	Time Resolved Photoluminescence
UV-visible-NIR	Ultraviolet visible Near Infrared
VSM	Vibrating Sample Magnetometer
XPS	X-ray Photoelectron Spectroscopy
XRD	X-ray Diffraction

Chapter 1

Introduction

The exploration of nanoscience and nanotechnology has led to the development of new materials with extraordinary enhanced properties, which are completely different from the bulk counterpart. In the past decades, different preparation methods have been used to synthesize varieties of nanostructures such as nanoparticles, nanotubes, nanowires, nanorods, nanoribbons etc. of metals and semiconductors and their properties and related technological applications were extensively studied. The reduction in size of crystalline structures primarily means that physical principles are more directly related to atoms, but it is normally negligible in bulk. High surface-to-volume ratio (which leads to a larger contact area) and quantum confinement effect are the two unique features of nanostructured materials that modify the characteristic properties, which include structural (unit cell size, network symmetry), electrical (electron transport), optical (band gap, absorption and photoluminescence emission), physico-chemical (crystalline structure, particles size, surface area, chemical reactivity/stability) and magnetic properties. These unique and enhanced properties compared to bulk can open opportunities for fabrication of nanoscale devices and find important technological and industrial applications, depending upon their specific properties, such as in biophysics, biochemistry, biomedicines, environmental purification, sensors, photocatalysts, microelectronic circuits and nanoelectronic devices etc. In this chapter a brief introduction to important features of the titanium dioxide (TiO_2) nanostructures and their potential use in different technological applications are presented. The fundamental issues related to growth mechanism, understanding of native defects, and intrinsic and extrinsic origin of ferromagnetism (FM) in TiO_2 nanostructures are discussed and the motivation for the present work is presented in this chapter. The outline of the thesis and major contributions of this thesis are described at the end of the chapter.

1.1. Polymorphs of TiO_2 and their crystal structures

TiO_2 is a wide band gap semiconductor well-known for its outstanding physical and chemical properties. It can exist mainly in one of the four crystalline forms in nature: tetragonal anatase, rutile, orthorhombic brookite and monoclinic TiO_2(B). Rutile is the most thermodynamically stable phase as compared to anatase, brookite and TiO_2(B) phases and usually convert to rutile upon heating. The conversion of anatase to rutile occurs in the temperature >700 °C, depending upon crystal size and impurity. Each of these forms has specific applications. Rutile is more easily formed as single crystals and thus, it has been the subject of the majority of previous research. Brookite phase is rarely found in nature, in contrast to rutile and anatase. The fourth naturally occurring polymorph is monoclinic TiO_2(B) and this mineral is more rare than brookite. TiO_2(B) is a high pressure phase of TiO_2, generally synthesized by hydrolysis of potassium-titanate or hydrogen-titanate at high temperature and pressure. For example, Marchand et al.[1] reported the first synthesis of TiO_2(B) phase by hydrolysis of $K_2Ti_4O_9$ followed by heating at 500 °C. The details of space group, lattice parameters and densities of various polymorphs are listed in the **Table 1.1**. Besides these polymorphs, other high-pressure polymorphs, i.e., columbite (TiO_2 II phase, space group *Pbcn*),[2] baddeleyite (MI, $P2_1/c$),[3] orthorhombic I (OI, *Pbca*),[4] and cotunnite (OII, *Pnma*),[5] were discovered experimentally. Out of these various polymorphs, we observed pure phase rutile, anatase, TiO_2(B) and their mixed phases in this thesis work under various growth conditions.

Table1.1. Different phases of TiO_2 and their crystal symmetry, space group, lattice parameters and densities are presented. Adapted from Ref.[**6**].

Polymorphs	Crystal structures	Space group	Lattice constants (Å)			Density (g cm^{-3})
			a	b	c	
Rutile	tetragonal	$P4_2/mnm$	4.595	4.595	2.943	4.27
Anatase	tetragonal	$I4_1/amd$	3.777	3.777	9.535	3.90
Brookite	orthorhombic	*Pbca*	9.172	5.443	5.129	4.15
TiO_2(B)	monoclinic	*C2/m*	12.173	3.732	6.537	3.73

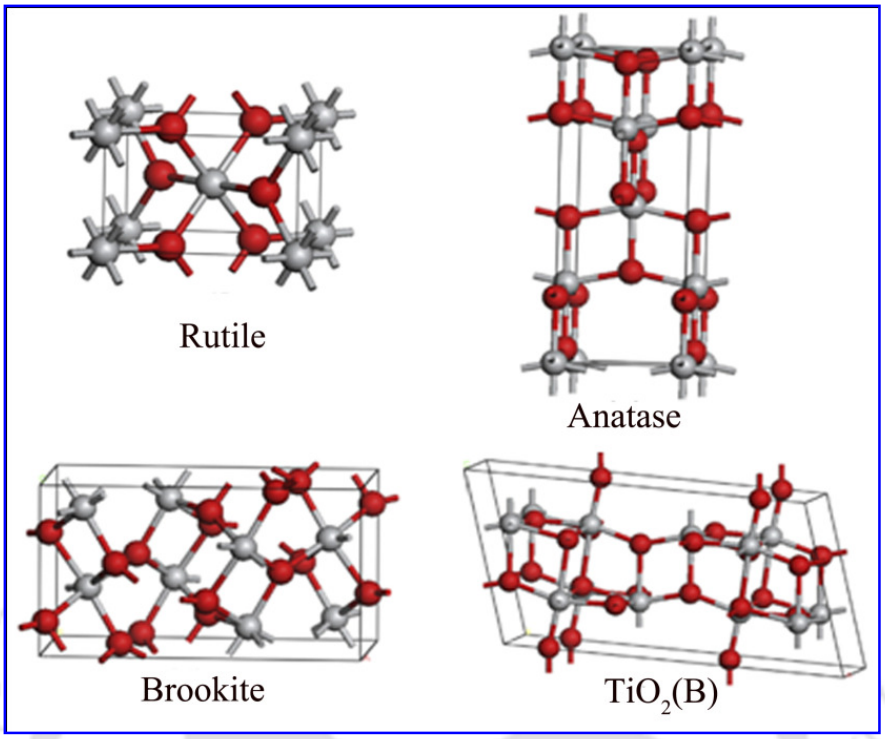

Fig. 1.1. Ball and stick presentation of crystal structure of rutile, anatase, brookite and TiO_2(B) polymorphs; Red ball: O atom, Grey ball: Ti atom. Adopted from Ref. [**6**].

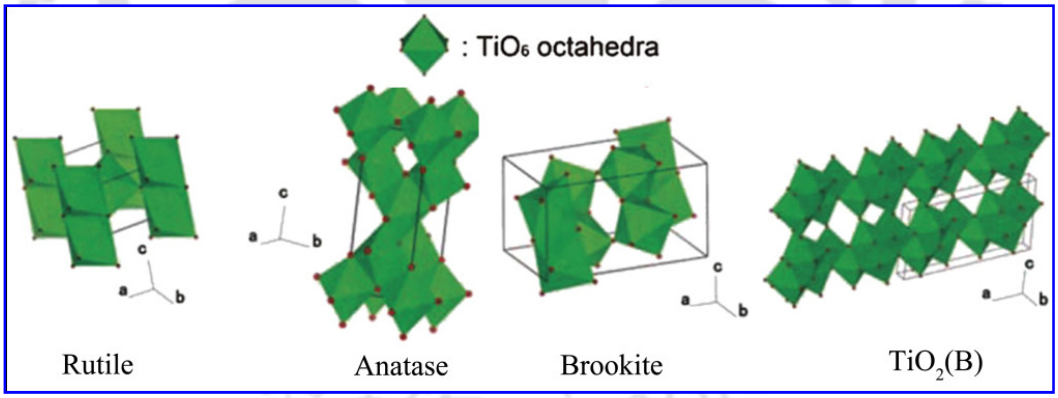

Fig. 1.2. Octahedral stacking representation of rutile, anatase, brookite and TiO_2(B) phases. Adopted from Ref. [**7**].

The crystal structures of anatase and rutile are based on a tetragonal symmetry, in which the Ti^{4+} ions are 6-fold coordinated to oxygen ions. Both are constructed from distorted TiO_6 octahedra, with the relative arrangement of these determining the overall structure. The rutile

structure is based on slightly distorted hexagonal close packing of oxygen ions, whereas the oxygen sublattice in anatase is cubic closed packed. Both structures have edge sharing TiO_6 octahedra, with two and four edges shared in rutile and anatase, respectively. Orthorhombic brookite is of lower symmetry due to its short range order being less regular. In brookite none of the six nearest-neighbor Ti-O bond lengths are identical. The principal structural feature of brookite is a chain of edge-sharing distorted TiO_6 octahedra parallel to c-axis of the orthorhombic lattice, where each octahedron shares three edges. The structure of TiO_2(B) is characterized by two edge-sharing TiO_6 octahedra which are linked to the neighboring doublet of octahedral by corners. The crystalline structures of rutile, anatase, brookite and TiO_2(B) and their polyhedral representation of TiO_6 octahedra are shown in **Fig. 1.1 and 1.2**, respectively.

1.2. TiO_2 nanostructures

Metal oxide semiconductors play a major role in many areas of chemistry, physics and materials science due to the suitability of various applications such as photocatalyst,[8-10] sensors,[11-14] waste-water and environmental cleaning,[15-18] drug delivery,[19] hydrogen production,[20-23] UV photodetectors,[24] dye sensitized solar cells,[25-30] Li ion battery[31-34] and may be applicable for future spintronic and magneto-optic devices[35-37] etc. Among the metal oxide semiconductors, TiO_2 has received wide-spread attention due to its following advantages: excellent stability against photo and chemical corrosion, non-toxicity and biocompatibility, strong oxidizing and reducing ability, low cost on the economical point of view and easily available, very efficient photocatalyst and the realization of room temperature ferromagnetism. Usually bulk TiO_2 is not very efficient for the industrial applications due to less surface area and interacting media, since the above mentioned properties are suitable for the functioning at surface and interface or atomic level. In case of nanostructured TiO_2, with the size reduction, the ratio of number of surface to volume increased which leads to a larger contact area, the decrease of surface free energy and hence a number of physical properties become noticeably pronounced in comparison with those of macroscopic systems. The high surface area brought about by the decreased size is beneficial to many TiO_2-based devices, as it facilitates the reaction/ interaction between the devices and

the interacting media, which mainly occurs on the surface or at the interface and strongly depends on the surface area of the material. Thus, the performance of TiO_2-based technology is largely influenced by the sizes of the TiO_2 building units, apparently at the nanometer scale. The properties also vary with shapes and crystal structures of the shrinking TiO_2 nanomaterials and play important roles for the device performances. The different shapes of the nanostructures highly influence the surface area, carrier mobility, transport and information processing. In this regard, one dimensional (1D) nanostructures such as nanotubes (NTs), nanorods (NRs), nanowires (NWs), nanopillars (NPls) and nanoribbons (NRbs) are more advantageous and promising candidates compared to nanoparticles (NPs) and thin films. 1D nanostructures have direct path for electron transport which helps in the reduction of electron recombination and hence enhance the carrier collections and fast information processing. The various shapes of nanostructures (i.e., nanoparticles, nanotubes, nanowires and nanorods) are shown in **Fig. 1.3**.

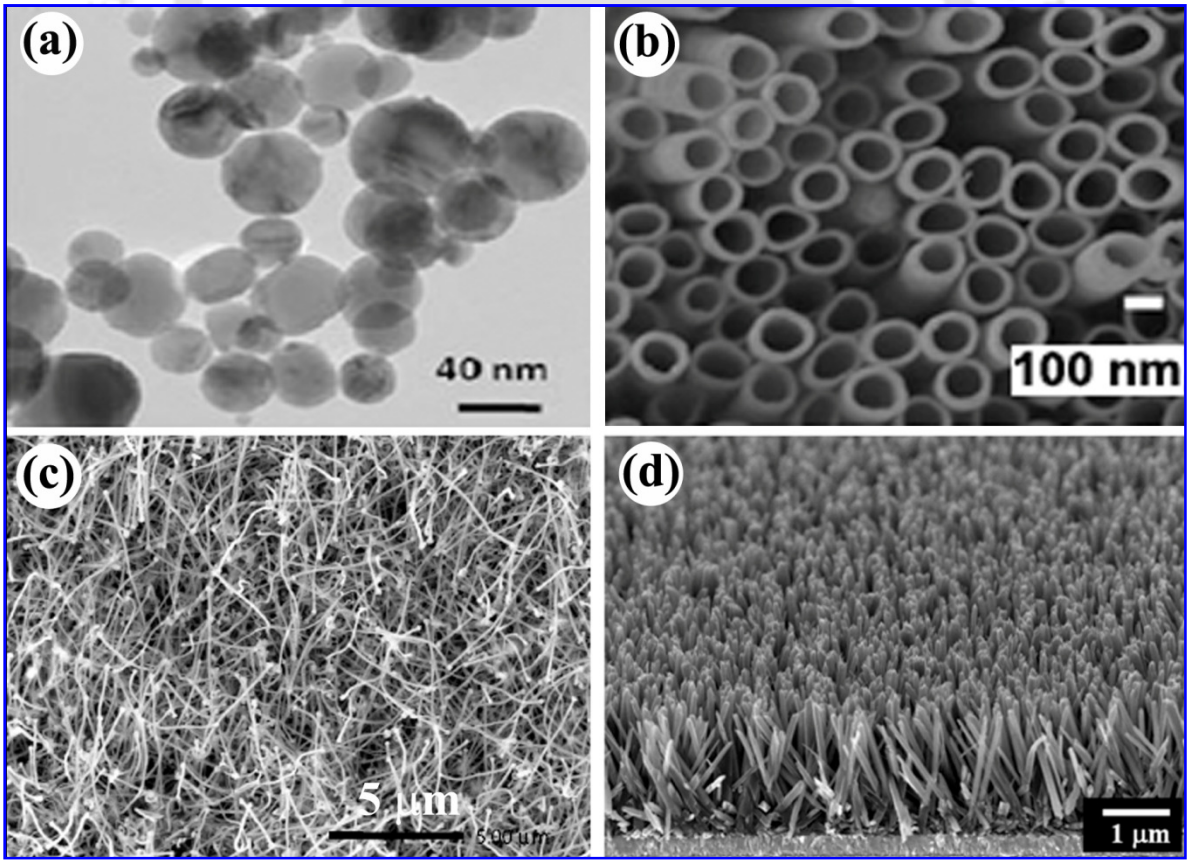

Fig. 1.3. Electron microscopy images of TiO_2: (a) nanoparticles, (b) nanotubes, (c) nanowires and (d) vertical aligned nanorods. Adapted from Ref. [**38, 39, 40, 27**].

1.3. Growth techniques of TiO_2 nanostructures

In a laboratory, TiO_2 is manufactured mainly using titanium isopropoxide ($Ti(OCH(CH_3)_2)_4$),[41] titanium butoxide ($Ti(OC_4H_9)_4$),[24, 27] titanium tetrachloride ($TiCl_4$)[42, 43] and titanium metal powder [40, 44] as precursor. Now-a-days, various shapes and designs of TiO_2 nanostructures have been prepared using commercial TiO_2 powder as precursor[12, 28, 45] and anodic oxidation of Ti foils.[39, 46, 47] TiO_2 nanostructures can be prepared in the form of powder, crystal and thin film. Various methods of preparation are used for the synthesis of different shapes and sizes of TiO_2 nanostructures. These include sol-gel,[42, 43, 48] hydrothermal,[9, 12, 13, 27] solvothermal,[33, 34, 41, 49] electrochemical anodization,[39, 46, 47, 50] chemical vapor deposition,[51-53] physical vapor deposition[40, 44, 54, 55] etc. These growth techniques are briefly discussed below.

1.3.1. Sol- gel method

In general, sol-gel process involves transformation of a colloidal suspension, or a sol, into a gel. A sol is formed from the hydrolysis and polymerization reactions of the precursors induced by water (aqueous sol-gel) or organic solvent (non-aqueous sol-gel) such as alcohol in the presence/ absence of acidic medium (acids adjust the pH and control the hydrolysis). The precursors are usually inorganic metal salts (chloride, nitrate, sulfate etc.) or metal organic compounds such as metal alkoxides. Complete polymerization and loss of solvent lead to the conversion from liquid sol into a gel phase. Further processing of the gel can produce dense thin films, ceramic fibers, ceramic powders and aero-gel.[56] For example, thin films can be prepared on a substrate by spin coating or dip coating using the prepared sol. Under proper synthesis conditions nanomaterials can be obtained. In particular, titanium tetrachloride, titanium isopropoxide and titanium butoxide are generally used as precursors for the typical synthesis of TiO_2 nanomaterial by sol-gel method.[42, 43, 57, 58] The titanium precursor is mixed with either water and/ or organic solvent (such as isopropyl alcohol, ethanol) under stirring for the preparation of homogeneous solution. The acid such as HNO_3 is also added to the homogeneous solution to adjust the pH value which may control the size of the TiO_2 NPs.[58] Then the solution is aged for several hours for hydrolysis and polymerization reactions and TiO_2 hydrosol is prepared. The hydrosol is gelled by drying

and/ or allowed for calcination at different temperatures for removal of residual organic impurities and good crystallinity and finally TiO_2 nanopowder is obtained.

The advantages of the sol-gel method are (i) it is low temperature process, usually room temperature; (ii) easy and simple process (doesn't require any specific costly instrument). However, it has several demerits such as (i) control of hydrolysis and condensation rate is not an easy task; (ii) method of mixing, control of pH, rate of oxidation is too difficult which determines the purity, uniformity and size of the nanoparticles and thus an open question for reproducibility; (iii) the as-prepared samples are amorphous and need annealing for crystallization; (iv) difficult to obtained tunable morphologies such as TiO_2 nanorods, nanowires, nanotubes without using any template.

1.3.2. Hydrothermal method

Hydrothermal process can be defined as any heterogeneous reaction in the presence of aqueous solvent under high pressure and temperature conditions for the dissolution and recrystallization of materials that are insoluble under ordinary conditions. The term hydrothermal has come from two Greek words "hydros" meaning water and "thermos" meaning heat. So, in the broad sense, hydrothermal is the technique that chemical reaction took place in water as a solvent and accelerated by the high temperature and pressure. Hydrothermal process for advanced material synthesis is a highly inter disciplinary subject that the technique is popularly used by chemist, physicists, biologist, hydro-metallurgists, material scientists and engineers, because this technique has several advantages over other synthesis methods, especially for the processing of nanomaterials.

Nanomaterials required control over their size, shape, surface morphologies, crystallinity and hence control on their physico-chemical properties for the application of advanced functional materials. The hydrothermal technique offers special advantages because of highly controlled solubility, diffusivity and reactivity in different solvent media in a closed system. There are several parameters such as temperature, pressure, stirring, reaction duration and pH value of the solution during the reaction which determines the shape, size and crystallinity of nanomaterials that in turn give the desired properties to such nanomaterials. Thus, hydrothermal technology and nanotechnology have a very close link. Usually nanomaterials are synthesized in the form of powder by hydrothermal method. The

nanomaterials of tunable architecture can also be grown on various substrates by this technique. Wide varieties of nanostructures such as NPs, nanosheets, NTs, NRs, NWs, NRbs and nanoflowers are grown by this technique depending upon reaction temperature, reaction duration and precursor used etc.[59-62] For the typical hydrothermal synthesis of TiO_2 nanostructures, titanium isopropoxide, titanium butoxide, titanium tetrachloride and commercial TiO_2 powders are used as precursors.[9, 12, 24, 27, 28, 63] One of the precursors is mixed in strong acidic or base solvent containing water according to the requirement and stirred for 10 - 30 minutes for a uniform mixture of the solution, Then the mixed solution is transferred to an Teflon-lined autoclave for the hydrothermal reaction at a particular temperature (usually varied in the range 120 - 200 °C depending upon the requirement) for a certain reaction duration (generally varied in the range 6 – 24 h). After as usual cooling to room temperature, the as-prepared precipitate is taken out from the autoclave and washed several times with water. If the solvent used is alkaline, then the aqueous acid is added to the precipitate for the ion-exchange reaction between the H^+ and alkali cation. Then, the precipitate is washed several times with water to obtain the pH ~7. Finally TiO_2 is obtained after calcinations at different temperatures (300 – 900 °C). Depending on the growth and calcination temperatures, various phases of TiO_2 like TiO_2(B), anatase and rutile phases are obtained. In particular, it has been reported that the size, morphology and structural properties TiO_2 nanostructures depend on the TiO_2 precursor, reaction temperature, reaction duration, pH of the solution which can be achieved by this technique.[59, 64]

Hydrothermal synthesis is normally conducted in high pressure reactor called autoclave. An ideal autoclave should have the following properties: [65]

(i) Inertness vessel lined within the autoclave to acid, bases or oxidizing agents.

(ii) Ease of assembly or disassembly.

(iii) Sufficient length to obtain a desired temperature gradient.

(iv) Leak-proof with unlimited capabilities of required temperature and pressure range.

(v) Rugged enough to bear high temperature and pressure experiments for long duration without any damage to the system.

(vi) Stirring facility should be maintained for the uniform mixture during the reaction.

The advantages of hydrothermal method includes (i) materials which have a high vapor pressure near their melting points can be grown; (ii) simple low temperature operation (< 200 °C) for large scale production; (iii) a large number of modification can be done during growth such as doping, nanocomposite and heterostructures; (iv) better nucleation control; (v) portable equipment; (vi) consume less energy; (vii) closed system processing; (viii) pollution free process etc. However, the disadvantages of this method include (i) long reaction duration needed; (ii) difficult to reproduce if proper care is not taken such as proper maintaining of temperature and pressure inside the chamber, control over solubility and hydrolysis rate etc.; (iii) dangerous if the pressure is suddenly raised beyond the limit of the autoclave (safety valve is needed); (iv) the reaction solution may come out of the vessel if the mouth lid is not properly tight. In this thesis, we have extensively used the hydrothermal technique for the growth of different TiO_2 nanostructures.

1.3.3. Solvothermal method

The working principle of solvothermal method is same as that of the hydrothermal method. In other words, it is an extension of hydrothermal technique. In this case of hydrothermal technique the solvent is restricted to water while in this case the solvent is non-aqueous (organic solvent). So, this technique is more flexible and better control in terms of morphology control, crystallinity, and chemical compositions. The organic solvent includes ethanol, ethylene glycol, poly ethylene glycol etc.[59] The solvent plays an important role in determining the nanomaterial morphology.[59, 66] Solvents with different physical and chemical properties can influence the solubility, reactivity, and diffusion behavior of the reactants; in particular, the polarity and coordinating ability of the solvent can influence the morphology and the crystallization behavior of the final products. Moreover, in the case of solvothermal technique, the temperature can be elevated much higher than that in hydrothermal method, since a variety of organic solvents with high boiling points can be chosen. We used the solvothermal growth technique for the synthesis of wide varieties of TiO_2 nanostructures in this thesis work.

1.3.4. Electrochemical anodization

Anodization is a promising method for fabricating immobilized TiO_2 NTs on the surface on Ti foil. Generally, the formation of TiO_2 by anodic oxidation depends on the reactions of electrochemical etching and chemical dissolution.[39] The surface morphologies and structures of the anodic TiO_2 films are significantly influenced by the interaction between these two reactions. By changing the electrolyte, the electrochemical etching and chemical dissolution can affect the tunable morphologies of TiO_2 NTs.[39, 46, 67, 68] For example, extremely long and larger pore diameter array of NTs can be achieved using nonaqueous organic polar electrolyte. For the typical synthesis of NTs by electrochemical anodization method requires simple experimental set up which include (i) beaker, (ii) two electrodes (working electrode and counter electrode), (iii) electrolyte, (iv) power supply, and (v) connecting wires.

Pure Ti foil and Pt foil are used as working electrode and counter electrode, respectively. Generally, fluorine ion-based electrolyte (HF/ KF/ NH_4F + H_2O) is used for the formation of TiO_2 NTs. However, HCl is also used as electrolyte, but the nanotube morphology is not so good. The electrolyte can be changed such as using the organic polar electrolyte (dimethyl sulfoxide (DMSO), ethylene glycol (EG)) containing HF/ NH_4F and H_2O instead of aqueous HF/NH_4F affects the tunable morphologies in terms of length, inner diameter, wall thickness, tube-to-tube distances etc.[39, 47, 68] Moreover, the use of different anodization voltage can alter the morphological parameters.[68]

Advantages of anodization method include (i) easy process, (ii) less energy consuming, (iii) growth of well aligned NTs of various lengths up to several microns and tube diameter in the range 20-135 nm. Disadvantages of this technique include (i) restricted to Ti substrate (can also be grown on FTO substrate, but not so good morphology), (ii) tubes are attached to the substrates (not flexible for various applications), (iii) NTs are amorphous in nature and need further annealing for crystallinity (which may affect the morphology), (iv) restricted to tube like structure only.

1.3.5. Vapor deposition technique

Vapor deposition is a technique that requires high temperature and refers to any process in which materials in a vapor state are condensed to form a solid-phase material. The process is generally carried out in a laboratory quartz tube furnace. One end of the tube is connected to

the gas cylinder while the other end is connected to rotary pump (used for evacuating and/ or transport of the vapor). In the vapor deposition process, if the chemical reaction occurs, then the process is called chemical vapor deposition (CVD), otherwise it is termed as physical vapor deposition (PVD).

CVD is the formation of a non-volatile solid film on a substrate by the reaction of vapor phase chemicals (reactants) that contain the desired constituent materials. The reactant gases are introduced into a reaction chamber and decomposed and reacted with precursor material at an elevated temperature and deposited on a substrate. In a typical procedure,[53] titanium acetylacetonate ($Ti(C_{10}H_{14}O_5)$) vaporizing in the low-temperature zone of a furnace at 200-230 °C is carried by a N_2/O_2 gas flow into the high-temperature zone of 500-700 °C, and TiO_2 nanostructures are grown directly on the substrates. The phase and morphology of the TiO_2 nanostructures can be tuned with the reaction conditions. For example, at 630 and 560 °C under a pressure of 5 Torr, single-crystalline rutile and anatase TiO_2 nanorods were formed, respectively, while at 535 °C under 3.6 Torr, anatase TiO_2 nanowalls composed of well-aligned nanorods were formed.[53] The disadvantages of this process are: (i) it includes very high temperature reaction, (ii) exhaust of toxic and hazardous gases, (iii) difficult to control the growth.

PVD process is similar to CVD except that raw material/ precursor, i.e., the staring material that is going to be deposited is in solid form, while in CVD the precursors are introduced to the reaction chamber in gaseous state. The working procedure consists of four steps, i.e. evaporation, transportation, reaction and deposition. It requires very high temperature for the growth of TiO_2 nanostructures. For a typical synthesis of TiO_2 NWs using Ti powder as a source material,[54] 1050 °C temperatures is needed for vaporization. In this system, the source material was in the high-temperature (HT) zone and the Au/Ti/Si substrate (Ti and Au are deposited on Si substrate by sputtering, the Au is used as catalyst) was in the low-temperature (LT) zone. The vacuum system was firstly evacuated down to about 10^{-5} Torr to ensure that the quartz reactor vacuum system was sufficiently clean. The heating ramp was set to 200 °C per minute until the HT zone reached 1050 °C and the LT zone reached 850 °C. For the first 30 min, the flowing argon was introduced into the vacuum system, and maintained at 1 Torr. For the last 30 min, the flow rate of argon and a gaseous mixture of 21% oxygen (O_2) + 79% nitrogen (N_2) were inserted into the vacuum system and

maintained at 600 Torr. After cooling to room temperature, the substrate was taken out of the furnace. The mechanism of growth is called as vapor-liquid-solid phase, since the precursor solid material is first evaporated at an elevated temperature, and transported the vapor to a low temperature zone of the furnace. At this stage, the vapor condenses and transforms to liquid phase and finally converted to solid phase. The demerit of this process involves the very high temperature and vacuum operation.

1.4. Defects in TiO_2 nanostructures: deviation from ideal crystal lattice

Defect engineered TiO_2 nanostructures have received unprecedented attention because intrinsic as well as extrinsic defects play a very crucial and fundamental role in enhancing the material/ device performance. The types, concentration and spatial distribution of intrinsic point defects such as vacancies and interstitial atoms influence the performance of metal oxides in gas sensing, electronics, photonics, solar-induced photochemistry for fuel production and environmental cleanup, and the realization of room temperature ferromagnetism. In particular, recent studies revealed that physical and chemical properties of TiO_2, such as light absorption, photocatalytic activity, gas sensing properties, electrical conductivity and magnetic properties etc. can be modulated by the defect/disorder.[8, 69-76]

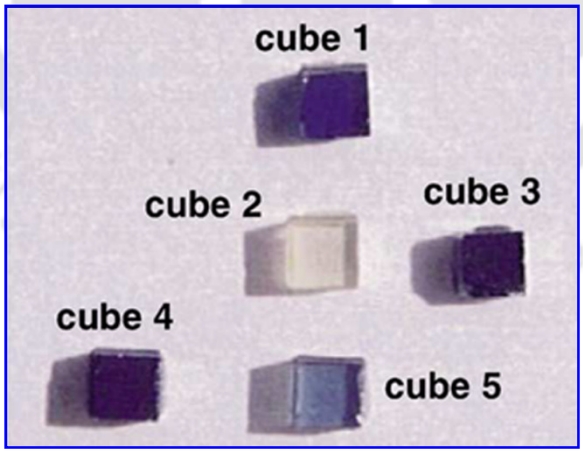

Fig. 1.4. Color centers associated with defects that are formed upon the reduction of rutile TiO_2 single crystals cause a change in crystal color. Digital images of five rutile crystals with increased amounts of bulk defects in the order of cube 2 < cube 5 < cube 1 < cube 4 < cube 3. The lighter crystal possesses a lower amount of bulk defects. The different colors due to the different concentration of oxygen vacancy defects that resulting the pronounced color change from initially transparent to light and eventually dark blue. Adapted from Ref. [**76, 77**].

Before going into the details of the defects, let us first introduce the types of defects and related modified properties of TiO_2 nanostructures. The nature of defects and their occurrences inside the nanomaterial are discussed in details in *Chapter 4*. Any form of deviation from perfect crystal can be treated as a defect. Generally, any real metal oxide material will not have a perfect crystal structures. Even in a single crystal of TiO_2, one finds point defects (misplaced lattice atoms/ ions, vacancies, foreign atoms/ ions) and/ or extended defects such as dislocations. Any interruption of the perfect crystal lattice will affect the band structure of the materials. For example, due to the defects, the single crystal of rutile TiO_2 shows different colors as shown in **Fig. 1.4**. Point defects are further classified into native defects and external impurity defects (dopants) which can be found either on the lattice (substitutional site) or at the interstitial positions. Dislocations are the kind of defects that an extra line of atoms inserted or removed in/ from the crystal which does not extend throughout the crystal.

1.4.1. Intrinsic (native) detects in TiO_2 nanostructures

Native defects in TiO_2 are widely investigated by using density functional theory calculations. All the fundamental native defects such as oxygen vacancy (O_v), O interstitial (O_i), Ti vacancy (Ti_v), and Ti interstitial (Ti_i) have low formation energy, depending upon the O-rich or Ti-rich growth environments and easily appear in non-stoichiometric TiO_2 material.[78-80] While the antisite defects, namely, Ti-antisite and O-antisite, have high formation energies and are hence unstable.[78] Reduced TiO_2 with a Ti excess can be accommodated as O_v and Ti_i. Both of these defect species are likely to be present in the reduced TiO_2 samples, with competition between defect types determined by synthesis conditions and sample history. If the electronic state of the defect (i.e., its charge and distribution) is different from its host TiO_2, it will introduce energy states in the band gap (gap between valence band (VB) and conduction band (CB)). For example, Morgan and Watson[79] reported using GGA+U calculation that the oxygen vacancies and Ti interstitial defects give rise to states within the band gap in both anatase and rutile TiO_2, corresponding to the electrons localized at the Ti^{3+} centers. Both experimental studies and theoretical calculations revealed the presence of defect states within the band gap of TiO_2 and it is identified that the band gap is shifted to visible region due to O_v and Ti_i defects which is

beneficial for visible-light photocatalytic applications.[70, 71, 79-82] The presence of defects thus alters the electronic band structure of the system which influences the operating efficiency of photocatalytic and photovoltaic applications. For examples, recently, Liu et al.[70] reported the enhanced visible-light photocatalysis in Ti^{3+} (originated from O_v) self-doped TiO_2 materials. Moreover, the conductive track in the on-state in resistive switching mechanism (resistive switching random access memory device) is believed to be arising from a percolation path of oxygen vacancies or similar defects across the thin films of TiO_2 material.[73] Thus, the behavior of extra electron and associated defects is critical to the performance of TiO_2 as a catalyst and electronics. The crystal lattice distortions are expected due to the presence of these defects. The lattice relaxation of antase TiO_2 due to various native defects was reported by Na-Phattalung et al.[78] The atomic structure of stoichiometric and defective anatase TiO_2 is shown in **Fig. 1.5**. Thus, intrinsic defects may also alter the lattice parameters in TiO_2, which may cause lattice strain and have some effect on the width of the band gap.[83] The oxygen interstitial O_i is the O-excess defect and is observed as a surface defect when TiO_2 is heat-treated in O-rich environment.

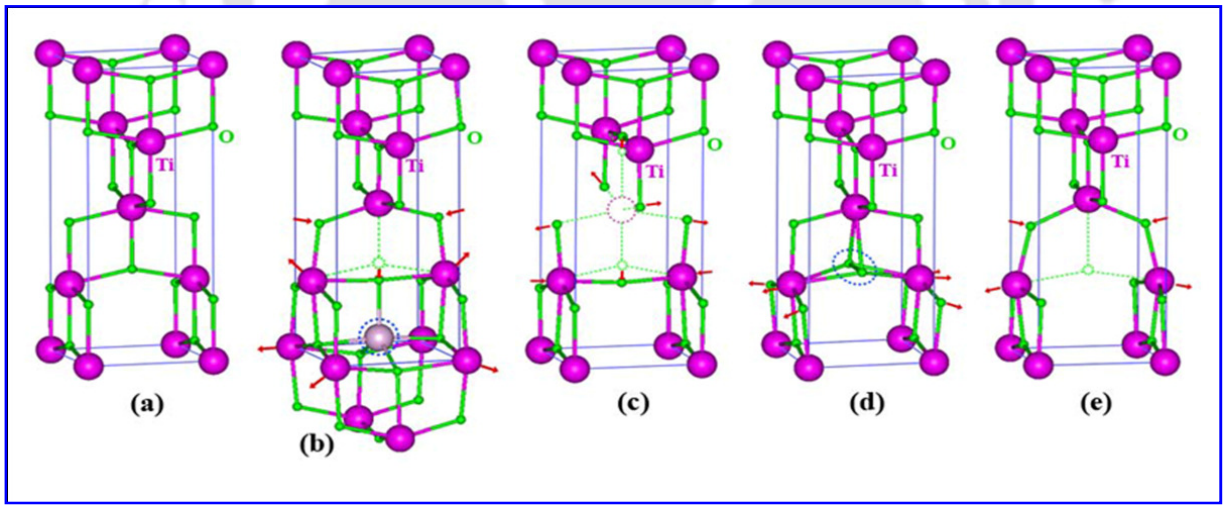

Fig. 1.5. Atomic structure of (a) stoichiometric TiO_2, (b) Ti_i^{4+}, (c) Ti_v^{4-}, (d) O_i^{2-} , and (e) O_v^{2+} defects. Ti atom: purple large sphere, O atom: green small sphere. Relaxation directions of neighboring atoms are indicated by arrows. Adapted from Ref. [**78**].

1.4.2. Extrinsic (dopant) defects in TiO_2 nanostructures

Doping is a process of adding small amount of a foreign atoms/ ions (dopant) into a parent material (host matrix) without forming a second phase. When a large amount of the dopant material is added, there is formation of either a mixed oxide or a second phase, which may or may not be the mixed oxide, depending on the mutual solubility limit of the two components. In this case, one can speak of mixed oxide or cluster formation rather than the doping. The distribution of the dopant in the crystals/ grains of the matrix material can be homogeneous or heterogeneous. In latter case, one speaks of dopant segregation or clustering, which is usually unwanted. Doping in TiO_2 is performed with the aim of the enhancing the properties of the parent TiO_2 for their potential applications. For example, doping cause the band gap narrowing of the TiO_2 nanostructure by introducing the defect states (as either donor or accepter level, depending on dopants) within the band gap. This helps in two ways to improve the photocatalytic reaction, i.e., (i) decrease the band gap energy (i.e. red shift the optical absorption edge) enabling photocatalytic activity under visible light illumination which makes it possible to use the photocatalyst in sunlight, eliminating the necessity to use UV lamps; (ii) increase the quantum efficiency, i.e. increase the number of photons effectively used for the catalyzed redox reaction. This can only be done by increasing the lifetime of the separated charge carriers (electron and hole) by inducing trap sites. However, there are controversies regarding the photocatalytic efficiency, some literatures reported the increase in photocatalytic activity with external doping while some other reported the decrease in the photocatalytic efficiency due to high doping concentration in TiO_2.[84-88]

Additionally, by introducing a dilute amount of cation (transition metal) doping, TiO_2 host exhibit room temperature ferromagnetic behavior which can be applied for the future spintronic and magneto-optic devices. The ferromagnetic properties in transition metal (TM) doped TiO_2 is due to the orbital overlapping of TM cations with the oxygen vacancy and forming a ferromagnetic polaron near the oxygen vacancy.[89, 90] But there are lots of controversy related to the ferromagnetism (FM) in TM doped TiO_2 system, whether the FM is due to the TM cluster, segregation of secondary magnetic phases [91, 92] or solely related to the intrinsic nature.[89, 90] The details of intrinsic and extrinsic nature of the FM will be discussed in *section 1.5.3.1 and 1.5.3.2*. Moreover, effects of introducing dopants can be an

increase in electrical conductivity and the compensation of other defects. These may also influence the semiconductor electronic devices.

Foreign atoms are associated with defect formation in the original crystal lattice. The addition of a dopant, i.e., a foreign atom/ion will affect the crystal lattice structure of the matrix, forming a defect. In the case of TiO_2 there are two possibilities for dopant introduction: (i) the dopant is introduced as a metal oxide $MO_{n/2}$, with the cation M^{n+} replacing Ti^{4+} or (ii) a dopant anion is introduced to replace O^{2-}. The exact nature of the defect depends on the position the dopant atom/ion occupying the lattice. To determine which lattice position the cation can occupy, one has to look at its size. The following discussion can only be an approximation as ion sizes are not constant for a given ion. They depend on the coordination environment defined by the site, the ion occupying the crystal lattice, the type and number of the ligands surrounding it as well as the nature of the bonding between them. The fact is that the ion adjusts its size to the lattice place it occupies. The ion sizes quoted in the following are average values for a coordination number of 6 in an octahedral site (**Table 1.2**). The larger (size) dopant cations than that of the parent TiO_2 cation can be expected to occupy the interstitial site while cations smaller than or similar in size to Ti^{4+} can occupy the substitutional lattice site. Some cations can take both positions due to their intermediate size. According to its valence and its occupation site, vacancies in the cation or anion lattice or charge carriers must be created for charge balance, which requires that the crystal is electrically neutral. For example, if the valence of the dopant cation is less than that of the lattice cation, then oxygen vacancy can be expected for charge neutrality. For example, Krol et al.[93] have revealed that the substitution of Fe^{3+} for Ti^{4+} ions in the lattice can result in formation of oxygen vacancies in the lattice of TiO_2. In addition, Domen et al.[94] have reported that the doping of a cation with valence lower than that of the parent cation (Ti) extrinsically introduces oxygen vacancies, inhibiting the formation of Ti^{3+}. The doping of the trivalent cation (M^{3+}) can occupy the Ti^{4+} sites as a lower valence cation. As a result, the formation of oxygen vacancies is facilitated without forming Ti^{3+} species. In contrast, the higher valence cation stabilizes the Ti^{3+} without producing oxygen vacancies. The pentavalent cation (M^{5+}) dopants occupying Ti^{4+} sites as a higher valence cation would result in the formation of Ti^{3+}.[74]

Since the nature of the individual dopant as well as its concentration and distribution determine the defect structure of the crystal, it will also influence the electronic and optical properties of the resulting TiO_2 crystal. In this study we have chosen to look at the doping of Fe, Cr and Co in TiO_2 nanostructures for their influence on the optical and magnetic properties. The average cation radii of Ti, Fe, Cr and Co in (Å) unit for the coordination number 6 of octahedral coordination system are shown in **Table 1.2**.

Table 1.2. Average cation radii of Ti, Fe, Cr and Co in (Å) unit for the coordination number 6 of octahedral coordination system. "NA (not applicable)" denotes this ion does not exist.

Valence → Element ↓	**+6**	**+5**	**+4**	**+3**	**+2**
Ti	NA	NA	0.75	0.81	1.0
Fe	NA	NA	0.73	0.69 0.79 (high spin)	0.75 0.92 (high spin)
Cr	0.58	0.63	0.69	0.76	0.87 0.94 (high spin)
Co	NA	NA	0.75 (high spin)	0.69 0.75 (high spin)	0.79 0.86 (high spin)

1.5. Properties of TiO_2

1.5.1. Electronic band structures

Band structure is one of the fundamental electronic properties of any semiconductor crystalline material. Wang and Lewis[95] used first principle tight-binding molecular dynamics simulation technique (called Fireball), which is based on density-functional theory (DFT) with a nonlocal pseudo potential scheme, for the band structure calculation of TiO_2 phases. From a theoretically predicted equilibrium structure, the self-consistent electronic band structure has been calculated for rutile and anatase TiO_2. Following the standard practice in presenting electronic band structures, band structures are calculated along the high-symmetry directions of the irreducible Brillouin zone. For the rutile structure, the calculated direct band

gap is 3.05 eV (Γ_v - Γ_c).[95] An indirect band gap of 2.92 eV is also obtained from Γ_v to M_c.[95] Ekuma and Bagayoko[83] reported similar direct band gap of 3.05 eV (Γ_v - Γ_c) and indirect band gap of 2.95 eV (R_v - Γ_c) for rutile TiO_2 using Bagayoko – Zhao – Williams (BZW) based on self-consistent *ab initio* calculation. For anatase, the indirect band gap of 3.0 eV (Γ_v - M_c) and direct band gap of 3.26 eV (Γ_v - Γ_c) is reported.[95] Zhang et al.[96] used hybrid DFT based on Dirac-Slater exchange, the HF (Hartree-fock) exchange, and the LDA (local density approximation) correlation to calculate the band structure of brookite TiO_2. A direct band gap of 3.1 eV was reported at Γ point. Yahia et al.[97] calculated the indirect band gap (M- Γ) of 2.68 eV for TiO_2(B). The band structures of rutile, anatase and brookite are displayed in **Fig. 1.6**.

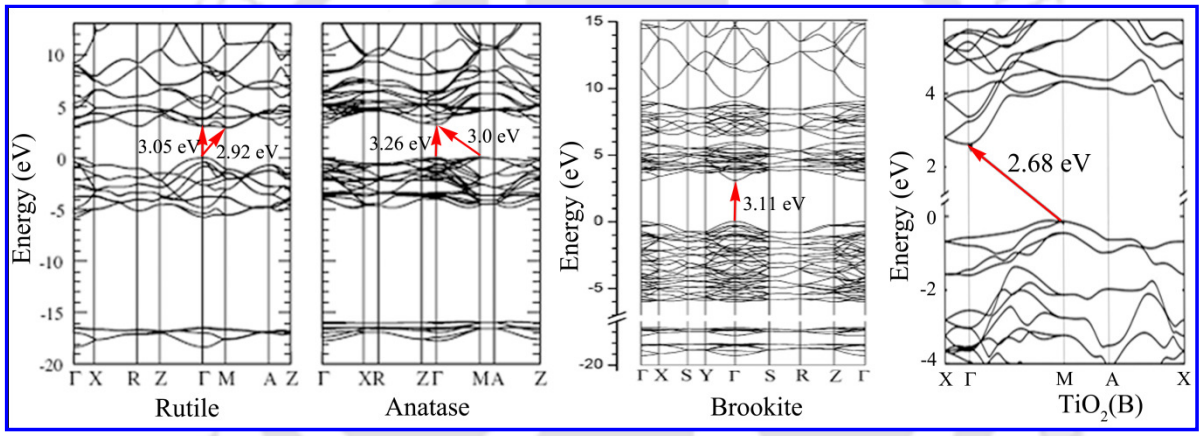

Fig. 1.6. Band structures of rutile, anatase, brookite and TiO_2(B) phases of TiO_2. The arrow in each case indicates the band transition from valence band maximum to conduction band minimum. Adapted from Ref. [**95, 96, 97**].

The electronic density of states (DOS) for rutile, anatase and brookite phases calculated by Landmann et al.[98] are shown in **Fig. 1.7**. The partial density of states feature shows predominantly O 2p-like valence band states and Ti 3d-like conduction band states around the band edges for all three major phases. As indicated in DOS, the broad Ti 3d-like bands show a distinct separation into two sub-bands which are assigned to e_g and t_{2g} states. Due to the different Ti-O bond lengths, Ti 3d orbitals will split into two sets of t_{2g} and e_g orbitals. In an octahedral-type crystal field, the five unoccupied d-states of the central Ti ion

are split into the twofold-degenerate e_g-like states with $d_{x^2-y^2}$ and d_{z^2} character and the energetically lower lying threefold-degenerate t_{2g}-like d_{xy}, d_{yz} and d_{xz} type states.[98]

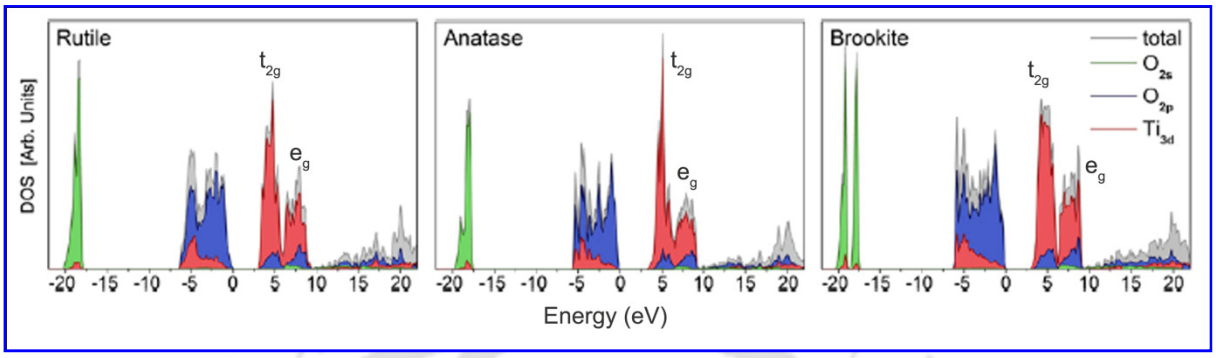

Fig. 1.7. Electron density of states in rutile, anatase and brookite TiO_2. Adapted from Ref. [**98**].

The electronic band structures are modified by the presence of native defects and/ or dopants in TiO_2 materials. The missing of an oxygen atom in TiO_2 from the bulk or surface results in one or two electrons localized in an oxygen vacancy state. As a result, the place occupied by the O^{2-} anion in the regular lattice is taken by one or two "free" electrons in the defective crystal. These electrons located on the oxygen vacancy states have a direct effect on the electronic structure of TiO_2 by forming a donor level below the conduction band.[74] From the ultraviolet photoemission spectroscopy and electron energy loss spectroscopy studies, it is known that the energy level of localized donor states originating from oxygen vacancies lie at about 0.7 – 1.0 eV below the conduction band of TiO_2.[99-101] Moreover, the removal of neutral oxygen atoms to form oxygen vacancies can also cause the redistribution of the excess electrons among the nearest neighboring Ti atoms around the oxygen vacancy site, and form shallow donor states below the conduction band originating from Ti 3d orbits (i.e. Ti^{3+}).[102] The formations of singly ionized oxygen vacancy states is also demonstrated as donor states in rutile TiO_2.[80] The electrons in Ti interstitial defects occupy localized states at the bottom of the conduction band and act as shallow donors in TiO_2.[80] These localized donor states are reported theoretically[78, 80, 81] and also probed experimentally.[82] The density of states of the defect sites for the neural oxygen vacancy, singly ionized and doubly ionized oxygen vacancy, and Ti interstitial defects in rutile TiO_2 are calculated by screened-exchange hybrid

density functional method, which are shown in **Fig. 1.8**. It has been demonstrated that for the neutral oxygen vacancy the defect state is occupied by two electrons while for the singly ionized oxygen vacancy the defect state is occupied by one electron. However, there is no gap state for doubly ionized oxygen vacancy because the excess electrons at the vacancy site have been ionized.[80]

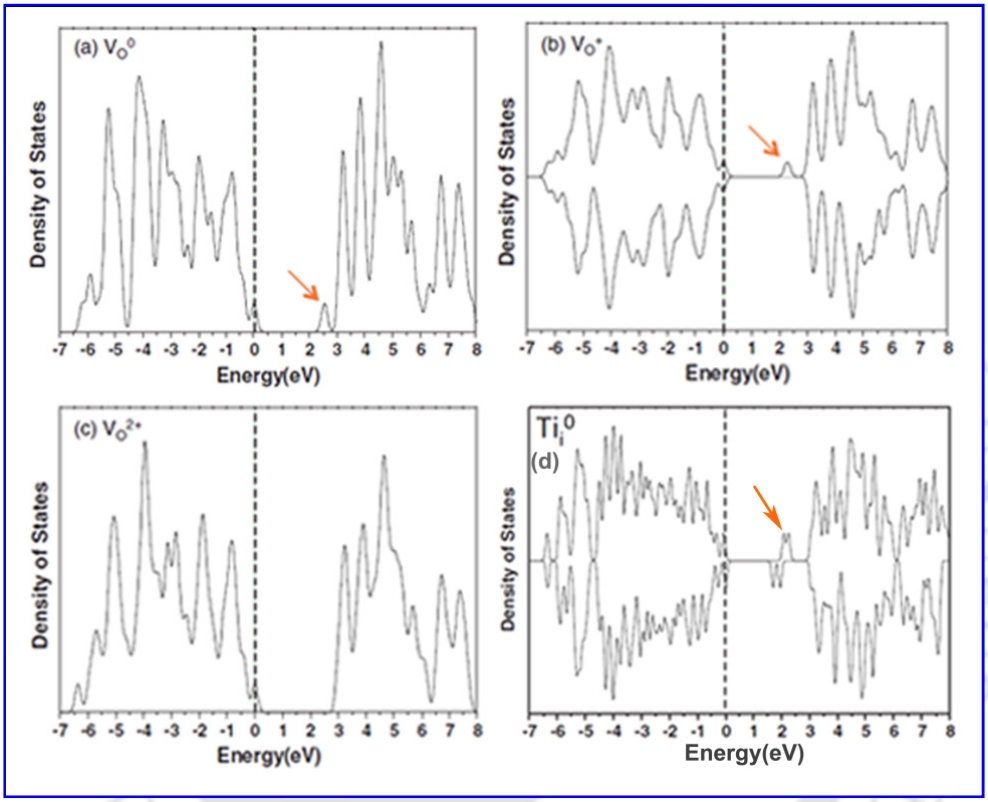

Fig. 1.8. Density of states for oxygen vacancy and Ti interstitial defects in rutile TiO_2: (a) neutral, (b) singly ionized and (c) doubly ionized oxygen vacancy; (d) Ti interstitial defects. The arrows indicate the defect states within the band gap. For singly ionized oxygen vacancy and Ti interstitial the spin-up and spin-down states are shown, respectively, above and below the abscissa. The top of the valence band is set to be the zero energy and is denoted by the vertical dash line. Adapted from Ref. [**80**].

1.5.2. Optical band gap

The electronic band gap of a semiconductor is the energy spacing between its valence band maximum (VBM) and its conduction band minimum (CBM). In all semiconductors the band gap transition can be facilitated with light, i.e., these materials are photo-activated. Upon the

illumination of light, the electrons are excited from valence band (VB) to conduction band (CB), the band gap of a semiconductor results in the resonance absorption of light at a particular wavelength λ_{bg} which corresponds to at least E_{bg} (the energy gap between VBM and CBM). There are two main types of band gap transition in semiconductors, i.e., (i) direct band gap, (ii) indirect band gap transition.

(i)Direct band gap transition:

In this case, the electronic transition from the VB to the CB is electrically dipole allowed. In some materials direct transitions are forbidden for the wave vector $k = 0$, but are allowed for values of $k \neq 0$. Here one speaks about a '*direct forbidden*' as compared to a '*direct allowed*' transition.

(ii) Indirect band gap transition:

In this case, the electronic transition from VB to CB is electrically dipole forbidden and the transition is phonon assisted, i.e., both energy and momentum of the electron-hole pair created are changed in the transition. Therefore, absorption and emission of light are weaker compared to those of direct band gap semiconductors, since they involve a change in momentum.

1.5.2.1. Calculation of the band gap from the optical absorption

The dependence of the band gap energy (E_{bg}) and absorption coefficient (α) of optical absorption is given by equation (1.3)[103]

$$\alpha h\nu = A\,(h\nu - E_{bg})^{\gamma} \qquad (1.1)$$

where A is a constant, γ a value representing the optical transition mode and $h\nu$ the photon energy (in eV). In other words, α is always proportional to the difference between the photon energy and the band gap, to some exponent γ. The exponent γ depends on the optical transition mode whose values are listed in **Table 1.3**. Fitting the experimental absorption data for correct choice of γ to this model reveals the band gap and the nature of transition that is occurring. From the optical absorption spectra, the band gap can be calculated by extrapolating the tangent of $(\alpha h\nu)^{1/2}$ *versus* $h\nu$ plot to $(\alpha h\nu)^{1/2} = 0$ for indirect allowed band gap and $(\alpha h\nu)^{2}$ *versus* $h\nu$ plot to $(\alpha h\nu)^{2} = 0$ for direct allowed band gap which are known as Tauc's plot.[104]

Table 1.3. List of values of the exponent γ with respect to different optical transition modes for the equation (1.1).

γ	Transition mode
1/2	Direct allowed
3/2	Direct forbidden
2	Indirect allowed
3	Indirect forbidden

1.5.2.2. Band gap transition in TiO_2

The different phases of TiO_2 exhibit different nature of band gap transition. According to the experimental results and theoretical calculations, rutile TiO_2 exhibits both direct and indirect band gap.[105, 106] Kavan et al.[107] reported that rutile TiO_2 has a direct band gap of 3.0 eV, while Tang et al.[108] determined an indirect band gap of 3.0 eV based on their experimental results. Most of the experimental studies[107, 108] suggested that anatase has an indirect band gap 3.2 eV. Yang et al.[9] and Welte et al.[109] reported the indirect band gap of 3.19 and 3.25 eV for anatase TiO_2, respectively. The experimental studies on band gap energy of brookite TiO_2 suggested a band gap ranging from 3.1 – 3.4 eV.[110, 111] The direct band gap transition having gap energy of 3.4 eV is reported by Hu et al.,[112] while Koelsch et al.[113] suggested an indirect band gap nature of 3.4 eV for brookite TiO_2. Paola et al.[114] determined that brookite has an indirect band gap of 3.25 eV. The indirect band gap of TiO_2(B) is reported to be 3.05 eV experimentally. Li et al.[10] reported a band gap of 3.2 eV for TiO_2(B) phase. The band gaps of all the main polymorphs of TiO_2 are in UV region of light irrespective of the nature of optical transition.

The optical absorption properties of TiO_2 can be manipulated by the defect engineering. The oxygen vacancy and Ti interstitial defect states give rise to localized states within the band gap of the TiO_2 materials.[70, 82] So, the light absorption is tuned from UV to visible light by introducing the native defects. Moreover, the Ti^{3+} which is formed due to oxygen vacancy can form a shallow donor states below the conduction band which contributes to visible light response. The anion and cation doping introduce the defect states

within the band gap of TiO_2. This results in red shift of the optical absorption edge which helps to absorb more light over the entire visible light and enable the material to utilize sun light more efficiently for photocatalytic applications.

1.5.3. Magnetic properties

Over the past decade, intensive research efforts have been made by researchers around the globe on exploring the effects of dilute doping of magnetic impurities on the physical properties of functional non-magnetic metal oxides such as TiO_2, after the discovery of room temperature ferromagnetism (RTFM) in Co doped TiO_2 material in 1980 by Matsumoto et al.[36] This effort is primarily aimed at exploring spin transport and magneto-optic effects in oxide based semiconductor TiO_2 nanomaterial for the future spintronic and magneto-optic device applications. Despite several studies reported on TiO_2-based diluted magnetic semiconductor (DMS), there is no clear agreement about the nature and origin of FM. Some reports suggested that the FM is originated from the secondary ferromagnetic phases, clusters and contaminations[91, 92] while some other reports supported the intrinsic nature of FM mediated by carriers or defects.[89, 90] The controversial results among different research groups suggest the sensitive dependence of magnetism on fabrication, growth and doping agents which led to interesting questions regarding the specific role played by defects. Indeed, most recent theoretical and experimental studies have led to the rapid development of the field of defect induced FM in TiO_2 system. Ogale[115] presented a succinct review article on the ferromagnetism of various doped and defective TiO_2 system and the interpretation of intrinsic and extrinsic FM in the TiO_2 DMS in thin films, based on the results of several authors. Based on the reported experimental and theoretical results for both undoped and doped TiO_2 system, the nature of FM in TiO_2 DMS can be categorized as: (i) intrinsic FM, and (ii) extrinsic FM.

1.5.3.1. Intrinsic FM in TiO_2

For the case of homogeneous dilute concentration of doping of transition metal into the TiO_2 crystal lattice, the resulting material exhibit ferromagnetic ordering. The most of the reported intrinsic FM is explained on the basis of either carrier mediated or bound magnetic polaron (BMP) model (F-center model, F is the color center arising due to oxygen vacancy). Yamada

et al.[116] reported a systematic study of the structural, electronic and magneto-optic properties of the thin films of anatase TiO_2 doped with Co using pulsed laser deposition (PLD). They did not observed any evidence of Co segregation by using different *in-situ* and *ex-situ* characterizations. Their magneto-optic circular dichroism (MCD) study indicated that the interaction between the charge carriers and Co impurities is essential to realize ferromagnetism in this system. Subsequently, Toyosaki et al.[117] also performed MCD studies on Rutile $Ti_{1-x}Co_xO_{2-d}$ as a function of "*x*" and "*d*" values to explore the phase diagram for the appearance of FM and to examine the connection between O(Optical)-MCD and anomalous hall effect (AHE). They correlate the optical absorption data and O-MCD results and suggested a carrier induced intrinsic mechanism of ferromagnetism.

Droubay et al.[118] studied the case of Cr doped TiO_2 for possible intrinsic DMS ferromagnetism. Cr was found to be in +3 state throughout the films found from Cr K-shell x-ray absorption near-edge spectroscopy and no evidence for either elemental Cr or half-metallic CrO_2 was found. RTFM was aligned in-plane, with a saturation magnetization of ~0.6 μ_B /Cr atom for Cr concentration of 9%. The films were found to be insulating as grown, which implied that the electrons associated with oxygen vacancies introduced for charge balance were localized. This further implied that a magnetic exchange other than carrier-mediated type could be operative. The authors suggested that the F-center model proposed by Coey[119] could be consistent with their results. In this model, the F-center electrons are suggested to polarize the Cr spins yielding ferromagnetic coupling.

Recently, RTFM have been observed in undoped TiO_2 which help to settle the controversies about the issues related to the role of defects in the ferromagnetic ordering.[72, 120, 121] The FM in undoped TiO_2 is mainly induced by oxygen vacancy. The presence of oxygen vacancy in TiO_2 locally traps the electrons forming the F center and one of the electrons tends to occupy the nearby localized 3d orbit and convert Ti^{4+} ions to Ti^{3+}, yielding F^+ center. The electron in F^+ center localizes and forms BMP by ordering the Ti^{3+} ($3d^1$) electron spin neighboring the oxygen vacancies, thereby gaining exchange energy. The s-d exchange interaction between the $1s^1$ electron spin in the F^+ center in the vicinity of $3d^1$ electron spin of Ti^{3+} ions within an orbit around oxygen vacancies favors long range FM.[122] The Ti^{3+} and F^+ defects are identified by x-ray photoelectron spectroscopy, electron spin resonance and photoluminescence measurement techniques.

1.5.3.2. Extrinsic FM in TM doped TiO_2

The extrinsic FM can occur in TM doped TiO_2 DMS due to the presence of ferromagnetic (dopant) clustering or formation of ferromagnetic secondary phases. Kim et al.[123] prepared epitaxial Fe-doped TiO_2 rutile films on rutile TiO_2 (110) substrates, and studied the compositional, structural, morphological and magnetic properties. Clusters of mixed TiO_2 rutile and Fe_3O_4 were seen to form on the surface of an epitaxial rutile film during the growth. The observed RTFM was attributed to the formation of secondary phase Fe_3O_4. The same group[92] investigated FM in Co-doped anatase TiO_2 thin films using magnetic circular dichroism (MCD) at the Co $L_{2,3}$ absorption edges. The magnetic moment was observed to be ~0.1 μ_B /Co, but the MCD spectral line shape was found to be nearly identical to that of Co metal implying that the ferromagnetism originated from a small amount of clustered Co. With thermal treatments at 400 °C, the MCD signal was seen to increase with an increase in the moment to ~1.55 μ_B /Co, close to ~90% of the moment of Co metal. The cluster size in the annealed sample was observed to be 20–60 nm. Their result once again emphasized the issue of cobalt in homogeneity and clustering in this system. Noh and co-workers[124] studied Co doped anatase films made by Co ion implantation and found clustering effects as reflected by the observation of superparamagnetism. Co clustering effects have also been reported by Kim and co-workers[125] in chemical vapor deposited Co doped TiO_2 films and nanobelts. These works collectively brought out the possibilities of extrinsic effects in the case of this TiO_2 based DMS system.

The research discussed in *section 1.5.3.1 and 1.5.3.2* leads one to conclude that transition element doped TiO_2 is a complex DMS system to understand the exact origin of FM. The intrinsic and extrinsic FM depends significantly on the growth methods and conditions as well as structural forms and conductivities. At high concentrations of doping, possibility of coexistence of intrinsic and extrinsic ferromagnetism exists; the concentration at which this would occur depends on the growth details.

1.6. Applications of TiO_2

TiO_2 powders have been commonly used as white pigments in sunscreens, paints, ointments, and toothpaste from ancient times. Among the other metal oxide semiconductors, TiO_2 has

been received wide-spread attention due to its unique properties such as stability against photo- and chemical corrosion, high oxidizing and reducing ability, excellent photocatalyst, hydrophilicity, nontoxicity, biocompatibility and low cost which make it a promising candidate for wide variety of potential applications such as water purification and environmental cleaning,[15-18] self cleaning,[126] antifogging,[126] lithium ion battery,[31-34] drug delivery,[19] hydrogen production,[20-23] gas sensors,[11-14] dye sensitized solar cell (DSSC)[25-30] and spintronic devices.[35, 36] Some of the potential applications of TiO_2 as an advanced material are discussed in this section.

1.6.1. Water splitting for hydrogen production

An enormous research effort has been devoted to the study of the properties and applications of TiO_2 nanomaterial under light illumination (both UV and visible) since the discovery of photocatalytic splitting of water on a TiO_2 electrode in 1972 (Fujishima and Honda).[23] Photocatalytic splitting of water into H_2 and O_2 using TiO_2 nanomaterials continues to be a dream for clean and sustainable energy sources to overcome the future energy crisis which are currently being faced by the humanity.

A schematic diagram of electrochemical photocell designed for the hydrogen and oxygen evolution from water splitting is shown in **Fig. 1.9**, which was exposed to UV light and was connected to platinum and TiO_2 electrode through an electrical load.[126] When TiO_2 electrode was irradiated with light consisting of energy larger than its band gap, electrons and holes are generated in the conduction and valence bands, respectively. Photocurrent flowed from Pt electrode to the TiO_2 electrode through the external circuit. The direction of current revealed the oxidation reaction (oxygen evolution) occurs at the TiO_2 electrode and the reduction reaction (hydrogen evolution) at the Pt electrode. This observation is an indication that water can be decomposed into oxygen and hydrogen, without application of external voltage which is known as "artificial photosynthesis process". The following equations (1.2) - (1.5) represent the chemical decomposition of water into O_2 (at TiO_2 electrode) and H_2 (at Pt electrode).[126]

$$TiO_2 + h\nu \rightarrow e^- + h^+ \qquad (1.2)$$

(at the TiO_2 electrode)

$$2H_2O + 4h^+ \rightarrow O_2 + 4H^+ \qquad (1.3)$$

(at the Pt electrode)

$$2H^+ + 2e^- \rightarrow H_2 \qquad (1.4)$$

The overall reaction is

$$2H_2O + 4h\nu \rightarrow O_2 + 2H_2 \qquad (1.5)$$

The photo-generated electrons and holes cause redox reactions. Water molecules are reduced by the electrons to form H_2 and oxidized by the holes to form O_2, leading to overall water splitting. The width of the band gap and the potentials of the conduction and valence bands are important. Surface properties such as surface states, surface chemical groups, surface area, and active reaction sites are also important. Other factors such as charge separation, mobility, and lifetime of photogenerated electrons and holes affect the photocatalytic properties of TiO_2.

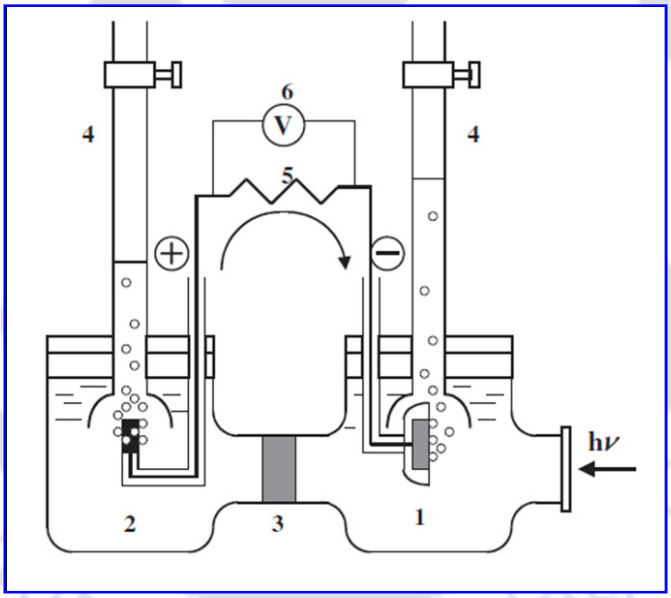

Fig. 1.9. Schematic diagram of electrochemical photocell. (1) n-type TiO_2 electrode; (2) platinum black counter electrode; (3) ionically conducting separator; (4) gas buret; (5) load resistance; and (6) voltmeter. Adapted from Ref. [**126**].

It has been reported that pure TiO_2 could not easily split water into H_2 and O_2 in the simple aqueous suspension system. The main problem is the fast, undesired electron-hole recombination reaction. Therefore, it is important to prevent the electron-hole recombination process. The Pt-TiO_2 system could be illustrated as a "short circuited" photoelectrochemical

cell, where a TiO_2 semiconductor electrode and a platinum-metal counter electrode are brought into contact. However, water splitting of hydrogen production has been done using TiO_2 powder in aqueous solution in the presence of sacrificial reagent by illuminating both UV and visible light. The role of sacrificial reagents is shown in **Fig. 1.10**.[56] When the photocatalytic reaction is carried out in aqueous solutions including easily oxidizable reducing reagents, photogenerated holes irreversibly oxidize the reducing reagents instead of water. This makes the photocatalyst electron-rich, and a H_2 evolution reaction is enhanced, as shown in **Fig. 1.10(a)**. On the other hand, in the presence of electron acceptors such as Ag^+ and Fe^{3+}, the photogenerated electrons in the conduction band are consumed by them and an O_2 evolution reaction is enhanced, as shown in **Fig. 1.10(b)**. The photoefficiency of the process can be improved by the addition of sacrificial reagents.[127] The sacrificial reagents help separation of the photoexcited electrons and holes. Various compounds such as methanol, ethanol, EDTA (an ethylenediaminetetraacetic derivative), Na_2S, and Na_2SO_4 or ions such as I^-, IO^{3-} and CN^- have been used as sacrificial reagents.[127-130]

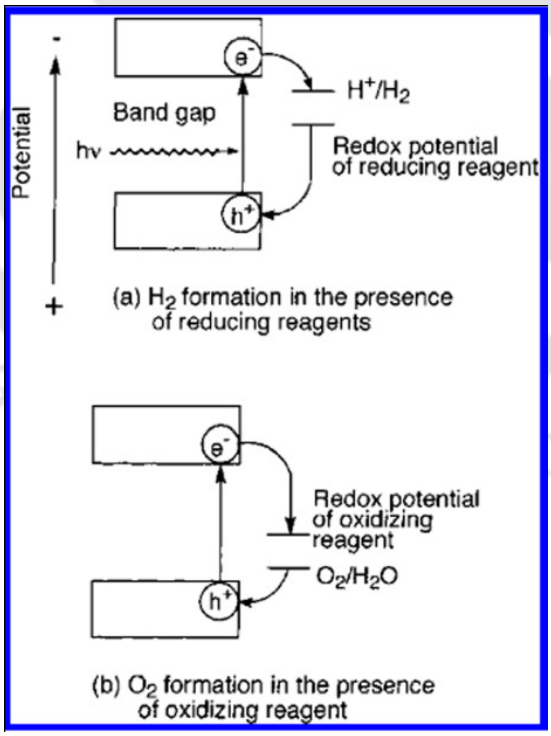

Fig. 1.10. Schematic diagram for photcatalytic (a) H_2 and (b) O_2 evolutions in the presence of the sacrificial reagents. Adapted from Ref. [**56**].

1.6.2. Degradation of organic pollutants (Water and air purification)

The photocatalytic activity is applied to the utilization of the strong photoproduced oxidation power of TiO_2 for the degradation of organic harmful pollutants. In this case, platinization of TiO_2 or use of scavengers are not necessary, TiO_2 powder itself can be used under ambient condition for the oxidation reaction of harmful compounds. For the first time, Frank and Brad in 1977 described the decomposition of cyanide in the presence of aqueous TiO_2 suspensions.[131] The detoxications of harmful compounds in both water and air were demonstrated using powder TiO_2 actively as potential purification methods of waste water and polluted air.[15, 16, 18]

When TiO_2 is exposed to light with photon energy equal or larger than the band gap, an electron in the VB jumps to the CB. The equations (1.6) - (1.10) describe the formation mechanism of hydroxyl radicals ($OH^{\bullet}$).[132] The highly reactive hole generated in TiO_2 in the VB can interact with water (H_2O) and/ or hydroxyl (OH^-) adsorbed on the TiO_2 surface and produce hydroxyl radicals ($OH^{\bullet}$). In addition to holes, electrons excited to the CB can interact with oxygen molecules (O_2) on the surface, leading to superoxide ions ($2O^{\bullet\,-}$). The resulting superoxide ions ($2O^{\bullet\,-}$) can further react with an adsorbed water, leading to hydroxyl radicals.

$$TiO_2 + h\nu \rightarrow TiO_2 + e^-_{cb} + h^+_{vb} \qquad (1.6)$$

$$h^+_{vb} + H_2O_{ads} \rightarrow OH^{\bullet} + H^+ \qquad (1.7)$$

$$h^+_{vb} + OH^-_{ads} \rightarrow OH^{\bullet} \qquad (1.8)$$

$$e^-_{cb} + O_2 \rightarrow O_2^{\bullet -} \qquad (1.9)$$

$$2O_2^{\bullet -} + H_2O \rightarrow 2OH^{\bullet} + 2OH^- + O_2 \qquad (1.10)$$

Thus, both holes in the VB and electrons in the CB can, via different reactions, participate in surface reactions that eventually produce hydroxyl radicals. These hydroxyl radicals are highly reactive and can rapidly oxidize/ mineralize organic compounds such as microorganisms. For example, a hydroxyl radical together with an oxygen molecule can decompose an organic compound $C_nO_mH_{(2n-2m+2)}$, into carbon dioxide molecules (CO_2) and water (H_2O) as described by

$$OH^{\bullet} + O_2 + C_nO_mH_{(2n-2m+2)} \rightarrow nCO_2 + (n\text{-}m\text{+}1)H_2O \qquad (1.11)$$

Since this redox reaction based mineralization has a power to decompose toxic organic pollutants, it has been widely used in waste water and air purification. A schematic diagram of principles oxidative decomposition of photocatalyst is shown in **Fig. 1.11**.

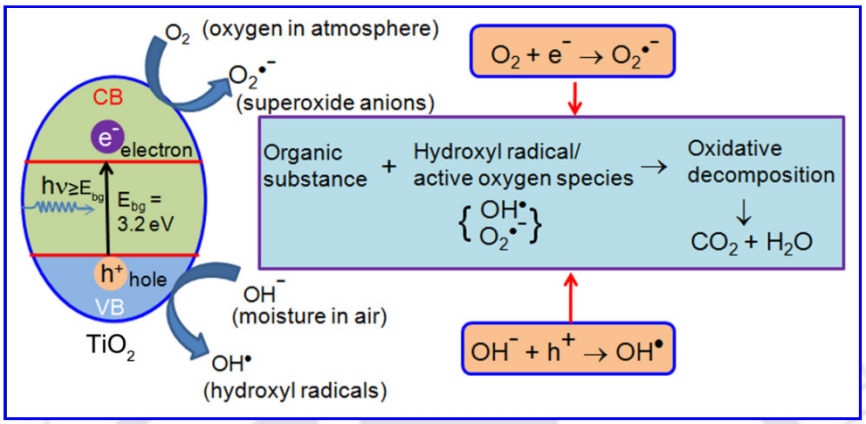

Fig. 1.11. Schematic of oxidative decomposition principle of TiO_2 photocatalyst.

1.6.3. Self-cleaning and antifogging

The photo-induced hydrophilicity[126] function of TiO_2 widened the application of TiO_2-coated materials. For example, the stains adsorbed on the TiO_2 surface can be easily washed away by water, because the soaks between the stains and the highly hydrophilic TiO_2 surface. The TiO_2 coated materials used outdoors (e. g., exterior tiles, glass, aluminum wall) when exposed to rain-fall show a very effective self-cleaning function and had already begun to be commercialized (**Fig. 1.12**).

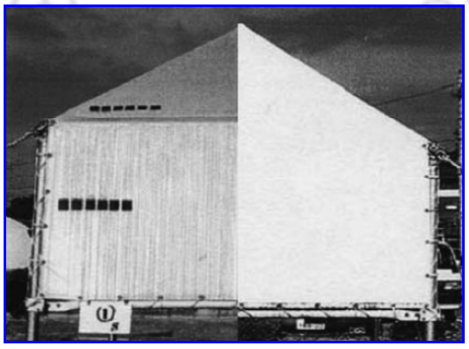

Fig. 1.12. Conventional tent material (left) and TiO_2-coated tent material (right). Adapted from Ref. [**126**].

Anti-fogging is another function of TiO_2 coated materials due to its photo-induced hydrophilicity properties.[126] The fogging on the surface of the mirrors and glasses occurs when steam cool down on these surface to form water droplets. On a highly hydrophilic surface, no water droplets are formed. Instead, a uniform thin film of water is formed on the surface and this prevents the fogging. This technology can be used in various glass products, mirrors, eyeglasses for antifogging function (**Fig. 1.13**).

Fig. 1.13. Anti-fogging effect of automobile side-view mirror: conventional mirror (left) and TiO_2-coated mirror (right). Adapted from Ref. [**126**].

1.6.4. Dye Sensitized Solar Cells

Dye sensitized solar cell (DSSC) with a high conversion efficiency and low production cost has been considered as a promising competitor to the well-developed, but relatively expensive, silicon solar cell. After first report of the TiO_2 based DSSC by O'Regan and Grätzel[30] in 1991, enormous effort has been made for the development of DSSC with higher efficiency and low cost to replace the costly silicon solar cell industry. A typical DSSC is assembled with a nanocrystalline TiO_2 film covered by a monolayer of dye molecules (N719) on fluorine doped tin-oxide (FTO) glass, redox electrolyte (I^-/I^{3-}), and counter electrode (Pt/FTO glass).[133] Due to the short electron diffusion length in TiO_2 nanoparticles film based DSSC, the recombination probability of the electrons with redox species and an oxidized dye increases. Compared with nanoparticles, highly ordered one-dimensional nanoarrays (NWs, NRs, and NTs) were found to be superior in chemical and photoelectrochemical performance due to their one-dimensional channel for carrier transportation, in which the efficiency of

charge collection is improved owing to a more rapid electron transport and slower charge recombination.

Innovative ideas are being continuously developed on the fabrication and design of solar cells with back-side and front-side light illumination for the enhancement of photovoltaic performance.[133] Shankar et al.[29] demonstrated self-assembled polymeric sensitized heterojunction solar cells of overall conversion efficiency of 2.1%. Recently, the photovoltaic performance of 8.07% and 7.29% of DSSCs based on 20.8 μm TiO_2 nanotube arrays on FTO glass with back-side and front-side light illumination, respectively, under simulated AM 1.5G illumination (10 mW cm^{-2}) was observed by Lei et al.[133] The schematic diagram of DSSC and the corresponding performance characteristics are shown in **Fig. 1.14**. This photovoltaic cell consists of TiO_2 nanotube arrays on FTO/glass substrate sensitized with N719 dye that serves as photoanode. A second FTO/glass substrate coated with Pt is used as photocathode. The space within the two electrodes is filled with electrolyte and the cell is illuminated from front-side as well as back-side and the comparison of the photovoltaic performances of front- and back-side light illumination is shown in **Fig. 1.14(b)**. The photovoltaic performance of the front-side illumination mode (8.07%) is found to be higher than that of the back-side illumination mode (7.29%) due to the reduction of incident light intensity in the latter case.[133]

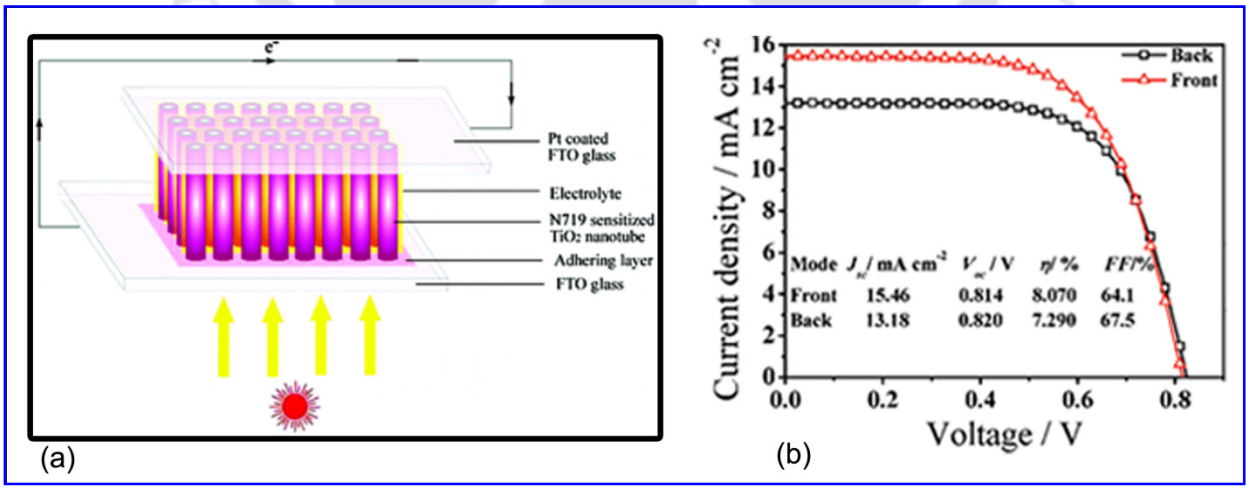

Fig. 1.14. (a) Schematic of TiO_2 nanotube arrays/ FTO-based DSSC and (b) comparison of the photovoltaic performance of the front-side and the back-side illumination modes under AM 1.5G illumination (100 mW cm^{-2}). Adapted from Ref. [**133**].

1.6.5. Gas sensors

The working principle of the TiO_2 gas sensors is based on the fact that the electrical conductivity changes when the TiO_2 nanomaterials are exposed to the tested gas due to the chemisorptions process of the reactive gas on the surface of the nanomaterials. The dominant electrical behavior due to the chemisorptions of hydrogen gas on the TiO_2 NTs surface make a partial charge transfer to TiO_2, thereby creating an electron accumulation layer that enhances the electrical conductance.[134] **Fig. 1.15(a)** shows a typical change in electrical resistance of TiO_2 nanotubes array when exposed to different hydrogen concentration at 290 °C.[134]

Ethanol gas sensing properties were studied by Wang et al.[135] The mechanisms of ethanol gas sensing on the surface of hierarchical TiO_2 nanostructures were demonstrated as follows: [136]

$$O_2\ (\text{gas}) \leftrightarrow O_2\ (\text{adsorption}) \qquad (1.12)$$

$$O_2\ (\text{adsorption}) + e^- \leftrightarrow O_2^-\ (\text{adsorption}) \qquad (1.13)$$

$$O_2^-\ (\text{adsorption}) + e^- \leftrightarrow 2O^-\ (\text{adsorption}) \qquad (1.14)$$

$$O^-\ (\text{adsorption}) + e^- \leftrightarrow O^{2-}\ (\text{adsorption}) \qquad (1.15)$$

When TiO_2 sensor is exposed to air, the oxygen species can be adsorbed on the surface of the sensor and ionized into O^- (adsorption) and O^{2-} (adsorption) by capturing free electrons from the conduction band of TiO_2 and increase the resistance.

$$C_2H_5OH\ (\text{gas}) + O^{2-}\ (\text{adsorption}) \rightarrow C_2H_5O^-\ (\text{adsorption}) + OH^-\ (\text{adsorption}) \qquad (1.16)$$

$$C_2H_5O^-\ (\text{adsorption}) \rightarrow (C_2H_5O^-)_2O\ (\text{adsorption}) + O^-(\text{adsorption}) + e^- \qquad (1.17)$$

When the sensor is exposed to ethanol gas, ethanol would react with O^-, O^{2-} and release electrons. This process lowers the resistance of the sensor [**Fig. 1.15(b)**].

The performance of the TiO_2 sensors with respect to the sensitivity, selectivity, stability, and reproducibility is generally determined by several factors, including the nature of the reactions occurring on the oxide surface, temperature, catalytic properties of the surface, defects and electronic structure of TiO_2 nanostructures.

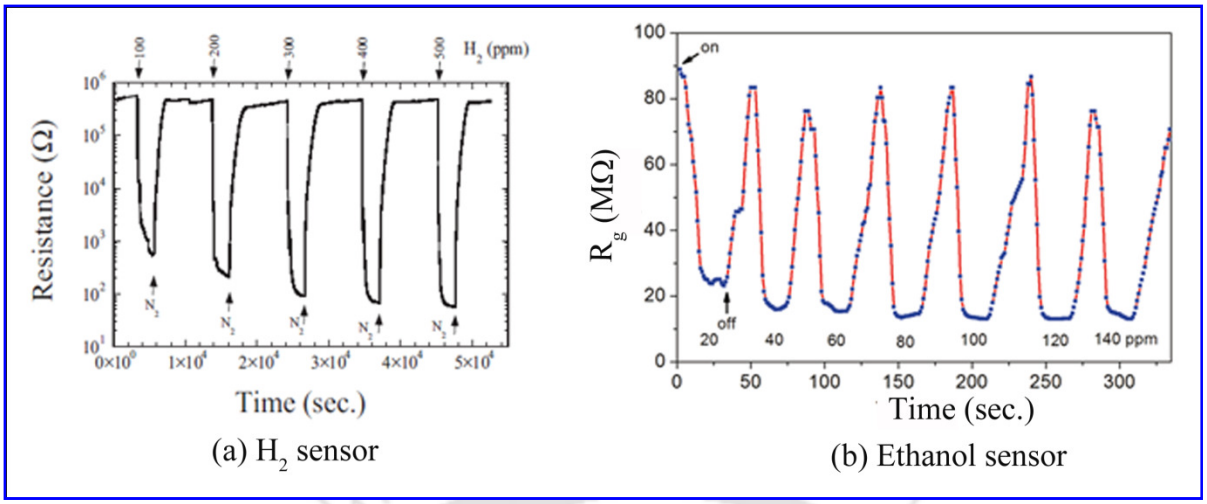

Fig. 1.15. Electrical response curve of (a) H_2 sensor for different hydrogen concentration at operating temperature 290 °C and (b) ethanol with increasing concentrations at 350 °C. Adapted from Ref. [**134, 135**].

1.7. Current challenges in TiO_2 nanostructures and focus of the present thesis

A. Understanding the formation mechanism of hydrothermally/ solvothermally synthesized different TiO_2 nanostructures:

After the first successful synthesis of titanate NTs by Kasuga et al.,[137] extensive research has been carried out on the hydrothermal growth of titanate and TiO_2 NRs, NTs and NWs by adjusting various growth parameters within the hydrothermal system to determine their effects on the nanostructure formation and resultant morphology. These parameters include reaction temperature, alkaline concentration, reaction duration, precursor phase, and crystallite size. Moreover, systematic study of solvent and temperature controlled growth of nanostructures and the exact growth mechanism of solvothermally synthesized titanate and TiO_2 NTs and NWs are still topics debated extensively in the contemporary literature. Understanding the formation mechanism and tuning the properties of TiO_2 nanostructures by manipulation of intrinsic defects and doping remain a challenge for exploiting their applications in various fields. In this thesis, we have studied the formation mechanism of solvothermally synthesized 1D TiO_2 NTs, NRs, NWs and nanoporous NRbs by varying the reaction temperatures, solvents and post-growth calcinations. The growth mechanism[138] of

the as-prepared nanostructures is elucidated from the systematic studies of field emission scanning electron microscopy (FESEM) and transmission electron microscopy (TEM) imaging.

B. Band gap tuning, visible light photocatalyst and identification of the native defects in TiO_2:

Anatase TiO_2 nanostructures having large surface area are used as a promising photocatalyst for the degradation of organic pollutants and in water splitting for hydrogen production. The band gaps of all TiO_2 polymorphs are in UV region which limits the industrial application to UV light only. Therefore, band gap engineering is essential to tune the band gap of TiO_2 into visible light so that it could be working using renewable solar light rather than using the costly, hazardous UV light. There are lots of challenges and fundamental issues related to the band gap tuning, electron-hole recombination in undoped and doped TiO_2 nanostructures and the visible light photocatalytic performance, which need to be explored further. Recently, some approaches based on dopant-free, pure TiO_2 phase were proposed to tune the band gap of TiO_2 to visible light region which showed enhanced photocatalytic efficiency. The decisive role of surface disorder and point defects, such as oxygen vacancy (O_v) and Ti interstitial (Ti_i) in dictating the band gap narrowing and related application of TiO_2 has been emphasized in the recent literatures, mainly through computational studies. However, experimental understanding on the actual nature of defects such as O_v and Ti_i in reduced TiO_2 and its role in the visible light photocatalysis are still unclear. The concentration of the native defects typically depends on the growth conditions. However, the nature of band gap states induced by the Ti_i is yet to be identified experimentally. It is therefore imperative to understand the evolution of the native defects in band gap engineered TiO_2 nanostructures with different growth/ processing conditions and identify the defects responsible for extended visible absorption and visible to near infrared photoluminescence in such nanostructures. In this work, through careful in-situ photoluminescence studies under controlled environment coupled with optical absorption measurement, we attempt to identify the specific defect responsible for the red shift in the absorption edge, visible and near infrared (NIR) photoluminescence (PL) emission in undoped TiO_2 NRbs grown by a solvothermal technique.[139] In particular, monitoring the time evolution of the visible and NIR PL

emissions at low temperature, under high vacuum and oxygen environment, allows us to distinguish and unambiguously identify the defect states associated with O_v, oxygen interstitial (O_i) and Ti_i. Our studies also reveal that these native defects are the microscopic origin of lattice expansion and contraction in undoped rutile TiO_2 nanostructures[140] by employing several structural and optical spectroscopic tools. The control of lattice parameters through the intrinsic defects may provide new routes to achieving novel functionalities in advanced materials that can be tailored for future technological applications.

C. Origin of ferromagnetism in TiO_2-based diluted magnetic semiconductors:

In the recent times, diluted magnetic semiconductors (DMS), in particular the ferromagnetic oxides, have been at the forefront of research for spintronics and magneto-optic device applications.[35, 36] The discovery of ferromagnetism in Co-doped TiO_2 with a Curie temperature (T_C) exceeding 300 K[36] lead the expansion of the field of DMS to oxides, leading to a rapid development of new materials and phenomena arising from a synergy of semiconductor physics and strongly correlated systems. However, in spite of several studies reported on TiO_2-based DMS, there is no clear agreement about the nature and origin of the observed ferromagnetism (FM). It is being currently debated whether the observed FM in oxide DMS has anything to do with transition metal (TM) doping or might be solely related to intrinsic defects. Some reports suggested segregation and the formation of TM metal clusters as the origin of FM signal, while most recent results strongly support the intrinsic nature of FM mediated by carriers or defects. These controversial results among research groups suggest that the magnetic properties of DMS materials are critically dependent on fabrication, growth conditions, and doping agents. However, unambiguous determination of the nature of defects responsible for the observed FM remains a considerable challenge to the researchers. Till date, most of the reported FM in undoped TiO_2 was for thin films and nanoparticles (NPs). The observed FM in undoped thin films and NPs are usually weak. Compared to thin films and nanoparticles, 1D TiO_2 nanostructures such as NWs, NRs and NRbs with high surface area can possess abundant surface defects, thus the intrinsic FM could be enhanced. Our present attempt in this work has been to enhance the magnetic moments which are solely due to intrinsic defects and explore a better understanding about the origin of observed ferromagnetism in undoped 1D TiO_2 system through systematic

studies of magnetic, structural and optical properties.[122] For further enhancement of the FM and to investigate the role of TM in the enhanced FM in TiO_2 system, we studied the optical and magnetic properties of Fe doped and Cr doped TiO_2 NRbs by a solvothermal method and Co doped TiO_2 NPs by a ball milling method, and elucidate the mechanism of enhanced FM in TM (Fe, Cr and Co) doped and undoped TiO_2 systems. From the temperature dependence magnetization (M-T) measurement, we observed a high Curie temperature (T_c) of ~793 K, i.e, ferromagnetic to paramagnetic transition, for Co doped TiO_2 NPs[141] and it is an important step for the development of practical commercial devices that can operate at and above RT.

1.8. Organization of the Thesis

The work reported in this thesis is presented in nine chapters. An introduction to the studies on the various growth processes, important features and technological applications of TiO_2 nanostructures and the motivation of the present work have been presented in *Chapter 1*. The *Chapter 2* presents a brief information about the experimental techniques used for the growth and characterization of the TiO_2 nanostructures. In the *Chapter 3*, details of the three-step growth and overall chemical processes of TiO_2 nanostructures are discussed and the formation mechanism of different nanostructures was elucidated. *Chapter 4* provides the critical role of native defects in the extended visible absorption and, visible and near infrared PL from undoped TiO_2 nanoribbons. The intrinsic defect induced room temperature ferromagnetism in undoped TiO_2 nanoribbons is presented in *Chapter 5*. In *Chapter 6*, we discuss the microscopic origin of lattice expansion and contraction in rutile TiO_2 nanostructures. *Chapter 7* and *8* present the optical and magnetic properties of Fe, Cr and Co doped TiO_2 nanostructures and discuss the origin of room temperature and high temperature ferromagnetism in these DMS systems. The highlights of the major contributions of the thesis, important conclusions of the work and scope for future studies on TiO_2 nanostructures are presented in the last chapter (*Chapter 9*).

References

1. R. Marchand, L. Brohan and M. Tournoux, Materials Research Bulletin **15**, 1129-1133 (1980).
2. J. C. Jamieson and B. Olinger, Science **161**, 893-895 (1968).
3. H. Sato, S. Endo, M. Sugiyama, T. Kikegawa, O. Shimomura and K. Kusaba, Science **251**, 786-788 (1991).
4. N. A. Dubrovinskaia, L. S. Dubrovinsky, R. Ahuja, V. B. Prokopenko, V. Dmitriev, H. P. Weber, J. M. Osorio-Guillen and B. Johansson, Physical Review Letters **87**, 275501 (2001).
5. L. S. Dubrovinsky, N. A. Dubrovinskaia, V. Swamy, J. Muscat, N. M. Harrison, R. Ahuja, B. Holm and B. Johansson, Nature **410**, 653-654 (2001).
6. Y. Ding and B. Xiao, Computational Materials Science **82**, 202-218 (2014).
7. M. Kakihana, M. Kobayashi, K. Tomita and V. Petrykin, Bulletin of the Chemical Society of Japan **83**, 1285-1308 (2010).
8. G. Wang, H. Wang, Y. Ling, Y. Tang, X. Yang, R. C. Fitzmorris, C. Wang, J. Z. Zhang and Y. Li, Nano Letters **11**, 3026-3033 (2011).
9. D. Yang, H. Liu, Z. Zheng, Y. Yuan, J.-c. Zhao, E. R. Waclawik, X. Ke and H. Zhu, Journal of the American Chemical Society **131**, 17885-17893 (2009).
10. W. Li, C. Liu, Y. Zhou, Y. Bai, X. Feng, Z. Yang, L. Lu, X. Lu and K.-Y. Chan, The Journal of Physical Chemistry C **112**, 20539-20545 (2008).
11. L. Hegang, D. Dongyan, N. Congqin and L. Zhaohui, Nanotechnology **23**, 015502 (2012).
12. B. Somaiah, W. Andrew See Weng and H. Ghim Wei, Journal of Physics D: Applied Physics **43**, 035401 (2010).
13. L. Dang Thi Thanh, V. Dang Duc and C. Nguyen Duc, Journal of Physics: Conference Series **187**, 012086 (2009).
14. Y. Zhang, W. Fu, H. Yang, Q. Qi, Y. Zeng, T. Zhang, R. Ge and G. Zou, Applied Surface Science **254**, 5545-5547 (2008).
15. L. Rizzo, S. Meric, M. Guida, D. Kassinos and V. Belgiorno, Water Research **43**, 4070-4078 (2009).

16. N. Miranda-García, S. Suárez, B. Sánchez, J. M. Coronado, S. Malato and M. I. Maldonado, Applied Catalysis B: Environmental **103**, 294-301 (2011).
17. M. Y. Ghaly, T. S. Jamil, I. E. El-Seesy, E. R. Souaya and R. A. Nasr, Chemical Engineering Journal **168**, 446-454 (2011).
18. K. Sunada, Y. Kikuchi, K. Hashimoto and A. Fujishima, Environmental Science & Technology **32**, 726-728 (1998).
19. Y.-Y. Song, F. Schmidt-Stein, S. Bauer and P. Schmuki, Journal of the American Chemical Society **131**, 4230-4232 (2009).
20. G. I. N. Waterhouse, A. K. Wahab, M. Al-Oufi, V. Jovic, D. H. Anjum, D. Sun-Waterhouse, J. Llorca and H. Idriss, Scientific Reports **3**, 2849 (2013).
21. Q. Tay, X. Liu, Y. Tang, Z. Jiang, T. C. Sum and Z. Chen, The Journal of Physical Chemistry C **117**, 14973-14982 (2013).
22. M. Ni, M. K. H. Leung, D. Y. C. Leung and K. Sumathy, Renewable and Sustainable Energy Reviews **11**, 401-425 (2007).
23. A. Fujishima and K. Honda, Nature **238**, 37-38 (1972).
24. C. Cao, C. Hu, X. Wang, S. Wang, Y. Tian and H. Zhang, Sensors and Actuators B: Chemical **156**, 114-119 (2011).
25. H.-P. Jen, M.-H. Lin, L.-L. Li, H.-P. Wu, W.-K. Huang, P.-J. Cheng and E. W.-G. Diau, ACS Applied Materials & Interfaces **5**, 10098-10104 (2013).
26. X. Yan, L. Feng, J. Jia, X. Zhou and Y. Lin, Journal of Materials Chemistry A **1**, 5347-5352 (2013).
27. B. Liu and E. S. Aydil, Journal of the American Chemical Society **131**, 3985-3990 (2009).
28. C. Xu, P. H. Shin, L. Cao, J. Wu and D. Gao, Chemistry of Materials **22**, 143-148 (2009).
29. K. Shankar, G. K. Mor, H. E. Prakasam, O. K. Varghese and C. A. Grimes, Langmuir **23**, 12445-12449 (2007).
30. B. O'Regan and M. Gratzel, Nature **353**, 737-740 (1991).
31. G. Kim, C. Jo, W. Kim, J. Chun, S. Yoon, J. Lee and W. Choi, Energy & Environmental Science **6**, 2932-2938 (2013).

32. J. Procházka, L. Kavan, M. Zukalová, O. Frank, M. Kalbáč, A. Zukal, M. Klementová, D. Carbone and M. Graetzel, Chemistry of Materials **21**, 1457-1464 (2009).
33. Y. Wang, M. Wu and W. F. Zhang, Electrochimica Acta **53**, 7863-7868 (2008).
34. Q. Wang, Z. Wen and J. Li, Inorganic Chemistry **45**, 6944-6949 (2006).
35. S. A. Wolf, D. D. Awschalom, R. A. Buhrman, J. M. Daughton, S. V. Molnar, M. L. Roukes, A. Y. Chtchelkanova and D. M. Treger, Science **294**, 1488 (2001).
36. Y. Matsumoto, M. Murakami, T. Shono, T. Hasegawa, T. Fukumura, M. Kawasaki, P. Ahmet, T. Chikyow, S.-y. Koshihara and H. Koinuma, Science **291**, 854-856 (2001).
37. H. Ohno, Science **281**, 951-956 (1998).
38. L. Braydich-Stolle, N. Schaeublin, R. Murdock, J. Jiang, P. Biswas, J. Schlager and S. Hussain, Journal of Nanoparticle Research **11**, 1361-1374 (2009).
39. S. Yoriya, M. Paulose, O. K. Varghese, G. K. Mor and C. A. Grimes, The Journal of Physical Chemistry C **111**, 13770-13776 (2007).
40. M. Lau, L. Dai, K. Bosnick and S. Evoy, Nanotechnology **20**, 025602 (2009).
41. Z. Sun, J. H. Kim, Y. Zhao, F. Bijarbooneh, V. Malgras, Y. Lee, Y.-M. Kang and S. X. Dou, Journal of the American Chemical Society **133**, 19314-19317 (2011).
42. D. S. Lee and T. K. Liu, Journal of Sol-Gel Science and Technology **25**, 121-136 (2002).
43. Y. Zhu, L. Zhang, C. Gao and L. Cao, Journal of Materials Science **35**, 4049-4054 (2000).
44. J.-M. Wu, H. C. Shih, W.-T. Wu, Y.-K. Tseng and I. C. Chen, Journal of Crystal Growth **281**, 384-390 (2005).
45. B. Zhao, F. Chen, W. Qu and J. Zhang, Journal of Solid State Chemistry **182**, 2225-2230 (2009).
46. H. E. Prakasam, K. Shankar, M. Paulose, O. K. Varghese and C. A. Grimes, The Journal of Physical Chemistry C **111**, 7235-7241 (2007).
47. S. P. Albu, A. Ghicov, J. M. Macak, R. Hahn and P. Schmuki, Nano Letters **7**, 1286-1289 (2007).

48. M. Kobayashi, V. V. Petrykin, M. Kakihana, K. Tomita and M. Yoshimura, Chemistry of Materials **19**, 5373-5376 (2007).
49. B.-M. Wen, C.-Y. Liu and Y. Liu, New Journal of Chemistry **29**, 969-971 (2005).
50. D. LOSIC and K. KANT, International Journal of Nanoscience **10**, 55-58 (2011).
51. J. A. Ayllón, A. Figueras, S. Garelik, L. Spirkova, J. Durand and L. Cot, Journal of Materials Science Letters **18**, 1319-1321 (1999).
52. S. K. Pradhan, P. J. Reucroft, F. Yang and A. Dozier, Journal of Crystal Growth **256**, 83-88 (2003).
53. J.-J. Wu and C.-C. Yu, The Journal of Physical Chemistry B **108**, 3377-3379 (2004).
54. J.-M. Wu, H. C. Shih and W.-T. Wu, Chemical Physics Letters **413**, 490-494 (2005).
55. B. Xiang, Y. Zhang, Z. Wang, X. H. Luo, Y. W. Zhu, H. Z. Zhang and D. P. Yu, Journal of Physics D: Applied Physics **38**, 1152 (2005).
56. X. Chen and S. S. Mao, Chemical Reviews **107**, 2891-2959 (2007).
57. T. Sugimoto, X. Zhou and A. Muramatsu, Journal of Colloid and Interface Science **259**, 43-52 (2003).
58. C. Su, B. Y. Hong and C. M. Tseng, Catalysis Today **96**, 119-126 (2004).
59. K. Das, S. K. Panda and S. Chaudhuri, Journal of Crystal Growth **310**, 3792-3799 (2008).
60. D. L. Morgan, H.-Y. Zhu, R. L. Frost and E. R. Waclawik, Chemistry of Materials **20**, 3800-3802 (2008).
61. D. V. Bavykin, V. N. Parmon, A. A. Lapkin and F. C. Walsh, Journal of Materials Chemistry **14**, 3370-3377 (2004).
62. D. Wu, J. Liu, X. Zhao, A. Li, Y. Chen and N. Ming, Chemistry of Materials **18**, 547-553 (2005).
63. Y. Su, S. Chen, N. Ma, X. Quan and H. Zhao, Separation and Purification Technology **68**, 255-260 (2009).
64. R. Ma, K. Fukuda, T. Sasaki, M. Osada and Y. Bando, The Journal of Physical Chemistry B **109**, 6210-6214 (2005).
65. K. Byrappa and T. Adschiri, Progress in Crystal Growth and Characterization of Materials **53**, 117-166 (2007).
66. X. Shen, J. Zhang and B. Tian, Journal of Materials Science **47**, 3855-3866 (2012).

67. M. Paulose, K. Shankar, S. Yoriya, H. E. Prakasam, O. K. Varghese, G. K. Mor, T. A. Latempa, A. Fitzgerald and C. A. Grimes, The Journal of Physical Chemistry B **110**, 16179-16184 (2006).
68. K. Shankar, J. I. Basham, N. K. Allam, O. K. Varghese, G. K. Mor, X. Feng, M. Paulose, J. A. Seabold, K.-S. Choi and C. A. Grimes, The Journal of Physical Chemistry C **113**, 6327-6359 (2009).
69. L. Jing, B. Xin, F. Yuan, L. Xue, B. Wang and H. Fu, The Journal of Physical Chemistry B **110**, 17860-17865 (2006).
70. X. Liu, S. Gao, H. Xu, Z. Lou, W. Wang, B. Huang and Y. Dai, Nanoscale **5**, 1870-1875 (2013).
71. X. Chen, L. Liu, Z. Liu, M. A. Marcus, W.-C. Wang, N. A. Oyler, M. E. Grass, B. Mao, P.-A. Glans, P. Y. Yu, J. Guo and S. S. Mao, Scientific Reports **3**, 1510 (2013).
72. N. H. Hong, J. Sakai, N. Poirot and V. Brizé, Physical Review B **73**, 132404 (2006).
73. D. Acharyya, A. Hazra, K. Dutta, R. K. Gupta and P. Bhattacharyya, Semiconductor Science and Technology **28**, 125001 (2013).
74. X. Pan, M.-Q. Yang, X. Fu, N. Zhang and Y.-J. Xu, Nanoscale **5**, 3601-3614 (2013).
75. J. Su, X.-X. Zou, Y.-C. Zou, G.-D. Li, P.-P. Wang and J.-S. Chen, Inorganic Chemistry **52**, 5924-5930 (2013).
76. M. Li, W. Hebenstreit, U. Diebold, A. M. Tyryshkin, M. K. Bowman, G. G. Dunham and M. A. Henderson, The Journal of Physical Chemistry B **104**, 4944-4950 (2000).
77. J. Su, X. Zou and J.-S. Chen, RSC Advances **4**, 13979-13988 (2014).
78. S. Na-Phattalung, M. F. Smith, K. Kim, M.-H. Du, S.-H. Wei, S. B. Zhang and S. Limpijumnong, Physical Review B **73**, 125205 (2006).
79. B. J. Morgan and G. W. Watson, The Journal of Physical Chemistry C **114**, 2321-2328 (2010).
80. H.-Y. Lee, S. J. Clark and J. Robertson, Physical Review B **86**, 075209 (2012).
81. E. Finazzi, C. Di Valentin and G. Pacchioni, The Journal of Physical Chemistry C **113**, 3382-3385 (2009).
82. S. Wendt, P. T. Sprunger, E. Lira, G. K. H. Madsen, Z. Li, J. Ø. Hansen, J. Matthiesen, A. Blekinge-Rasmussen, E. Lægsgaard, B. Hammer and F. Besenbacher, Science **320**, 1755-1759 (2008).

83. C. E. Ekuma and D. Bagayoko, Japanese Journal of Applied Physics **50**, 101103 (2011).

84. K. B. Jaimy, V. P. Safeena, S. Ghosh, N. Y. Hebalkar and K. G. K. Warrier, Dalton Transactions **41**, 4824-4832 (2012).

85. G. Yang, Z. Jiang, H. Shi, T. Xiao and Z. Yan, Journal of Materials Chemistry **20**, 5301-5309 (2010).

86. K. Zhang, X. Wang, X. Guo, T. He and Y. Feng, Journal of Nanoparticle Research **16**, 1-9 (2014).

87. B. Xin, P. Wang, D. Ding, J. Liu, Z. Ren and H. Fu, Applied Surface Science **254**, 2569-2574 (2008).

88. U. G. Akpan and B. H. Hameed, Journal of Hazardous Materials **170**, 520-529 (2009).

89. R. K. Singhal, A. Samariya, S. Kumar, Y. T. Xing, D. C. Jain, S. N. Dolia, U. P. Deshpande, T. Shripathi and E. B. Saitovitch, Journal of Applied Physics **107**, 113916 (2010).

90. K. Griffin Roberts, M. Varela, S. Rashkeev, S. T. Pantelides, S. J. Pennycook and K. M. Krishnan, Physical Review B **78**, 014409 (2008).

91. J. Xu, S. Shi, L. Li, X. Zhang, Y. Wang, X. Chen, J. Wang, L. Lv, F. Zhang and W. Zhong, Journal of Applied Physics **107**, 053910 (2010).

92. J. Y. Kim, J. H. Park, B. G. Park, H. J. Noh, S. J. Oh, J. S. Yang, D. H. Kim, S. D. Bu, T. W. Noh, H. J. Lin, H. H. Hsieh and C. T. Chen, Physical Review Letters **90**, 017401 (2003).

93. Q. Wu, Q. Zheng and R. van de Krol, The Journal of Physical Chemistry C **116**, 7219-7226 (2012).

94. T. Takata and K. Domen, The Journal of Physical Chemistry C **113**, 19386-19388 (2009).

95. H. Wang and J. P. Lewis, Journal of Physics: Condensed Matter **18**, 421 (2006).

96. Y.-f. Zhang, W. Lin, Y. Li, K.-n. Ding and J.-q. Li, The Journal of Physical Chemistry B **109**, 19270-19277 (2005).

97. M. Ben Yahia, F. Lemoigno, T. Beuvier, J.-S. Filhol, M. Richard-Plouet, L. Brohan and M.-L. Doublet, The Journal of Chemical Physics **130**, 204501 (2009).

98. M. Landmann, E. Rauls and W. G. Schmidt, Journal of Physics: Condensed Matter **24**, 195503 (2012).

99. M. Nolan, S. D. Elliott, J. S. Mulley, R. A. Bennett, M. Basham and P. Mulheran, Physical Review B **77**, 235424 (2008).

100. M. A. Henderson, W. S. Epling, C. H. F. Peden and C. L. Perkins, The Journal of Physical Chemistry B **107**, 534-545 (2002).

101. V. E. Henrich, G. Dresselhaus and H. J. Zeiger, Physical Review Letters **36**, 1335-1339 (1976).

102. E. Finazzi, C. Di Valentin, G. Pacchioni and A. Selloni, The Journal of Chemical Physics **129**, 154113 (2008).

103. J. Bardeen, F. J. Blatt and L. H. Hall, in proceedings of the conference on photoconductivy, Atlantic city (1954).

104. J. Tauc, R. Grigorovici and A. Vancu, Physica Status Solidi (b) **15**, 627-637 (1966).

105. J. Pascual, J. Camassel and H. Mathieu, Physical Review B **18**, 5606-5614 (1978).

106. N. Daude, C. Gout and C. Jouanin, Physical Review B **15**, 3229-3235 (1977).

107. L. Kavan, M. Grätzel, S. E. Gilbert, C. Klemenz and H. J. Scheel, Journal of the American Chemical Society **118**, 6716-6723 (1996).

108. H. Tang, K. Prasad, R. Sanjinès, P. E. Schmid and F. Lévy, Journal of Applied Physics **75**, 2042-2047 (1994).

109. A. Welte, C. Waldauf, C. Brabec and P. J. Wellmann, Thin Solid Films **516**, 7256-7259 (2008).

110. A. Di Paola, M. Bellardita and L. Palmisano, Catalysts **3**, 36-73 (2013).

111. V. Štengl and D. Králová, Materials Chemistry and Physics **129**, 794-801 (2011).

112. W. Hu, L. Li, G. Li, C. Tang and L. Sun, Crystal Growth & Design **9**, 3676-3682 (2009).

113. M. Koelsch, S. Cassaignon, J. F. Guillemoles and J. P. Jolivet, Thin Solid Films **403–404**, 312-319 (2002).

114. A. Di Paola, G. Cufalo, M. Addamo, M. Bellardita, R. Campostrini, M. Ischia, R. Ceccato and L. Palmisano, Colloids and Surfaces A: Physicochemical and Engineering Aspects **317**, 366-376 (2008).

115. S. B. Ogale, Advanced Materials **22**, 3125-3155 (2010).

116. Y. Yamada, H. Toyosaki, A. Tsukazaki, T. Fukumura, K. Tamura, Y. Segawa, K. Nakajima, T. Aoyama, T. Chikyow, T. Hasegawa, H. Koinuma and M. Kawasaki, Journal of Applied Physics **96**, 5097-5102 (2004).
117. H. Toyosaki, T. Fukumura, Y. Yamada and M. Kawasaki, Applied Physics Letters **86**, 182503 (2005).
118. T. Droubay, S. M. Heald, V. Shutthanandan, S. Thevuthasan, S. A. Chambers and J. Osterwalder, Journal of Applied Physics **97**, 046103 (2005).
119. J. M. D. Coey, A. P. Douvalis, C. B. Fitzgerald and M. Venkatesan, Applied Physics Letters **84**, 1332-1334 (2004).
120. K. Dongyoo, H. Jisang, P. Young Ran and K. Kwang Joo, Journal of Physics: Condensed Matter **21**, 195405 (2009).
121. N. Hoa and D. Huyen, Journal of Materials Science: Materials in Electronics **24**, 793-798 (2013).
122. B. Santara, P. K. Giri, K. Imakita and M. Fujii, Nanoscale **5**, 5476-5488 (2013).
123. Y. J. Kim, S. Thevuthasan, T. Droubay, A. S. Lea, C. M. Wang, V. Shutthanandan, S. A. Chambers, R. P. Sears, B. Taylor and B. Sinkovic, Applied Physics Letters **84**, 3531-3533 (2004).
124. D. H. Kim, J. S. Yang, Y. S. Kim, T. W. Noh, S. D. Bu, S. I. Baik, Y. W. Kim, Y. D. Park, S. J. Pearton, J. Y. Kim, J. H. Park, H. J. Lin, C. T. Chen and Y. J. Song, Physical Review B **71**, 014440 (2005).
125. S.-H. Kang, H. N. T. Quynh, S.-G. Yoon, E.-T. Kim, Z. Lee and V. Radmilovic, Applied Physics Letters **90**, 102504 (2007).
126. K. Hashimoto, H. Irie and A. Fujishima, Japanese Journal of Applied Physics **44**, 8269-8285 (2005).
127. R. Abe, K. Sayama and H. Arakawa, Chemical Physics Letters **371**, 360-364 (2003).
128. R. Abe, K. Sayama and H. Sugihara, The Journal of Physical Chemistry B **109**, 16052-16061 (2005).
129. A. Galińska and J. Walendziewski, Energy & Fuels **19**, 1143-1147 (2005).
130. S. G. Lee, S. Lee and H.-I. Lee, Applied Catalysis A: General **207**, 173-181 (2001).
131. S. N. Frank and A. J. Bard, Journal of the American Chemical Society **99**, 303-304 (1977).

132. T. Hirakawa and Y. Nosaka, Langmuir **18**, 3247-3254 (2002).
133. B.-X. Lei, J.-Y. Liao, R. Zhang, J. Wang, C.-Y. Su and D.-B. Kuang, The Journal of Physical Chemistry C **114**, 15228-15233 (2010).
134. O. K. Varghese, D. Gong, M. Paulose, K. G. Ong, E. C. Dickey and C. A. Grimes, Advanced Materials **15**, 624-627 (2003).
135. C. Wang, L. Yin, L. Zhang, Y. Qi, N. Lun and N. Liu, Langmuir **26**, 12841-12848 (2010).
136. X.-H. Wu, Y.-D. Wang, H.-L. Liu, Y.-F. Li and Z.-L. Zhou, Materials Letters **56**, 732-736 (2002).
137. T. Kasuga, M. Hiramatsu, A. Hoson, T. Sekino and K. Niihara, Langmuir **14**, 3160-3163 (1998).
138. B. Santara and P. K. Giri, Materials Chemistry and Physics **137**, 928-936 (2013).
139. B. Santara, P. K. Giri, K. Imakita and M. Fujii, The Journal of Physical Chemistry C **117**, 23402-23411 (2013).
140. B. Santara, P. K. Giri, K. Imikita and M. Fujii, Journal of Physics D: Applied Physics **47**, 215302 (2014).
141. B. Santara, B. Pal and P. K. Giri, Journal of Applied Physics **110**, 114322 (2011).

Chapter 2

Experimental techniques

In this chapter, a brief account of the growth techniques used for the preparation of various samples and the in–house development of the vacuum annealing system is presented. For the characterization of the both undoped and doped nanostructures, several standard analytical, spectroscopic and magnetic measurement tools are used, which are presented in details. The methodology adopted to analyze the data from various spectroscopic tools is also discussed in brief.

2.1. Growth techniques for the synthesis of TiO_2 nanostructures

We have used two different growth techniques for the fabrication of undoped and doped TiO_2 nanostructures. One dimensional (1D) nanostructures, i.e., NTs, NRs, NWs and NRbs are grown using hydrothermal/ solvothermal techniques. For the hydrothermal/ solvothermal techniques, we used a stainless steel high pressure reactor, known as autoclave with Teflon-liner (Bergof-100, Germany). Several growth parameters such as solvents, reaction temperatures and reaction durations were varied for the growth of wide variety of nanostructures and their formation mechanisms are described in *Chapter 3*. Planetary ball-milling machine (Retsch, PM 100) is used for the growth of Co doped TiO_2 NPs.

2.1.1. High pressure reactor for the Hydrothermal/ Solvothermal growth

The hydrothermal set-up used in our laboratory consists of three parts, i.e., Teflon-lined stainless steel autoclave (reaction vessel), rectangular hot box (prevent for heat radiation) and hot plate (provide heat for a particular set temperature) with stirring facility. The photograph of the complete hydrothermal set-up used in this study is shown in **Fig. 2.1**. The autoclave consists of a stainless steel vessel (outer) with stainless steel cap and clamp. A Teflon inner

vessel (capacity 100 ml) is lined inside the stainless steel vessel and this is used as the container for the precursor solutions to avoid the unwanted mixing of impurities during reaction. An O-ring is placed on the mouth of the Teflon vessel. The stainless steel cap mounted with Teflon in the inner part is used as lid to close the vessels. The autoclave has a thermal sensor with immersion tube inside the Teflon vessel, which is connected to a PID controller to measure the exact internal temperature of the reaction solution. A monometer is in-built with the autoclave to measure the pressure inside the autoclave during the reaction. The autoclave has also gas feeding and liquid samples extraction facility during the reaction. The rectangular hot box is placed on the top of the hot plate with stirring facility which is placed on a table. The hot plate has two knobs, one for setting the required temperatures and the other for stirring. The hot box is used to prevent the heat radiation to the outside of the autoclave. After filling the precursor mixed solutions inside the autoclave, the system is closed with the stainless steel clamp. Then the autoclave is placed inside the rectangular hot box which is placed on the top of the hot plate. The thermal sensor is connected with a PID controller through a connecting wire which display the inside temperature of the autoclave. This allows a precise measurement of the reaction temperature. Finally, the hot plate is connected to the main power supply to heat the hot plate and carry out the hydrothermal reaction at a particular set temperature and stirring condition.

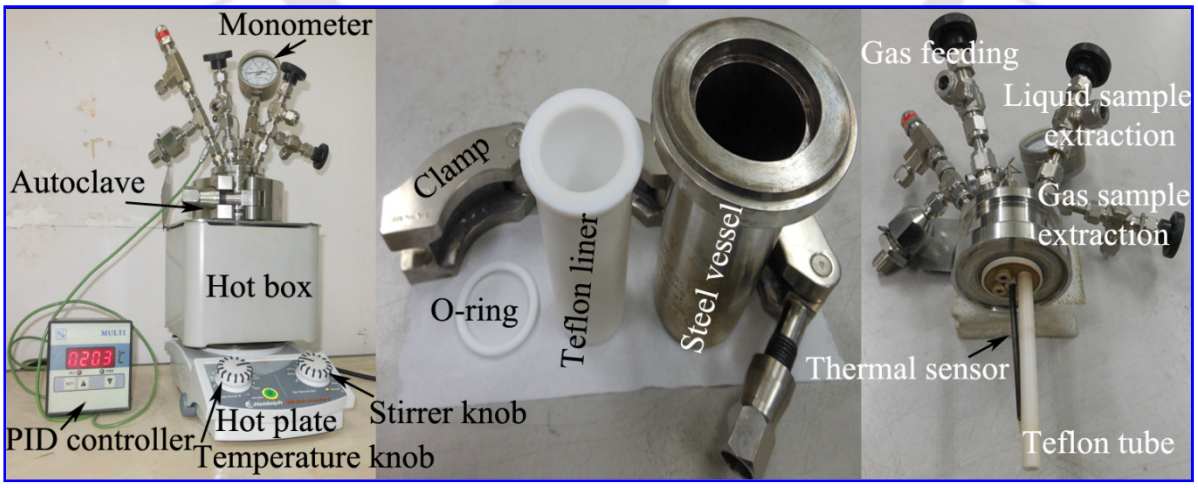

Fig. 2.1. Photograph of high pressure reactor (autoclave) (Berghof, BR-100; Germany).

2.1.2. High temperature furnace for calcinations and vacuum annealing

A High temperature split type furnace (Indfurr, India) is used for the calcinations of the samples obtained from hydrothermal method. It consists of a horizontal muffle furnace, a cylindrical quartz/ alumina tube (placed inside the muffle furnace). The furnace is connected to programmable controller to control the set temperature, the heating rate and tune duration of heating at a particular temperature. For vacuum annealing, we designed the vacuum system in our laboratory. The photograph of vacuum annealing system is shown in **Fig. 2.2**. The one end of the alumina tube is closed. The other end of the alumina tube is connected to a rotary pump for evacuation of the tube chamber. The pressure inside the tube is monitored by a pirani gauge connected to the exhaust side of the rotary pump. We achieved a pressure of 1.2×10^{-2} mbar inside the tube, which was displayed in the pirani gauge.

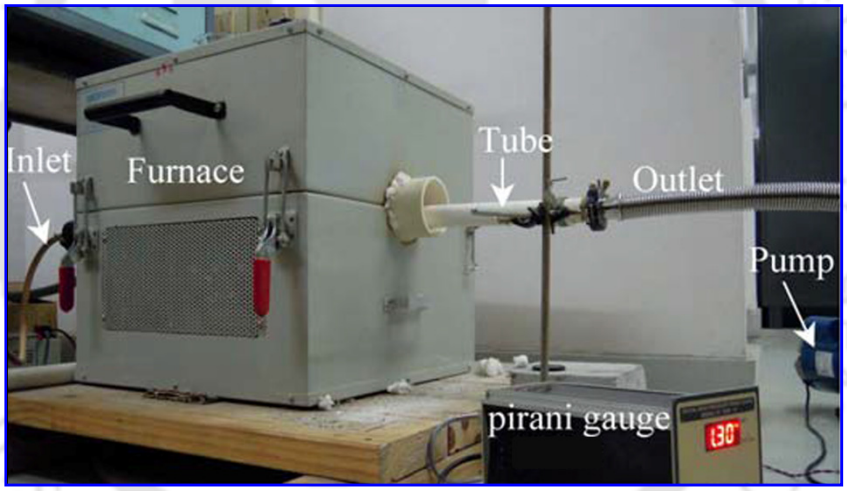

Fig. 2.2. Photograph of high temperature furnace with vacuum system.

2.1.3. Hydrothermal/ Solvothermal technique for the growth of TiO_2 nanostructures

For the hydrothermal/ solvothermal growth of TiO_2 nanostructures, four parameters are usually controlled i.e., precursors, solvents, reaction temperatures and reaction durations. We used commercial TiO_2 anatase powders (Merck), titanium butoxide, $Ti(OC_4H_9)_4$ (Sigma Aldrich) as precursors and alkaline water, alkaline water-ethanol, water-ethylene glycol as base solvents and water-HCl as acid solvent. The reaction temperatures are maintained at

130, 155, 180, 205 °C with autogeneous pressure inside the autoclave throughout the reaction and reaction durations are varied as 12, 16, 24, and 48 hours. At first, we prepared the precursor solution by mixing the TiO_2 precursor (anatase TiO_2 powder/ titanium butoxide) in alkaline (10M NaOH) aqueous or non-aqueous solvent for the base-mediated growth and water-HCl mixed solvent for the acid-mediated growth. The mixed solution is stirred for 30 minutes in a conical flax and then transferred to the autoclave for hydrothermal/ solvothermal reactions. Next the precipitates are taken out of the autoclave and further processed such as ion-exchange reaction and calcinations (for base-mediated preparation only) to obtain the final samples. The as-obtained precipitate from the base-mediated reaction after washing several times with de-ionized (DI) water is allowed to react with 0.1M HCl for ion exchange between Na^+ and H^+. After ion-exchange reaction and several times washing is hydrogen-titanate, the product is calcined at different temperatures (500, 700 and 900 °C) for dehydration and to remove the residual organic impurities. Finally, depending upon the calcinations temperatures, TiO_2 nanostructure samples with different phases are obtained. The ion exchange reaction was not needed for acid-mediated precipitates; several times washing with DI water and heat treatment were needed for better crystallinity.

2.1.4. Ball milling method for Co doped TiO_2 nanoparticles

Planetary Ball milling is used to grow Co doped TiO_2 nanoparticles. In our laboratory, we have a programmable ball milling machine (Retsch, PM 100) that is shown in **Fig. 2.3**. It consists of vial, balls and a planetary platform with a certain rotation speed. The important precaution is the use of non-corrosive vial and balls and their cleanliness. For example, to study the magnetic properties, one should avoid the use of metal vial and balls because these may add impurity to the sample that may cause a change in magnetic property of the sample.

For the present study, we used contamination free zirconia (ZrO_2) balls and vial for the growth of Co doped TiO_2 nanoparticles. At first, the required amount of Co powder and TiO_2 powder are mixed in a ceramic mortar and ground for 10 minutes. Then the mixed powder is put inside the vial with required amount of balls (powder: ball = 1:10) and set at 350 rpm for 5 h duration.

Fig. 2.3. Photographs of the planetary ball-mill machine (Retsch, PM 100), grinding station and Zirconia balls.

2.2. Characterization techniques

Several experimental tools are used to study the characteristic properties of the different samples. Morphological and structural characterizations were performed by the field emission scanning electron microscopy (FESEM), transmission electron microscopy (TEM), high resolution TEM (HRTEM) and x-ray diffraction (XRD) techniques. These studies help us to learn about the surface morphologies, crystal structure and phases. For optical characterizations, we used micro-Raman, UV-visible-near infrared (UV-vis-NIR) optical absorption, steady state photoluminescence (PL), time-resolved photoluminescence (TRPL), x-ray photoelectron spectroscopy (XPS), and Fourier transform infrared (FTIR) spectroscopy. We used vibrating sample magnetometer (VSM) and electron spin resonance (ESR) measurements to study the magnetic properties of the samples.

2.2.1. Morphological and structural characterization

A. Field emission scanning electron microscopy (FESEM)

The FESEM is a very powerful tool for high resolution surface imaging of nanomaterials. The FESEM use a beam of electrons to probe objects on a very fine scale. The use of electrons has two main advantages over optical microscopes: much larger magnifications are

possible since electron wavelengths are much smaller than photon wavelengths and the depth of field is much higher. The electron wavelength λ_e depends on the electron velocity v or the accelerating voltage V as

$$\lambda_e = \frac{h}{mv} = \frac{h}{\sqrt{2qmV}} = \frac{1.22}{\sqrt{V}} \text{ nm} \qquad (2.1)$$

Thus, for a 30 kV acceleration voltage, the resolution is extremely high.

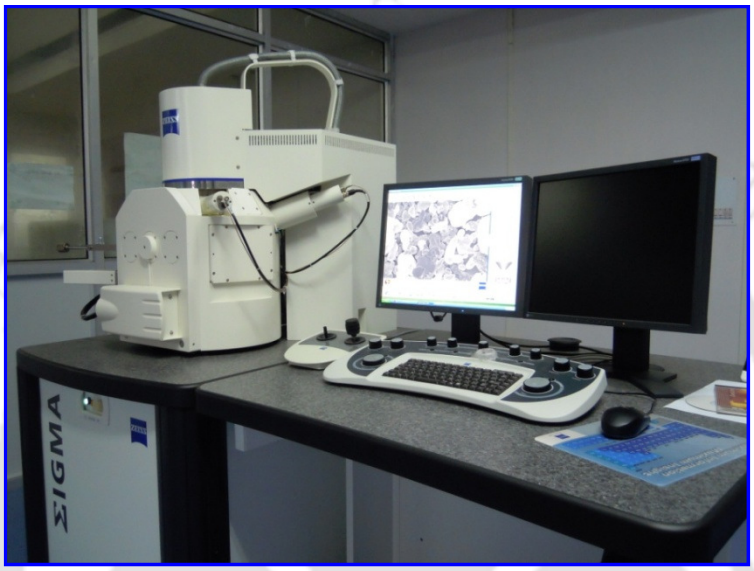

Fig. 2.4. Photograph of the Field Emission Scanning Electron Microscope (Sigma Zeiss, Germany).

A photograph of the FESEM (Sigma Zeiss, Germany) used in the present study is shown in **Fig. 2.4**. In the FESEM, electrons are emitted from a field emission source under extreme vacuum. The vacuum allows the electrons movement along a column without scattering which helps to prevent discharges inside the instrument. The field emission source is tungsten filament (cathode) with sharp tip which is placed in a huge electrical potential gradient. The significance of extremely thin and sharp tip (diameter 10-100 nm) is that an electric field can be concentrated to an extreme level so that the work function of the material is lowered and electrons can leave the cathode. After emission, the electrons are accelerated by the two anodes. An accelerating voltage (0.5- 30 kV) between the cathode and anode is commonly used. This voltage combined with beam diameters determines the resolution of the image. As the voltage increases, better point-to-point resolution can be obtained. Because

of the smaller size of the electron source, the beam produced by this emitter is about 1000 times smaller than that in a standard scanning electron microscope (SEM), which markedly improves the image. The beam is collimated by electromagnetic condenser lenses, focused by an objective lens, and scanned across the surface of the sample by electromagnetic deflection coils. The primary imaging method is by collecting emitted secondary electrons that are released by the sample. A secondary electron detector is placed near to the specimen. By correlating the sample scan position with the resulting signal, an image is formed on the screen that is strikingly similar to what would be seen through an optical microscope. The FESEM is equipped with a special objective or focusing lens that projects the magnetic field below the lens. Very high resolution is obtained by shortening the specimen–lens distance and using a specially designed in–lens. The distance is shortened by placing the specimen in the lens magnetic field. In this case, secondary electron detector is placed above the objective in–lens (called as in–lens detector), which makes difference in the image compared to the conventional image of the secondary electron detector. Very high resolution and contrast can be obtained by using in–lens detector. The type of electron source is the main difference between SEM and FESEM. In SEM, electrical current is used to heat up the filament and when the heat is enough to overcome the work function of the filament, electron escape from the material.

For the sample preparation of the FESEM imaging, as-synthesized TiO_2 powder was directly mounted on the FESEM stub using a carbon tape. Here the carbon tape is used as adhesive to stick the powder and also provides an electrical conduction path to the sample.

B. Transmission Electron Microscopy (TEM)

TEM is one of the best characterization techniques of nanomaterials in which structural information can be acquired by high resolution imaging close to the atomic level (0.2 nm) as well as by electron diffraction. The high resolution TEM (HRTEM) known as lattice imaging, gives the structural informations and presence of defects or dislocations. The growth orientation and lattice spacing can be studied from the lattice fringe image. The crystallographic information about the nanomaterials such as crystal structure (cubic, tetragonal, hexagonal or monoclinic etc.), crystallinity (single crystalline, poly-crystalline or amorphous) can be drawn from the selected area electron diffraction (SAED) patterns. In

case of a crystalline material, electron diffraction will only occur at specific angles which are the characteristic features for the crystal structures present. Moreover, elemental and chemical composition analysis down to sub-nanometer scale can be acquired with additional detector such x-ray detector which is known as energy dispersive x-ray (EDX) analysis. **Fig. 2.5** shows the schematic diagram of a TEM. It works on the principle of optical projection; when an object is placed in front of a light source, its image is enlarged and shadow is created on the screen placed far distance behind this object. Electrons emitted from an electron gun are accelerated to high voltages (typically 100 to 400 kV) and focused on the sample by a number of condenser lenses.[1] We used a lanthanum hexaboride (LaB_6) crystal for thermionic electron emission. The emitted electrons pass through a series of lenses to be focused and scanned across the sample. The sample is placed on a small copper grid a few mm (~3 mm) in diameter. The static beam has a diameter of a few microns. The sample must be sufficiently thin (a few tens to a few hundred nm) to be transparent to electrons. The transmitted and forward scattered electrons form a diffraction pattern in the back focal plane and a magnified image in the image plane. With additional lenses, either the image or the diffraction pattern is projected onto a fluorescent screen for viewing or photographic recording.

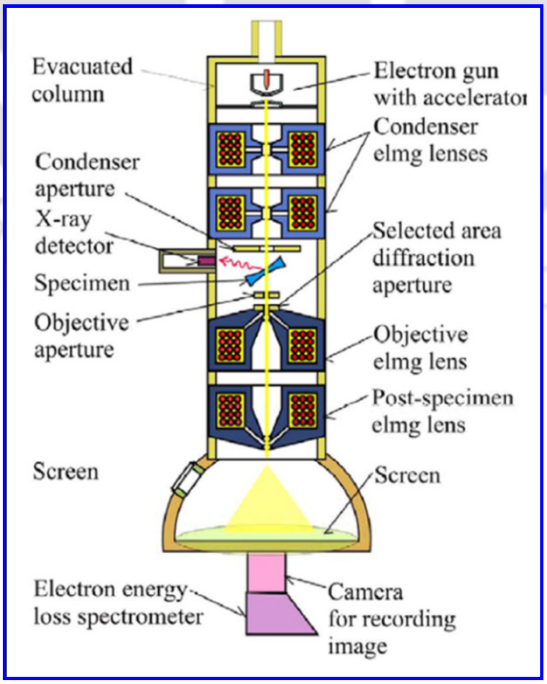

Fig. 2.5. Schematic diagram of Transmission Electron Microscope.

In our present study, a TEM (JEM2100, JEOL, Japan) operating at 200 kV with high resolution CCD camera (Gatan, USA) is used for the normal TEM and HRTEM imaging. Sample for the TEM imaging was prepared by well dispersing the nanostructured samples in an ethanol solvent. A transparent dispersion of nanostructures was prepared by long time high frequency sonication and then drop casted on the carbon coated copper grid containing few hundreds of square shaped hollow meshes with dimension of ~1 μm. After normal dry for prolong time this grid is used for TEM imaging. Improved resolution of the lattice image is obtained after processing of fast Fourier transformation (FFT) using '*Digital Micrograph* (Gatan, USA)' image analysis software. In addition, we used SAED pattern to get crystallographic information about the TiO_2 nanostructures.

C. Powder x-ray diffraction (XRD)

Powder XRD is the most widely used non–destructive technique for general crystalline material characterization. The XRD patterns provide information on crystal phases, lattice parameters, crystallite size and strain in the material. In XRD, a collimated beam of x–rays, with wavelength λ = 0.5–2.0 Å, is incident on a sample and is diffracted by the atoms of the crystalline phases in the sample according to 'Bragg's law',

$$2dsin\theta = n\lambda \qquad (2.2)$$

where d is the spacing between atomic planes in the crystalline phase, θ is the angle of incidence of the x–ray beam with the atomic plane, n represents the order of diffraction (we consider only the first order diffraction, n =1, because the second order peaks are mostly difficult to detect experimentally). The intensity of the diffracted x–rays is measured as a function of the diffraction angle 2θ. In powder samples, the crystallites are oriented in various possible orientations, giving reflections from all possible planes. However, the preferred orientation of the crystallites can occur. In an x-ray diffraction pattern, the position and intensity of the diffraction peaks are characteristic for the crystallographic structure and the atomic composition of the material. In case of a multi-phase composition, the resulting pattern is a combination of the patterns of all structures present. Phase identification can be done by matching the XRD pattern with reference patterns of pure substances. Owing to the huge data bank available from JCPDS Powder Diffraction Files covering practically every phase of every known material, crystal phase of the sample is identified from the peak

positions of the diffractogram. Homogeneous or uniform elastic strain in the (hkl) direction can also be calculated from the shift in the diffraction peak positions, and the d_{hkl} spacing of the unstrained crystal. From the peak shapes and width of the diffraction peak, average crystallite size can be calculated.

Fig. 2.6. Photograph of the X-ray Diffractometer (Rigaku RINT 2500, TTRAX III).

X–ray diffraction patters of the synthesized nanostructure samples were obtained using a commercial XRD (TTRAX III, Rigaku 2500) using a Cu $K_{\alpha 1}$ (λ = 1.5406 Å) radiation. A photograph of the XRD instrument in our laboratory is shown in **Fig. 2.6**. All measurements were carried out at an accelerated voltage of 50 kV and tube current of 200 mA. The scanning step size was 0.01°. The exact peak position and full width half maxima (FWHM) of the XRD peak is obtained from the Lorentzian fitting to the experimental data, using following expression

$$y = y_0 + \frac{2A}{\pi}\frac{w}{4(x-x_c)^2 + x^2} \qquad (2.3)$$

Where y_0 is the offset constant, x_c, w and A are the peak position, FWHM and area, respectively. FWHM gives the crystallite size (using Scherrer formula[2]) and lattice strain is calculated from the shift in x_c using Williamsons-Hall method.[3, 4]

2.2.2. Optical characterization

A. Micro-Raman spectroscopy

Raman spectroscopy is a vibrational spectroscopic technique generally used to study properties such as crystalline phases, strain, phonon confinement effect and defects present in the material. It is based on the Raman scattering process that corresponds to the interaction between the incident photons and optical phonon of the material. For the micro-Raman spectroscopy measurement, an intense laser beam is incident on the sample through a commercial microscope with spot size about few microns. The weak back-scattered light or signal is passed through a double monochromator to reject the Raleigh scattered signal and the Raman shifted wavelengths are detected by a photodetector or CCD detector. The distinction between crystalline and amorphous phases can be made by observing the sharpness or broadness of the various vibrational modes of materials, respectively. The nature of stress can be determined by observing the upward shift for compressive stress and downward shift for tensile stress compared to the peak position of the vibrational modes of unstrained crystal.

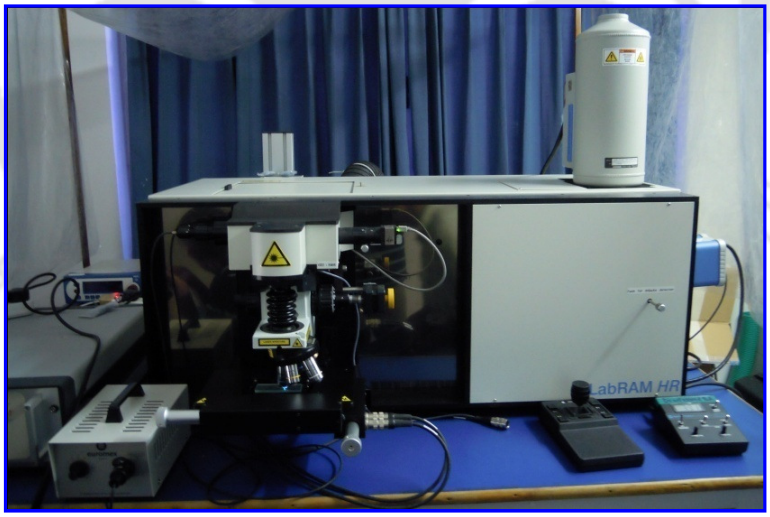

Fig. 2.7. Photograph of the micro-Raman spectrometer (LabRAM HR-800, Jobin Yvon, USA).

A high resolution micro-Raman (LabRAM HR-800, Jobin Yvon, USA) instrument with liquid nitrogen cooled CCD detector is used for the characterization of TiO_2

nanostructure samples. **Fig. 2.7** is the photograph of micro-Raman set up used to observe the Raman spectrum for the present study. This instrument is used to study the identification of various phases of TiO_2 nanostructures, oxygen vacancy defects and stress present in our samples. All the measurements are carried out at room temperature. Some of the samples are characterized using 488 nm and others using 514 nm Ar^+ laser with source laser power fixed at 22 mW.

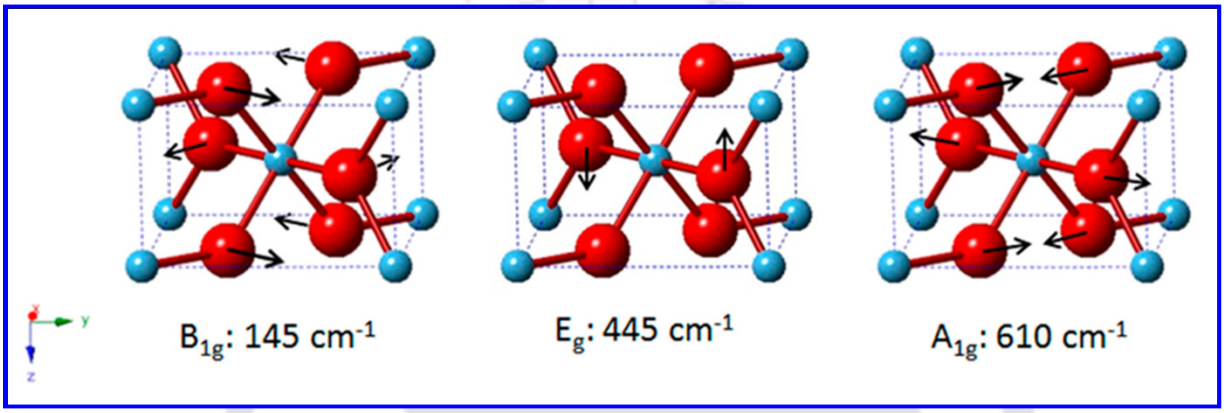

Fig. 2.8. Schematic diagram, illustrating the displacements of each atom for Raman active lattice vibrations of rutile TiO_2. Red ball: Ti atom, Blue ball: O atom. Adapted from Ref. [**5**].

Rutile TiO_2 is tetragonal structure having space group $P4_2/mnm$ and has 6 atoms in the primitive cells. Thus there should be 15 optical and 3 acoustic modes. From the group analysis, the optical modes at Γ point belong to the following irreducible presentations:[5, 6]

$$\Gamma_{opt} = 1A_{1g} + 1A_{2g} + 1A_{2u} + 2B_{1u} + 1B_{1g} + 1B_{2g} + 1E_g + 3E_u,$$

where symbol "*g*" represents Raman active, "*u*" infrared (IR) active and "E" degenerate modes. The vibrational modes B_{1g}, E_g, A_{1g} and B_{2g} are Raman active and A_{2g} and B_{1u} modes, however, are Raman and infrared silent modes.[6] The Raman active modes consists of motions of anions with respect to central cations either perpendicular to *c* axis (modes A_{1g}, B_{1g} and B_{2g}) or along the *c* axis (mode E_g). The illustration of the displacements of each atom for the Raman active lattice vibration in rutile TiO_2 is shown in **Fig. 2.8**.[5] Anatase is tetragonal structure with space group $I4_1/amd$ and has 15 optical modes at the Γ point of

Brillouin zone are expected on the basis of factor group analysis with the following irreducible representation of the normal vibrational modes:[7]

$$\Gamma_{opt} = 1A_{1g} + 1A_{2u} + 2B_{1g} + 1B_{2u} + 3E_g + 3E_u,$$

Six Raman modes, i.e., the A_{1g}, $2B_{1g}$, and $3E_g$ are Raman active, whereas the three modes A_{2u} and $2E_u$ are IR active. The mode B_{2u} is silent. TiO_2(B) is monoclinic structure having space group *C*2/*m* and its primitive cell contains four formula unit, i.e., 12 atoms with following irreducible representation:[8]

$$\Gamma_{opt} = 12A_g + 6B_g + 6A_u + 12B_u,$$

Among these modes, the selection rules give 18 A_g and B_g Raman active modes and 15 IR active A_u and B_u modes whereas one A_u and two B_u correspond to cell translations.[8]

B. Diffuse reflectance spectroscopy (DRS)

DRS is a technique generally used to study the reflectance or absorbance properties and to measure the band gap energy, i.e., the energy gap between the valence band maximum (VBM) and conduction band minimum (CBM) of semiconductor materials. The energy gap (E_{bg}) is an important feature of semiconductors which determines their applications in optoelectronics, photocatalysts and photovoltaics. The optical reflectance or absorbance is a result of interaction of light with the material. The basic principle is that UV, visible or near infrared (NIR) light is used to excite electrons from VB to empty CB. A sharp increase in absorption (or reflection) at energy close to the band gap that manifests the absorption edge (or reflectance threshold) in the UV-visible-NIR absorbance (or reflectance) spectra. This technique is mostly applicable to powder samples and thin films. For powder samples, usually UV-visible absorption spectroscopy is carried out by dispersing the sample in a liquid medium like water, ethanol or methanol. If the particle size of the sample is not small enough or not well dispersed in the solvent media, it precipitates and the absorption spectrum is more difficult to interpret. In order to avoid these complications, it is desirable to use DRS, which enables to obtain absorbance as well as the band gap energy (E_{bg}) of un-supported materials with more accuracy.[9] Reflectance of samples can be measured using either an integrating sphere or a specular reflectance accessory. Integrating spheres are used for samples with a significant diffuse reflectance component such as powders and other 'rough' materials. Samples are placed at the back of the sphere and the light is reflected back off the sample and

collected by the sphere. Measurements typically provide the total reflectance but if required the diffuse reflectance (specular excluded) portion can be measured independently. The latter measurement is achieved by allowing the specular component to exit the sphere through the open specular port. The theory which makes possible to use diffuse reflectance spectra was proposed by Kubelka and Munk.[10] The absorbance can be calculated using Kubelka-Munk formula as

$$F(R_\infty) = \frac{(1-R_\infty)^2}{2R} = \frac{k}{s} \qquad (2.4)$$

$F(R_\infty)$ is called the Kubelka-Munk (K-M) function, where $R_\infty = \frac{R_{Sample}}{R_{Standard}}$, k = K-M absorption coefficient and s = K-M scattering coefficient.

In the parabolic band structure, the band gap (E_{bg}), and absorption coefficient (α) of a direct band gap and indirect band gap semiconductor are related through the well known equation (2.5) and (2.6), respectively:[11, 12]

$$(\alpha h\nu)^2 = C_1\,(h\nu - E_{bg}) \qquad (2.5)$$

$$(\alpha h\nu)^{1/2} = C_2\,(h\nu - E_{bg}) \qquad (2.6)$$

Where α is the linear absorption coefficient of the material, $h\nu$ is the photon energy and C_1, C_2 are the proportionality constant. When the material scatters in a perfectly diffuse manner, the scattering coefficient is considered as constant with respect to wavelength. So, by comparing equation (2.4) with equations (2.5) and (2.6), one can obtain expressions for relation between the K-M function and band gap of the material as

$$(F(R_\infty)h\nu)^2 = C_3(h\nu - E_{bg}), \text{ direct band gap} \qquad (2.7)$$

$$(F(R_\infty)h\nu)^{1/2} = C_4(h\nu - E_{bg}), \text{ indirect band gap} \qquad (2.8)$$

Here C_3, C_4 are the proportionality constant.

Fig. 2.9. Photograph of the Diffuse Reflectance Spectrometer (Perkin Elmer, LAMBDA 750).

We used a Perkin Elmer (LAMBDA 750) spectrophotometer for the DRS measurements. **Fig. 2.9** shows a photograph of the DRS spectrophotometer used in this study. It performs the measurement in the UV/visible/ NIR (i.e., 200 – 2500 nm wavelength range) region. The deuterium and tungsten halogen light sources are provided to perform the measurements in the UV/Visible/NIR region. An integrating sphere along with PMT (photomultiplier), InGaAs and PbS detectors is used to collect the diffuse reflectance light being reflected from the sample in all direction. Calibrated spectralon diffuse reflectance standard is used as reference. A sample holder kit with a quartz piece on the front is used to hold the powder sample. A schematic diagram of diffuse reflectance mechanism is shown in **Fig. 2.10**. We measured the diffuse reflectance in absorbance mode, i.e., using K-M function. The band gap is calculated from the linear fit of linear portion of $(F(R_\infty)h\nu)^2$ vs $h\nu$ plot with $(F(R_\infty)h\nu)^2 = 0$ for direct band gap and $(F(R_\infty)h\nu)^{1/2}$ vs $h\nu$ plot with $(F(R_\infty)h\nu)^{1/2} = 0$ for indirect band gap.

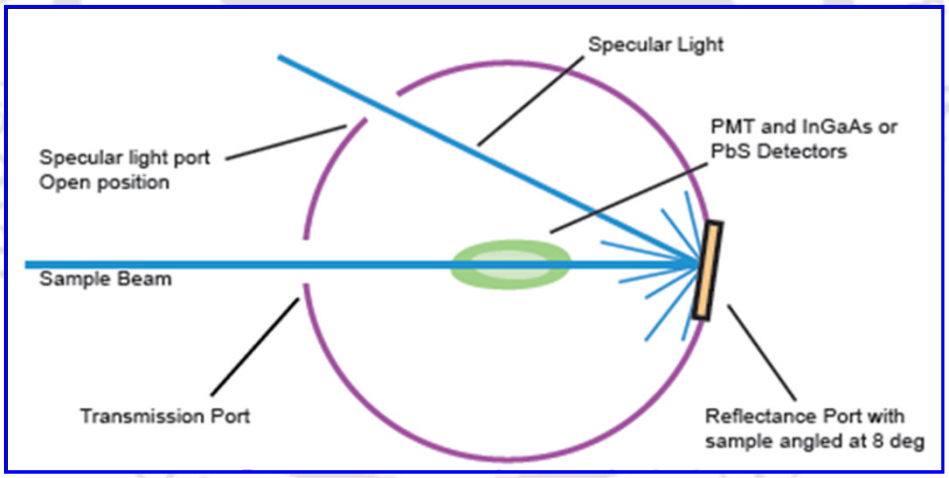

Fig. 2.10. Schematic diagram illustrating diffuse reflectance mechanism, excluding the specular reflectance.

C. ***Photoluminescence (PL) spectroscopy***

Photoluminescence (PL) is the emission of light from a material under optical excitation. Excitation energy is required to excite the electron from lower energy level (ground state/ equilibrium state) to higher energy level (excited state). Light of suitable energy is directed

onto a sample, where it is absorbed and imparts excess energy into the material in a process called photo-excitation. This causes electron-hole pair generations within the material and those electrons move into permissible excited states. The excess energy can be released by the sample through the emission of light or luminescence, when these electrons return to their equilibrium states and the whole process is called photoluminescence. The energy of the emitted light (photoluminescence) relates to the difference in energy levels between the two electron states involved in the transition between the excited state and the equilibrium state. The quantity of the emitted light is related to the relative contribution of the radiative process between the various excited states (as defect states near the conduction act as a luminescence centers) and the equilibrium states. Features of the emission spectrum provide the information about the band gap energy, impurity level/ defect level detection, and electron-hole recombination mechanism. The intensity of the PL signal can be used to extract the qualitative information about the contribution of various defect states. The most common radiative transition in semiconductors is between the states in the conduction and valence bands, with the energy difference being known as the band gap. Radiative transitions in semiconductors also involve localized defect levels within the band gap of the semiconductor. The photoluminescence energy associated with these levels can be used to identify specific defects, and the amount of photoluminescence can be used to determine their relative concentration. The return of the excited electrons to equilibrium state to recombine with holes, also known as "recombination," can involve both radiative and non-radiative processes. The amount of photoluminescence and its dependence on the level of photo-excitation and temperature are directly related to the dominant recombination process. Analysis of photoluminescence helps to understand the underlying physics of the recombination mechanism. The fundamental limitation of PL analysis is its reliance on radiative events. Materials with poor radiative efficiency, such as low-quality indirect band gap semiconductors, are difficult to study via ordinary PL. Similarly, identification of impurity and defect states depends on their optical activity. More intense laser PL is generally preferred to study the defect/ impurity states such as oxygen vacancy as compared to ordinary Xenon-lamp based PL system.

We used 325 nm He-Cd laser and 405 nm diode laser (Coherent, Cube) excitation with the help of a spectrometer (focal length: 15 cm; blaze wavelength: 500 nm; groove

density: 150 g mm^{-1}) equipped with a cooled charge-coupled device (Princeton Instruments, PIXIS 100B) detector. Extended NIR PL measurements were carried out using a liquid N_2 cooled InGaAs detector (OMA-V-SE, Roper Scientific). **Fig. 2.11** shows a photograph of the PL instrument which is used in the present study. The PL measurements were carried at room temperature for most of the samples. We have also performed low temperature (10 K- 280 K) PL measurement and room temperature PL under high vacuum (5×10^{-5} torr), and with oxygen gas into the vacuum chamber for some of the samples. We put the powder samples on a conductive black carbon tape for PL measurements. Each spectrum was corrected for the detector response as a function of wavelength after background subtraction. The steady state PL peaks are usually of Gaussian shape expressed by

$$y = y_0 + A\, exp\,[-(\frac{(x-x_c)^2}{2w^2})] \qquad (2.9)$$

Where y_0 is the offset constant, x_c, w and A are the peak position, width and peak amplitude, respectively. The measured spectral profile of the PL spectrum is analyzed by fitting with Gaussian line-shape function or multiple Gaussian functions using a PeakFit software.

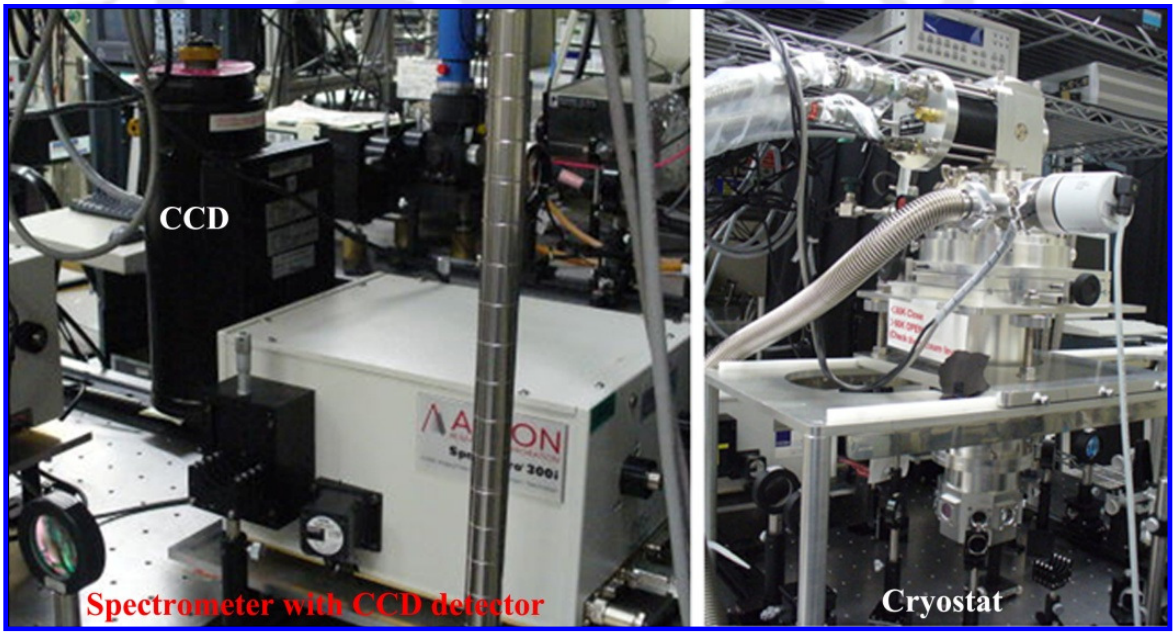

Fig. 2.11. Photograph of the Photoluminescence spectrometer with CCD detector and Cryostat.

D. Time-resolved photoluminescence (TRPL) spectroscopy

Time resolved photo-luminescence (TRPL) is a useful characterization technique that provides the spectral and temporal evolution of the emission of a sample following its illumination by a short pulse of light. More precisely, the short pulse of light generates electron-hole pairs (excitons) that decay to lower energy levels of the sample. These electron-hole pairs can subsequently recombine and emit light. The emitted light is composed of a set of wavelengths corresponding to transition energies of the sample and, as a result, the measurement of the optical spectrum as a function of time provides a means to measure the transition energies and their lifetimes. The measurement basically counts the number of photons of fixed wavelength with time. The emitted photon is analyzed by a spectrometer and detected by a micro-channel-plate photomultiplier tube (MCP-PMT) detector. A Multi Channel Analyzer (MCA) board in the computer analyzes the output pulse voltages into various channels, which correspond to different times. In this way, the MCA can record each photon arriving at the MCP–PMT at a particular time. The number of output pulses from the MCP–PMT is directly proportional to the number of incident photons. Averaging over millions of photons, the measurement creates a histogram which shows how long excitons "live" after being created by the laser pulse. Thus, the carrier dynamics occurring during these processes provides not only information about the position of the peak emission, as in a normal steady state PL experiment, but also the lifetime of the excitons involved in the recombination.

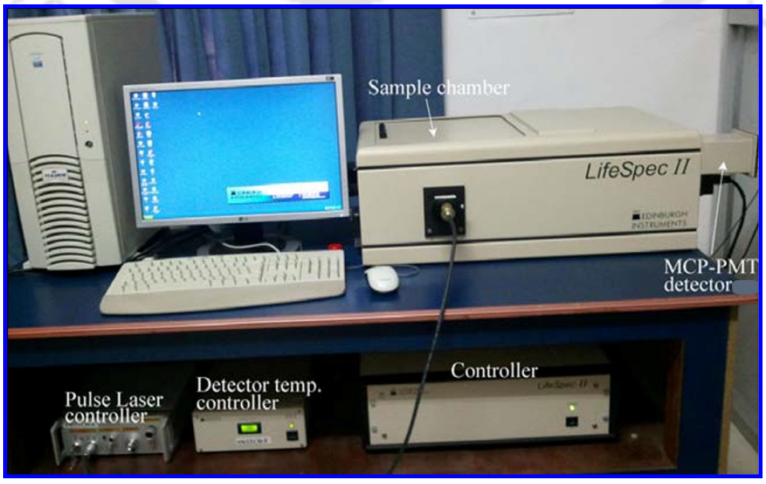

Fig. 2.12. Photograph of the Time-Resolved Photoluminescence spectrometer (LifeSpec II, Edinburgh Inst., UK).

The photograph of the TRPL spectroscopy (LifeSpec II, Edinburgh Inst., UK) instrument used in the present study is shown in **Fig. 2.12**. We used adjustable nanosecond pulsed pump laser (EPL series, Edinburgh Inst., UK) of wavelength 405 nm to measure the PL decay of the defects related visible emission in the TiO_2 nanostructures. This instrument has a time resolution of ~50 ps. The TRPL data usually follow an exponential decay behavior or combination of such function depending upon the number of decay channels available in the sample. The PL decay equation is expressed as

$$I(t) = I_1\ exp\ (\bar{t}/\tau_1) + I_2\ exp\ (\bar{t}/\tau_2) + I_3\ exp\ (\bar{t}/\tau_3) + \ldots\ \ldots\ \ldots + I_0 \qquad (2.10)$$

Where $I(t)$ is the PL count, I_1, I_2, I_3 …. …. are decay channel amplitudes and τ_1, τ_2 ,τ_3 …. …. are the decay time constants and I_0 accounts for the background noise. Measurement of τ provides information on the mechanism of recombination.

E. X-ray photoelectron spectroscopy (XPS)

XPS is a key surface characterization tool which combines surface sensitivity with the ability to quantitatively obtain both elemental and chemical state information for each element detected, through the chemical shift. It is widely used for studies of surface defects and chemical environment, because of its high sensitivity to surface (i.e., up to 10 nm from the sample surface). It also provides useful information about the depth profile (i.e., an evaluation of the variation of composition with depth) and the surface impurities present in the sample. The principle of XPS is based on the photoelectric effect outlined by Einstein in 1905 was developed by Siegbahn and his research group,[13] where the concept of the photon was used to describe the ejection of electrons from a sample surface when photons impinge upon it. This process can be expressed by the following equation:

$$BE = h\nu - KE - \emptyset, \qquad (2.11)$$

where BE is the binding energy of the electron in the atom, $h\nu$ is the photon energy of x-ray source, KE is the kinetic energy of the emitted electron that is measured in the XPS spectrometer and $\emptyset$ is the spectrometer work function. For XPS, Al $K\alpha$ (1486.6 eV) or Mg $K\alpha$ (1253.6 eV) is generally used as the source of x-rays. The photon is absorbed by an atom of the sample, leading to emission of a core (inner shell) electron. The energy of the photoelectrons leaving the sample is determined using an appropriate electron energy analyzer and this gives a spectrum with a series of photoelectron peaks. For each and every

element, there will be a characteristic binding energy associated with each core atomic orbital, i.e., each element will give rise to a characteristic set of peaks in the photoelectron spectrum at kinetic energies determined by the photon energy and the respective binding energies. The peak intensities measure how much of a material is at the surface, while the peak positions indicate the elemental and chemical composition. Other values, such as the full width at half maximum (FWHM) are useful indicators of chemical state changes and physical influences.

In this study, XPS measurements were carried out with a PHI X-Tool automated photoelectron spectrometer (ULVAC-PHI, Inc.) using Al $K\alpha$ X-ray beam (1486.6 eV) with a beam current of 20 mA. Some of the samples were characterized with ESCALAB 3400 (Shimadzu, Japan) instrument using Mg $K\alpha$ X-ray beam (1253.6 eV). Carbon 1s spectrum was used for the calibration of the XPS spectra recorded for various samples. **Fig. 2.13** shows the photograph of XPS instrument used for this study. The broad peaks with shoulder are fitted with Gaussian line-shape using a PeakFit software followed by the expression

$$y = y_0 + A\ exp\ [-(\frac{(x-x_c)^2}{2w^2})] \qquad (2.12)$$

Where y_0 is the offset constant, x_c, w and A are the peak position, width and peak amplitude, respectively.

Fig. 2.13. Photograph of the X-ray photoelectron spectrometer (ULVAC-PHI, Inc.).

F. Fourier transform infrared (FTIR) spectroscopy

FTIR is one of the powerful spectroscopic tools generally used to determine the structural bonding information, impurities and chemical functional groups in the sample. The FTIR is based on the phenomena "*Michelson interference"* combined with Fourier transformation of the source spectrum.[14] FTIR interferogram consists of spectral information of the source along with the transmittance characteristic of the sample. We used FTIR spectroscopy in transmittance mode of operation for our few samples to confirm the formation of pure TiO_2 phases and shifting of Ti-O related vibration modes due to oxygen vacancy defects in TiO_2 nanostructures. In this study, we used a commercial FTIR spectrometer (Perkin Elmer, Spectrum BX) to obtain the transmission spectrum of the TiO_2 nanostructures at room temperature in the range 400- 4000 cm^{-1} at a resolution of 2 cm^{-1}. All the spectra were taken after background corrections. For the sample preparation, TiO_2 powder of very small quantity is mixed with KBr and ground in ceramic mortar, then prepared pellets using KBr press and die.

2.2.3. Magnetic characterization

A. Vibrating sample magnetometer (VSM)

VSM is a scientific instrument used to measure magnetic properties of materials. A VSM uses an induction technique to measure magnetic moment of a sample. In a VSM the sample is mounted at one end of a rigid rod which is driven by a vibrator. The sample is then oscillating in a vertical direction at a fixed frequency. The sample can be magnetized by a horizontal magnetic field generated by an electromagnet. Surrounding the sample is a set of sensing coils (pick-up coils). As the sample moves, its magnetic moment alters the magnetic flux through these coils. The alternating magnetic field will cause an electric field in the pick-up coils according to Faraday's law of induction. This current will be proportional to the magnetization of the sample and can be detected using a lock-in amplifier. The various components are hooked up to a computer interface. Using controlling and monitoring software, the system can tell us how much the sample is magnetized and how its magnetization depends on the strength of the constant magnetic field.

The magnetic properties of the undoped and doped TiO_2 nanostructures were measured using a Lakeshore (Model 7410) VSM. **Fig. 2.14** shows the photograph of the

VSM instrument used in this study. It mainly consists of water cooled electromagnet, power supply, vibration exciter, sample holder, sensors coil, lock in amplifier and computer interface. The sample is mounted at the end of a quartz rigid rod using Teflon tape. Before sample placement inside the electromagnet, the magnetic moment is calibrated using the standard Ni sample. A certain amount of TiO_2 nanostructures powder is put on a Teflon tape and weighed using a digital micro-balance. Then the sample is wrapped tightly with the Teflon tape. We measured both field-dependent and temperature (high temperature)-dependent magnetization for our samples.

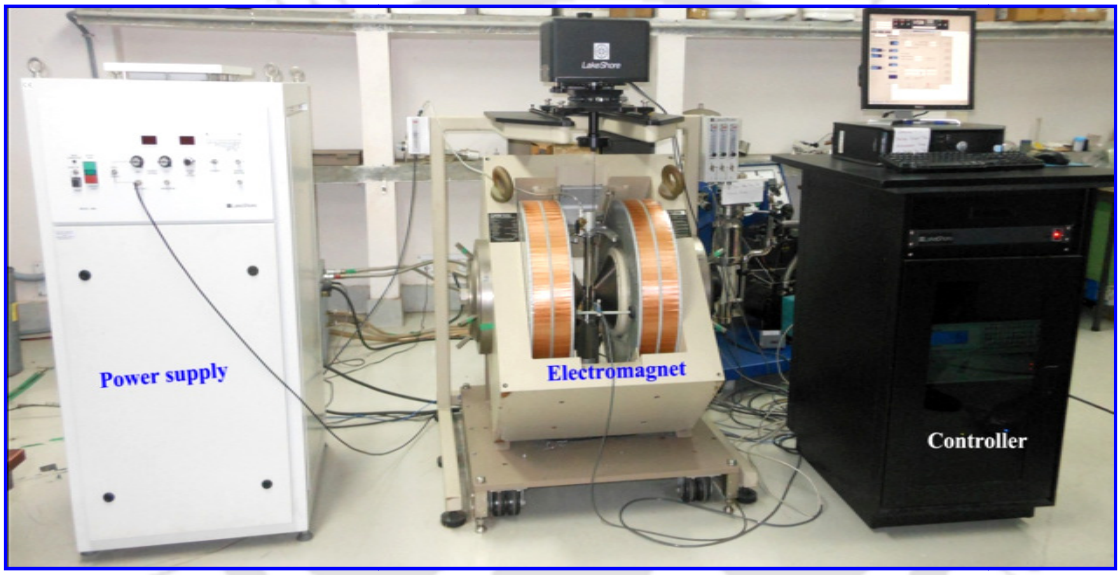

Fig. 2.14. Photograph of the Vibrating Sample Magnetometer (Lakeshore, Model 7410) with power supply, electromagnet and VSM controller.

B. Electron spin resonance (ESR) spectroscopy

ESR spectroscopy is a very powerful, sensitive and informative technique for the characterization of the electronic structures of materials with unpaired electrons. ESR is based on the fact that the electron interacts with the external static magnetic field H via its magnetic moment

$$\vec{\mu} = -\mathrm{g}\,\mu_B \boldsymbol{S} \qquad (2.13)$$

Here μ_B is the dipole moment of a electron (Bohr magneton) equal to 9.274×10^{-24} JT^{-1}, $\boldsymbol{S}$ is the electron spin, and g is dimensionless constant called electron g-factor, which is equal to 2.0023 for the free electron.

The spin Hamiltonian is read as

$$\mathcal{H} = -\vec{\mu}\cdot\vec{H} = \mathrm{g}\,\mu_B\,SH \qquad (2.14)$$

Taking $S = \pm\frac{1}{2}$ for up spin and down spin, the energy Eigen values becomes

$$E = \pm\frac{1}{2}\,\mathrm{g}\,\mu_B\,H \qquad (2.15)$$

Thus, the energy levels are quantized in an external magnetic field and the transitions are induced between these levels (energy difference, $\Delta E = \mathrm{g}\,\mu_B\,H$) by the oscillating magnetic field of suitable frequency. In ESR spectroscopy, the magnetic component of a microwave energy, which is perpendicular to the magnetic field H, induces microwave energy absorption subject to the resonance condition ($\Delta E = h\nu$). The g-value for the observed resonance peak can be calculated as

$$\mathrm{g} = \frac{h\nu}{\mu_B H}, \qquad (2.16)$$

where ν is microwave frequency, H is the magnetic field and h is plank's constant equal to 6.626×10^{-34} J·s.

Fig. 2.15. Photograph of the Electron Spin Resonance spectrometer (JEOL, JES-FA200).

In this work, ESR measurements have been done using a JEOL (JES-FA200) instrument operating in the X-band. **Fig. 2.15** shows the photograph of the ESR instrument used for the present study. The microwave source is a Gunn oscillator operating at a frequency of 9.4 GHz (X-band). We used this technique for detection of unpaired electron spin associated with Cr^{3+}, Fe^{3+}, Ti^{3+}, F^{+} center in our defective undoped and Fe, Cr-doped TiO_2 nanostructures.

References

1. D. K. Schroder, Semiconductor material and device characterization, 3rd ed., Wiely-Interscience , New Jercy, USA (2006).
2. K. Ishikawa, K. Yoshikawa and N. Okada, Physical Review B **37**, 5852-5855 (1988).
3. G. K. Williamson and W. H. Hall, Acta Metallurgica **1**, 22-31 (1953).
4. S. B. Qadri, J. P. Yang, E. F. Skelton and B. R. Ratna, Applied Physics Letters **70**, 1020-1021 (1997).
5. Y. Zhang, C. X. Harris, P. Wallenmeyer, J. Murowchick and X. Chen, The Journal of Physical Chemistry C **117**, 24015-24022 (2013).
6. I. Lukačević, S. K. Gupta, P. K. Jha and D. Kirin, Materials Chemistry and Physics **137**, 282-289 (2012).
7. M. Giarola, A. Sanson, F. Monti, G. Mariotto, M. Bettinelli, A. Speghini and G. Salviulo, Physical Review B **81**, 174305 (2010).
8. M. Ben Yahia, F. Lemoigno, T. Beuvier, J.-S. Filhol, M. Richard-Plouet, L. Brohan and M.-L. Doublet, The Journal of Chemical Physics **130**, 204501 (2009).
9. A. E. Morales, E. S. a. Mora and U. Pal, REVISTA MEXICANA DE F´ISICA S **53**, 18-22 (2007).
10. P. Kubelka and F. Munk, Z. Tech. Phys. **12**, 593–601 (1931).
11. J. Bardeen, F. J. Blatt and L. H. Hall, Indirect Transition from the Valence to the Conduction Bands, in proceedings of the conference on photoconductivy, Atlantic city (1954).
12. J. Tauc, R. Grigorovici and A. Vancu, Physica Status Solidi (b) **15**, 627-637 (1966).

13. K. Siegbahn, C. Nordling, A. Fahlman, R. Nordberg, K. Hamrin, J. Hedman, G. Johansson, T. Bergmark, S. E. Kerlsson, I. Lindgren and B.Lindberg, Nova Acta Regiae Soc. Sci., Ser IV **20** (1967).

14. C. R. Brundle, J. Charles, A. Evans and S. Wihon, Encyclopedia of material characterization: surfaces, interfaces, thin films (1992).

Chapter 3

Controlled Growth of TiO_2 Nanostructures: Elucidating the Growth Mechanism

The one-dimensional (1D) TiO_2 nanostructures such as nanotubes (NTs), nanorods (NRs), nanoribbons (NRbs) and nanowires (NWs) have a large surface area, with a unique 1D morphology providing a direct path for electron transport with enhanced carrier collection. As a result, 1D nanostructures of TiO_2 have gained huge attention for several promising and high performance applications. In this study, TiO_2 1D nanostructures are grown by a simple low temperature solvothermal route followed by the Na^+/H^+ ion-exchange and final calcinations process. We investigated the impact of reaction temperature, stirring condition and cosolvent on the morphologies of the as-prepared nanostructures. Growth mechanism is elucidated from the systematic studies of FESEM and TEM imaging. The structural characterizations of as-synthesized nanostructures are studied by using XRD and micro-Raman spectroscopy. This work will be valuable for controlled growth of TiO_2 NTs, NRs, NWs and nanoporous NRbs, and understanding the formation mechanism of various nanostructured TiO_2 synthesized under different growth conditions.

3.1. Introduction

The design and fabrication of 1D TiO_2 NRs, NTs and NWs have attracted intensive interest due to their unique architectures, extraordinary physical and chemical properties and potential applications such as gas sensor, water and environmental purification, lithium ion battery, water splitting of hydrogen production and dye-sensitized solar cells. To realize these promising high performance applications, the control of the highly desirable properties upon their inherent crystal structure, morphology, surface area, and porosity through their nanostructures and understanding the formation mechanism are challenging today.

Considerable effort has been made to explore novel approaches from vapor-phase technique to solution-growth process to grow TiO_2 nanostructures with various properties by

controlling their size and morphology. The typical vapor-phase technique requires high temperature and the control over morphology is not an easy task. Moreover, growth of anatase TiO_2 nanostructures that has more photocatalytic activity than the rutile is not possible through this technique. On the other hand, hydrothermal method is an effective technique to synthesize TiO_2 nanostructures at relatively low temperature with optimal control over morphology, structure and phase composition without the requirement of templating. This approach requires neither expensive equipments nor specific chemicals, hence provide a more promising approach in terms of cost. In particular, it has been reported that the size, morphology and structural properties of TiO_2 nanostructures depend on the TiO_2 precursors and reaction parameters such as reaction temperature, reaction time and pH of the solution during the reaction,[1, 2] which can be achieved by this technique. After the first successful synthesis of titanate nanotubes by Kasuga et al.,[3] extensive research has been carried out on the hydrothermal growth of titanate and TiO_2 NTs, NRs and NWs by adjusting various parameters within the hydrothermal system to determine their effects on the nanostructure formation and resultant morphology.[4] These parameters include reaction temperature, alkaline concentration, reaction duration, precursor phase, and crystallite size. Lan et al.[5] reported that NTs are formed after hydrothermal treatment of TiO_2 particles in 10 M NaOH solution at 150 °C for 24 h, whereas NRbs appeared at higher temperature (180 °C). Morgan et al.[6] reported that NTs are formed at lower temperature and at 200 °C, NTs transformed to NRbs using anatase TiO_2 powder as precursor. It is accepted by several authors[7, 8] that NTs are formed at mild hydrothermal temperatures in the range of 130 - 150 °C, while only NWs or NRbs are observed at higher temperature (>180 °C). Additionally, titanate NTs can further transform into NWs with prolonged reaction duration.[9] However, two additional important parameters such as cosolvent and stirring effect during the hydrothermal process have rarely been reported to achieve 1D titanate and TiO_2 nanostructures. More recently, Shen et al.[10] reported the effect of cosolvent, temperature and NaOH concentration on the morphology of titanate nanostructures. However, systematic study of solvent controlled nanostructures and the exact growth mechanism of solvothermally synthesized titanate and TiO_2 NTs and NWs is still a topic debated extensively in the contemporary literature.

In this Chapter, we study the temperature and solvent controlled hydrothermal growth of hybrid TiO_2/titanate NTs, NRs and NWs and pure phase TiO_2(B) nanoporous NRbs, NRs. The growth mechanism of the as-prepared nanostructures is elucidated from the systematic studies of structure and morphology through FESEM and TEM imaging. One of the merits of our synthesis process is the knowledge of the actual internal growth temperature of the solvent during the reaction process. In most of the earlier reports on the hydrothermal method, the autoclave is placed on a heated base set at an elevated temperature; this set temperature may not be the actual temperature of the solvent during the reaction. Moreover, growth temperature inside the autoclave depend on the solvent used in the reaction, as we have set a particular temperature on the hot plate, though the observed temperature on the PID controller is different for different solvents of the same amount. Hence, the exact growth temperatures usually reported in the literature for the solvent controlled synthesis of TiO_2 nanostructures are not precisely known. Note that the high-pressure reactor set up (autoclave) in our laboratory has a thermal sensor with immersion tube inside the Teflon vessel, which is connected to a PID temperature controller. Here we studied the actual internal growth temperature of the solvent during the reaction, which is displayed on the PID temperature controller.

3.2. Growth of TiO_2 nanostructures

I. Solvothermal reaction

All the chemicals were used as-received without further purification. Anatase TiO_2 powders (average particle size ~80 nm), sodium hydroxide (NaOH) pellets, ethanol and ethylene glycol were purchased from Merck. Doubly distilled deionized (DI) water was used during all the experiments. In a typical synthesis, 0.275 g of anatase TiO_2 powder was mixed with 60 ml of aqueous 10 M NaOH under stirring for 1 h, a milky solution is obtained. Then the mixed solution was transferred into a Teflon-lined autoclave (Berghof, BR- 100) of 100 ml capacity. The temperatures inside the autoclave were maintained at 130, 155, 180 °C under autogenous pressure and constant magnetic stirring at 250 rpm for 16 h. The formed precipitates were obtained by centrifugation and washed several times with DI water. To investigate the growth mechanism, some additional experiments were carried out using different mixed cosolvents (DI water:ethanol = 1:1, DI water:ethylene glycol = 1:1).

II. Ion-exchange reaction

The products obtained after solvothermal synthesis was Na-titanate. Next, to allow ion-exchange reaction between Na^+ and H^+, the product Na-titanate underwent an ultrasonic treatment with 0.1 M HCl till the pH ~7. After HCl treatment, the precipitates were washed several times with DI water to remove the residual impurities. The product after HCl treatment became H-titanate.

III. Calcinations

Finally the precipitates (H-titanate) were calcined at 500 °C for 5 h in air for dehydration using a high temperature furnace. During this process, the organic impurities were removed due to high temperature heat treatment. The product obtained after calcinations were pure TiO_2(B) and anatase phase, mixed anatase-ruile phase and TiO_2/titanate nanostructures, as confirmed from XRD and micro-Raman studies.

3.3. Structural studies

The XRD patterns of precursor anatase TiO_2 powder and solvothermal products synthesized at 130 °C using different solvents are shown in **Fig. 3.1(a)**. Commercial anatase TiO_2 precursor was used as a reference to identify the anatase peak unambiguously. All the peaks except the peaks at $2\theta = 31.7°$ and 45.45° correspond to anatase TiO_2 structure for the nanostructures synthesized in alkaline water and alkaline water-ethanol mixed solvent. These additional peaks are attributed to hydrated hydrogen pentatitanate ($H_2Ti_5O_{11}\cdot H_2O$) nanostructures (JCPDS # 44-0131), indicating the presence of TiO_2/titanate hybrid structure in the 1D nanostructures synthesized at 130 °C reaction temperature. **Fig. 3.1(b)** shows the XRD patterns of the samples synthesized at 180 °C using different solvents. All the diffraction peaks correspond to TiO_2(B) phase for the samples grown under alkaline DI water solvent and ethylene glycol cosolvent. While mixed anatase-rutile phase is observed for the sample grown under ethanol cosolvent. We also observed pure anatase TiO_2 phase in the samples synthesized at 130, 155 °C using ethylene glycol solvent in the XRD patterns (not shown). The XRD patterns of the samples (grown under ethylene glycol cosolvent) before HCl treatment and after HCl treatment prior to calcinations are shown in **Fig. 3.1(c)**. The

diffraction peaks of the sample prior to HCl treatment correspond to $Na_2Ti_4O_9$ (JCPDS # 33-1294) structure and after HCl treatment , Na^+ ion is replaced by H^+ ion and formed $H_2Ti_5O_{11}{\cdot}H_2O$ (JCPDS # 44-0131). The calcinations process helps in dehydration of $H_2Ti_5O_{11}{\cdot}H_2O$ to form TiO_2 structures.

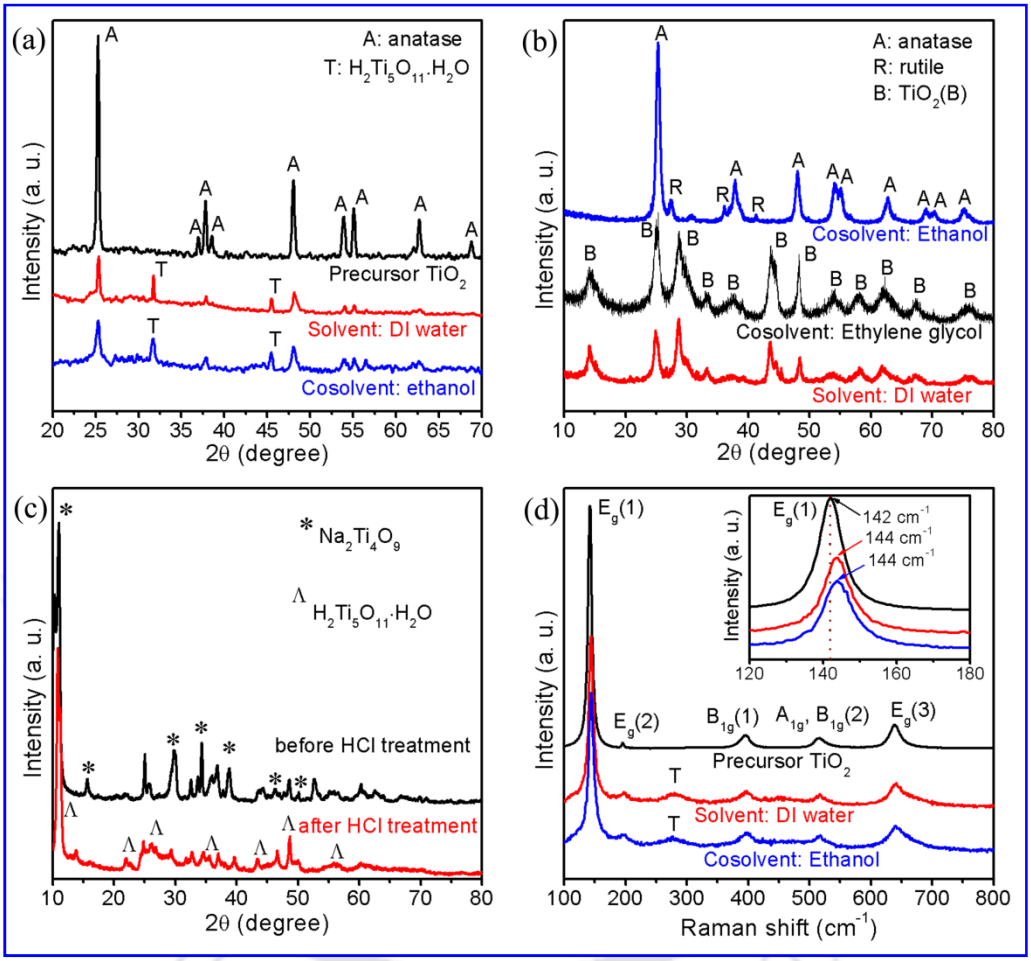

Fig. 3.1. XRD pattern of (a) precursor TiO_2 and the samples synthesized at 130 °C using alkaline DI water solvent, ethanol cosolvent, (b) samples synthesized at 180 °C using different solvents, (c) samples synthesized using alkaline ethylene glycol cosolvent before HCl treatment and after HCl treatment prior to calcination. (d) Raman spectra of precursor TiO_2 and the samples synthesized at 130 °C using alkaline DI water solvent and ethanol cosolvent.

Raman scattering is one of the most effective tool for the study of crystallinity, phase composition, phonon confinement effect and defect structures associated with the materials. More importantly, the XRD peaks are very similar for sodium titanates, hydrogen titanates

and among the polymorph of TiO_2 such as anatase, rutile, brookite and TiO_2(B). So, XRD results do not give a conclusive idea about the structure and phase composition. The as-synthesized samples are further characterized by Raman spectroscopy to clarify about the structure and phase composition associated with the materials. All the Raman peaks of as-grown nanostructures corresponds to tetragonal anatase TiO_2 phase except the broad peak at ~278 cm^{-1} for the sample grown by using highly alkaline water and alkaline ethanol cosolvents, as shown in **Fig. 3.1(d)**. This additional peak corresponds to hydrogen titanate, which indicates the presence of hybrid anatase TiO_2/titanate nanostructures in the sample grown at 130 °C. This is consistent with the XRD analyses. Further, the most intense E_g(1) Raman mode of anatase at 142 cm^{-1} shows a considerable blue shift as compared to anatase TiO_2 precursor shown in inset of **Fig. 3.1(d)**. This blue shift of the main E_g(1) Raman mode was interpreted as arising from different competing mechanism such as the non-stoichiometry due to oxygen vacancies or disorder induced defects and phonon confinement effects.[11, 12] From the FESEM and TEM images, we observed that the size of the 1D nanostructures is often orders of magnitude larger than the size of the precursor TiO_2 nanoparticles. So, the phonon confinement effect is easily discarded. We believe that the blue shift of as-synthesized nanostructures may be due to vacancies and/or defects created during the successive transformation from 2D nanosheets to 1D NTs, NRs/NWs and NRbs.[13] Moreover, the presence of defects is necessary to release the stress as the TiO_6 octahedral layers, the basic unit of the crystalline structure of TiO_2 polymorphs, along with the intercalated Na^+ are subsequently rolled up into NTs and/or splitting into NRs. Further studies may shed more light on the actual growth mechanism.

3.4. Morphology studies: FESEM imaging

The morphologies of the synthesized samples as obtained by FESEM are shown in **Figs. 3.2, 3.3 and 3.4. Fig. 3.2(a)** shows the early growth stage of 1D nanostructures at 130 °C reaction temperature using alkaline water solvent. The layered nanosheets coexisting with some partially developed NTs are observed at 130 °C, which confirms that the 1D nanostructures are formed from the intermediate layered nanosheets. At 155 °C reaction temperature, we observed both NTs and NRs in the sample synthesized from alkaline water solvent as shown

in **Fig. 3.2(b) and (c)**, respectively. The length and the diameter of the NTs are observed to be ~7 μm and 20 - 40 nm, respectively. The NTs are form a bunch and are oriented in a particular direction. The bunching of adjacent parallel NTs into larger bundles can be explained by the oriented attachment (OA) theory. According to the OA theory,[14] when structurally similar surfaces approach, atoms of opposing surfaces may combine chemically with each other. The chemical coordination results in NTs bundles bunching along identical crystal faces. In the present case, when the reaction temperature is increased to 180 °C, comparatively longer (613 - 3000 nm) and thicker (35 - 159 nm) NRs are formed using the same alkaline water as a solvent, which is shown in **Fig. 3.2(d)**. It has been argued that the higher temperature favors the formation of NRs by virtue of its enhanced thermal stability as compared that of NTs.[15] Other possible explanation for such transformation is explored further in the 'growth mechanism' section discussed later.

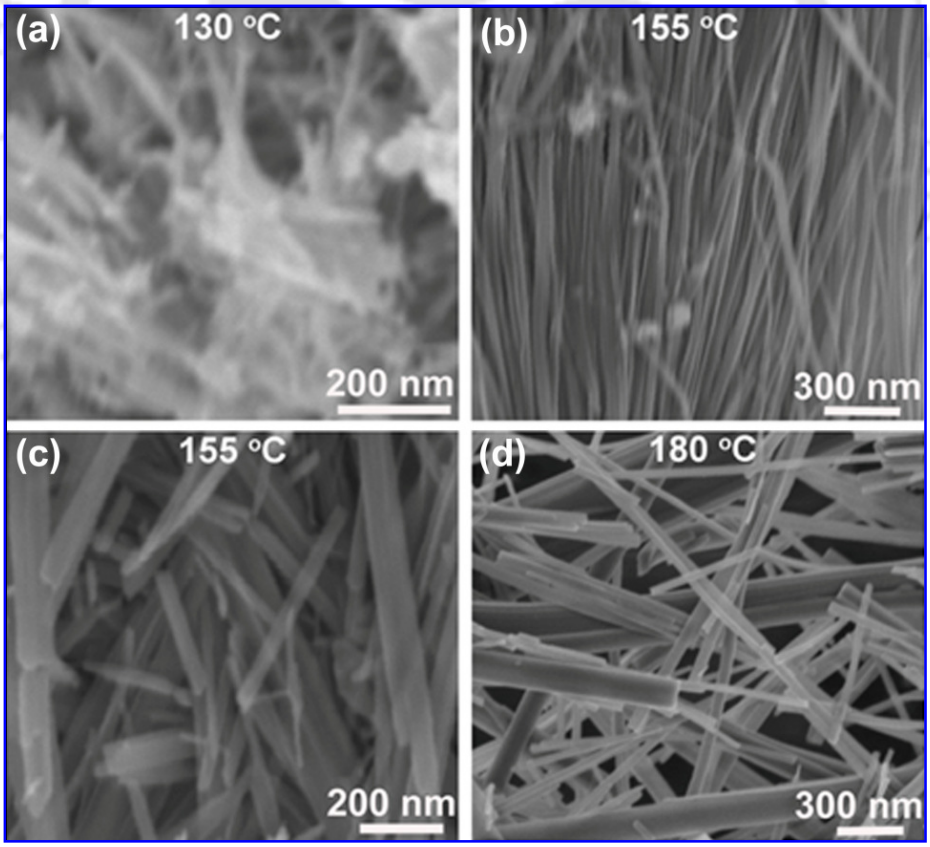

Fig. 3.2. FESEM images of morphology of the TiO_2 nanostructures synthesized in alkaline water solvent at reaction temperatures: (a) 130 °C, (b)-(c) 155 °C and (d) 180 °C.

The morphologies of nanostructures synthesized using alkaline ethanol cosolvent are shown in **Fig. 3.3**. **Fig. 3.3(a)** shows the layered nanosheets as well as splitting of the nanosheets formed at 130 °C reaction temperature, which further confirmed that 1D nanostructures are actually obtained from the layered nanosheets irrespective of the solvents used. The growth of NRs at 155 °C reaction temperature using ethanol cosolvent is shown in **Fig. 3.3(b)**. The NRs have diameter ranging from 28 nm to 95 nm and length up to ~ 3000 nm. However, we observed NRs of diameter 38 - 144 nm and length up to 4500 nm coexisting with some NWs having diameter in the range 7 - 20 nm as the reaction temperature increased to 180 °C, shown in **Fig. 3.3(c)**. The NRs are thick and straight due to their rigidness while NWs are thin and flexible and are found to be curved, as shown in **Fig. 3.3(c)**.

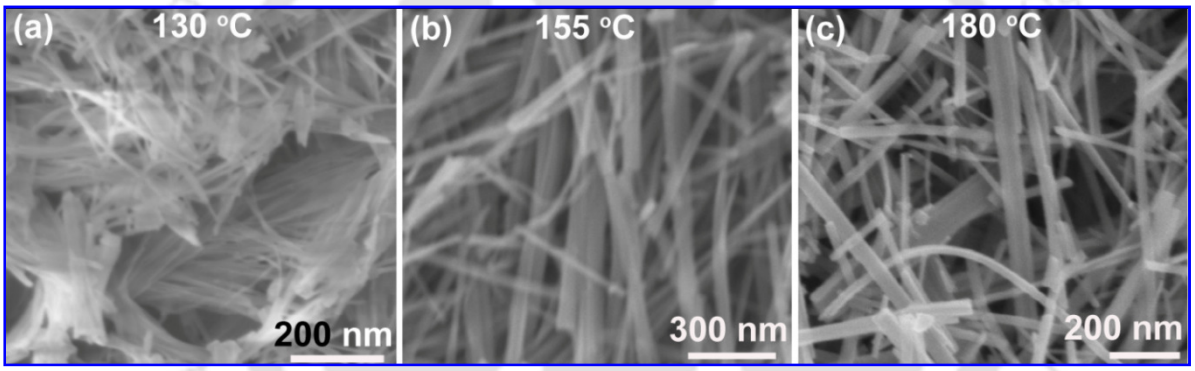

Fig. 3.3. FESEM images of the morphology of the TiO_2 nanostructures synthesized in alkaline ethanol cosolvent at the reaction temperatures: (a) 130 °C, (b) 155 °C and (c) 180 °C.

The morphology of the synthesized samples under alkaline ethylene glycol cosolvent is shown in **Fig. 3.4**. The sample grown at 130 °C exhibits thick nanosheet like morphology, while the sample grown at 155 °C exhibits small NRs like structures. **Fig. 3.4(c)** shows long and straight NRbs of TiO_2 grown at 180 °C. Thus, from the **Fig. 3.4(a-c)**, we found that nanosheets are formed at low temperature (130 °C), then small NRs are formed at 155 °C and finally NRbs are obtained at 180 °C from the TiO_2 NPs.

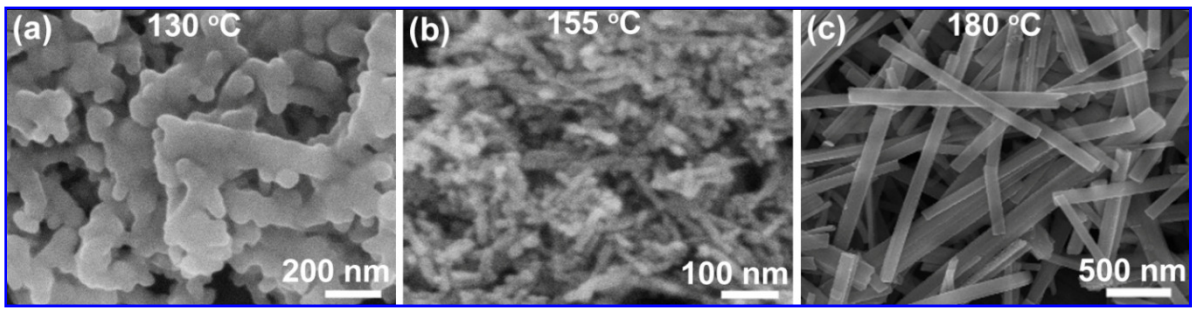

Fig. 3.4. FESEM images of the morphology of the TiO_2 nanostructures synthesized in alkaline ethylene glycol cosolvent at the reaction temperatures: (a) 130 °C, (b) 155 °C and (c) 180 °C.

3.5. Morphology studies: TEM imaging

In order to develop a better understanding of the growth mechanism and the structure, more detailed studies were conducted by means of TEM and HRTEM. The growth of the different TiO_2 nanostructures at different temperatures using various solvents is clearly monitored by TEM. **Figs. 3.5(a) - (c)** show the TEM images of the as-prepared nanostructures in alkaline water solvent. A mixture of both NTs and NRs is grown at 155 °C reaction temperature as shown in **Fig. 3.5(a) and (b)**, which is consistent with the FESEM images. The inner and outer diameters of the NTs are measured to be 5 nm and 9 nm, respectively. Note that the diameter of the NTs measured by TEM is considerably less than the diameter measured from FESEM images. This may be due to the shrinkage of the NTs due to the high operating electron gun voltage of the TEM. When the solvothermal reaction temperature was increased to 180 °C, we observe the formation of NRs only, as shown in **Fig. 3.5(c)**. The NTs that are formed at 155 °C are not found at 180 °C, which clearly reveals that the transformation of NTs to NRs occurs at higher temperature. We also noticed that the diameter and length of the NRs increase considerably with increase in reaction temperature. The higher temperature may accelerate the solvothermal reaction and consequently the growth rate is increased. **Fig. 3.5(d) and (f)** shows the TEM images of TiO_2 NRs grown at 155 °C and 180 °C, respectively, using ethanol cosolvent. **Fig. 3.5(d)** shows a single NR of diameter ~45 nm grown at 155 °C. The lattice fringes and EDX result of the corresponding NR are shown in inset of **Fig. 3.5(d) and (e)**, respectively. The d-spacing of 3.3 Å corresponds to (101) plane of anatase TiO_2, while the d-spacing of 2.61 Å corresponds to (311) plane of $H_2Ti_5O_{11}{\cdot}H_2O$.

This reveals the presence of some amount of unconverted titanate with the anatase TiO_2 nanostructures. The chemical composition is confirmed using the EDX spectra which detected Ti, O, Cu and C elements, as shown in **Fig. 3.5(e)**. The Cu and C signals are due to the TEM grid used for the imaging. The absence of Na in the EDX spectra may suggest that Na^+ ion is successfully replaced by H^+ during the ion-exchange reaction when treated with HCl. The hydrogen element is unlikely to be detected in the EDX spectra. Thus, hybrid anatase TiO_2/hydrogen titanate NRs are successfully synthesized at 155 °C in highly alkaline ethanol cosolvent. A high magnification TEM image of a single NR grown at 180 °C is shown in **Fig. 3.5(f)**. Note that a unique nanostructure is obtained at 180 °C when ethylene glycol was used as cosolvent. We observed TiO_2 NRbs of length up to ~2.6 μm and width in

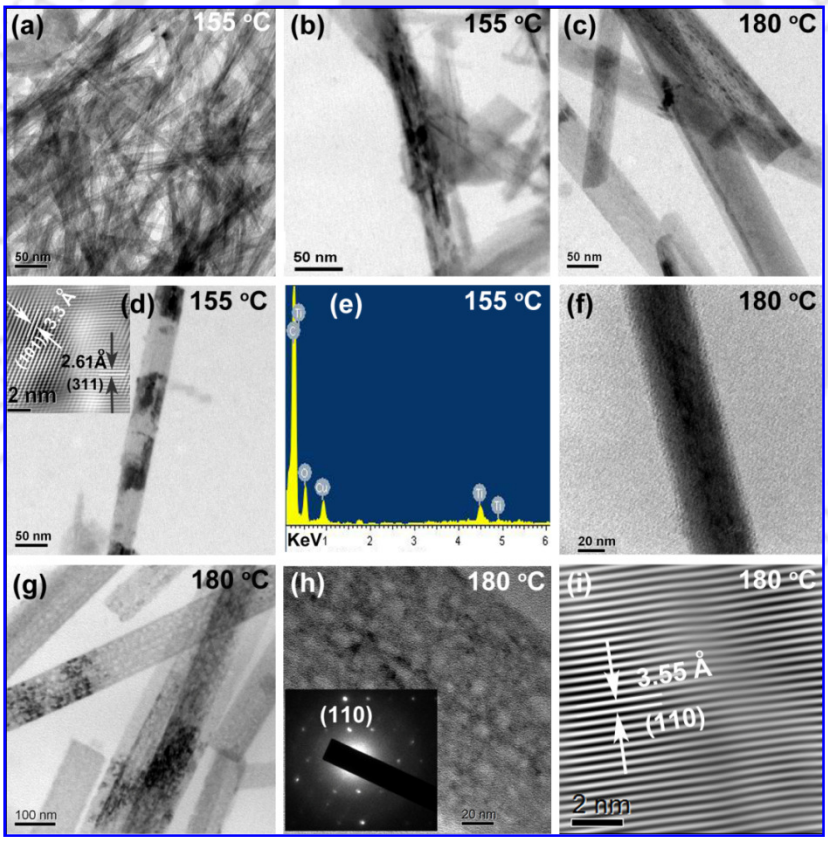

Fig. 3.5. TEM images of the as-synthesized TiO_2 nanostructures. Using alkaline water solvents (a) and (b) at 155 °C, (c) at 180 °C reaction temperature; using alkaline ethanol cosolvent (d) at 155 °C, (f) at 180 °C reaction temperature; using alkaline ethylene glycol cosolvent (g) and (h) at 180 °C reaction temperature. The inset of (h) shows the corresponding SAED pattern, and (i) shows the HRTEM lattice fringes of the NRbs. The inset in (d) shows the corresponding HRTEM lattice fringes of the nanorod and (e) shows the EDX spectrum of the NRs.

Table. 3.1. The effect of solvent and reaction temperature on the morphologies, sizes and structures of the 1D TiO_2 nanostructures.

Solvent	Reaction temperature (°C)	Morphology	Diameter (nm) from FESEM	Diameter (nm) from HRTEM	Structure
DI water	130	Nanosheets, Nanotubes	…..	…..	Anatase TiO_2/titanate
	155	Nanotubes, Nanorods	15 – 20 39 – 59	9 37	…..
	180	Nanorods	35 – 159	35 - 79	TiO_2(B)
DI water: ethanol	130	Splitted nanosheets	…..	…..	Anatase TiO_2/titanate
	155	Nanorods	28 - 95	~45	…..
	180	Nanorods, Nanowires	38 – 144 …..	40 – 65 20 - 25	Anatase/rutile TiO_2
DI water: ethylene glycol	130	Thick nanosheets	…..	…..	Anatase TiO_2
	155	Small nanorods	…..	…..	Anatase TiO_2
	180	Nanoribbons	64 - 260	75 - 125	TiO_2(B)

the range 75 - 125 nm having well-resolved uniform nanopores of 8 nm diameter as shown in **Fig. 3.5(g) and (h)**. This indicates that solvent also plays an important role for the formation of various nanostructures, because the solvent has a strong effect on the solubility, reactivity, and diffusion behavior of the reactants and ultimately influencing the structural and morphological features. **Fig. 3.5(h)** shows the high magnification TEM images of a single nanoribbon having nanopores of uniform shape and sizes. The SAED pattern of the corresponding nanoporous nanoribbon is shown in the inset of **Fig. 3.5(h)**, which indicates the single crystalline nature of TiO_2(B). A typical HRTEM image of the nanoporous nanoribbon is shown in **Fig. 3.5(i)**, the clear lattice fringes indicating the as-synthesized products are well-crystalline. The d-spacing of 3.55 Å corresponds to (110) crystal plane of TiO_2(B) phase, which is also the highest intensity peak observed in the XRD pattern. Note that no lattice fringe corresponding to the d-spacing of any titanate phase is found. Thus the pure phase TiO_2(B) nanostructures are obtained using ethylene glycol cosolvent, which is consistent with the XRD result. The nanoporous NRbs might possess very high surface area and can be suitably applied in photocatalysis,[16] environmental cleaning[17] and Li ion battery,[18]

etc. The diameters of the different nanostructures measured from the FESEM and TEM images are shown in **Table 3.1**.

3.6. Growth mechanism

Presently there is an incomplete understanding on the formation mechanism of solvothermally synthesized different TiO_2 nanostructures. It is unclear whether it is due to the rolling of nanosheets exfoliated from crystalline TiO_2 precursors or rolling and/or splitting of layered titanate nanosheets that gives rise to different morphologies. To understand the growth mechanism of different 1D nanostructures, controlled experiments were carried out at different temperatures under continuous stirring during the reaction and the products using different cosolvents were also examined. A systematic study on the mechanism of formation of the as-prepared nanostructures is explored on the basis of our experimental findings.[13]

Wu et al.[7] argued that titanate nanosheets were first splitted and then rolling of the splitted sheets formed the nanotubes. They also claimed that the thickening of thin nanosheets is accelerated by increasing the reaction temperature and finally splitted into nanowires instead of rolling. Huang et al.[19] proposed that the transformation from NTs to NWs is due to an oriented attachment (OA)[14] and Ostwald ripening (OR)[2] cooperative mechanism based on their TEM observations. With these backgrounds information, we carried out the experiments at different reaction temperatures under constant stirring to clarify the possible formation mechanism. It was earlier proposed that sodium titanate NTs were formed by rolling crystalline nanosheets exfoliated from crystalline TiO_2 materials (anatase/rutile). If this is one of the possible formation mechanisms, then the length of the NTs should be restricted by the size of the raw TiO_2 materials. However, we observed that the NTs and NRs are often orders of magnitude larger than the size of the raw anatase TiO_2 particles (~80 nm particle size). The similar results were reported by several authors.[15, 20, 21] For example Huang et al.[19] reported titanate NTs of several hundreds of nanometer in length derived from the anatase TiO_2 powder with particle size of about 10 nm. Moreover, it is postulated that crystalline TiO_2 either anatase or rutile, does not possess any layered structure that can form the final nanotubes.[22-24] So this assumption could not be a possible growth mechanism for the 1D NTs and NRs observed in this work.

When anatase TiO_2 powder precursor reacts with concentrated alkaline NaOH solution, Ti-O-Ti bonds are broken and the Na^+ ions intercalated within the TiO_6 octahedral units and then recrystallized into layered $Na_2Ti_5O_{11}{\cdot}H_2O$ nanosheets. After ultrasonic HCl treatment and washing, hydrated hydrogen pentatitanate ($H_2Ti_5O_{11}{\cdot}H_2O$) is formed by the ion exchange of Na^+ with H^+ and the by-product NaCl is formed. The final anatase TiO_2 products are obtained by dehydration process during the calcinations at 500 °C for 5 h. For simplification, the overall chemical processes of the as-prepared samples are as follows.

$$4TiO_2 + 2NaOH \rightarrow Na_2Ti_4O_9 + H_2O \quad (3.1)$$

$$5Na_2Ti_4O_9 + 10HCl \rightarrow 4H_2Ti_5O_{11} \cdot H_2O + 10NaCl \quad (3.2)$$

$$H_2Ti_5O_{11} \cdot H_2O \rightarrow 5TiO_2 + 2H_2O \quad (3.3)$$

Thus, the final anatase TiO_2 nanostructured products are obtained by the three steps reaction process: (i) the reaction of TiO_2 precursor with alkaline NaOH solution, (ii) the ion exchange between Na^+ and H^+ and (iii) the final calcination. The early growth stage of 1D nanostructure at 130 °C in alkaline water solvent shows the coexistence of nanosheets and partially developed NTs, indicating that NTs are formed from the layered titanate nanosheets. At comparatively higher temperature (155 °C) and pressure, the nanosheets completely roll up to form a bunch of NTs well oriented in a particular directions as shown in **Fig. 3.2(b)**. The driving force for the rolling may be asymmetric due to the hydrogen deficiency in surface layers[23] together with unsymmetrical surface forces due to locally high surface energy. Another reason for the rolling of nanosheets at high temperature and pressure may be due to the mechanical tension that arises during the process of dissolution/crystallization in nanosheets.[8] When structurally similar surfaces approach, atoms of opposing surfaces may combine chemically with each other. The chemical coordination results in NTs bundles bunching along identical crystal faces.[14, 25] Interestingly, note that NRs are also observed in the same product shown in **Fig. 3.2(c) and 3.5(b)**. This reveals that some of the NTs detached from the bundles of NTs and transformed into NRs. At comparatively higher temperature (180 °C), we observed only NRs instead of any intermediate NTs. This is expected because during the stirring, the bunch of NTs may split and simultaneous shrinkage and growth may occur due to high temperature and pressure to form condensed NRs. The main advantage of the stirring is the splitting of the NTs and nanosheets. At the same time, the constant motion due to stirring prevents sedimentation and forces the intimate mixing of

the system. After splitting of the bunch of NTs, the NTs are detached from the bundles and the pressure acts on the individual nanotube and hence the effect is more as compared to the pressure acting on the bunch of the NTs. That is why the NTs transform to condensed NRs. The observed pressure is 8 bar showing in manometer which is in-built with the high pressure reactor set up, when the temperature is 180 °C under stirring condition for the alkaline water solvent. In addition, constant motion fields created by internal stirring are probably effective in continuously breaking up freshly formed nanotube assemblies, so bundling is prevented again. The thickening and splitting nature of the nanosheets are clearly shown in **Fig. 3.3(a)** for the early growth stage at 130 °C in alkaline ethanol cosolvent. However, no such NTs are observed at 155 °C as observed in case of alkaline water solvent, when ethanol was used as a cosolvent under similar conditions.

Note that the length of the NRs is more than that of the NRs grown in alkaline water solvent at the same reaction temperature, indicating the fast growth rate of the samples in ethanol cosolvent. The rapid growth rate in alkaline ethanol mixed solvent accelerates the formation of thick nanosheets and further splitting of the thick nanosheets results in the formation of NRs at higher temperature and pressure. When the reaction temperature increased to 180 °C, only NRs and NRs/NWs are observed in alkaline water solvent and alkaline ethanol cosolvents, respectively. The possible reasons are (i) the thickening of nanosheets unable to fold and split into NRs/NWs. The high temperature as well as stirring may help to accelerate the reaction for the nucleation of thicker nanosheets and subsequently splitting of the thick nanosheets; (ii) the very fast growth rate and stirring promoted detachment of the NTs from the bunch of NTs which results in rapid shrinkage of the NTs to ultimately form NRs at higher temperature and pressure. The observed pressures at 180 °C reaction temperature under stirring condition are 8 and 16 bar for the alkaline water solvent and alkaline ethanol cosolvent, respectively. In case of ethylene glycol cosolvent, the TiO_2 nanoparticles react with NaOH to form thick layered nanosheets at low growth temperature (130 °C) and then the nanosheets are splitted to form small NRs at comparatively high temperature (155 °C) and further growth of small nanorods turns to NRbs at 180 °C.

Note that a quite unique morphology is formed at 180 °C in ethylene glycol cosolvent, i.e., uniform nanoporous TiO_2 NRbs which are observed from the TEM images as shown in **Fig. 3.5(g) and (h)**. At low growth temperature, the growth/ reaction rate is low

compared to alkaline water solvent and ethanol cosolvent by comparing the FESEM images. However, at 180 °C, the growth rate is more in case of ethylene glycol cosolvent compared to water solvent and ethanol cosolvent. These results indicate that the solvent plays an important role to control the morphology of the products. A possible reason for this type of morphology may be due to the polarity and coordinating ability of a cosolvent have a strong effect on the solubility, reactivity and diffusion behavior of the reactants, thus ultimately influencing the structure and morphological features of the resulting products.[26] The parent TiO_6 octahedra of TiO_2 materials may coordinate with glycol to form chain-like structure,[27] whereas the NaOH may form titanate nanosheets by sharing the vertices edges of the octahedra and resulting NRbs with nanopores are formed at high temperature and pressure. The growth mechanism and evolution of different 1D nanostructures are better elucidated in the schematic diagram shown in **Fig. 3.6**. The crossed dashed-line in the diagram indicates that the NRs/NTs are not formed directly from the TiO_2 NPs and it essentially involves the formation of the nanosheets followed by splitting and/or rolling to form NRs/ NTs of TiO_2.

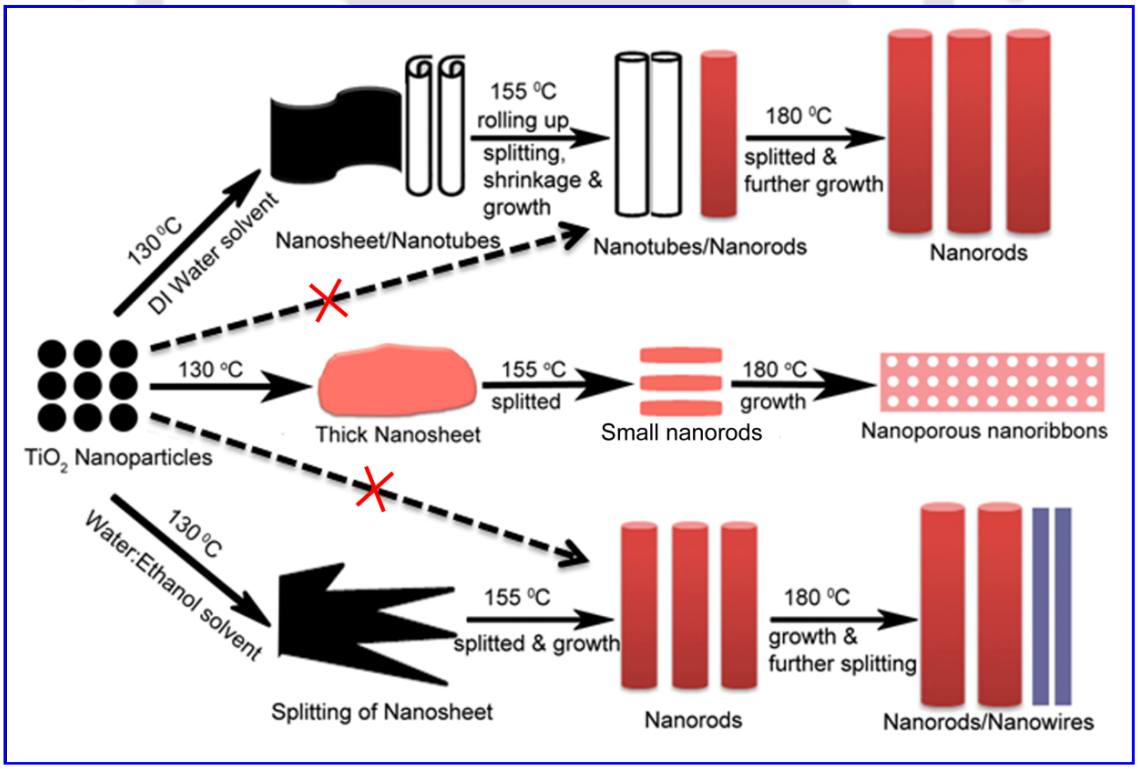

Fig. 3.6. Schematic of the growth mechanism of different 1D nanostructures of TiO_2 formed at different temperatures using various solvents.

3.7. Conclusions

One-dimensional nanostructured TiO_2 of different morphologies, including NTs, NWs, NRs and nanoporous NRbs were successfully synthesized by a simple solvothermal route. The impact of reaction temperature, stirring during the reaction and different cosolvents on the morphology of the products was studied systematically. It is found that the NTs and/or NRs are formed in highly alkaline water solvent, while NRs/NWs are formed in highly alkaline ethanol cosolvent. When ethylene glycol was used as cosolvent, nanoporous NRbs are obtained at 180 °C. We observed that the maximum temperature limit for the transformation of NTs to NRs starts at ~155 °C in case of alkaline water solvent. However, the NRs grown in alkaline ethanol cosolvent is directly from the splitting of nanosheets at 155 °C. The growth rate and morphologies of the 1D nanostructures are shown to be dependent on the growth temperature and the solvent used. The growth rate is faster in alkaline ethylene glycol and ethanol cosolvent as compared to the alkaline water solvent at higher growth temperature (180 °C). XRD and micro-Raman scattering studies confirm the pure phase TiO_2(B), anatase, mixed anatase-rutile TiO_2 phase and anatase/titanate hybrid structures of the as-synthesized products. Based on the FESEM and TEM analyses, we have explained the mechanism of growth of different nanostructures through a schematic diagram. This study will enable more controlled growth of TiO_2 NTs, NRs and nanoporous NRbs with tunable properties for practical applications such as energy conversion and storage.

References

1. R. Ma, K. Fukuda, T. Sasaki, M. Osada and Y. Bando, The Journal of Physical Chemistry B **109**, 6210-6214 (2005).
2. A. Elsanousi, E. M. Elssfah, J. Zhang, J. Lin, H. S. Song and C. Tang, The Journal of Physical Chemistry C **111**, 14353-14357 (2007).
3. T. Kasuga, M. Hiramatsu, A. Hoson, T. Sekino and K. Niihara, Langmuir **14**, 3160-3163 (1998).
4. K. Das, S. K. Panda and S. Chaudhuri, Journal of Crystal Growth **310**, 3792-3799 (2008).

5. Y. Lan, X. P. Gao, H. Y. Zhu, Z. F. Zheng, T. Y. Yan, F. Wu, S. P. Ringer and D. Y. Song, Advanced Functional Materials **15**, 1310-1318 (2005).
6. D. L. Morgan, H.-Y. Zhu, R. L. Frost and E. R. Waclawik, Chemistry of Materials **20**, 3800-3802 (2008).
7. D. Wu, J. Liu, X. Zhao, A. Li, Y. Chen and N. Ming, Chemistry of Materials **18**, 547-553 (2005).
8. D. V. Bavykin, V. N. Parmon, A. A. Lapkin and F. C. Walsh, Journal of Materials Chemistry **14**, 3370-3377 (2004).
9. E. Horváth, Á. Kukovecz, Z. Kónya and I. Kiricsi, Chemistry of Materials **19**, 927-931 (2007).
10. X. Shen, J. Zhang and B. Tian, Journal Materials Science **47**, 3855-3866 (2012).
11. J. C. Parker and R. W. Siegel, Applied Physics Letters **57**, 943-945 (1990).
12. W. F. Zhang, Y. L. He, M. S. Zhang, Z. Yin and Q. Chen, Journal of Physics D: Applied Physics **33**, 912 (2000).
13. B. Santara and P. K. Giri, Materials Chemistry and Physics **137**, 928-936 (2013).
14. J. Zhang, Z. Lin, Y. Lan, G. Ren, D. Chen, F. Huang and M. Hong, Journal of the American Chemical Society **128**, 12981-12987 (2006).
15. Z.-Y. Yuan and B.-L. Su, Colloids and Surfaces A: Physicochemical and Engineering Aspects **241**, 173-183 (2004).
16. J. Du, W. Chen, C. Zhang, Y. Liu, C. Zhao and Y. Dai, Chemical Engineering Journal **170**, 53-58 (2011).
17. F. Liang, T. L. Kelly, L.-b. Luo, H. Li, M. J. Sailor and Y. Y. Li, ACS Applied Materials & Interfaces **4**, 4177-4183 (2012).
18. M. Zukalová, M. Kalbáč, L. Kavan, I. Exnar and M. Graetzel, Chemistry of Materials **17**, 1248-1255 (2005).
19. J. Huang, Y. Cao, Q. Huang, H. He, Y. Liu, W. Guo and M. Hong, Crystal Growth & Design **9**, 3632-3637 (2009).
20. C. B. Almquist and P. Biswas, Journal of Catalysis **212**, 145-156 (2002).
21. T. Sreethawong, Y. Suzuki and S. Yoshikawa, Journal of Solid State Chemistry **178**, 329-338 (2005).

22. G. H. Du, Q. Chen, R. C. Che, Z. Y. Yuan and L.-M. Peng, Applied Physics Letters **79**, 3702-3704 (2001).

23. S. Zhang, L. M. Peng, Q. Chen, G. H. Du, G. Dawson and W. Z. Zhou, Physical Review Letters **91**, 256103 (2003).

24. A. Thorne, A. Kruth, D. Tunstall, J. T. S. Irvine and W. Zhou, The Journal of Physical Chemistry B **109**, 5439-5444 (2005).

25. R. L. Penn and J. F. Banfield, Science **281**, 969-971 (1998).

26. B.-M. Wen, C.-Y. Liu and Y. Liu, New Journal of Chemistry **29**, 969-971 (2005).

27. X. Jiang, Y. Wang, T. Herricks and Y. Xia, Journal of Materials Chemistry **14**, 695-703 (2004).

Chapter 4

Intrinsic Defect Induced Extended Visible Absorption, Visible and Near-infrared Photoluminescence from Undoped TiO_2 Nanoribbons

Despite decades of research on the role of intrinsic defects in enhancing the performance of reduced TiO_2 based materials, unambiguous identification of defects responsible for visible light absorption, and near-infrared (NIR) photoluminescence from undoped TiO_2 has remained challenging. The decisive role of surface disorder and point defects such as oxygen vacancies (O_v), Ti interstitial (Ti_i) in dictating the band gap narrowing and related application of TiO_2 has been emphasized in the recent literature, mainly through computational studies. However, experimental understanding on the actual nature of defects such as O_v and Ti_i in reduced TiO_2 and its role in the visible light photocatalysis are still unclear. In this work, through careful *in-situ* photoluminescence (PL) studies under a controlled environment coupled with optical absorption measurement, we investigated the origin of an extended visible absorption, visible and NIR PL emission from undoped TiO_2 nanoribbons (NRbs) grown by a solvothermal route. Based on our experimental observations, the origin of the tunable NIR PL from TiO_2 NRbs has been traced to surface Ti interstitials for the first time.

4.1. Introduction

Defect engineered TiO_2 nanostructures have received unprecedented attention because intrinsic as well as extrinsic defects play a very crucial and fundamental role in enhancing the material/device performance. In particular, understanding the origin of red-shifts of the absorption edge of undoped reduced TiO_2 and the visible-light photoactivity of undoped and doped TiO_2 remains a hot topic of discussion.[1-4] Despite numerous studies, some of which

have recognized that intrinsic defects such as oxygen vacancies (O_v) and associated defects contribute to the absorption of light in the visible spectral region,[1] a detailed understanding on the optical properties of such defects and the conditions needed for the formation of such defects remain experimentally somewhat elusive. Chen et al.[5] reported that mid-gap states above the valence band maximum, instead of Ti^{3+} ions associated with O_v, are responsible for the visible and infrared absorption in disordered engineered black TiO_2. Numerous theoretical as well as experimental investigations though favor the O_v model to explain the band gap states and band gap narrowing in TiO_2, the crucial role of Ti interstitials (Ti_i) in the near surface region for the band gap states was elucidated by Wendt et al.[6] Earlier, through an elegant set of experiments, Henderson[7] demonstrated that the major diffusing species in the bulk-assisted reoxidation of ion-sputtered TiO_2 are Ti_i rather than O_v. However, optical spectroscopic evidence of Ti interstitials and identification of the electronic states associated with them are not established yet.

Attempts have been made to dope metal[8, 9] or nonmetal[4, 10] impurities to optimize the band gap of TiO_2 to visible light. However, there are controversies regarding the photocatalytic efficiency, since some literatures reported the increase in photocatalytic activity with external doping, while some others reported the decrease in the photocatalytic efficiency due to high doping concentration in TiO_2.[11-15] The introduction of dopants acts as charge carrier recombination centers, which reduce the chance of the carriers to reach the particle surface to participate in the desired reaction and becomes a major issue affecting the photocatalytic efficiency.[16] Studies on the reduction of TiO_2 during the doping process have indicated the dominant role of F-type color centers in the visible-light-activity of TiO_2 photocatalysts. Recently, some approaches based on dopant-free, pure TiO_2 phase were proposed in order to overcome this limitation.[2, 17] The decisive role of surface disorder and point defects, such as O_v and Ti_i in dictating the band gap narrowing and related application of TiO_2 has been emphasized in the recent literatures. However, the actual nature of defects such as O_v and Ti_i in reduced TiO_2 and its role in the visible light photocatalysis are still under intense debate. Interestingly, both Ti_i and O_v may coexist in the reduced TiO_2 though in different concentration, depending on the chemical synthesis and post-growth thermal treatments under different environments. Therefore, it is important to provide a detailed description and understand the specific role of each native defect in reduced TiO_2. Native

defects could influence both visible light absorption and may reduce the electron-hole recombination, which results in enhancement of highly promising photocatalytic effect in this novel material. Recently, Liu et al.[3] reported the enhanced visible light photocatalysis in Ti^{3+} self-doped TiO_2 materials. The concentration of the native defects typically depends on the growth conditions. However, the nature of band gap states induced by the Ti_i is yet to be identified experimentally. It is therefore imperative to understand the evolution of the native defects in band gap engineered TiO_2 nanostructures with different growth/processing conditions and identify the defects responsible for enhanced photocatalytic and photovoltaic performance.

The recent growth in theoretical interest in the electronic structure of point defects in TiO_2 has yielded powerful calculation approaches that predict more precise energy levels in the band gap caused by O_v and Ti_i.[18, 19] Though there have been some experimental confirmations of these native defects by various groups,[2, 6, 17, 20] experimental confirmation of predicted energy levels of Ti_i have remained challenging. The diffusion of Ti_i defects from surface to bulk during heating in reduced atmosphere and opposite effect that occurs in oxygen atmosphere have been addressed by some groups.[6, 7] However, the assignment of the point defects to specific photoluminescence (PL) emission in TiO_2 polymorphs (mainly anatase and rutile) remains unclear and is highly debated. Though visible PL emission is common in defective TiO_2, which has been attributed to oxygen vacancies,[21-23] there is no systematic understanding on the near-infrared (NIR) PL emission in TiO_2. Some reports suggested that it is the intrinsic defects in rutile TiO_2[21, 24] that gives rise to NIR PL. Montoncello et al.[25] reported the NIR PL at 1.51 eV for both phases (anatase and rutile) at low temperature (11 K), and the spectra were interpreted as the phonon replica effect, originating from ionization of oxygen vacancies. A recent report on the NIR PL emission from large band gap ZnO was explained on the basis of donor-acceptor transition between O_v and Zn vacancies and the radiative recombination of shallowly trapped electrons with deeply trapped holes at interstitial O_i.[26] However, there is no *in-situ* study, to the best of our knowledge, on the evolution and origin of NIR PL emission and its relation, if any, to the enhanced visible absorption in TiO_2 nanostructures in pure TiO_2(B), anatase, rutile, and its mixed phases.

Herein, through careful *in-situ* photoluminescence studies under controlled environment, we attempt to identify the specific defect responsible for the red shift in the absorption edge, visible and NIR PL emission in undoped TiO_2 NRbs grown by a solvothermal technique. In particular, monitoring the time evolution of the visible and NIR PL emissions at low temperature, under high vacuum and oxygen environment, allows us to distinguish and unambiguously identify the defect states associated with O_v and Ti_i.[27] Interestingly, we observed a wide range of visible absorption from these undoped TiO_2 NRbs fabricated under various growth conditions, and we demonstrate that Ti_i rich samples have higher red shifts in the absorption edge, which is crucial for more efficient visible light photocatalysis in TiO_2-based materials. Based on our experimental observations, the origin of the tunable NIR PL from TiO_2 NRbs has been traced to surface Ti interstitials for the first time.[27] The identification of Ti_i states in the band gap of undoped TiO_2 NRbs is considered an important step in further exploitation of defect engineered undoped TiO_2 nanostructures and is believed to be an important milestone in realizing improved visible light photocatalytic and photovoltaic applications of this novel material.

4.2. Growth of TiO_2 nanoribbons

Anatase TiO_2 powders (average particle size ~80 nm), sodium hydroxide (NaOH) pellets, and ethylene glycol were used as received from Merck. In a typical synthesis, 0.275 g of anatase TiO_2 powder was mixed with 60 ml of 10 M NaOH in mixed solvent (DI water/ethylene glycol = 1:1) under stirring for 1 h, a milky solution was obtained. Afterward, the mixed solution was transferred into a Teflon-lined autoclave. During the growth process, the temperature inside the autoclave was monitored and maintained at 180, 205, and 235 °C under autogenous pressure and constant magnetic stirring at 250 rpm for 16–24 h. The formed precipitates were obtained by centrifugation and washed several times with DI water. Subsequently, the products underwent an ultrasonic treatment with 0.1 M HCl until the pH ~7 and finally the precipitates were calcined at different temperatures in the range 500–900 °C for 5 h in air. The vacuum annealing of the sample grown for 16 h followed by 500 °C calcinations was performed at 300 °C under 1.2×10^{-2} mbar pressures for 2 h. For convenience of discussion, the TiO_2 NRbs samples are categorized according to different growth temperature, reaction duration and calcinations temperatures. Samples grown at fixed

reaction temperature of 180 °C, 16 h are categorized as "A" series and after calcination at 500, 700, and 900 °C are named as A500, A700, and A900, respectively. The A500 after vacuum annealing is named as A500V. The samples grown at 235 °C, 16 h reaction are termed as 'B' series and after calcinations at 500, 700, and 900 °C are named as B500, B700, B900, respectively. Sample grown at 205 °C for 16 h reaction and calcined at 500 °C is named as C500. Samples grown at 180 °C after reaction time 24 h followed by calcinations at 500 and 900 °C are termed as D500 and D900, respectively. Samples grown at 130 and 155 °C for 16 h reaction duration and calcined at 500 °C are named as E500 and F500, respectively. The details of the sample nomenclature and growth conditions are presented in **Table 4.1**.

Table 4.1. Details of the samples: Crystal structure obtained from XRD and micro-Raman studies, Morphology obtained from FESEM and TEM analyses, Band gap calculated from DRS absorption spectra, and NIR PL peak position in PL spectra.

Sample name	Growth temperature, duration, calcinations	Crystal structure	Morphology	Nanoribbon surface features	Band gap (eV)	Center of NIR PL peaks (eV)	
						Peak P1	Peak P2
A500	180 °C, 16 h, 500 °C	TiO_2(B)	Nanoribbons	Nanopits	2.34	1.21	1.47
A700	180 °C, 16 h, 700 °C	TiO_2(B)-anatase	Nanoribbons	Nanobricks	2.48	…..	…..
A900	180 °C, 16 h, 900 °C	Anatase-rutile	Nanoribbons	…..	2.29	1.35	1.47
A500V	A500 vac. annealed	TiO_2(B)	…..	…..	…..	…..	…..
B500	235 °C, 16 h, 500 °C	Anatase	Nanoribbons	Nanopits, nanostones	2.64	1.30	1.47
B700	235 °C, 16 h, 700 °C	Anatase-rutile	Nanoribbons	Nanostones	2.09	1.34	1.47
B900	235 °C, 16 h, 900 °C	Rutile	Nanoribbons	Nanostones, nanobricks	1.98	1.23	1.47
C500	205 °C, 16 h, 500 °C	Anatase	Nanoribbons	…..	2.77	1.27	1.47
D500	180 °C, 24 h, 500 °C	TiO_2(B)	Nanoribbons	Nanobricks	…..	…..	…..
D900	180 °C, 24 h, 900 °C	Anatase-rutile	Nanoribbons	Nanostones, nanobricks	2.17	…..	…..
E500	130 °C, 16 h, 500 °C	Anatase	Nanosheets	…..	…..	…..	…..
F500	155 °C, 16 h, 500 °C	Anatase	Nanorods	…..	…..	…..	…..

4.3. Structural studies

X-ray diffraction: The XRD patterns of solvothermal products synthesized at two different growth temperatures (i.e., 180 and 235 °C) after a 16 h reaction and different calcinations temperatures are shown in **Fig. 4.1(a) and (b)**, respectively. All the peaks correspond to TiO_2(B) phase for A500; however, for A700 and A900, mixed phase TiO_2(B)-anatase and anatase-rutile TiO_2 with little signature of TiO_2(B) are observed, respectively (**Fig. 4.1(a)**). We observed pure anatase phase for B500, mixed phase anatase-rutile for B700, and pure rutile TiO_2 for B900. At low growth temperature (180 °C) and calcinations temperature (500 °C), pure TiO_2(B) phase is formed irrespective of reaction duration (**Fig. 4.1(c)**). On the other hand, at higher growth temperature of 235 °C, anatase, mixed anatase-rutile and pure rutile phases were formed after 500, 700, and 900 °C calcinations, respectively (**Fig. 4.1(b)**). The XRD patterns of the samples grown at 130 and 155 °C correspond to anatase phase, which are shown in **Fig. 4.1(c)**.

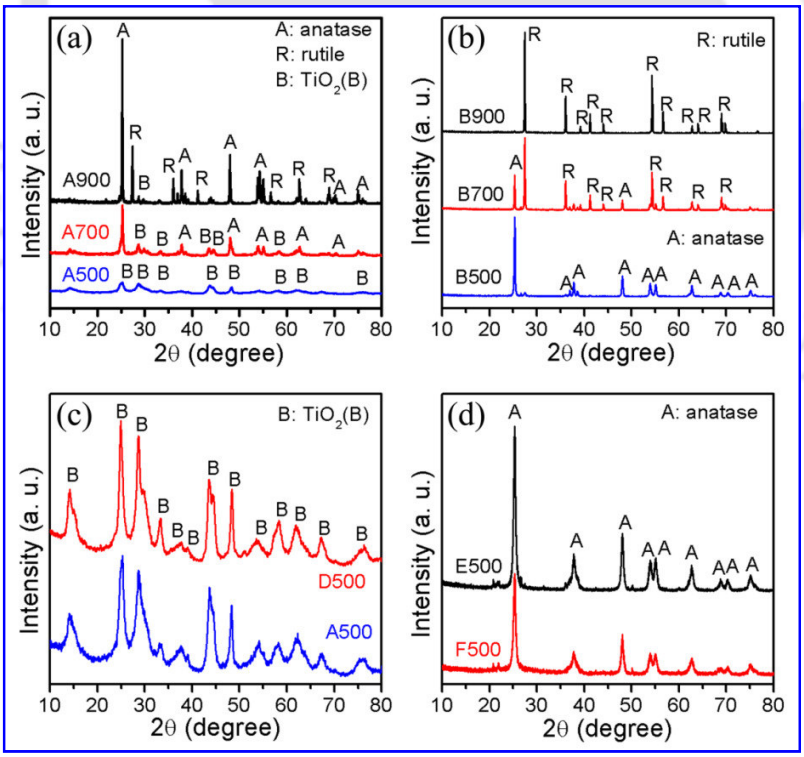

Fig. 4.1. XRD patterns of: (a) A500, A700, A900; (b) B500, B700, B900; (c) A500, D500; (d) E500, F500. Besides the pure TiO_2(B), anatase and rutile phases, mixed phase TiO_2(B)-anatase and anatase-rutile are obtained for A700, A900, B700.

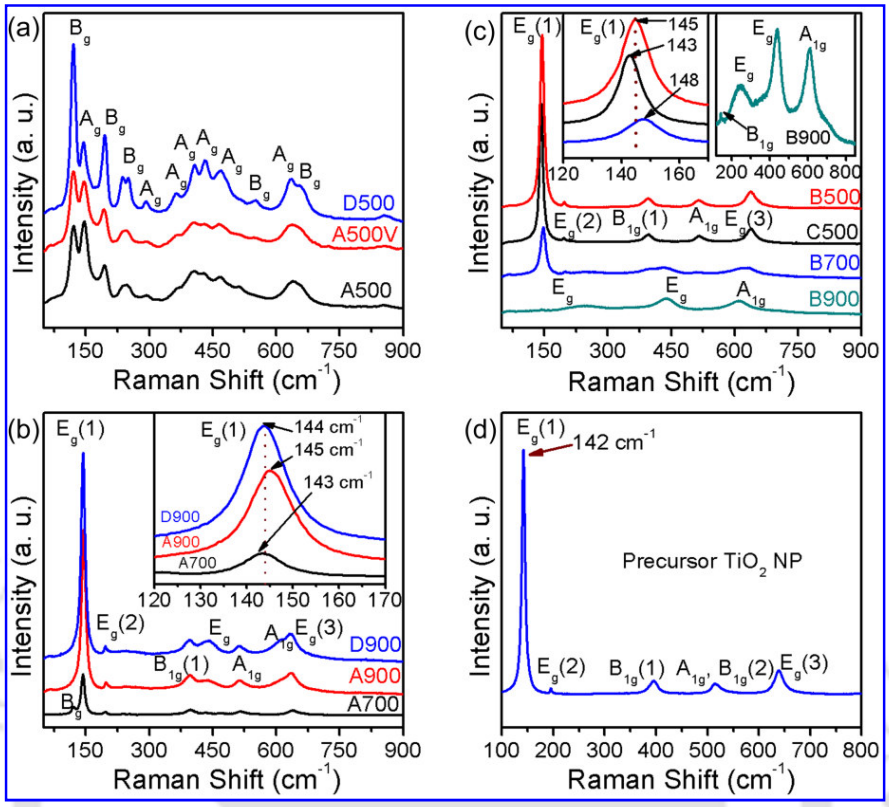

Fig. 4.2. Raman spectra for TiO_2 NRbs: (a) samples A500, A500V, D500; (b) A700, A900, D900; inset shows the relative shifts for $E_g(1)$ mode; (c) samples B500, B700, B900, C500; inset shows the relative peak shift of $E_g(1)$ mode (left panel) and magnified view with characteristic Raman modes of rutile TiO_2 of sample B900 (right panel); (d) precursor TiO_2 NPs. The peak positions are marked with corresponding to the wavenumber (cm^{-1}).

Micro-Raman studies: Various phases of the as-prepared NRbs were further confirmed from micro-Raman analysis. Raman modes in A500, A500V, and D500 correspond to pure TiO_2(B) phase, as shown in **Fig. 4.2(a)**. The intensity of A_g mode at 147 cm^{-1} is decreased considerably for the A500V and D500 compared to A500. Because A500V is vacuum annealed, the reduction in intensity of the A_g mode is attributed to the higher concentration of oxygen vacancies. A900 and D900 show (**Fig. 4.2(b)**) the Raman modes of mixed phase anatase-rutile, while A700 shows mixed phase TiO_2(B)-anatase, consistent with the XRD analysis. An up shift of $E_g(1)$ mode for the as-synthesized NRbs compared to the precursor TiO_2 powder is shown in the inset of **Fig. 4.2(b)**. Note that the Raman mode of precursor TiO_2 powder is at 142 cm^{-1} (**Fig. 4.2(d)**). The blue shift of as-synthesized NRbs is primarily due to the oxygen vacancies in TiO_2.[28-30] B500 and C500 show the characteristic Raman

modes of anatase TiO_2, while B900 shows the Raman modes of rutile TiO_2 (**Fig. 4.2(c)**). B700 shows a mixed phase anatase-rutile TiO_2. The inset of **Fig. 4.2(c)**, shows the blue shifting of the $E_g(1)$ Raman mode of the as-grown samples compared to precursor TiO_2. Note that the larger blue shift is observed for the B500 and B700 compared to C500. From the PL study discussed later, we found that C500 contains a high concentration of oxygen vacancies as compared to B500 and B700. Hence, it is likely that the blue shift of the $E_g(1)$ mode in anatase TiO_2 is not only associated with O_v, but also related to other defects, for example, Ti_i in the NRbs. The Raman spectra are fully consistent with the XRD patterns for phase confirmation among different TiO_2 polymorphs.

4.4. FESEM and TEM studies

FESEM imaging: The morphologies of the as-synthesized nanostructures as observed by FESEM are shown in **Fig. 4.3**. The low magnification image of sample A500 (**Fig. 4.3(a)**) shows long and straight NRbs of TiO_2 having length ~300 to ~3000 nm and width ~64 to ~260 nm. The corresponding high magnification image of the sample shows well resolved nanopits on the surface of the NRbs, as shown in inset of **Fig. 4.3(a)**. The low magnification of sample A700 shows NRbs of length ~870 to ~3300 nm and width ~45 to ~180 nm (**Fig. 4.3(b)**). The inset in **Fig. 4.3(b)** shows the magnified image of sample A700, where NRbs with nanobrick-like structure on the surface are observed. The energy dispersive x-ray (EDX) spectrum of A900 is shown in **Fig. 4.3(c)**, which shows only Ti and O elements, indicating there is no impurity element. The atomic ratio of O/Ti is 1.72, which is less than 2, indicating oxygen deficiency and thus, oxygen vacancies are present. **Fig. 4.3(d)** shows the FESEM image of B500. Nanostones and nanopits like structure on the surface of NRbs are clearly seen for B500 sample. The FESEM image of B700 is shown in **Fig. 4.3(e)**, which shows the nanostones of comparative larger size and are closely packed on the surface of NRbs. This indicates that the growth of the nanostones is increased as the calcination temperature is increased to 700 °C. Further increase of calcination temperature to 900 °C leads to large size nanobricks and nanostones like structures on the surface. The nanostones and nanobricks are arranged in a nice pattern that builds a micro-bridge like structures shown in **Fig. 4.3(f)**. Thus the calcination temperature plays a vital role for the formation of different surface morphologies on the NRbs. The NRbs with moderate to high O_v and diffusion of Ti_i exhibits

a wide variety of restructuring surface morphologies which includes nanopits and nanostones during various calcinations temperatures. These surface structures result from various $Ti_{lattice}-$ O and Ti_i- O bond rearrangement due to the Ti interstitials that diffuse from the bulk to the surface during calcinations. Thus, the diffusion of Ti_i in TiO_2 plays a major role in surface and interface-related phenomena when high temperature calcinations are involved. This may be similar to the TiO_x (where x = ~2) islands found by Wendt et al.[6] due to the diffusion of Ti_i in their scanning tunneling microscopy (STM) images during annealing.

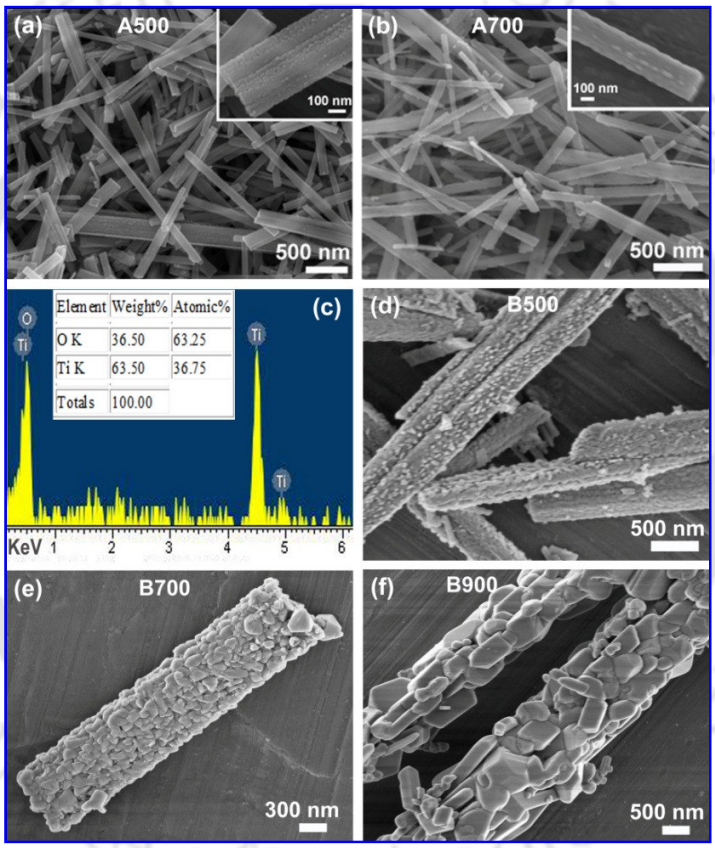

Fig. 4.3. FESEM image of the morphology of TiO_2 nanostructures: (a) A500 and (b) A700 grown at 180 °C; (d) B500, (e) B700 and (f) B900 grown at 235 °C. (c) EDX spectrum of A900.

TEM imaging: **Fig. 4.4(a)** shows a typical TEM image of the sample A500 showing nanoribbon like structure. **Fig. 4.4(b)** shows the high magnification TEM image of a single nanoribbon having well resolved nanopits of uniform shapes and sizes (diameter ~8 nm) on the surface of the nanoribbon. The selected area electron diffraction (SAED) pattern of the

corresponding nanoporous nanoribbon is shown in the inset of **Fig. 4.4(a)**, which indicates the single crystalline nature of TiO_2(B) phase. The (110) crystal plane of TiO_2(B) is indexed in the figure. A typical HRTEM lattice image of the nanoribbon is shown in **Fig. 4.4(c)**, the clear lattice fringe indicates that the as-synthesized products are well crystalline. The d-spacing of 3.55 Å corresponds to the (110) crystal plane of TiO_2(B) phase, which is also the highest intensity peak observed in the XRD pattern. The TEM images of A700 are shown in **Fig. 4.4(d) – (f)**. Here again, NRbs with nanobrick and nanopit-like structures on the surface are clearly observed in high magnification image in **Fig. 4.4(e)**. The nanopits of diameter 5–13 nm and nanobricks of width ~13 nm are formed on the surface of NRbs making them porous like structures, with highly active surface. The inset of **Fig. 4.4(d)** shows the corresponding SAED pattern. It clearly dictates the tetragonal pattern of anatase TiO_2 and

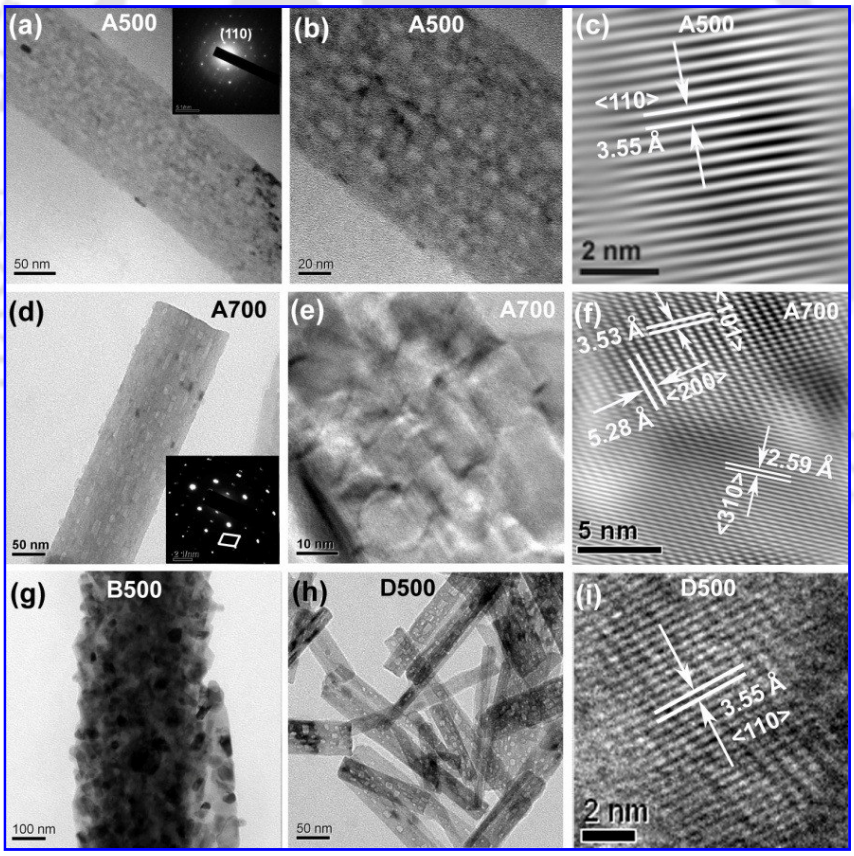

Fig. 4.4. TEM images: (a) A500; (b) A500 at higher magnification showing nanopits; (c) A500, lattice fringe; (d) A700; (e) A700 at higher magnification showing nanobricks; (f) A700, lattice fringe; (g) B500 showing nanostones and nanopits; (h) D500, NRbs with nanobricks; (i) D500, lattice fringe. The inset in (a) and (d) shows the corresponding SAED patterns.

monoclinic pattern of TiO_2(B) phase indicating mixed phase TiO_2(B)-anatase is formed. The electron diffraction spots of monoclinic nature are joined by lines shown in the inset of **Fig. 4.4(d)**. **Fig. 4.4(f)** shows the HRTEM lattice fringe with a d-spacing of 5.28 Å and 2.59 Å corresponding to (200) and (310) plane of TiO_2(B) phase, respectively. The d-spacing of 3.53 Å corresponds to (101) plane of anatase TiO_2. **Fig. 4.4(g)** shows the TEM image of the sample B500. Nanostones and nanopits-like surface morphology is observed on the NRbs surface. The TEM images are fully consistent with the FESEM images. **Fig. 4.4(h)** shows the TEM image of sample D500. Nanoporous NRbs with nanobricks on the surface are observed with no nanopits. The lattice fringe of a nanoribbon of sample D500 is shown in **Fig. 4.4(i)**. The d-spacing of 3.55 Å corresponds to (110) plane of TiO_2(B) phase. Thus, growth temperature, reaction duration and calcination temperature strongly influence the surface morphology and resulting defects, for example, O_v , Ti_i etc. in TiO_2 and this plays a crucial role in tuning the electronic, optical and magnetic properties of the nanostructures.

4.5. Optical absorption and Photoluminescence studies

UV-Vis-NIR absorption studies: Light absorption characteristics of the solvothermally synthesized TiO_2 nanostructures are shown in **Fig. 4.5(a) and (b)**. All the as-synthesized samples exhibit a red shift of the absorption edge and considerable absorption in the visible region (>447 nm) compared to precursor TiO_2 (380 nm). The absorption spectra for B500, B700, B900 and precursor TiO_2 ($PTiO_2$) NPs are shown in **Fig. 4.5(a)**. Note that with higher calcinations temperature, the absorption edge extends up to yellow region of the visible spectrum. In **Fig. 4.5(a)**, three steps of absorptions (i.e., 380–420, 420–580, and 660–840 nm) can be distinguished. The absorption in the 380–420 nm range (violet region) arises due to the self-trapped states and shallow trap states $Ti^{3+}_{lattice}$ centers, while absorption in the range 420–580 nm (blue, green, and yellow region) arises due to the deep trap states F^+ centers associated with the oxygen vacancies. However, the absorption in the range 660–840 nm (red region and extended up to NIR region) is prominent for samples calcined at higher temperature and it may be originated from the Ti_i defects that migrate to the near surface region during calcination. Note that B500, B700 and B900 grown at higher reaction temperature show systematic red shift in the band gap to pure visible region, enabling strong

visible absorption in the undoped TiO_2 and this is expected to exhibit strong visible light photocatalytic activity for hydrogen generation. The presence of regular lattice $Ti^{3+}_{lattice}$ trap center, F^+ center, and interstitial Ti_i^{3+} are confirmed from our electron spin resonance (ESR) measurement discussed later.

Fig. 4.5(b) shows the absorption spectra of the samples grown with different reaction durations (i.e., 16 and 24 h) and calcined at 900 °C. With an increase in reaction duration, visible absorption is clearly increased and this is caused by higher concentration of defects. The band gap is calculated from the linear fit to the linear portion of $(\alpha hv)^{1/2}$ *versus hv* plot and the data are presented in **Table 4.1**. Note that the band gaps of pure anatase phase of TiO_2 NRbs (C500 and B500) are relatively large (2.77 and 2.64 eV, respectively) compared to the other as-grown samples. However, we noticed that within the same phase, the band gap of B500 is narrower than that of C500 grown at lower temperature. This indicates that samples grown at higher temperature followed by calcination at high temperature possess higher concentration of a particular defect that is largely responsible for reduction in the band gap. This is consistent with the theoretical predictions made by various groups.[18, 19, 31] Interestingly, experimental evidence of band gap narrowing due to Ti_i defects is reported by Wendt et al.[6] Morgan et al.[31] reported a larger red-shift of absorption edge due to Ti_i defects as compared to that due to $O_v$defects.

Theoretical calculations suggested that a high vacancy concentration could induce a band of electronic states just below the conduction band.[32] Zuo et al.[33] reported the presence of a mini-band closely below the conduction band minimum, which is related to the oxygen vacancy, associated with Ti^{3+} and is responsible for the band gap narrowing in TiO_2. Similar observation related to oxygen vacancy induced band gap narrowing has been reported in ZnO system.[34] More recently, Liu et al.[3] reported the band gap narrowing of undoped TiO_2 due to oxygen vacancies and Ti^{3+} species which showed enhanced visible light-driven photocatalytic oxidation on methylene blue and water splitting. Finazzi et al.[19] reported that the presence of both $Ti^{3+}_{lattice}$ and Ti_i^{3+} species resulted in new states in the band gap (about 1−1.5 eV below the conduction band) of TiO_2 materials. It will be shown that our results are more consistent with the Ti interstitial mediated red-shift of the band gap to visible region.[27] Note that the absorption edge of precursor TiO_2 powder is at ~380 nm (3.26 eV), although PL studies show high concentration of oxygen vacancies present in it. Thus, oxygen

vacancies alone do not give rise to visible absorption. On the other hand, high temperature calcined NRbs shows considerable decrease in band gap from 2.77 to 1.98 eV (shown in **Table 4.1**) under different growth conditions as compared to precursor TiO_2 powder (3.2 eV). Our PL data presented below is consistent with the fact that these samples contain very low vacancy concentration. Thus, the control of Ti interstitials in TiO_2 nanostructures hold the key to enhanced visible absorption and enhanced photocatalytic performance without introducing any external doping/impurities.

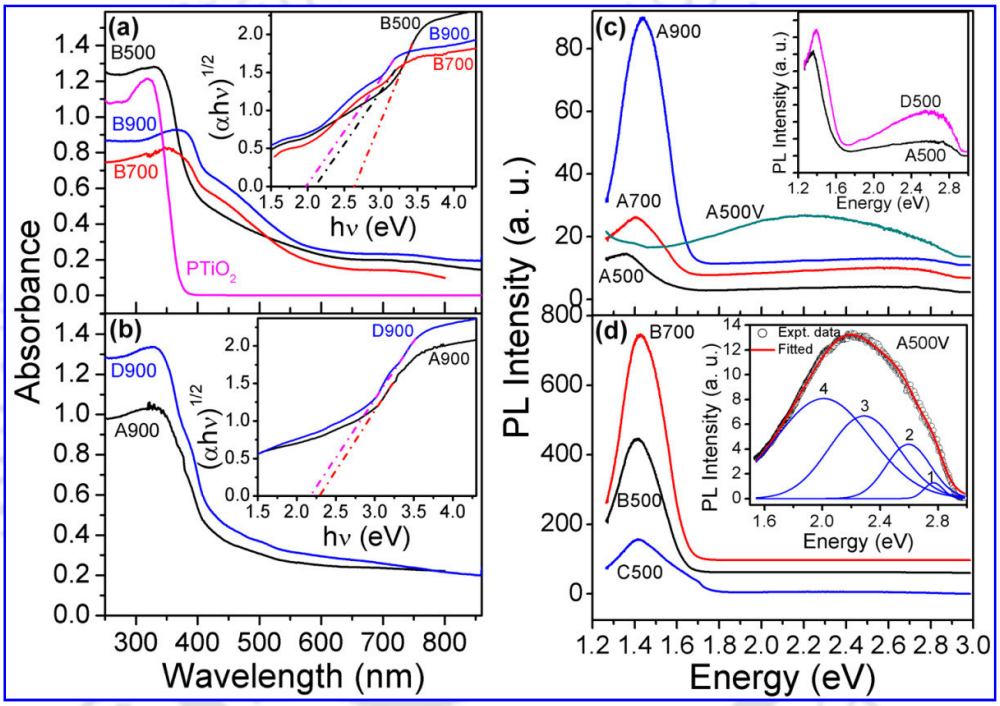

Fig. 4.5. UV-visible-NIR absorption spectra: (a) B500, B700, and B900 grown at 235 °C and different calcinations along with precursor TiO_2 NPs ($PTiO_2$); (b) A900 and D900 grown at different reaction duration and 900 °C calcinations; The insets in each case show the $(\alpha h\nu)^{1/2}$ *vs* $h\nu$ plot, indicating the indirect band gap for the corresponding absorption spectrum of each sample. Band gap energy is calculated from the extrapolated line (dashed) fitted to respective linear portions. Room temperature PL spectra for (c) A500, A700, A900, and A500V; inset is the comparison of A500 and D500; Spectrum for A500V is vertically shifted for clarity. (d) B500, B700, and C500; inset shows the magnified view of the visible PL in A500V with Gaussian peak fitting.

Room temperature photoluminescence studies: To enable a more precise understanding on the nature of defects and related trap states within the band gap in TiO_2 NRbs, PL studies are

performed on different samples. **Fig. 4.5(c)** shows the room temperature and atmospheric pressure PL spectra of the samples grown at 180 °C, 16 h. All the samples show broadly two peaks, one peak in the NIR range at ~1.4 eV and the other peak in the visible range at ~2.2 eV. The broad visible PL is usually ascribed to oxygen vacancies in TiO_2.[21, 23] The vacuum annealed sample A500V shows highly enhanced visible PL emission as compared to as-synthesized A500, indicating that the concentration of oxygen vacancies are dramatically increased after vacuum annealing, as expected. However, as calcination temperature is increased from 500 to 900 °C, the intensity of NIR PL is clearly increased and the peak is blue-shifted. Similar features are observed for the samples grown at 235 °C (**Fig. 4.5(d)**), where the PL intensity is about one order of magnitude higher. On the other hand, the intensity of visible PL is very low and does not change significantly with calcination temperatures. Further, comparison of PL intensity for B500 and C500 shows that NIR PL intensity is higher for growth at higher temperature (**Fig. 4.5(d)**). Thus, it is evident that higher the growth temperature and/ or higher the calcinations temperature, higher the NIR PL intensity. Further, no correlation is found between the visible PL and NIR PL intensity in each sample, which indicates that the origin of these PL emissions is associated with distinctly different defects species (e.g., O_v and Ti_i). The inset in **Fig. 4.5(c)** shows the comparison of PL spectra for A500 and D500 that are grown/ calcined at low temperature. It is clear that at low growth temperature, NIR PL intensity is very low compared to higher growth temperature and both NIR and visible PL intensity increase with reaction durations. The broad visible PL could be fitted properly with four Gaussian bands centered at 2.01, 2.29, 2.60, and 2.77 eV for A500V (inset of **Fig. 4.5(d)**). Note that the higher energy tail of the PL spectra is truncated due to the use of a 435 nm filter during the PL measurement. Peak 1 is ascribed to self-trapped excitons located at TiO_6 octahedra, while peaks 2 and 3 are ascribed to oxygen vacancy related trap states.[21] The peak 4 is attributed to the presence of hydroxyl (OH) species which may form an acceptor level just above the valence band.[23] Moreover, upon the loss of an O atom in the TiO_2 lattice, the electron pair that remains trapped in the vacancy cavity give rise to an F center and one of the electrons in the F center tends to occupy the neighboring Ti^{4+} ion and yield $Ti^{3+}_{lattice}$ center and F^+ center states within the band gap of the material. More details of the formation mechanism will be discussed in

Chapter 5. Here, we focus our attention to understand the evolution of visible and NIR PL emission and their origin.

4.6. Temporal decay of visible photoluminescence

The temporal decay of visible PL intensity with respect to increasing laser exposure time in air medium for the sample E500 and F500 are shown in **Fig. 4.6(a) and (b)**, respectively. We observed that the PL intensity decays tri-exponentially with increase in laser exposure time after each 3 second intervals, as shown in the inset of **Fig. 4.6(a)** (top panel) for the sample E500. The deconvolution of the visible emission is fitted by four Gaussian peaks as in the previous graph for A500V sample, which is shown in the inset of **Fig. 4.6(a)** (bottom panel). The three oxygen vacancy related trap states (major peaks 2, 3 and 4) may be the reason for the tri-exponential PL decay with time. This indicates that after laser heating in air, the samples got oxidised and thus the defect concentrations due to oxygen vacancy are considerably reduced which results in the reduction of PL intensity in the visible region. A similar behaviour is observed for the sample F500 (**Fig. 4.6(b)**).

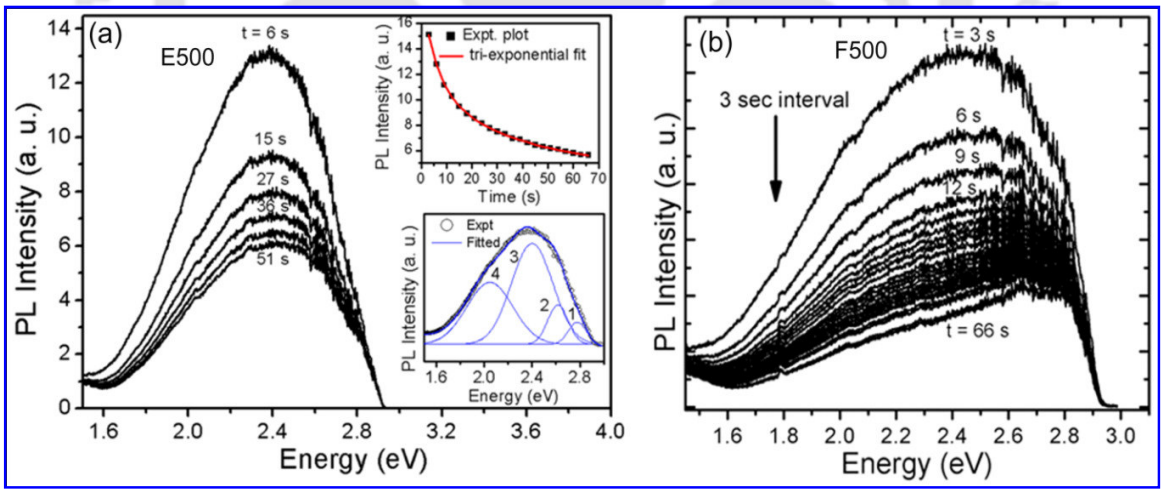

Fig. 4.6. Temporal decay of visible PL with laser on: (a) E500, (b) F500. The inset in (a), top panel shows the plot of integrated PL intensity vs time and tri-exponential decay fitting, indicating the tri-exponential decay of visible PL with time. The inset in (a), bottom panel is the Gaussian fitting of the visible PL. Note that the spectra in case were taken for a 3 sec interval, some of the spectra for E500 are not shown.

Fig. 4.7 shows the splitting of PL emission of sample E500 after long time laser exposure in air with different laser power (mW). After long time laser exposure in air, we observed that the oxygen vacancy concentration is reduced considerably due to laser induced oxidation. Since the oxygen vacancies are more in these samples (E500 and F500), it is expected that the atmospheric O_2 adsorbed on the surface of the sample and may inject rapidly into the TiO_2 to occupy the oxygen vacancy positions with laser exposure in air which is similar to air annealing and occupy the vacancy site; as a result the oxygen vacancy concentration decreased considerably after laser exposure, which is reflected in our PL spectra (reduction of broad visible PL). After long time laser exposure with higher laser power, it is observed that the broad visible PL is splitted into two peaks, i.e., an additional peak at 1.9 eV (visible red) besides the broad visible peak. However, the increase of both the splitted visible red peak and broad visible peak with increasing laser power may be due to more intense laser light. A linear relationship between the integrated PL intensity and laser power is observed and is shown in the inset of **Fig. 4.7**. Note that before long time laser exposure in air, the PL emission shows high oxygen vacancy concentration having single peak, i.e., fresh spot with initial high vacancy concentration, which is shown in **Fig. 4.7**. It was recently reported that adsorbed isotopic oxygen is injected into the bulk rutile TiO_2 as O_i^{2-} which underwent drift towards the surface due to space charge layers and retarded the diffusion of interstitials, promoting the exchange with lattice oxygen.[35, 36] Presuming most of the O_v near the surface in the sample E500 are annihilated due to diffusion of atmospheric O_2 and shut down the path for further diffusing O_i and creating separate O_i^{2-} ions which facilitates creation of surface electronic bands. So, the PL emission at 1.9 eV may be attributed to the surface electronic bands created by O_i^{2-} ions within the band gap. Note that Kamisaka et al.[37] and Bjørheim et al.[38] reported occupied states of $(O_2)_o^q$ with q = -1, -2 within the band gap of anatase and rutile TiO_2, respectively, using theoretical calculations. An interstitial oxide ion O_i^q binds with lattice oxygen and forming the most stable configuration of peroxide defects as $(O_2)_o^q$.[38-40] Lee et al.[18] reported that O_i exhibits all three charge states, i.e., q = 0, -1 and -2 using screen-exchanged hybrid density functional calculations. They observed that neutral O interstitial and its -1 configuration form a dumbbell O-O bonded with a lattice oxygen while in -2 configuration, the O interstitial forms a separate ions, O_i^{2-}.

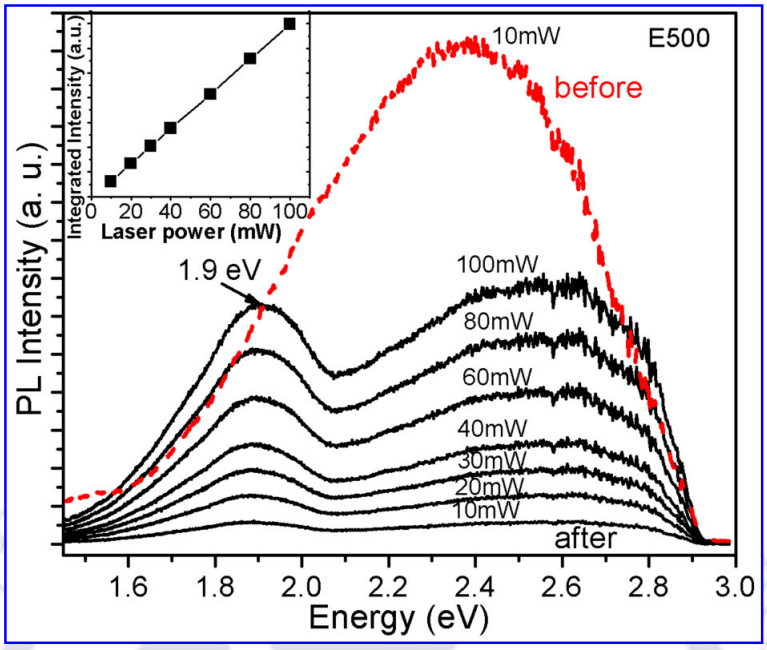

Fig. 4.7. Laser power dependence visible PL for E500 sample, showing the splitting of visible PL. The inset shows the linear relationship between integrated PL intensity and laser power.

4.7. ESR studies

ESR is an exceptionally powerful technique in detecting the spin polarized charge state of defective TiO_2 nanostructures. ESR spectra shown in **Fig. 4.8** reveals that g = 1.972 and 1.942 for B500 and g = 1.970 and 1.944 for B700, indicating the presence of Ti^{3+} at regular lattice position and interstitial position, respectively.[33, 41, 42] Note that Chester[41] and Kingsbury et al.[42] assigned ESR signal at g = 1.94 to Ti^{3+} interstitial. More recently, Zuo et al.[33] reported the ESR signals at g = 1.975 and 1.944 to Ti^{3+} species which were observed from experimental and simulation studies. These results are in close agreement with our ESR results. The g-value at 1.994, 1.993, and 2.001 are attributed to singly ionized oxygen vacancy F^+ center in B500, B700 and C500, respectively. It is also believed that surface Ti^{3+} would react with adsorbed O_2 which reduced to O^- species and show an ESR signal at g = 2.02.[43] It may be noted that ESR is insensitive to Ti^{4+} species and hence no signal is expected from these species. This observation is very useful to identify the Ti_i^{3+} defects as well oxygen vacancy related $Ti^{3+}_{lattice}$ and F^+ centers.

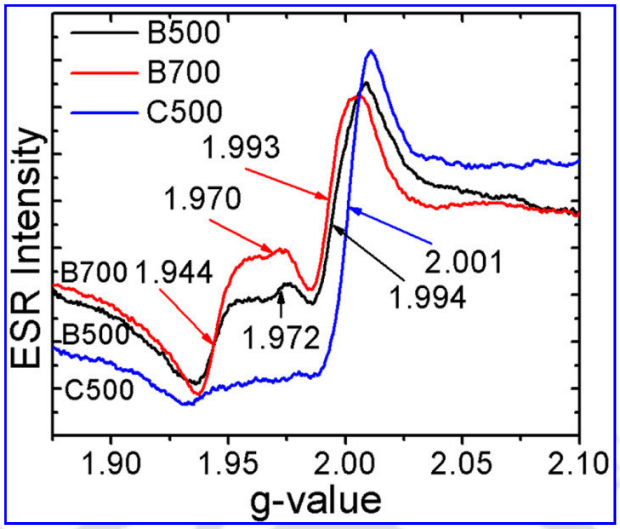

Fig. 4.8. Room temperature ESR spectra for B500, B700, and C500. The respective g-values are indicated in each case.

4.8. In-situ photoluminescence under controlled environment

To ascertain further the origin of visible and NIR PL emission from TiO_2 nanostructures, we performed *in-situ* PL measurements under controlled environments. The enhancement of visible PL after vacuum annealing strongly supports the fact that the visible PL in the TiO_2 NRbs is due to oxygen vacancy induced states. For monitoring the NIR PL under controlled environment, the Ti interstitial rich A900 was mounted inside a high vacuum chamber and the chamber was evacuated to a pressure of 5×10^{-5} mbar and PL measurements were performed with 405 nm laser at room temperature (RT) with 10 mW power (at source). Interestingly, the RT PL spectrum under vacuum shows both visible and NIR emission bands (with two peaks at 1.47 and 1.40 eV), as shown in **Fig. 4.9(a)**. On the other hand, with the controlled introduction of air (oxygen) into the vacuum chamber, the PL spectrum evolves to a very weak visible emission and a strong NIR emission with a single peak at 1.47 eV. The disappearance of visible emission with air/oxygen exposure is consistent with the fact that oxygen vacancy concentration is dramatically reduced due to the laser induced heating in oxygen environment. This is also accompanied by the disappearance of one of the NIR peak at 1.40 eV. Note that A900 underwent calcinations at 900 °C in air before the PL measurement. During PL measurement under vacuum, the laser exposure causes local

heating of the sample and introduces oxygen vacancies, and some of the lattice Ti^{3+} migrates to the interstitial sites, since the process is equivalent to vacuum annealing. Thus, the strong visible band and the lower energy NIR PL band (at ~1.40 eV) observed under high vacuum arise from the oxygen vacancy and Ti^{3+} interstitial defects, respectively. The strong NIR PL at ~1.47 eV remains unchanged in intensity and center position when oxygen is introduced in the vacuum chamber. Thus, the NIR PL originates from a defect that is independent of the oxygen vacancy and Ti^{3+} defects in reduced TiO_2. Our results strongly indicate that Ti^{4+} interstitials that migrate to the surface during the high temperature calcinations are indeed responsible for the NIR PL at 1.47 eV. Thus, the *in-situ* PL under vacuum and oxygen environment enables us to clearly distinguish between the defect states caused by Ti^{3+}, Ti^{4+} and O_v defects.[27]

Since the laser exposure during the PL measurement at RT causes dynamic change in defect population in reduced TiO_2 owing to the local heating and oxidation effects, we undertook low temperature PL measurements under high vacuum to ascertain further the origin of NIR PL at ~1.47 eV. For this experiment, Ti interstitial rich A900 was again chosen that shows strong NIR PL at room temperature and atmospheric pressure (**Fig. 4.5(c)**) and the sample was cooled down to a temperature of 11 K under high vacuum. In-situ temperature-dependent PL spectra for A900 are shown in **Fig. 4.9(b)**. We noticed that at very low temperatures (21-61 K), there is no remarkable change in NIR PL intensity with temperature indicating that laser-induced local heating is not efficient at such low temperatures. Further, the temperature quenching of PL is not significant since PL intensity at low temperature and room temperature was equally high. However, a marked reduction of PL intensity is observed when the sample temperature increased beyond 61 K up to 281 K (see inset of **Fig. 4.9(b)**). Note that the intensity of NIR PL at RT and atmospheric pressure for A900 was very high prior to the cooling for low temperature PL measurement under high vacuum. Since the measurement was carried out under high vacuum, it may be possible that the oxygen vacancies are increased with the increasing laser heating at higher temperature. If the evolution of NIR PL has any relation to the oxygen vacancy, then the intensity should be enhanced with increasing the temperature. However, since we observed a systematic reduction in NIR PL intensity with increasing sample temperature, the NIR PL cannot be related to oxygen vacancy as well as $Ti^{3+}_{lattice}$ defects. We believe that the gradual decrease of

NIR PL by the laser annealing in vacuum is due to the Ti_i migration from the near surface region to the bulk in A900, which occupy the regular Ti lattice site so that there is a reduction of Ti_i defects. Note that laser induced local heating is effective when the sample temperature is near room temperature, while for the sample maintained at low temperature the local heating is less efficient due to heat dissipation to the sample holder, despite tight focusing of the laser beam on the sample.

Interestingly, direct evidence for Ti_i migration from surface to bulk of rutile TiO_2 under similar experimental conditions were provided by Henderson[44] through temperature programmed static secondary ion mass spectrometry (SSIMS) measurements. It was demonstrated that when a rutile reduced TiO_2 is vacuum heated above 700 K, the diffusion of Ti interstitial from the surface to bulk takes place, instead of out diffusion of bulk oxygen atoms. More recently, this was demonstrated for anatase TiO_2 as well.[45] Therefore, our results provide clinching evidence that due to the migration of Ti interstitials from surface to the bulk region, the NIR PL at ~1.47 eV gradually diminishes and these surface Ti^{4+} interstitials are unambiguously the origin of the NIR PL at ~1.47 eV in undoped TiO_2 NRbs. Note that in the present case Ti interstitial migration may be taking place at a temperature much lower than 700 K, because local heating may not be as high as 700 K with 10 mW (at source) laser excitation. We believe that due to lower sensitivity of the SSIMS that the sensitivity of PL technique, the Ti migration was detected at a higher temperature than the actual temperature required to initiate the process of Ti migration under high vacuum. We anticipate that during laser exposure of the TiO_2 NRbs near room temperature, the local temperature rise may be as high as 500 K in TiO_2 nanopowders that may have relatively weak thermal contact with the Si substrate used for the PL measurements and around this temperature Ti_i migration starts taking place that could be monitored through PL due to its extremely high sensitivity. In the case of Si nanocrystal film on quartz substrate, the local temperature rise was found to be as high as ~1000 K for a laser power density of 5 $kWcm^{-2}$ during laser Raman measurements with continuous wave 488 nm laser.[46] Unfortunately, no such data is available for TiO_2 nanostructures. Though the incident laser power density is estimated to be about 1 $kWcm^{-2}$ in our case, accurate estimate of the local temperature rise is not feasible here due to nonavailability of thermal conductivity data for TiO_2 NRbs.

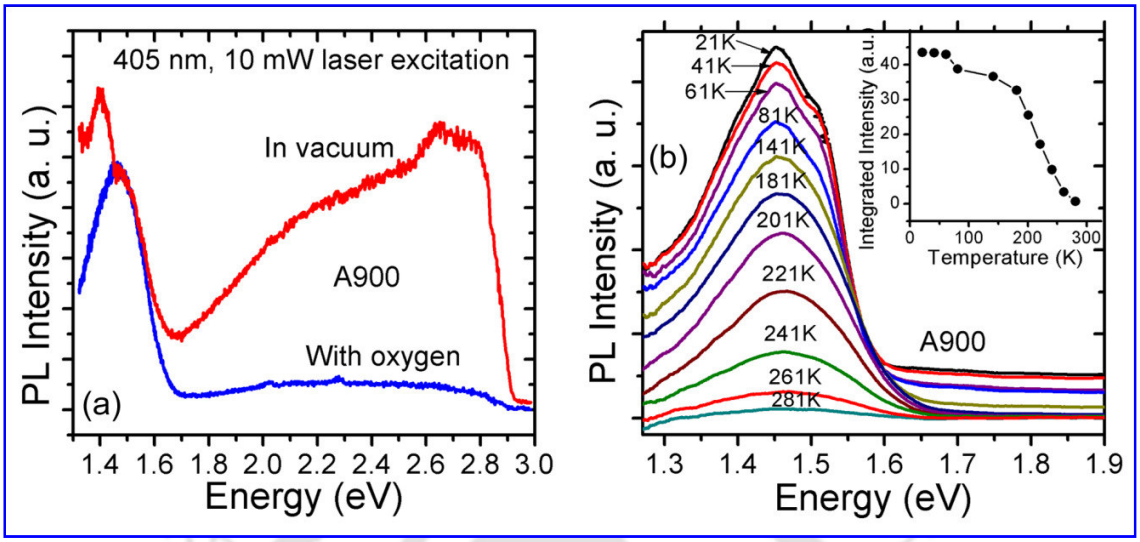

Fig. 4.9. (a) In-situ PL spectra for A900 under vacuum and after oxygen exposure with laser ON. The visible emission and lower energy NIR peak drastically goes down, while the other NIR peak at ~1.47 eV remains unchanged. (b) Low temperature PL spectra under high vacuum for A900 at different temperatures. The inset shows change in integrated PL intensity as a function of temperature.

In order to gain a better insight into the entire range of band gap states responsible for the NIR PL peaks, we measured extended NIR PL at RT using an InGaAs detector and results are shown in **Fig. 4.10(a)**. The NIR peaks are found to be broad and the mean position shows a blue-shift as the calcinations temperature is increased. The broad peak consists of two Gaussian peaks centered at 1.27 and 1.47 eV for C500, as shown in **Fig. 4.10(b)**. The broad peak may be due to the size distribution of the NRbs and broad distribution of electronic sates in the band gap causes band gap reduction, as observed from absorption studies. As discussed before, these peaks are attributed to Ti^{3+} and Ti^{4+} interstitials. The peak position for Ti^{3+} slightly varies in different samples and the extracted peak positions (peaks P1 and P2) are presented in **Table 4.1**. The time-resolved PL (TRPL) studies on C500 at emission energy 1.30 eV show PL decay in microsecond time scale (**Fig. 4.10(c)**). The TRPL spectra can be fitted by a bi-exponential decay curve with time constant τ_1 = 1.1 μS and τ_2 = 32.8 μS. This result reveals that two defect states contribute to the broad NIR PL, consistent with the steady state PL spectrum. The fast decay and slow decay correspond to contributions from peaks at 1.27 eV (P1) and 1.47 eV (P2), respectively. It is observed that peak P2 at 1.47 eV remains unchanged in energy for all samples, while the peak P1 at lower energy side

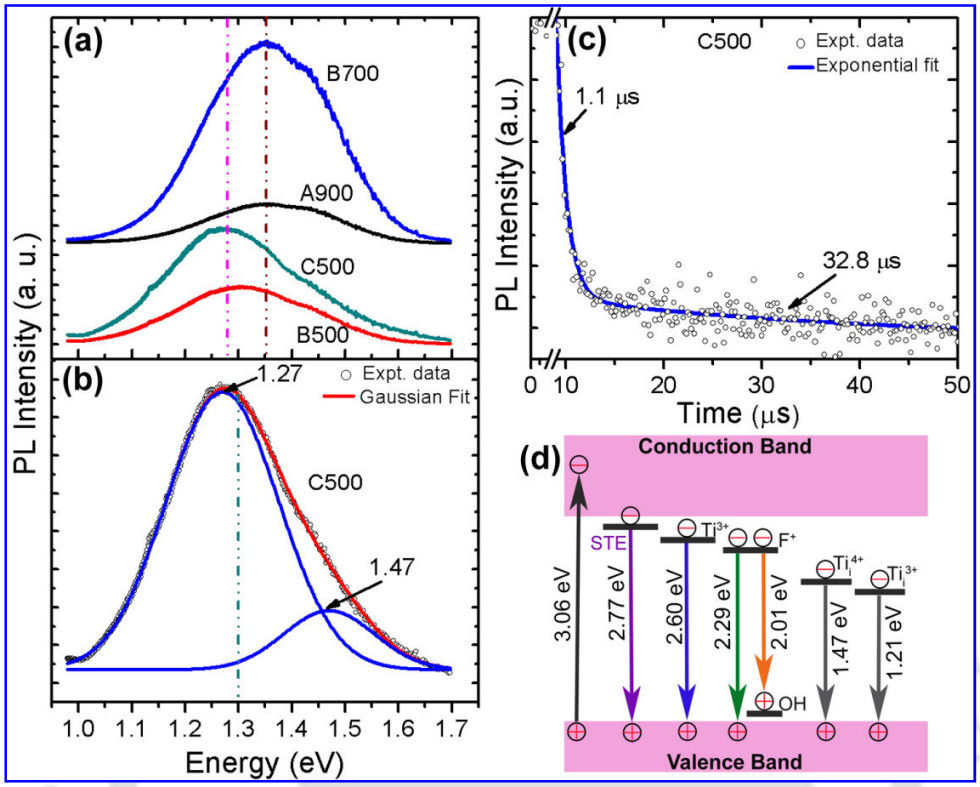

Fig. 4.10. (a) Extended range NIR PL spectra of A900, B500, B700, and C500 using an InGaAs detector. The spectra are vertically shifted for clarity of presentation. Vertical dotted lines indicate the respective peak positions for two groups of samples. (b) Gaussian fit to the NIR PL for C500 showing two symmetric peaks centered at 1.27 and 1.47 eV. (c) TRPL spectrum of C500 at 1.30 eV emission, the symbols represent experimental data and the solid line represents fitted curve with double exponential decay. The time constants of decay are indicated in each case. (d) Schematic band diagram illustrating the physical origin of the visible and NIR PL emissions. See text for details.

varies from 1.21 to 1.34 eV depending upon the samples growth and calcinations temperatures. Hence, the peak P2 at 1.47 eV is attributed to Ti_i^{4+}, while the peak P1 is assigned to Ti_i^{3+} defects. The relative intensities of these two peaks depend on the history of PL measurements environment. Note that ESR spectra confirmed the presence of Ti_i^{3+} defects. Therefore, our results are consistent with the fact that the migrated Ti_i^{3+} at the surface interact with O_2 in air during high temperature calcinations and a majority of these species are converted to Ti^{4+} oxidation states.[27] So, the peak P1 is shifted toward higher energy as the calcinations temperature increases. Note that a very weak and broad NIR PL is also observed for oxygen vacancy rich A500V compared to other as-synthesized samples,

with the InGaAs detector, indicating the presence of low concentration of Ti_i defects in A500V. Further, we noticed that as the growth temperature increases from 180–235 °C, visible PL band decreases systematically and NIR PL band successively evolves and intensity increases. So, the evolution of NIR PL is dominant at higher temperature heat treatment, that is, both higher growth and calcinations temperatures in air. The samples with strong NIR PL have stronger and extended range visible absorption, as shown in **Fig. 4.5**. These results strongly suggest that strong visible absorption and NIR PL emission are caused primarily by the Ti interstitial defects. Finally, the effect of various surface morphologies that evolve during calcinations on the visible and NIR PL cannot be fully ignored. Further studies combined with *in-situ* STM and photoelectron spectroscopy may shed more light on the local structure of these defects and distribution of band gap states in undoped TiO_2 nanostructures.

4.9. Discussion

Lauer[47] reported a 1.70 eV NIR PL emission for high temperature annealed (900–1000 °C) ZnO in O_2 ambient and suggested that the PL results from electron transition from the conduction band edge to a hole trapped in the bulk at 1.60 eV above the valence band edge. Recently, Wang et al.[26] reported splitting of broad visible-NIR PL to separate green (2.31 eV) and NIR (1.64 eV) emissions for 800 °C air-annealed ZnO microstructure and finally the NIR band dominated at 1000 °C. They suggested that the NIR emission is due to donor-acceptor transition between oxygen vacancy and zinc vacancy and/or radiative recombination of shallowly trapped electrons with deeply trapped hole at interstitial O_i defect. Shi et al.[21] reported the NIR PL emission at ~1.49 eV when the TiO_2 was calcined at >500 °C and the peak was more intense after 900 °C calcinations. The authors carried out *in-situ* PL measurement with O_2 and H_2 treatment as an oxidation and reduction atmosphere for the 900 °C calcined sample and observed that the NIR PL bands are increased after oxidation treatment in O_2 and decreased after reduction treatment in H_2. It was suggested that NIR luminescence is due to intrinsic defects in rutile TiO_2. Note that here the B500 is purely of anatase phase, as confirmed from the XRD and Raman analyses. We observed strong NIR PL signal in B500 and A900. Further, we observed the NIR PL emission in pure TiO_2(B), mixed phase TiO_2(B)-anatase and anatase-rutile besides the broad visible PL emission. Our results suggest that NIR PL in TiO_2 is not the intrinsic property of rutile phase only, contrary to the

earlier report.[21] Therefore, it appears that the high temperature heat treatment actually results in the migration of intrinsic defects from the bulk to the surface and evolution of NIR PL emissions in both TiO_2 and ZnO systems.

We noticed that A500, A700, and A900 show the visible PL band intensity in the order A700 > A900 > A500, whereas the NIR PL in the order A900 > A700 > A500. Our experimental results reveal that the calcinations of as-grown solvothermal product at various temperatures in air is a more complex than a simple vacancy filling process as is usually believed, owing to the peculiar behavior of NIR and visible bands observed here. At a typical calcinations temperature, the samples with moderate to high oxygen vacancies and Ti_i defects exhibit a wide variety of restructuring surface morphologies that includes the formation of nanopits, nanobricks and nanostones on the surface of TiO_2 NRbs. These surface structures result from the various $Ti_{lattice}$-O and Ti_i-O bond rearrangements due to the Ti interstitials that diffuse from the bulk to the surface during calcinations. There has been evidence for diffusing native point defects in bulk rutile playing a major role in surface and interface related phenomena when high temperature annealing is involved.[48, 49] When a reduced rutile TiO_2 (110) crystal is exposed to O_2 at elevated temperatures, diffusion of Ti interstitial to the surface has been reported[6, 50, 51] and the opposite effect occurs during vacuum annealing.[7, 52] Iddir et al.[53] reported that the Ti interstitials with small migration barriers are the major diffusive species compared to oxygen vacancies by using *ab initio* calculation. Since the behavior of two PL bands (NIR and visible) are different, it is ascribed to a difference in trapping probability and expected to originate from different sources of point defects in TiO_2 NRbs. Therefore, besides the O_v, Ti_i must be also considered as an active defects in reduced TiO_2 and it may strongly influence various properties of the material, such as band gap narrowing and photocatalytic activity. At moderate calcinations temperature of 700 °C, the dehydration of as-grown solvothermal products takes place and the oxygen vacancies are increased for the A700 as compared to A500 and the molecular O_2 may not interact with the material at this stage. At higher temperature 900 °C, the molecular O_2 interacts with surface of the materials and start filling oxygen vacancies and the near surface Ti_i diffuse to the upper surface layer, where reaction with O_2 molecules is more likely. The Ti interstitial diffusion proceeds via an exchange mechanism[53] in which a Ti atom on a regular lattice site is released to an interstitial site toward the surface and subsequently

the lattice site is occupied by the original Ti interstitial atom from a deeper layer. So, we believe that the gradual increase of NIR PL with calcinations temperature may be due to the creation of more Ti_i defects in the near surface layers.

Therefore, our experimental finding provide convincing evidence that visible PL primarily originates from oxygen vacancies, while the extended visible absorption as well as NIR PL emission are due to the interstitial Ti_i defects in reduced TiO_2. The native defects such as O_v and Ti_i create deep trap states within the band gap of TiO_2 which act as luminescence centers for visible and NIR PL, respectively. Note that the Ti_i defect trap states are deeper than the O_v trap states below the conduction band as theoretically predicted by Lee et al.[18] and Finazzi et al.[19] Interestingly, the measured energies for the Ti_i states are close to the theoretically predicted energy levels of 1.3 eV above the valence band[54] or 1.3 eV below the conduction band.[18] Since the measured band gap in the Ti interstitial rich TiO_2 NRbs lies in the range 1.98 to 2.64 eV (see **Table 4.1**), the predicted results matches remarkably well with our experimental data. The location of these trap states which are responsible for the evolution of strong visible and NIR PL emissions is summarized in the schematic band diagram shown in **Fig. 4.10(d)**. The photogenerated electrons are initially excited to the conduction band of TiO_2 on irradiating laser light (405 nm) and then relaxed to the defect states. The visible PL is due to the transition of electrons from self-trap exciton, Ti_i^{3+} center, F^+ center trap states to the valence band and F^+ center state to acceptor level due to OH^- species.[23] The NIR PL emissions are due to the transition of electron from Ti_i^{4+} and Ti_i^{3+} defect trap states to the valence band.

4.10. Conclusions

Undoped TiO_2 NRbs with nanopits, nanobricks, and nanostones like surface morphologies were successfully synthesized by a simple solvothermal method followed by calcinations. With higher calcination temperatures, absorption edge systematically red-shift up to visible (yellow-red) region for these undoped NRbs, which is very important for enhanced visible light photocatalysis. Our *in-situ* PL studies under controlled environment provide conclusive evidence that visible PL band originate from oxygen vacancy states that can be manipulated easily. Low temperature *in-situ* PL studies provide clinching evidence for the Ti surface

interstitials being responsible for the NIR PL emission at 1.27 and 1.47 eV, identified for the first time. The UV-visible-NIR absorption spectroscopy shows reduced band gap due to the presence of O_v and Ti_i defect states within the band gap of TiO_2 NRbs. Furthermore, ESR studies confirmed the presence of O_v and Ti_i defects in the NRbs in different samples, depending upon different growth conditions and post growth processing. The highly porous TiO_2 NRbs developed in this work accompanied by identification of the defects responsible for strong visible absorption and NIR PL emission is considered as an important milestone for engineering the efficient visible light photocatalytic and photovoltaic applications of undoped TiO_2-based materials.

References

1. V. N. Kuznetsov and N. Serpone, The Journal of Physical Chemistry C **113**, 15110-15123 (2009).
2. A. Naldoni, M. Allieta, S. Santangelo, M. Marelli, F. Fabbri, S. Cappelli, C. L. Bianchi, R. Psaro and V. Dal Santo, Journal of the American Chemical Society **134**, 7600-7603 (2012).
3. X. Liu, S. Gao, H. Xu, Z. Lou, W. Wang, B. Huang and Y. Dai, Nanoscale **5**, 1870-1875 (2013).
4. X. Chen and C. Burda, Journal of the American Chemical Society **130**, 5018-5019 (2008).
5. X. Chen, L. Liu, Z. Liu, M. A. Marcus, W.-C. Wang, N. A. Oyler, M. E. Grass, B. Mao, P.-A. Glans, P. Y. Yu, J. Guo and S. S. Mao, Scientific Reports **3**, 1510 (2013).
6. S. Wendt, P. T. Sprunger, E. Lira, G. K. H. Madsen, Z. Li, J. Ø. Hansen, J. Matthiesen, A. Blekinge-Rasmussen, E. Lægsgaard, B. Hammer and F. Besenbacher, Science **320**, 1755-1759 (2008).
7. M. A. Henderson, Surface Science **419**, 174-187 (1999).
8. M. R. Hoffmann, S. T. Martin, W. Choi and D. W. Bahnemann, Chemical Reviews **95**, 69-96 (1995).
9. W. Choi, A. Termin and M. R. Hoffmann, Angewandte Chemie **106**, 1148-1149 (1994).

10. R. Asahi, T. Morikawa, T. Ohwaki, K. Aoki and Y. Taga, Science **293**, 269-271 (2001).
11. K. B. Jaimy, V. P. Safeena, S. Ghosh, N. Y. Hebalkar and K. G. K. Warrier, Dalton Transactions **41**, 4824-4832 (2012).
12. G. Yang, Z. Jiang, H. Shi, T. Xiao and Z. Yan, Journal of Materials Chemistry **20**, 5301-5309 (2010).
13. K. Zhang, X. Wang, X. Guo, T. He and Y. Feng, Journal of Nanoparticle Research **16**, 1-9 (2014).
14. B. Xin, P. Wang, D. Ding, J. Liu, Z. Ren and H. Fu, Applied Surface Science **254**, 2569-2574 (2008).
15. U. G. Akpan and B. H. Hameed, Journal of Hazardous Materials **170**, 520-529 (2009).
16. W. Choi, A. Termin and M. R. Hoffmann, The Journal of Physical Chemistry **98**, 13669-13679 (1994).
17. J. Tao, T. Luttrell and M. Batzill, Nature Chemistry **3**, 296-300 (2011).
18. H.-Y. Lee, S. J. Clark and J. Robertson, Physical Review B **86**, 075209 (2012).
19. E. Finazzi, C. Di Valentin and G. Pacchioni, The Journal of Physical Chemistry C **113**, 3382-3385 (2009).
20. M. A. Henderson, W. S. Epling, C. H. F. Peden and C. L. Perkins, The Journal of Physical Chemistry B **107**, 534-545 (2003).
21. J. Shi, J. Chen, Z. Feng, T. Chen, Y. Lian, X. Wang and C. Li, The Journal of Physical Chemistry C **111**, 693-699 (2007).
22. M. Yang, W. Liu, J.-L. Sun and J.-L. Zhu, Applied Physics Letters **100**, 043106 (2012).
23. B. Santara, P. K. Giri, K. Imakita and M. Fujii, Nanoscale **5**, 5476-5488 (2013).
24. X. Wang, Z. Feng, J. Shi, G. Jia, S. Shen, J. Zhou and C. Li, Physical Chemistry Chemical Physics **12**, 7083-7090 (2010).
25. F. Montoncello, M. C. Carotta, B. Cavicchi, M. Ferroni, A. Giberti, V. Guidi, C. Malagù, G. Martinelli and F. Meinardi, Journal of Applied Physics **94**, 1501-1505 (2003).

26. M. Wang, Y. Zhou, Y. Zhang, E. Jung Kim, S. Hong Hahn and S. Gie Seong, Applied Physics Letters **100**, 101906 (2012).
27. B. Santara, P. K. Giri, K. Imakita and M. Fujii, The Journal of Physical Chemistry C **117**, 23402-23411 (2013).
28. J. C. Parker and R. W. Siegel, Applied Physics Letters **57**, 943-945 (1990).
29. W. F. Zhang, Y. L. He, M. S. Zhang, Z. Yin and Q. Chen, Journal of Physics D: Applied Physics **33**, 912 (2000).
30. B. Santara, B. Pal and P. K. Giri, Journal of Applied Physics **110**, 114322 (2011).
31. B. J. Morgan and G. W. Watson, The Journal of Physical Chemistry C **114**, 2321-2328 (2010).
32. I. Justicia, P. Ordejón, G. Canto, J. L. Mozos, J. Fraxedas, G. A. Battiston, R. Gerbasi and A. Figueras, Advanced Materials **14**, 1399-1402 (2002).
33. F. Zuo, L. Wang, T. Wu, Z. Zhang, D. Borchardt and P. Feng, Journal of the American Chemical Society **132**, 11856-11857 (2010).
34. J. Wang, Z. Wang, B. Huang, Y. Ma, Y. Liu, X. Qin, X. Zhang and Y. Dai, ACS Applied Materials & Interfaces **4**, 4024-4030 (2012).
35. P. Gorai, A. G. Hollister and E. G. Seebauer, Applied Physics Letters **103**, 141601-141604 (2013).
36. A. G. Hollister, P. Gorai and E. G. Seebauer, Applied Physics Letters **102**, 231601-231605 (2013).
37. H. Kamisaka and K. Yamashita, The Journal of Physical Chemistry C **115**, 8265-8273 (2011).
38. T. S. Bjørheim, A. Kuwabara and T. Norby, The Journal of Physical Chemistry C **117**, 5919-5930 (2013).
39. M. Setvín, U. Aschauer, P. Scheiber, Y.-F. Li, W. Hou, M. Schmid, A. Selloni and U. Diebold, Science **341**, 988-991 (2013).
40. S. Na-Phattalung, M. F. Smith, K. Kim, M.-H. Du, S.-H. Wei, S. B. Zhang and S. Limpijumnong, Physical Review B **73**, 125205 (2006).
41. P. F. Chester, Journal of Applied Physics **32**, 2233-2236 (1961).
42. P. I. Kingsbury, W. D. Ohlsen and O. W. Johnson, Physical Review **175**, 1091-1098 (1968).

43. M. Anpo, M. Che, B. Fubini, E. Garrone, E. Giamello and M. Paganini, Topics in Catalysis **8**, 189-198 (1999).
44. M. A. Henderson, Surface Science **343**, L1156-L1160 (1995).
45. G. S. Herman, R. T. Zehr and M. A. Henderson, Surface Science **612**, L5-L8 (2013).
46. H. S. Mavi, S. Prusty, A. K. Shukla and S. C. Abbi, Thin Solid Films **425**, 90-96 (2003).
47. R. B. Lauer, Journal of Physics and Chemistry of Solids **34**, 249-253 (1973).
48. U. Diebold, Surface Science Reports **48**, 53-229 (2003).
49. O. Dulub, W. Hebenstreit and U. Diebold, Physical Review Letters **84**, 3646-3649 (2000).
50. H. Onishi and Y. Iwasawa, Physical Review Letters **76**, 791-794 (1996).
51. R. A. Bennett, P. Stone, N. J. Price and M. Bowker, Physical Review Letters **82**, 3831-3834 (1999).
52. K. T. Park, M. Pan, V. Meunier and E. W. Plummer, Physical Review B **75**, 245415 (2007).
53. H. Iddir, S. Öğüt, P. Zapol and N. D. Browning, Physical Review B **75**, 073203 (2007).
54. M. Nolan, S. D. Elliott, J. S. Mulley, R. A. Bennett, M. Basham and P. Mulheran, Physical Review B **77**, 235424 (2008).

भारतीय प्रौद्योगिकी संस्थान गुवाहाटी
Indian Institute of Technology Guwahati

Chapter 5

Intrinsic Defect Induced Room Temperature Ferromagnetism in Undoped TiO_2 Nanoribbons

Spintronic is an emerging technology where both charge and spin are used to transport, store, and process information in novel ways, providing enhanced performance and new functionalities in order to increase both speed and storage capacity in traditional microelectronic devices. In the recent decade, diluted magnetic semiconductors (DMS), in particular the ferromagnetic oxides have been at the forefront of research for spintronics and magneto-optic device materials.[1-3] More importantly, it was reported that transition metal (TM) doped as well as undoped TiO_2 nanostructures exhibits room temperature ferromagnetism (RTFM). However, in spite of several studies reported on TiO_2-based DMS there is no clear agreement about the nature and origin of observed ferromagnetism (FM). In this study, we report on the intrinsic defects, i.e., oxygen vacancy induced FM at and above room temperature (RT) in undoped TiO_2 nanoporous nanoribbons (NRbs) synthesized by a solvothermal method. The origin of FM in as-synthesized and vacuum annealed undoped NRbs grown for different reaction durations followed by calcinations was investigated by several experimental tools. It will be demonstrated that a large concentration of oxygen vacancies with high thermal stability indeed results in stronger RTFM compared to those previously reported in undoped/ doped TiO_2 systems.

5.1. Introduction

The discovery of ferromagnetism in Co-doped TiO_2 with a Curie temperature (T_C) exceeding 300 K [3] was crucial in expanding the field of DMS to oxides, leading to a rapid development of new materials and phenomena arising from a synergy of semiconductor physics and

strongly correlated systems. As a result, intensive attention has been focused on DMS such as transition metals (TM) doped ZnO,[4] SnO_2,[5] In_2O_3[6] and TiO_2[7] due to realization of room temperature ferromagnetism (RTFM) in these systems. Among various oxide based DMS, TiO_2 has drawn extensive research interest because it is an excellent photo-catalyst for water splitting and it possesses good optical transmission in the visible and near infrared region making it a suitable candidate for magneto-optic devices as well. However, in spite of several studies reported on TiO_2-based DMS, there is no clear agreement about the nature and origin of the observed ferromagnetism (FM). Some reports suggested segregation and the formation of TM clusters as the origin of FM signal,[8, 9] while most recent results strongly hints at the intrinsic nature of FM mediated by carriers or defects.[7, 10, 11] These controversial results among research groups suggest that the magnetic properties of DMS materials are critically dependent on fabrication, growth conditions, and doping agents. Compared to other methods of preparation, solvothermal method is very simple, low cost, and one can easily tune the surface defects by controlling the growth temperature, reaction duration etc. Interestingly, some of the outstanding works revealed no evidence of ferromagnetic ordering of the active doped metal in Co, Mn doped ZnO systems.[12-14] Using *ab initio* electronic structure calculation, Pandey and Choudhary[15] argued that an oxygen vacancy leads to electron doping in TiO_2 system, but does not induce an appreciable magnetic moment. More recently, Hoa and Huyen[16] reported enhanced FM in undoped TiO_2 nanowire as compared to Ni doped TiO_2 nanowire. Further, RTFM have been observed in a wide range of undoped oxides such as TiO_2,[17] HfO_2,[18] In_2O_3,[17] SnO_2[19] and ZnO.[20] These help to settle the controversies about the issues related to the role of defects in the ferromagnetic ordering. In fact, Sundaresan and Rao[21] suggested FM as a universal feature of inorganic nanoparticles where the FM was confined to the surface of the nanoparticles. However, unambiguous determination of the nature of defects responsible for the observed FM remains a considerable challenge to the researchers. It is unclear whether oxygen vacancy or Ti vacancy defects contribute to the magnetic moments, since both titanium and oxygen vacancies were proposed to be responsible for the FM in undoped TiO_2. On the other hand, theoretical[22] studies indicated that cation vacancies and divacancies are ferromagnetically coupled. Interestingly, more and more theoretical and experimental[23, 24] evidences show that the magnetic ordering of undoped

TiO_2 is strongly related to oxygen vacancy and thus it was thought to be source of RTFM in undoped semiconducting oxides.

Till date, most of the reported FM in undoped TiO_2 was for thin films[11, 17, 23, 24] and nanoparticles.[21, 25] The observed FM in undoped thin films and nanoparticles are usually weak and might originate from surface defects such as oxygen vacancies and/or interface defects. Compared to thin films and nanoparticles, one dimensional (1D) TiO_2 nanostructures such as nanowires, nanorods and nanoribbons (NRbs) with high surface area can possess abundant surface defects, thus the intrinsic FM could be enhanced. Moreover, 1D nanostructures are favored over nanoparticles in terms of electron transport, storage and information processing that can enhance the performance of spintronic devices at the nanoscale for practical applications. Although little information about the magnetic properties of 1D anatase TiO_2 nanowire,[26] rutile TiO_2 nanowire[16] and vanadium doped TiO_2(B)[27] nanotubes are available in the literature, to the best of our knowledge, there is no report on the intrinsic RTFM in undoped TiO_2(B) nanoporous NRbs.

Our present attempt in this study is to control the magnetic moments which are solely due to intrinsic defects and explore a better understanding about the origin of observed FM in undoped 1D TiO_2 system. Here, we grow TiO_2 nanoporous NRbs by an ethylene glycol mediated solvothermal method. We investigate the optical and magnetic properties and the origin of RTFM in the undoped TiO_2 NRbs. The high surface area and higher concentration of surface defects, such as oxygen vacancies, expected in these nanoporous NRbs could ultimately lead to enhanced ferromagnetic ordering and strong ferromagnetism even at room temperature.[28]

5.2. Growth of TiO_2 nanoporous nanoribbons

The growth of undoped TiO_2 NRbs was already described in the previous chapter (*Chapter 4*). Here one more sample, which is grown at 180 °C for 48 h reaction and calcined at 500 °C is included in this study. The sample is named as G500. The nomenclatures of the other samples are same as those in the *Chapter 4* (see **Table 4.1**). The samples A500, A700, A900, A500V, B500, B700, B900, D500 and D900 are considered for the study of structural, optical and magnetic properties in this chapter.

5.3. Structural and morphological studies

XRD patterns: The XRD patterns of the samples are shown in the previous chapter, **Fig. 4.1** except the sample G500. For the ease of discussion and understanding, the XRD patterns of some of the samples are shown in **Fig. 5.1**, which are important in this study. **Fig. 5.1(a)** shows the XRD patterns of samples of "A" series, i.e., the samples grown at 180 °C after 16 h reaction and different calcinations (500, 700 and 900 °C). Samples A500, A700 and A900 show the diffraction peaks corresponded to pure TiO_2(B), mixed TiO_2(B)-anatase and mixed anatase-rutile phase, respectively. **Fig. 5.1(b)** shows the XRD patterns of A500, D500 and G500, and all the diffractions indicate the TiO_2(B) phase. Thus, the TiO_2(B) phase is formed after 500 °C calcinations irrespective of the growth durations.

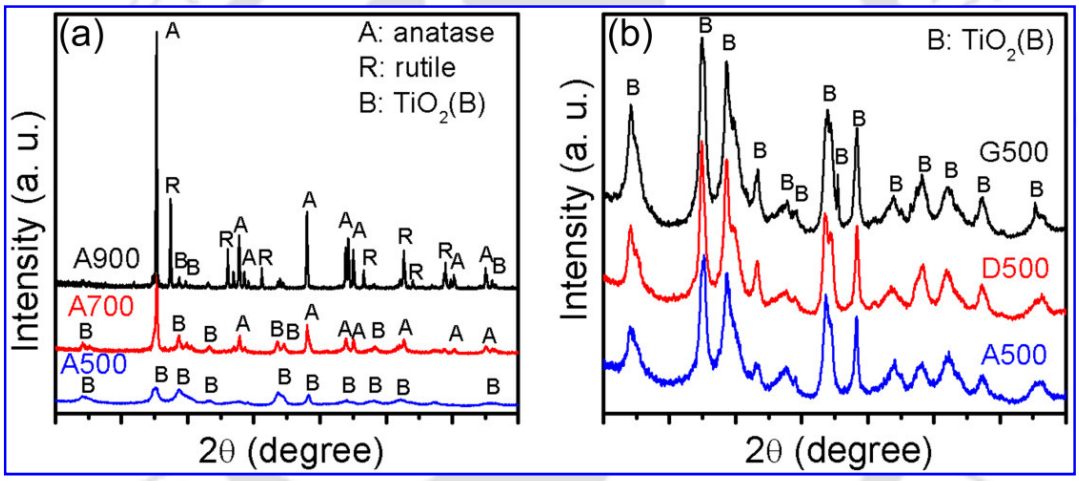

Fig. 5.1. XRD patterns: (a) A500, A700 and A900, grown at 180 °C after 16 h reaction and different calcinations; (b) A500, D500 and G500, grown at 180 °C for the different reaction durations and calcined at 500 °C.

Micro-Raman studies: The Raman spectra of the samples A700, A900 and D900 were shown in *Chapter 4* (**Fig. 4.2**), which are considered here for the magnetic property studies. The Raman modes for the samples A700, A900 and D900 shows the mixed phase TiO_2(B)-anatase and anatase-rutile, respectively (see **Fig. 4.2(b)**, *Chapter 4*). The most intense Raman mode of anatase at 142 cm^{-1} in precursor TiO_2 (**Fig. 4.2(d)**, *Chapter 4*) is found to be blue shifted for the as-synthesized samples. Such a blue shift of the $E_g(1)$ Raman mode was interpreted as arising from different competing mechanism such as non-stoichiometry due to

oxygen vacancies or disorder induced defects and phonon confinement effects.[29, 30] From FESEM and TEM images, we observed that the size of the NRbs is too large to induce phonon confinement effect and it is often orders of magnitude larger than the size of the precursor TiO_2 nanoparticles. So, the phonon confinement effect is easily discarded. Therefore, we believe that the blue-shift in as-synthesized NRbs is due to the reduced oxygen stoichiometry. The Raman spectra for A500, A500V and D500 are shown in **Fig. 5.2**. We notice a relative reduction in intensity of the A_g mode at 147 cm^{-1} after vacuum annealing of A500, while the intensities of other Raman modes remain almost unchanged. Moreover, the B_g mode of A500 at 194 cm^{-1} is red shifted to 192 cm^{-1} after vacuum annealing (sample A500V) indicating the introduction of additional defects, i.e., oxygen vacancies, by annealing in reduced atmosphere. Thus, Raman studies revealed that nonstoichiometric defects are present in the as-grown NRbs and additional defects are created by annealing the sample in reduced atmosphere, as expected. The intensity of A_g mode at 147 cm^{-1} is decreased considerably for sample D500 while other modes are more intense as compared to A500. This result indicates that higher concentration of oxygen vacancy may be present in sample D500 as compared to A500.

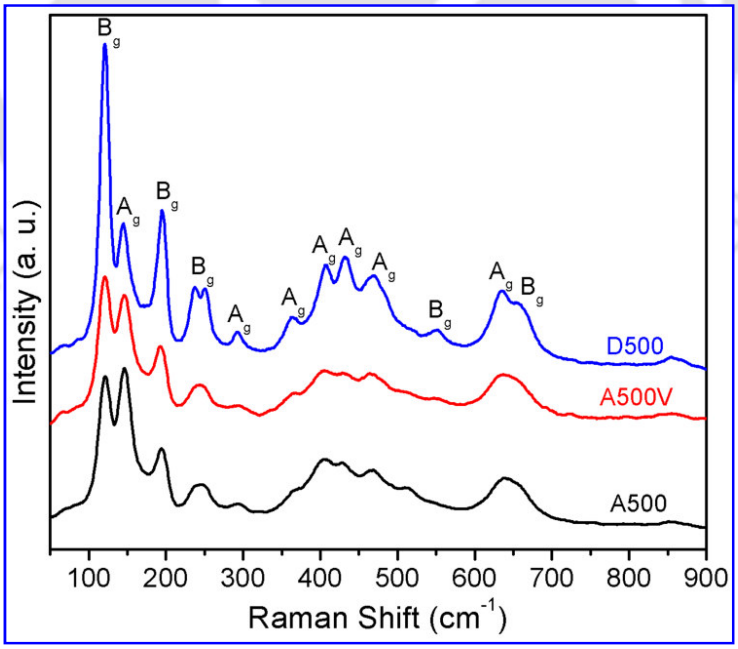

Fig. 5.2. Raman spectra for A500, A500V and D500 showing various Raman modes of TiO_2(B) phase.

FESEM and TEM imaging: The morphologies of the precursor TiO_2 ($PTiO_2$), A500, D500 and G500 are shown in **Fig. 5.3**. The FESEM image of $PTiO_2$ (**Fig. 5.3(a)**) shows the average particle size of ~80 nm. The high magnification FESEM image of sample A500 in **Fig. 5.3(b)** shows the nanopits on the surface of NRbs grown at 180 °C using the $PTiO_2$ nanoparticles as precursor. TEM images of D500 and G500 in **Fig. 5.3(b) and (c)** show the nanobricks-like structures on the surface of NRbs. The selected area electron diffraction (SAED) pattern of the sample D500 in inset of **Fig. 5.3(c)** shows the single crystalline nature of TiO_2(B) phase.

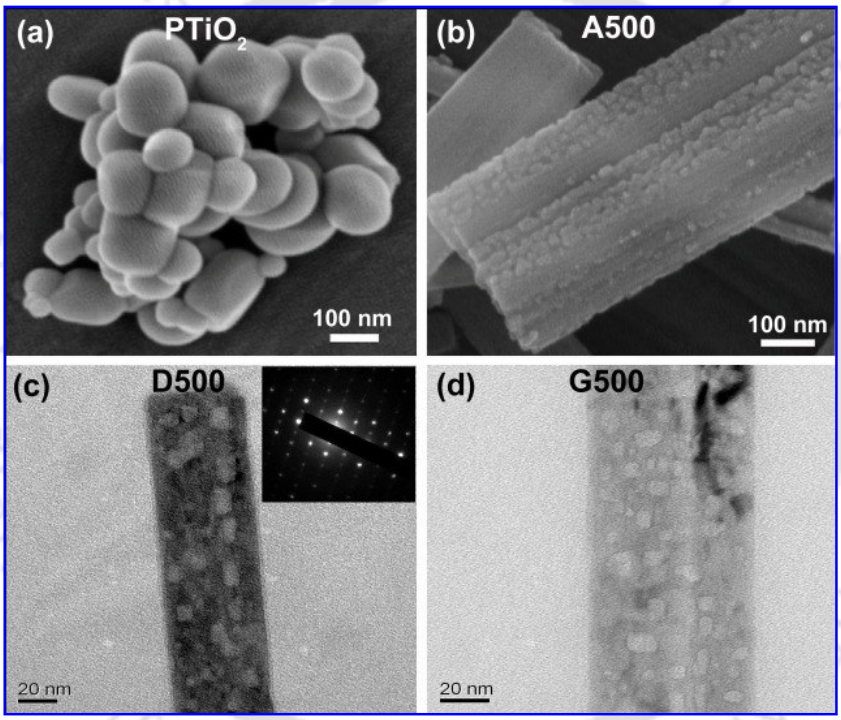

Fig. 5.3. FESEM image: (a) Precursor TiO_2 NPs, (b) A500; TEM images: (c) D500, (d) G500. The inset in (c) shows the SAED pattern of the corresponding NRbs.

5.4. Optical absorption studies

Light absorption characteristics of the solvothermally synthesized 1D TiO_2 nanostructures and the precursor TiO_2 ($PTiO_2$) are shown in **Fig. 5.4(a)**. All the as-synthesized samples exhibit a red shift of the absorption edge and considerable absorption in the visible region (>420 nm). With the increase in calcination temperature from 500 to 700 °C, the absorption

edge shows slight blue shift whereas it is again red shifted for the sample calcined at 900 °C. It is reported that the band gap of TiO_2(B), anatase and rutile TiO_2 are 3.1, 3.2 and 3 eV,[31] respectively. Since there is a phase transition from TiO_2(B) to mixed phase TiO_2(B)–anatase and mixed phase anatase–rutile with calcination temperatures from 500–900 °C, respectively, the blue shift and red shift of absorption edges are expected. Interestingly, a clear absorption band at ~484 nm for the samples A500 and A700 indicates the transition involving oxygen vacancy-related intermediate deep trap states, which is shown in the inset of **Fig. 5.4(a)**. The indirect band gap of the samples are calculated from the $(\alpha hv)^{1/2}$ *versus hv* plot (**Fig. 5.4(b)**). The band gaps are 2.34, 2.48 and 2.29 eV for the samples A500, A700 and A900, respectively.

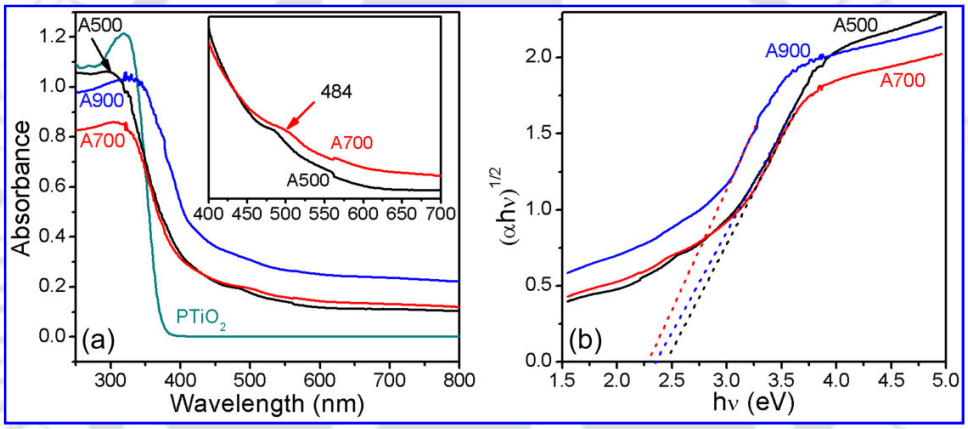

Fig. 5.4. (a) UV-visible absorption spectra for $PTiO_2$, A500, A700, A900; (b) $(\alpha hv)^{1/2}$ *versus hv* plot, band gap is calculated from the extrapolated line (dashed) fitted to the respective linear portions.

Theoretical calculations suggested that a high vacancy concentration could induce a vacancy band of electronic states just below the conduction band.[32] Zuo et al.[33] reported that the presence of a mini-band closely below the conduction band minimum which is related to the oxygen vacancy associated with Ti^{3+} and is responsible for the band gap narrowing in TiO_2. A similar observation related to oxygen vacancy induced band gap narrowing has been reported in the ZnO system.[34] Recently, Hoang et al.[35] reported that interaction between Ti^{3+} and N modified the band structure of TiO_2 and are responsible for the enhancement in the water oxidation performance under visible light illumination. Note that the absorption edge of precursor TiO_2 powder is at 380 nm, the large red shift of the as-synthesized NRbs may be

due to the shallow trap states created by oxygen vacancies associated with Ti^{3+}, leading to a band gap narrowing.

5.5. Photoluminescence studies

In order to confirm the nature of defects, photoluminescence (PL) studies are performed on different samples. **Fig. 5.5(a)** shows the room temperature PL spectra of samples A500, A700, A900, A500V, D500 and G500 under identical conditions of measurement with excitation of a 325 nm laser wavelength. The observed broad visible luminescence is primarily related to self trapped excitons and oxygen vacancy related defect states in TiO_2. Note that the PL intensity is lowest for the sample A500, while it is highest for A500V, about two orders of magnitude higher in intensity than that of A500, as shown in **Fig. 5.5(b) and (c)**. The inset of **Fig. 5.5(a)** shows the integrated PL intensity for various samples. For a clearer understanding on the origin of the broad PL emission, the deconvolution of the peak was necessary. The broad emission peak could be fitted properly with four Gaussian bands centered at 425.0 (peak 1), 467.7 (peak 2), 516.8 (peak 3), 611.7 (peak 4) nm for A500 and at 432.6 (peak 1), 470.1 (peak 2), 530.5 (peak 3), 618.3 (peak 4) for A500V, respectively as shown by the solid lines (blue curves). According to the literature, peak 1 may be ascribed to self trapped excitons located at TiO_6 octahedra, while peak 2 and 3 are ascribed to oxygen vacancy related trap states.[36] Peak 4 is attributed to the presence of hydroxyl (OH^-) species which may form an accepter level just above the valence band.[28]

It is reported that the visible luminescence band originates from the oxygen vacancies associated with Ti^{3+} in anatase TiO_2.[36] More importantly, the PL emission is enhanced by about two orders of magnitude in the vacuum annealed sample A500V as compared to A500, strongly indicating that concentration of oxygen vacancies are dramatically high in vacuum annealed samples, as expected. Similarly, the PL intensity is high for D500. From the XPS analyses, it will be evident that the TiO_2 NRbs are primarily oxygen deficient. Upon the loss of an O atom in TiO_2 lattice, the electron pair that remains trapped in the vacancy cavity V_o left behind a pair of electrons which give rise to an F center (eqn (5.1)).[37] The basic assumption is that one of the electron in F centre tends to occupy the neighboring Ti^{4+} ion and yield Ti^{3+} center and F^+ center (eqn (5.2)) forming a shallow and deep trap states, respectively which is explained in the following equations.

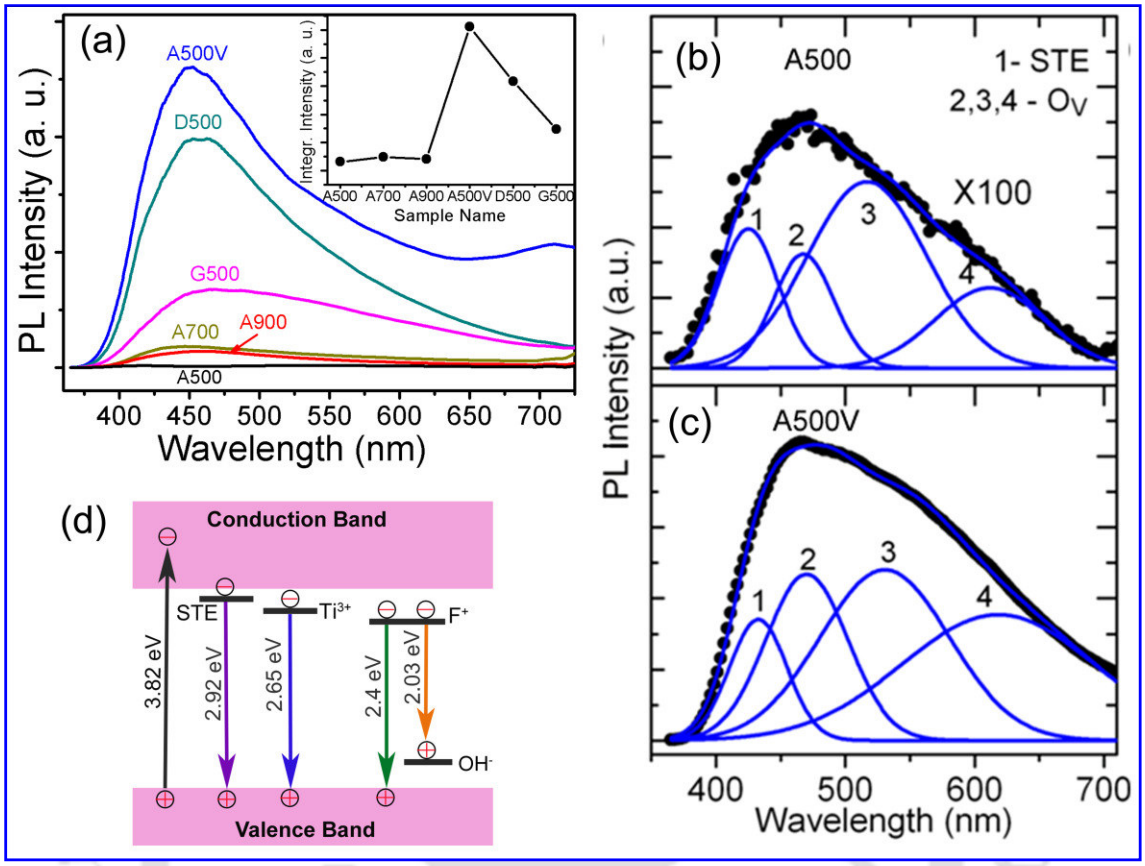

Fig. 5.5. Room temperature PL spectra in the visible region: (a) A500, A700, A900, A500V, D500, and G500, inset shows the integrated PL intensity for different samples; (b) and (c) comparison of PL intensity for A500 and A500V. Each spectrum was fitted with four Gaussian peaks (1, 2, 3 and 4). The deconvoluted spectra are shown with solid lines and experimental data are shown with symbols. (d) Schematic diagram illustrating the physical origin of visible PL emissions. See text for details.

$$V_o + 2e^- \rightarrow F \qquad (5.1)$$

$$F + Ti^{4+} \rightarrow F^+ + Ti^{3+} \qquad (5.2)$$

$$V_o + e^- \rightarrow F^+ \qquad (5.3)$$

$$Ti^{4+} + e^- \rightarrow Ti^{3+} \qquad (5.4)$$

Thus, Ti^{3+} center and F^+ center (single electron associated with oxygen vacancies) are formed due to the absence of an oxygen atom. Shallow trap states identified with oxygen vacancies were reported at 0.51eV[38] and 0.8 eV[39] below the conduction band. The PL peak at 467.7 nm is coincident with shallow trap which can be assigned to Ti^{3+} states just below the conduction band, while PL emission at 516.8 nm is due to deep trap state which is associated with the F^+

center.[40] The location of these trap centers responsible for the strong visible PL from TiO_2 NRbs can be understood from the schematic band diagram shown in **Fig. 5.5(d)**. The photogenerated electrons are initially excited to the conduction band of TiO_2 on irradiating the UV-light (325 nm) and then relaxed to the defect states. The defect states in TiO_2 are attributed to three different physical origins: self trapped exciton, oxygen vacancies and surface states. The emission at 425.0 nm originates from the self trapped excitons (STE) localized in TiO_6 octahedra.[40] The emission at 467.7 nm is attributed to shallow trap states originated from oxygen vacancies associated with Ti^{3+}, while the emission at 516.8 nm is attributed to deep trap states originated from oxygen vacancy associated with F^+ center. Photoluminescence is mostly a surface phenomenon, and a change in the surface environment would have a significant effect on the photoluminescence process. Due to a large surface area and strong presence of defects in the NRbs, defect related PL emission is found to be strong. The emission at 611.7 nm may be assigned to electron transition from the F^+ center to the acceptor level just above the valence band. The presence of hydroxyl (OH) species is detected in the XPS and FTIR spectra, discussed later in this chapter, which may form an acceptor level just above the valence band and may be responsible for the observed 611.7 nm PL emission. Recently, Yang et al.[41] assigned the PL bands at 520 nm (2.38 eV) and 568 nm (2.18 eV) to the oxygen vacancies in TiO_2 nanotubes. Note that out of the integrated PL intensity, 82% of PL in A500 and 90% of PL in A500V are related to oxygen vacancies with two orders of magnitude increase in overall intensity of oxygen vacancy (O_v) peaks after vacuum annealing. From our XPS studies, we observed that Ti^{3+} and O_v concentrations are significantly increased in sample A500V. This strongly suggests that the concentration of oxygen vacancies is increased considerably in the vacuum annealed sample consistent with the PL analysis. Note that all the PL peaks are red shifted for vacuum annealed sample A500V indicating that the number of defects states increases and overlapping of this large number of defect states broadens the Ti^{3+} center states as well as F^+ center states leading to a narrow band gap. It was found that the width of the band related to the concentration of Ti^{3+} or oxygen vacancies increased as the concentration of oxygen vacancies increased from 1 per 32 to 1 per 16 oxygen atoms.[33] Guillemot et al.[42] reported that the low temperature vacuum annealing could create a controlled number of defects ranging from low concentration (<3% Ti^{3+}/Ti^{4+}) to high concentration (~21% Ti^{3+}/Ti^{4+}) at 323 and

573 K, respectively. Liu et al.[43] reported that concentration of both Ti^{3+} and oxygen vacancies are increased with H_2 treatment temperature up to 500 °C. This literature is consistent with our observation of the vacuum annealed sample and provides convincing evidence that different concentrations of oxygen vacancies are present in these TiO_2 NRbs.

5.6. XPS studies

XPS is a unique tool to investigate surface defects and chemical environment, because of its high sensitivity to surface. Evidence of oxygen vacancy related surface defect states in samples A500 and A500V is further confirmed from the XPS measurements. To investigate the surface defect states such as Ti^{3+} and F^{+}, Ti 2p and O 1s core levels were measured. **Fig. 5.6(a) and (b)** show the Ti 2p core level spectra of samples A500 and A500V, respectively. For the sample A500, the deconvolution of Ti 2p core level yields two major characteristic doublets for Ti $2p_{3/2}$ and $2p_{1/2}$, encompassing a set of two $2p_{3/2}$ peaks at 456.5 eV and 458.6 eV. The 456.5 eV peak is attributed to 3+, while the 458.6 eV peak is assigned to 4+ valence states of Ti, respectively. This result demonstrates that Ti^{4+} ions near oxygen vacancies occupy an electron from the oxygen vacancy cavity V_o and transform to Ti^{3+} ions yielding an F^{+} center. Similarly for the sample A500V, the deconvolution of Ti 2p core level yields two major characteristic doublets ($2p_{3/2}$, $2p_{1/2}$), encompassing a set of two $2p_{3/2}$ (456.2, 458.8 eV) and two $2p_{1/2}$ (461.1, 464.8 eV) peaks. The peaks at 458.8 eV and 464.8 eV are attributed to 4+ valence state for Ti $2p_{3/2}$ and $2p_{1/2}$, respectively, while 456.2 eV and 461.1 eV are assigned to 3+ valence state for Ti $2p_{3/2}$ and $2p_{1/2}$, respectively. This additional 3+ valence state of Ti $2p_{1/2}$ and the increased intensity of Ti^{3+} $2p_{3/2}$ for the sample A500V strongly indicates that high concentration of oxygen vacancies are created in the reduced atmosphere that results in the increase of Ti^{3+} states.[28] We noticed that after vacuum annealing, the Ti^{3+} concentration is nearly doubled and the intensity of Ti^{3+} band increases along with significant increase in intensity of O_H (hydroxyl group) and O_C (C-O bonds) peaks (shown in **Fig. 5.6(d)**) due to the dramatic increase in defects in A500V.

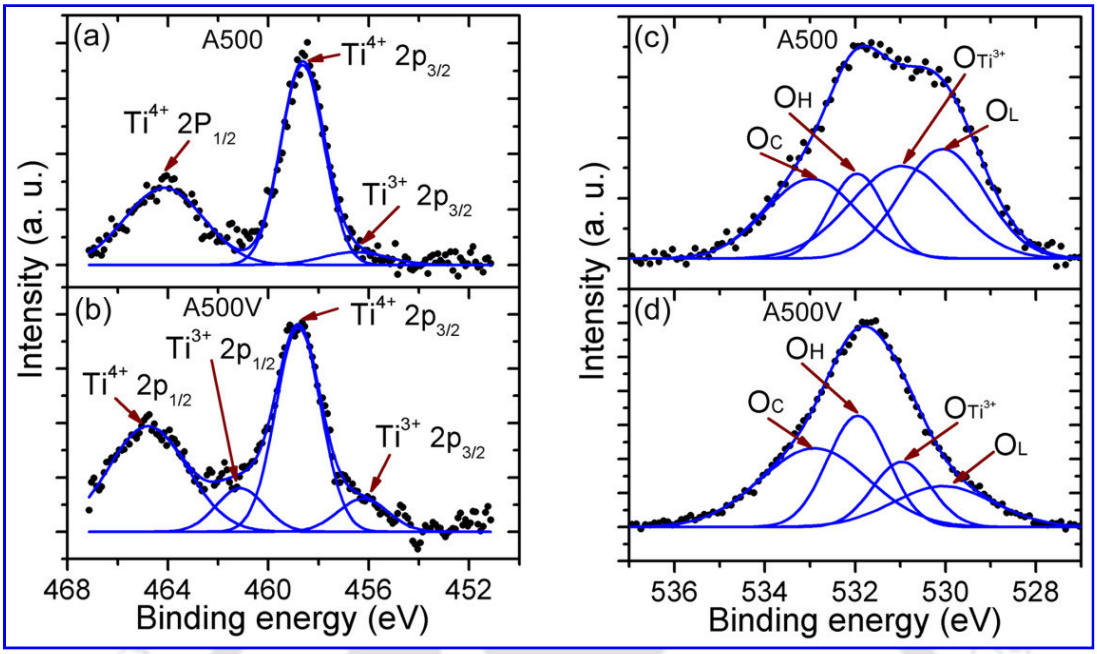

Fig. 5.6. XPS spectra: (a) and (b) show the Ti 2p core level spectra of samples A500 and A500V, respectively. (c) and (d) show the O 1s core level spectra of samples A500 and A500V, respectively. Symbols are for experimental data and the solid lines are fits with Gaussian peak shapes.

Fig. 5.6(c) and (d) show the O 1s spectra of samples A500 and A500V, respectively. Both the O 1s spectra exhibit an asymmetric curve and a broad shoulder to the higher binding energy side, indicating that several oxygen species are present in the near surface region.[44] The O 1s spectra can be deconvoluted by four symmetric Gaussian curves, similar to that reported in the literature.[44] The intense peak at about 530.1 eV is attributed to the oxygen in the TiO_2 crystal lattice (O_L), while the other three oxygen peaks can be assigned to the Ti–O bonds ($O_{Ti^{3+}}$, 531.0 eV), the hydroxyl group (O_H, 532.0 eV), and the C–O bonds (O_C, 532.9 eV), respectively.[44, 45] By comparing the contribution of each type of the oxygen species in the samples A500 and A500V, it is observed that the intensity of $O_{Ti^{3+}}$ increases along with increase in O_H and O_C peaks for the sample A500V compared to A500. This result reveals that the $O_{Ti^{3+}}$ defect concentration dramatically increases after vacuum annealing of A500, which increases the reactivity and binds more hydrogen and carbon as impurities. The Ti^{3+}% in Ti 2p spectra for A500 and A500V are 9% and 15%, respectively. The O_v% in O 1s spectra are 70% and 83% for A500 and A500V, respectively. Both A500 and A500V show

high concentration of oxygen vacancies. These results are fully consistent with the PL analysis and provide rather direct evidence that oxygen vacancies accompanied by Ti^{3+} are the dominant defects in the as-grown and vacuum annealed TiO_2 NRbs.

5.7. FTIR studies

FTIR spectroscopy has been employed to investigate the vibration modes of the TiO_2 crystal lattice, which are considerably affected by the presence of oxygen vacancies. **Fig. 5.7(a)** shows the FTIR spectra in transmission mode of as-synthesized nanostructures. The absorption peaks around 1600 and 3400 cm^{-1} are due to the adsorption of atmospheric water on the surface of the samples.[46] The vibration modes at 476, 774, and 980 cm^{-1} are assigned to TiO_2(B) phase[27, 47] and the vibration modes at 574 and 708 cm^{-1} are assigned to anatase TiO_2. The vibration mode at 476 cm^{-1} of TiO_2(B) slightly shifted to higher wave number is due to the phase transition from TiO_2(B) to mixed phase TiO_2(B)-anatase and anatase-rutile, as shown in the inset of **Fig. 5.7(a)**. **Fig. 5.7(b)** shows the FTIR spectra of as-synthesized sample A500 and vacuum annealed sample A500V. The characteristic vibration modes of TiO_2(B) phase is observed in vacuum annealed sample indicating that the sample retains its phase after vacuum annealing and it is consistent with the Raman analysis. However, an obvious red shift of vibration modes at 476 cm^{-1} to 470 cm^{-1} is observed after vacuum annealing and it is attributed to the higher concentration of oxygen vacancies induced by vacuum annealing. A similar shift is reported in Co doped TiO_2 system and it was suggested that the shift was due to the oxygen vacancy.[48] Further, we noticed that the vibration mode at 774 cm^{-1} is blue shifted and 980 cm^{-1} is red shifted in the vacuum annealed sample. Note that the vibration modes at 476 and 980 cm^{-1} are due to the O-Ti-O bending and Ti-O stretching vibrations, respectively, while the 774 cm^{-1} mode is due to O-Ti-O bending and Ti-O stretching vibrations in TiO_2(B).[49] The shifting of the vibration bands is expected due to the presence of oxygen vacancies. We also observed the shift of vibration modes at 574 and 708 cm^{-1} towards a lower frequency in the as-synthesized anatase sample D900 compared to the precursor anatase TiO_2 powder, as shown in **Fig. 5.7(a)**. Such a shift is expected due to oxygen vacancies in our as-synthesized samples, which manifest in interesting room temperature ferromagnetism discussed below.

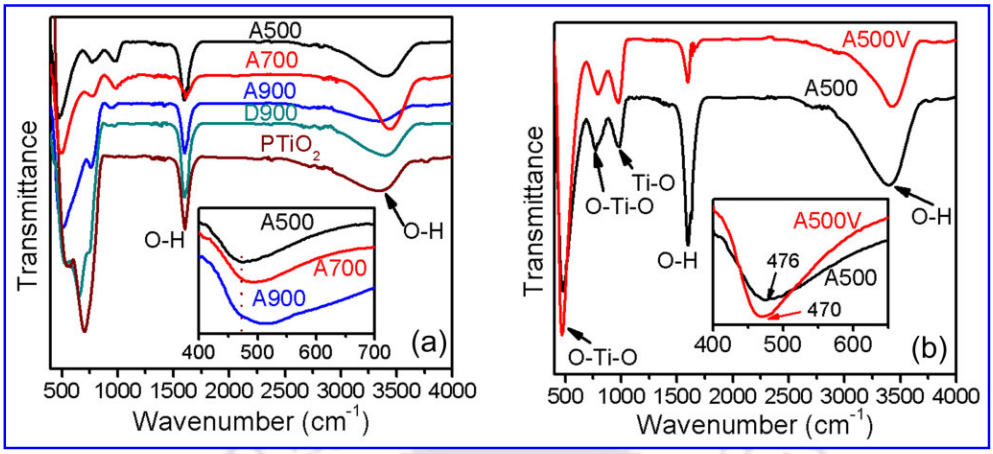

Fig. 5.7. FTIR spectra: (a) samples A500, A700, A900, D900, and precursor TiO_2; (b) samples A500 and A500V. The inset in (a) and (b) show the shifting of the vibration modes.

5.8. Magnetization studies

The magnetic properties of as-synthesized samples were investigated using VSM. The field dependent magnetic (M–H) measurements are shown in **Fig. 5.8**. **Fig. 5.8(a)** shows a clear ferromagnetic hysteresis loops for samples D500, D900, and G500. The samples D500 and D900 show large magnetic moments compared to sample G500. Moreover, D900 shows a higher magnetic moment than that of D500. **Fig. 5.8(b)** shows the M–H loops of the samples A500, A700 and A900. These samples show hysteresis loops at low field, but lacks the saturation magnetization, perhaps due to paramagnetic contribution from the conduction electron.[50] Note that the magnetic moment is relatively high for A700 and this may be due to the relatively large concentration of O_v or may be related to nanobrick-like surface morphology of A700 and/or due to mixed phase of TiO_2(B)–anatase. It has been reported that the FM is sensitive to the shape and size of the nanostructures.[20, 51, 52] Note that the samples (D500, D900, G500) grown at 180 °C after 24 h and 48 h reactions are nanoporous NRbs with nanobrick-like structures on the surface. Such complex structures may contain a large concentration of defects, supported by our PL analysis. The concentration of oxygen vacancies are found to depend on the different surface morphologies and size of the nanostructures, which is the reason for the observed different magnetic moments. Nanosize TiO_2 usually shows weak FM at RT and the FM depends very much on the synthesis

procedure, due to the different defects, especially the oxygen vacancies in TiO_2 nanomaterials. One of the most important reasons of relatively strong ferromagnetism in our samples may come from the formation of porous like structures, since we are using ethylene glycol as a cosolvent which has chelating properties. Due to the chelating properties of ethylene glycol, it forms several bonds with metal ions and form cage like structures which helps the formation of porous structure creating more oxygen vacancies. Further, it has been reported that the oxygen vacancies induce lattice distortion in rutile TiO_2 and induces strong FM in undoped TiO_2 films due to charge redistribution.[23] The magnitude of the magnetic moment in the rutile phase was predicted to be about four times higher than that in anatase TiO_2. This is consistent with the observation of highest magnetic moment seen in sample D900 with a mixed rutile-anatase phase as compared to D500 and G500 with TiO_2(B) phase.

It is well known that the structure of TiO_2 is very sensitive to oxygen and can be easily reduced under an oxygen deficient environment. Therefore, the sample A500 was annealed at 300 °C under moderate vacuum (1.2×10^{-2} mbar) in order to induce a higher concentration of oxygen vacancies in the sample. Interestingly, the vacuum annealed sample A500V shows enhanced ferromagnetism with a well-defined hysteresis loop having saturation magnetization (M_s) of 0.191 emu g^{-1}, remanent (M_r) of 0.02 emu g^{-1} and coercive field (H_c) of 99 Oe, as shown in **Fig. 5.8(c)**. Such enhancement of FM in oxygen deficient TiO_2 NRbs strongly suggests that RTFM and concentration of oxygen vacancies are directly correlated. Indeed the samples exhibiting a high intensity of visible PL (see inset of **Fig. 5.5(a)**) only show clear ferromagnetic hysteresis loops with saturation magnetization plateau. Note that the observed M_s at room temperature (RT) in our undoped TiO_2 NRbs is more than three times higher than that reported for Fe and N co-doped TiO_2 nanorods[53] and other reported literatures.[27, 53, 54] Achievement of such a high magnetic moment in defect engineered undoped TiO_2 is remarkable and our studies provide clinching evidence that oxygen vacancies mediate the ferromagnetic interaction. The magnetization parameters for different samples are listed in **Table 5.1**. **Fig. 5.8(d)** shows the M-H measurement of B500, B700 and B900 samples. The M-H curve indicates almost paramagnetic nature (or very weak ferromagnetic behavior at low field). Note that these samples show the Ti interstitial-rich defects with negligible O_v defects as observed from the PL studies (see **Fig. 4.5(d)**, *Chapter 4*). This result again supports the oxygen vacancy mediated FM in undoped TiO_2

nanostructures system and further indicates that Ti interstitial defects are not responsible for the observed FM in our TiO_2 NRbs.

Table 5.1. Magnetization parameters of the as-synthesized and vacuum annealed samples: saturation magnetization (M_s), remanent magnetization (M_r), and Coercive field (H_c) were determined from M–H loops; M_0 , m_{eff}, χ_m, N were evaluated from fitting of the M–H curve with BMP model.

Sample name	M_s (emu/g)	M_r (emu/g)	H_c (Oe)	M_0 (emu/g)	$m_{eff} \times 10^{-17}$(emu)	$\chi_m \times 10^{-6}$ (cgs)	$N \times 10^{15}$ (cm^{-3})
A500V	0.191	0.02	99	0.190	8.86	1.32	8.83
D500	0.061	0.004	99	0.070	6.21	0.22	4.63
D900	0.109	0.007	87	0.097	8.28	2.17	4.77
G500	0.054	0.003	90	0.048	6.54	1.02	3.02

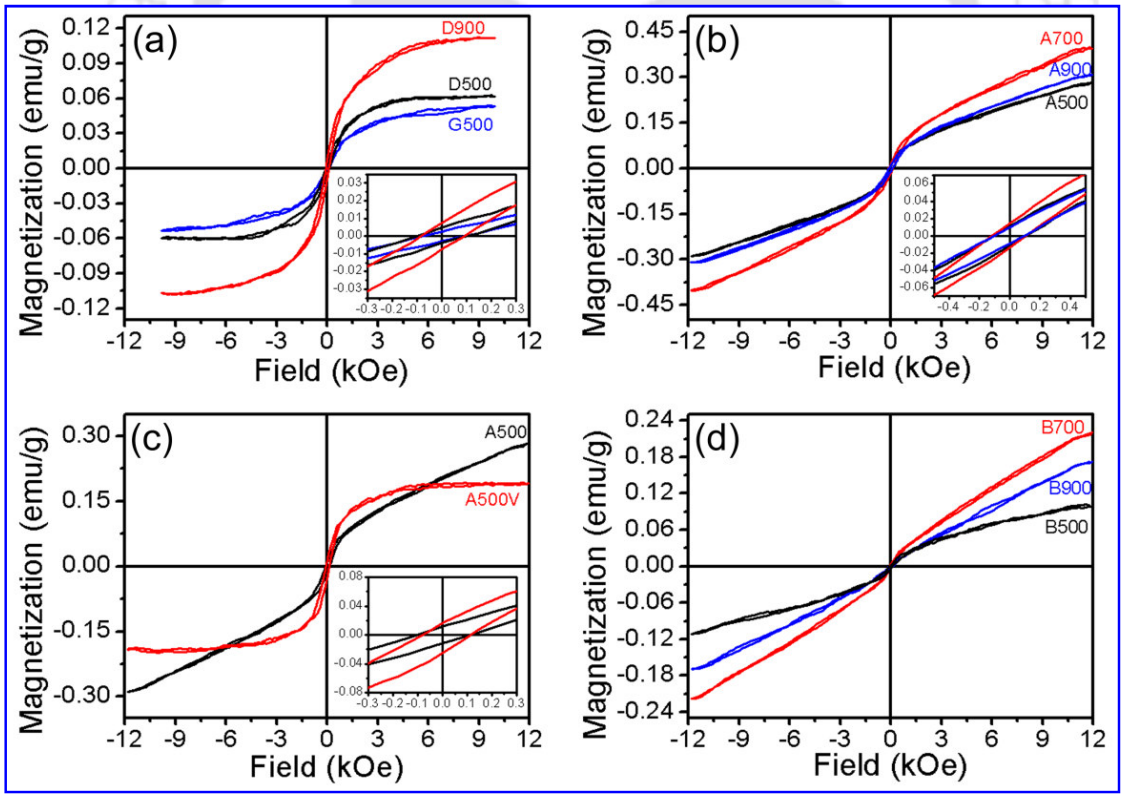

Fig. 5.8. Magnetic field versus magnetization (M–H) loop at room temperature showing hysteresis in as-synthesized samples: (a) D500, D900 and G500; (b) A500, A700 and A900; (c) A500 and A500V; (d) B500, B700 and B900. The insets show the magnified M–H loop showing clear ferromagnetic hysteresis behaviour.

It is understood that for use in a wide range of applications without temperature control, the ferromagnet should have a transition Curie temperature (T_C) enough above RT (300 K). **Fig. 5.9** shows the temperature dependent magnetization (M-T) of the sample G500 in the temperature range 290 to 860 K. Since the effect of high temperature VSM measurement in atmospheric conditions is equivalent to the post annealing of the as-grown samples in air that can destroy the ferromagnetic coupling, we performed the high temperature VSM measurement in a nitrogen atmosphere. From the differential plot of the M-T curve, we obtained a T_C at ~799 K. Interestingly, the gradual increase in magnetization from 290 K to around 334 K is observed in the M-T curve,[28] as shown in the inset of **Fig. 5.9**. This indicates that the oxygen vacancies are increased during the early stages of the heating process in a nitrogen atmosphere and these defects contribute to the observed FM. Note that defect mediated bound magnetic polaron (BMP) model has been invoked to explain the RTFM. Due to increased vacancy concentration, more BMPs are likely to form, which include electrons locally trapped by the oxygen vacancy, giving rise to gradual increase in magnetization. The thermal fluctuations of the localized spins may have comparatively less effect in this temperature range. Very recently, Tian et al.[55] reported nearly temperature-independent saturation magnetization up to 600 K, which strongly favored the BMP model. The strength of exchange interaction is stronger in nanostructured magnetic semiconductors where the mean distance between the localized spins is small, which may enhance the thermal stability.

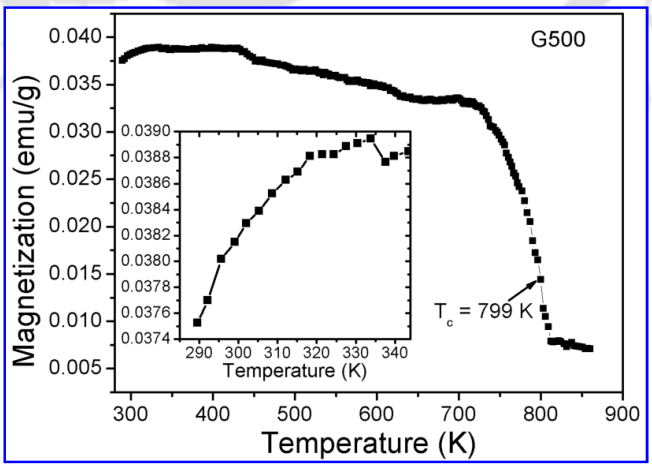

Fig. 5.9. Temperature dependent magnetization (M–T) curve of sample G500, showing a ferromagnetic to paramagnetic transition at 799 K.

5.9. Origin of ferromagnetism

At the present time, there is an incomplete understanding on the origin of ferromagnetism in an undoped TiO_2 semiconductor, whether the Ti vacancy or oxygen vacancy defects are responsible for the observed FM. If the Ti vacancy is the reason for the observed FM in our samples, then ferromagnetic ordering is expected to decrease after vacuum annealing. However, the enhanced magnetic moment with clear saturation magnetization confirms that the FM in our samples is primarily due to the oxygen vacancy, since no other impurities are present. Several spectral features, i.e., relative shift (B_g mode at 194 cm^{-1}) and reduction in intensity (A_g mode at 147 cm^{-1}) of Raman modes, systematic shift in infrared band at 476 cm^{-1} towards lower frequency, oxygen vacancy related strong visible PL emission, high oxygen vacancy and Ti^{3+} concentrations observed from XPS spectra and stronger ferromagnetic ordering in vacuum annealed sample strongly suggest that the observed FM in undoped TiO_2 NRbs is induced by oxygen vacancies. The presence of an oxygen vacancy on the surface of TiO_2 locally traps the electrons forming F center and one of the electrons tends to occupy the nearby localized Ti 3d orbit and convert Ti^{4+} ions to Ti^{3+} ions, yielding F^+ center. The electrons in F^+ center localize and may form bound magnetic polarons by ordering the Ti^{3+} ($3d^1$) electron spin neighboring the oxygen vacancies, thereby gaining exchange energy. The s-d exchange interaction between the $1s^1$ electron spin in the F^+ center which is localized in the vicinity of $3d^1$ electron spin of Ti^{3+} ions within an orbit around oxygen vacancies favors long range FM.[28] The electrons in doubly occupied oxygen vacancies (F center) form $1s^2$ state, which only mediates weak antiferromagnetic exchange.[56] Thus the formation of BMP, which includes electrons locally trapped by oxygen vacancies, with the trapped electron in the F^+ center occupying an orbital overlapping with the unpaired electron ($3d^1$) of Ti^{3+} is proposed to explain the origin of FM observed in our samples.[28]

Theoretical studies suggested that oxygen vacancies can cause an obvious change of band structure of the host oxides and makes a significant contribution to the FM.[56, 57] The absorption edges of as-synthesized NRbs are red shifted compared to the precursor TiO_2 powder, which may increase the overlapping of oxygen vacancies with the empty conduction band and favor the observed FM. Note that the precursor TiO_2 powder did not show any trace of FM, despite the presence of a large concentration of oxygen vacancies as evidenced by a strong visible PL band (integrated PL intensity of 2840.2 arb. unit). Note that integrated

visible PL intensities in A500V (2555.2 arb. unit) and precursor TiO_2 powder (2840.2 arb. unit) are comparable. Thus, concentration of defects such as oxygen vacancies alone does not decide the magnitude of magnetic moment. Our results suggest that the defect environment (i.e., the distribution of point defects and formation of F^+ and Ti^{3+} defects and their interactions) and the surface morphology of the NRbs, in particular the nanopores and nanobrick like structures, are critical ingredients for the buildup of measurable ferromagnetic interaction.

Note that the relatively weak ferromagnetic hysteresis loops for the samples A500, A700, A900 observed at low magnetic field may be due to oxygen vacancies and the linear M-H behavior observed at high field without any saturation magnetic moment up to 12 kOe may be due to the conduction band electrons.[50] When the oxygen content of the unit cell is decreased, ferromagnetism is dominant. Interestingly, we notice a clear hysteresis loop with enhanced magnetic properties in terms of M_s, M_r and H_c in the vacuum annealed sample owing to increased oxygen vacancy concentration that may increase the BMP density. This seems to support the percolation model of BMP developed by Kaminski and Das Sarma and Coey et al.[56, 58] Our systematic study shows that the oxygen vacancy defect constituted BMP is one of the most promising candidates to manifest the RTFM in this system. Within the BMP model, the greater density of the oxygen vacancy helps to produce more BMP which yields a greater overall volume occupied by BMP, leading to an overlap of BMPs and enhancing ferromagnetic behavior. This evolution is observed in our case, enhancing the ferromagnetic nature in the post-growth vacuum annealed sample indicating that a large density of defects overcomes the percolation threshold and establishes a long-range magnetic ordering.

For a more quantitative understanding about the suitability of the BMP model and its relationship to the oxygen vacancy concentration as revealed from PL analyses, we attempted to fit the observed *M versus H* data to the BMP model by following McCabe et al.[59] According to the BMP model, the measured magnetization can be fitted to the relation

$$M = M_0\, L(x) + \chi_m H, \qquad (5.5)$$

where the first term is from BMP contribution and the second term is due to paramagnetic matrix contribution. Here, $M_0 = Nm_s$, N is the number of BMP involved (per gram) and m_s is the effective spontaneous moment per BMP. $L(x) = coth(x) - 1/x$ is the Langevin

function with $x = m_{eff}H/k_BT$, where m_{eff} is the true spontaneous moment per BMP, and at higher temperature it can be approximated to $m_s = m_{eff}$. We have analyzed the M–H curve by using eqn (5.5). The parameters M_0 , m_{eff}, and χ_m are free variable in the fitting process. The experimental data along with the fitted data are shown in **Fig. 5.10** for the samples D900 and G500. We notice that the fitted data closely follows the experimental data and the fitted parameters are tabulated in **Table 5.1**. The total BMP magnetization M_0 values are found to be in the order of 0.048–0.19 emu g^{-1}. The paramagnetic susceptibility χ_m is found to be of the order of 10^{-6} cgs unit and its value marginally changes with different growth conditions. The spontaneous moment per BMP, m_{eff} is found to be in the order of 10^{-17} emu. By assuming $m_s = m_{eff}$, we have estimated the concentration of BMP, which was found to be in the order of 10^{16} cm^{-3} (see **Table 5.1**). Note that BMP concentration is highest in A500V, followed by D900, D500 and G500. Interestingly, we found a strikingly linear correlation between the BMP concentration and the integrated PL intensity due to oxygen vacancies, as shown in **Fig. 5.10(c)**. The symbols are for calculated BMP density from the fitting of experimental data and the solid line is a linear fit to the experimental data. It implies a one to one correlation of the BMP density with oxygen vacancy concentration. Despite the fact that quantitative estimation of defects is rarely possible from the PL intensity comparison due to possible presence of nonradiative channels, our observed correlation is remarkable. This is the first time such a linear relation has been found between the densities of BMP and oxygen vacancies. This provides a more conclusive evidence that observed RTFM is directly induced by oxygen vacancies.

Recently, in Ag doped ZnO system, He et al.[60] fitted the experimental M–T curve with the BMP model and the concentration of BMP was found to be of the similar order (~$10^{15}cm^{-3}$). However, the reported T_C was relatively higher (995 K), though the feature of the M-T curve was identical to our observation. Since the polarons we have described in this system are bound to oxygen vacancies, the term bound magnetic polaron is justified. Interestingly, the BMP remains localized over a wide temperature range, presumably due to strong localization provided by the defect site and stability of these defects. Note that the as-prepared samples have undergone high temperature calcination that indicates high thermal stability of the oxygen vacancies and a large concentration of oxygen vacancies may aid to form even small clusters of vacancies that can provide higher localization of the charges

nvolved in the exchange interaction. However, more studies are required to pinpoint the exact mechanism of high temperature FM. Nevertheless, besides the established applications of TiO_2 nanostructures, these results open up the possibility of defect engineered TiO_2 nanostructures as potential platform for future spintronic and magneto-optic devices.

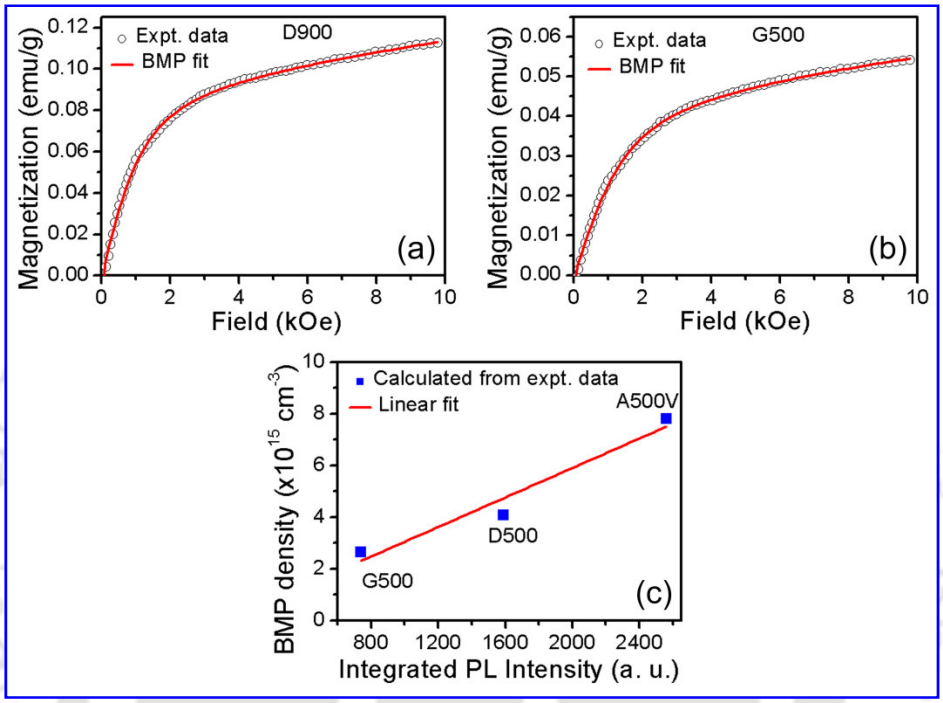

Fig. 5.10. Initial portion of the M–H curve fitted with BMP model (eqn (5.5)) for samples (a) D900 and (b) G500. Symbols are for experimental data and the solid line is a fit with the BMP model. Extracted parameters are listed in **Table 5.1**. (c) Integrated PL intensity versus calculated BMP density showing a nearly linear behavior.

5.10. Conclusions

We successfully prepared undoped TiO_2 nanoporous NRbs under different growth conditions and investigated the origin of room temperature ferromagnetism in this novel system using several experimental tools. Micro-Raman studies show systematic shift and decrease in intensity of $E_g(1)$ and A_g (at 147 cm^{-1}) Raman modes of anatase and $TiO_2(B)$, respectively, in as-synthesized and vacuum annealed samples. The UV-visible absorption studies support the oxygen vacancy defects related band gap narrowing in as-synthesized samples. The enhanced

intensity of oxygen vacancy related peak in the PL spectra, large concentration of O_v and Ti^{3+} states revealed from XPS, shifting of infrared vibration modes at 476 cm^{-1} towards the lower frequency after vacuum annealing confirm the presence of large concentration of oxygen vacancies and these are shown to be responsible for the enhanced FM in as-grown and vacuum annealed sample. The observed RTFM is explained on the basis of a BMP model and extracted density of BMP is shown to directly scale with the integrated PL intensity that arises from oxygen vacancies. Thus, our results provide convincing evidence for oxygen vacancy induced strong ferromagnetism at and above room temperature in the undoped TiO_2 nanoporous NRbs. These findings not only help to gain better insight into the defect engineering of RTFM in undoped TiO_2, but also constitute an important step for the development of practical nanospintronic devices which can be operated at and above RT.

References

1. S. A. Wolf, D. D. Awschalom, R. A. Buhrman, J. M. Daughton, S. von Molnár, M. L. Roukes, A. Y. Chtchelkanova and D. M. Treger, Science **294**, 1488-1495 (2001).
2. H. Ohno, Science **281**, 951-956 (1998).
3. Y. Matsumoto, M. Murakami, T. Shono, T. Hasegawa, T. Fukumura, M. Kawasaki, P. Ahmet, T. Chikyow, S.-y. Koshihara and H. Koinuma, Science **291**, 854-856 (2001).
4. B. Pal and P. K. Giri, Journal of Applied Physics **108**, 084322 (2010).
5. X. Liu, J. Iqbal, Z. Wu, B. He and R. Yu, The Journal of Physical Chemistry C **114**, 4790-4796 (2010).
6. G. Z. Xing, J. B. Yi, D. D. Wang, L. Liao, T. Yu, Z. X. Shen, C. H. A. Huan, T. C. Sum, J. Ding and T. Wu, Physical Review B **79**, 174406 (2009).
7. B. Santara, B. Pal and P. K. Giri, Journal of Applied Physics **110**, 114322-114327 (2011).
8. J. Y. Kim, J. H. Park, B. G. Park, H. J. Noh, S. J. Oh, J. S. Yang, D. H. Kim, S. D. Bu, T. W. Noh, H. J. Lin, H. H. Hsieh and C. T. Chen, Physical Review Letters **90**, 017401 (2003).

9. J. Xu, S. Shi, L. Li, X. Zhang, Y. Wang, X. Chen, J. Wang, L. Lv, F. Zhang and W. Zhong, Journal of Applied Physics **107**, 053910 (2010).
10. K. Griffin Roberts, M. Varela, S. Rashkeev, S. T. Pantelides, S. J. Pennycook and K. M. Krishnan, Physical Review B **78**, 014409 (2008).
11. P. Mohanty, N. C. Mishra, R. J. Choudhary, A. Banerjee, T. Shripathi, N. P. Lalla, S. Annapoorni and R. Chandana, Journal of Physics D: Applied Physics **45**, 325301 (2012).
12. T. Thomas, G. Milan, S. Gisela, J. Gerhard, B. Sebastian and G. Eberhard, New Journal of Physics **10**, 055009 (2008).
13. M. Gacic, G. Jakob, C. Herbort, H. Adrian, T. Tietze, S. Brück and E. Goering, Physical Review B **75**, 205206 (2007).
14. Q. Xu, H. Schmidt, L. Hartmann, H. Hochmuth, M. Lorenz, A. Setzer, P. Esquinazi, C. Meinecke and M. Grundmann, Applied Physics Letters **91**, 092503 (2007).
15. K. P. Sudhir and R. J. Choudhary, Journal of Physics: Condensed Matter **23**, 276005 (2011).
16. N. Hoa and D. Huyen, Journal of Materials Science: Materials in Electronics **24**, 793-798 (2013).
17. N. H. Hong, J. Sakai, N. Poirot and V. Brizé, Physical Review B **73**, 132404 (2006).
18. M. Venkatesan, C. B. Fitzgerald and J. M. D. Coey, Nature **430**, 630-630 (2004).
19. N. H. Hong, N. Poirot and J. Sakai, Physical Review B **77**, 033205 (2008).
20. X. Xu, C. Xu, J. Dai, J. Hu, F. Li and S. Zhang, The Journal of Physical Chemistry C **116**, 8813-8818 (2012).
21. A. Sundaresan and C. N. R. Rao, Nano Today **4**, 96-106 (2009).
22. H. Peng, J. Li, S.-S. Li and J.-B. Xia, Physical Review B **79**, 092411 (2009).
23. K. Dongyoo, H. Jisang, P. Young Ran and K. Kwang Joo, Journal of Physics: Condensed Matter **21**, 195405 (2009).
24. A. K. Rumaiz, B. Ali, A. Ceylan, M. Boggs, T. Beebe and S. Ismat Shah, Solid State Communications **144**, 334-338 (2007).
25. H. Li, Y. Zeng, T. Huang and M. Liu, Journal of Nanoparticle Research **14**, 1-6 (2012).

26. H.-m. Li, M. Liu, Y.-s. Zeng and T.-c. Huang, Journal of Central South University of Technology **17**, 239-243 (2010).
27. S. K. S. Patel and N. S. Gajbhiye, Solid State Communications **151**, 1500-1503 (2011).
28. B. Santara, P. K. Giri, K. Imakita and M. Fujii, Nanoscale **5**, 5476-5488 (2013).
29. J. C. Parker and R. W. Siegel, Applied Physics Letters **57**, 943-945 (1990).
30. W. F. Zhang, Y. L. He, M. S. Zhang, Z. Yin and Q. Chen, Journal of Physics D: Applied Physics **33**, 912 (2000).
31. D. Yang, H. Liu, Z. Zheng, Y. Yuan, J.-c. Zhao, E. R. Waclawik, X. Ke and H. Zhu, Journal of the American Chemical Society **131**, 17885-17893 (2009).
32. I. Justicia, P. Ordejón, G. Canto, J. L. Mozos, J. Fraxedas, G. A. Battiston, R. Gerbasi and A. Figueras, Advanced Materials **14**, 1399-1402 (2002).
33. F. Zuo, L. Wang, T. Wu, Z. Zhang, D. Borchardt and P. Feng, Journal of the American Chemical Society **132**, 11856-11857 (2010).
34. J. Wang, Z. Wang, B. Huang, Y. Ma, Y. Liu, X. Qin, X. Zhang and Y. Dai, ACS Applied Materials & Interfaces **4**, 4024-4030 (2012).
35. S. Hoang, S. P. Berglund, N. T. Hahn, A. J. Bard and C. B. Mullins, Journal of the American Chemical Society **134**, 3659-3662 (2012).
36. J. Shi, J. Chen, Z. Feng, T. Chen, Y. Lian, X. Wang and C. Li, The Journal of Physical Chemistry C **111**, 693-699 (2006).
37. N. Serpone, The Journal of Physical Chemistry B **110**, 24287-24293 (2006).
38. N. Serpone, D. Lawless and R. Khairutdinov, The Journal of Physical Chemistry **99**, 16646-16654 (1995).
39. S. T. Kshirsager, S. B. Ogale, S. R. Sainkar, S. I. Patil and L. V. Saraf, International Journal of Modern Physics B **12**, 2635-2647 (1998).
40. Y. Lei, L. D. Zhang, G. W. Meng, G. H. Li, X. Y. Zhang, C. H. Liang, W. Chen and S. X. Wang, Applied Physics Letters **78**, 1125-1127 (2001).
41. M. Yang, W. Liu, J.-L. Sun and J.-L. Zhu, Applied Physics Letters **100**, 043106 (2012).
42. F. Guillemot, M. C. Porté, C. Labrugère and C. Baquey, Journal of Colloid and Interface Science **255**, 75-78 (2002).

43. H. Liu, H. T. Ma, X. Z. Li, W. Z. Li, M. Wu and X. H. Bao, Chemosphere **50**, 39-46 (2003).
44. J. Zhuang, S. Weng, W. Dai, P. Liu and Q. Liu, The Journal of Physical Chemistry C **116**, 25354-25361 (2012).
45. J. C. Yu, J. Yu, H. Y. Tang and L. Zhang, Journal of Materials Chemistry **12**, 81-85 (2002).
46. T. M. H. Costa, M. R. Gallas, E. V. Benvenutti and J. A. H. da Jornada, The Journal of Physical Chemistry B **103**, 4278-4284 (1999).
47. S. Chatterjee, K. Bhattacharyya, P. Ayyub and A. K. Tyagi, The Journal of Physical Chemistry C **114**, 9424-9430 (2010).
48. K. Das, S. N. Sharma, M. Kumar and S. K. De, The Journal of Physical Chemistry C **113**, 14783-14792 (2009).
49. M. Ben Yahia, F. Lemoigno, T. Beuvier, J.-S. Filhol, M. Richard-Plouet, L. Brohan and M.-L. Doublet, The Journal of Chemical Physics **130**, 204501 (2009).
50. A. Sundaresan, R. Bhargavi, N. Rangarajan, U. Siddesh and C. N. R. Rao, Physical Review B **74**, 161306 (2006).
51. J. M. D. Coey, P. Stamenov, R. D. Gunning, M. Venkatesan and K. Paul, New Journal of Physics **12**, 053025 (2010).
52. Y. Li, Y. Li and T. Wang, Journal of Nanomaterials **2012**, 897203 (2012).
53. H. Wang, J. Wei, R. Xiong and J. Shi, Journal of Magnetism and Magnetic Materials **324**, 2057-2061 (2012).
54. S. K. S. Patel and N. S. Gajbhiye, Journal of Magnetism and Magnetic Materials **330**, 21-24 (2013).
55. Y. Tian, Y. Li, M. He, I. A. Putra, H. Peng, B. Yao, S. A. Cheong and T. Wu, Applied Physics Letters **98**, 162503 (2011).
56. J. M. D. Coey, M. Venkatesan and C. B. Fitzgerald, Nature Materials **4**, 173-179 (2005).
57. J. E. Jaffe, T. C. Droubay and S. A. Chambers, Journal of Applied Physics **97**, 073908 (2005).
58. A. Kaminski and S. Das Sarma, Physical Review Letters **88**, 247202 (2002).

59. G. H. McCabe, T. Fries, M. T. Liu, Y. Shapira, L. R. Ram-Mohan, R. Kershaw, A. Wold, C. Fau, M. Averous and E. J. McNiff, Physical Review B **56**, 6673-6680 (1997).

60. M. He, Y. F. Tian, D. Springer, I. A. Putra, G. Z. Xing, E. E. M. Chia, S. A. Cheong and T. Wu, Applied Physics Letters **99**, 222511 (2011).

Chapter 6

Microscopic Origin of Lattice Contraction and Expansion in Undoped Rutile TiO_2 Nanostructures

To understand the enhanced properties of the TiO_2 nanostructures (NS), successful fabrication of a wide range of materials is significant where the morphologies can be precisely controlled with designed functionalities. In particular, lattice parameters are very important structural characteristics and thus their variations directly affect the properties of nanomaterials and the relevant applications. The control of lattice parameters through the intrinsic defects may provide new routes to achieving novel functionalities in advanced materials that can be tailored for future technological applications. In this chapter, we have investigated the microscopic origin of lattice expansion and contraction in undoped rutile TiO_2 nanostructures by employing several structural and optical spectroscopic tools. Depending on the growth conditions and post growth annealing, lattice contraction and expansion are observed in the nanostructures and it is found to correlate with the nature and density of intrinsic defects in rutile TiO_2.

6.1. Introduction

TiO_2 is considered to be one of the most useful semiconducting metal oxides for applications ranging from sensors to energy storage, and photocatalysis. The unubiquitous presence of intrinsic point defects such as oxygen vacancies (O_v) and Ti interstitial (Ti_i) in TiO_2 play a key role in enhancing the electrical, chemical and optical properties of the materials at nanoscale. In particular, lattice parameters are very important structural characteristics and thus their variations directly affect the properties of nanomaterials and the relevant applications. Therefore, a large number of studies concentrated on the size dependent

variation of lattice parameters and subsequently studied the linear/nonlinear expansion/contraction of TiO_2[1-3] and other metal-oxide nanomaterials.[4, 5]

It is well-established that the reduction of particle size below a finite size at the nanoscale causes variations in lattice parameters.[1-4, 6, 7] However, the origin of size induced changes in lattice volume of TiO_2 nanomaterials has been a subject of debate. Most of the metal-oxides nanocrystals[4, 5, 8] and in particular rutile TiO_2[1, 6] and anatase TiO_2[3] exhibit lattice expansion as the crystalline size reduces in contrast to the lattice contraction in metal nanoparticles (NPs)[9, 10] and is considered to be a general characteristic of all metal-oxide nanomaterials. On the other hand, lattice contraction has been reported[2] in anatase TiO_2 NPs as the particle size reduces and it was more pronounced for the crystallite sizes below ~15 nm. From the thermodynamic point of view, the lattice expansion for smaller particle sizes in oxide materials is quite surprising, since surface stresses would cause small particles to compress due to higher surface curvature as is observed in non-oxide nanomaterials such as Si,[11] ZnS[12] and CdSe[13] etc. Therefore, the mechanism of lattice expansion/contraction in TiO_2 is not understood clearly. The existing reports suggest contradicting results on the size dependence of the lattice contraction/expansion in TiO_2 and other oxide materials at the nanoscale.

In CeO_2 nanocrystals, Deshpande et al.[4] proposed that oxygen vacancy and accompanying valence reduction from Ce^{4+} to Ce^{3+} might cause lattice expansion as the particle size decreases, while Li et al.[2] found no oxygen vacancy in anatase TiO_2 NPs in their size-induced changes in lattice volume. Swamy et al.[3] reported small lattice expansion in anatase TiO_2 NPs and it was attributed to increased Ti vacancy and lattice strain. A correlation between Ti vacancy abundance and lattice volume increase in rutile TiO_2 was suggested by Kuznetsov et al.[6] A surface defect dipole model was proposed by Li et al.[1] to explain the linear lattice expansion in rutile TiO_2. In case of $BaTiO_3$, an increase in iconicity of Ti ions with particle size reduction was proposed as a possible reason for the lattice expansion.[5] These studies indicate that there exists substantial controversy regarding the origin of lattice expansion/contraction in TiO_2 and other metal oxide semiconductors. Using *ab-initio* calculations, Iddir et al.[14] predicted lattice expansion in rutile TiO_2 via Ti_i and O_v defects. However, there is no experimental evidence of Ti_i and O_v defects in rutile TiO_2

causing the lattice expansion. Hence, a thorough understanding on the microscopic origin of lattice parameter variation through experimental studies is essential to resolve the controversy.

Most of the studies reported till date on the size-dependent lattice expansion/ contraction in TiO_2 are for extremely small size NPs/ nanocrystals less than ~15 nm in anatase[2] and less than ~27 nm in rutile TiO_2.[1, 6] So, it has been very challenging to identify the individual contribution of quantum confinement, strain, intrinsic defects (i. e., O_v, Ti_i, Ti vacancy etc.) and other surface defects towards the lattice parameter variation in TiO_2 NS. In this work, we report on the variation of lattice parameters in hydrothermally synthesized rutile TiO_2 nanorods (NRs), nanopillars and nanoflowers of comparatively large sizes and find its correlation with the O_v, Ti_i and O interstitial (O_i) defects in TiO_2.[1, 2, 6] Lattice contraction and expansion are observed in the as-grown NS, depending upon the growth temperature, reaction duration and stirring during the growth, which is due to the different concentrations and types of intrinsic defects associated with the materials.[15]

6.2. Growth and processing of TiO_2 nanostructures

Titanium butoxide (Sigma-Aldrich) and 35% HCl (Merck) were used as the precursor material. Doubly distilled deionized (DI) water was used during all the experiments. In a typical synthesis, 1 ml of titanium butoxide is added to 60 ml of mixed DI water and 35% HCl (1:1) with constant stirring for 15 min. Afterwards, the mixed solution was transferred into a Teflon-lined autoclave and the temperature inside the autoclave was monitored and maintained at 150-190 °C under autogenous pressure for 12- 48 h. Some of the samples were grown at 150 °C under constant magnetic stirring at 250 rpm during the reactions. The formed precipitates were obtained and finally heat treated at 500 °C for 4 h in air. For convenience of discussion, the TiO_2 NS grown at 150 °C are categorized as 'A' and samples are named as A12, A18, A48 for the growth duration of 12 h, 18 h and 48 h, respectively. Samples grown at 170 and 190 °C after 18 h are termed as B18 and C18, respectively. Sample grown at 150 °C after 18 h reaction under stirring throughout the reaction is termed as A18s. The details of the samples nomenclature are shown in **Table 6.1**.

6.3. Structural studies

XRD patterns: The XRD patterns of as-synthesized samples are shown in **Fig. 6.1**, where all the peaks correspond to rutile TiO_2 phase. The XRD patterns of A12, A18 and A48 are shown in **Fig. 6.1(a)**. It is observed that with the increase in reaction duration, the diffraction peaks are shifted to higher angle (2θ). The inset of **Fig. 6.1(a)** shows the corresponding shift and broadening of (110) peak. Sample A12 grown for lower reaction duration shows higher broadening and lower intensity than those of A48. **Fig. 6.1(b)** shows the XRD patterns of A18, B18 and C18. As the growth temperature increases, the diffraction peaks are systematically shifted to lower 2θ values (**Fig. 6.1(b)**). The magnified view of (110) peak shows a clear shift and broadening of line shape with different growth temperatures (inset of

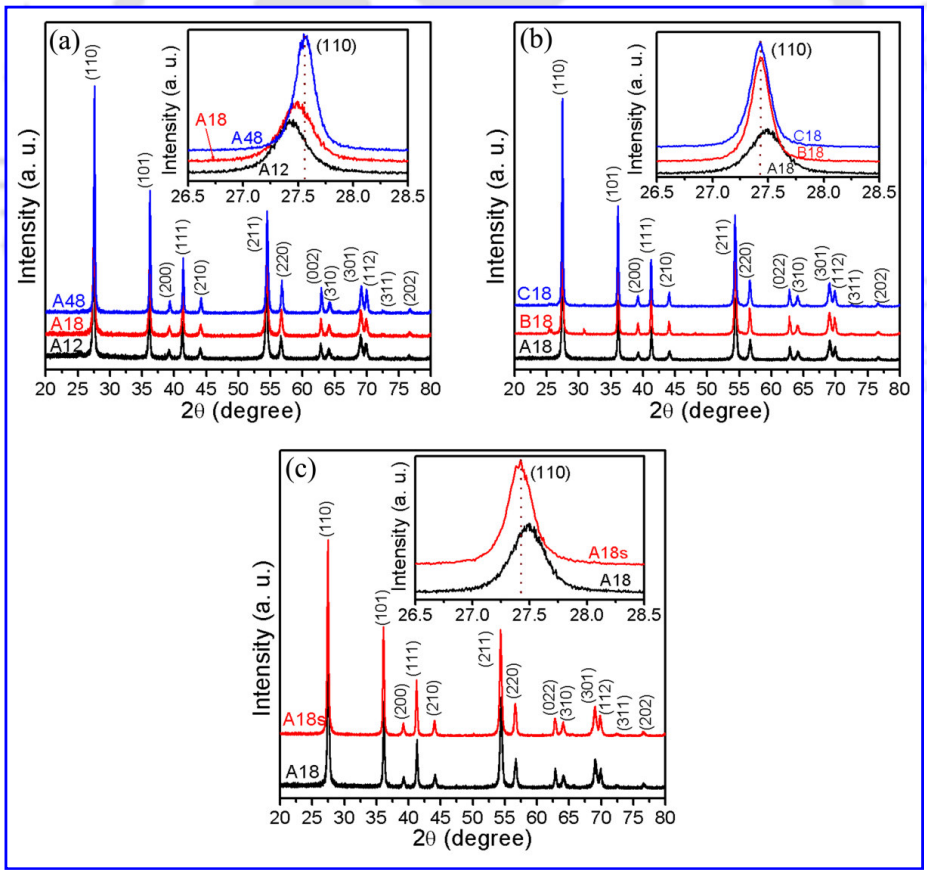

Fig. 6.1. Comparison of XRD patterns for different samples: (a) A12, A18 and A48; (b) A18, B18 and C18; (c) samples A18 and A18s. The inset in each graph shows the magnified view of corresponding (110) brag peak indicating systematic shift in peak position.

Table 6.1. Details of the sample preparation conditions, morphology, lattice parameters (*a, c*), and band gap (calculated from the absorption spectra).

Sample Names	Growth temperature, Reaction duration	Morphology	Lattice parameter (Å)		Volume ($Å^3$)	Band gap (eV)	
			a	c	a ×a× c	Direct	Indirect
A12	150 °C, 12 h	Nanorod	4.597	2.959	62.531	2.92	2.69
A18	150 °C, 18 h	Nanopillar	4.588	2.956	62.223	3.01	2.86
A18s	150 °C, 18 h, stirring	Nanorod	4.599	2.959	62.585	2.90	2.68
A48	150 °C, 48 h	Nanopillar	4.576	2.950	61.772	2.94	2.79
B18	170 °C, 18 h	Nanopillar	4.597	2.958	62.510	2.94	2.77
C18	190 °C, 18 h	Nanoflower/ Nanopillar	4.598	2.959	62.558	2.93	2.74

Fig. 6.1(b)). It is observed from the FESEM and TEM images that as the growth temperature increases, the size of the NS increases. According to the earlier reports,[1, 6] with increase in NS size the lattice volume decreases in rutile TiO_2. This would imply higher 2θ value, if strain contribution is neglected. More importantly, the size of the NS is increased with higher growth temperature and reaction duration. However, we observed two different trends, i.e., lattice contraction with increase in reaction duration and lattice expansion with increase in growth temperature. So, the shift and broadening of XRD peaks in our case cannot be explained from size effect alone. **Fig. 6.1(c)** shows the effect of stirring on the sample during the reaction. Comparison of the XRD patterns for A18 and A18s clearly show that the peaks are shifted to lower 2θ for the sample grown under stirring condition. The change in lattice parameters *a, c* and the cell volume with respect to reaction duration and growth temperatures are shown in **Fig. 6.2(a) and (b)**, respectively and the corresponding parameters are presented in **Table 6.1**. Interestingly, the axial ratio c/a, representing the lattice symmetry, remains almost constant at 0.644. The lattice parameters are calculated by using (110) and (101) peaks in the XRD pattern. The shift and broadening of diffraction peaks are generally related to size and strain effects of rutile TiO_2 NS.

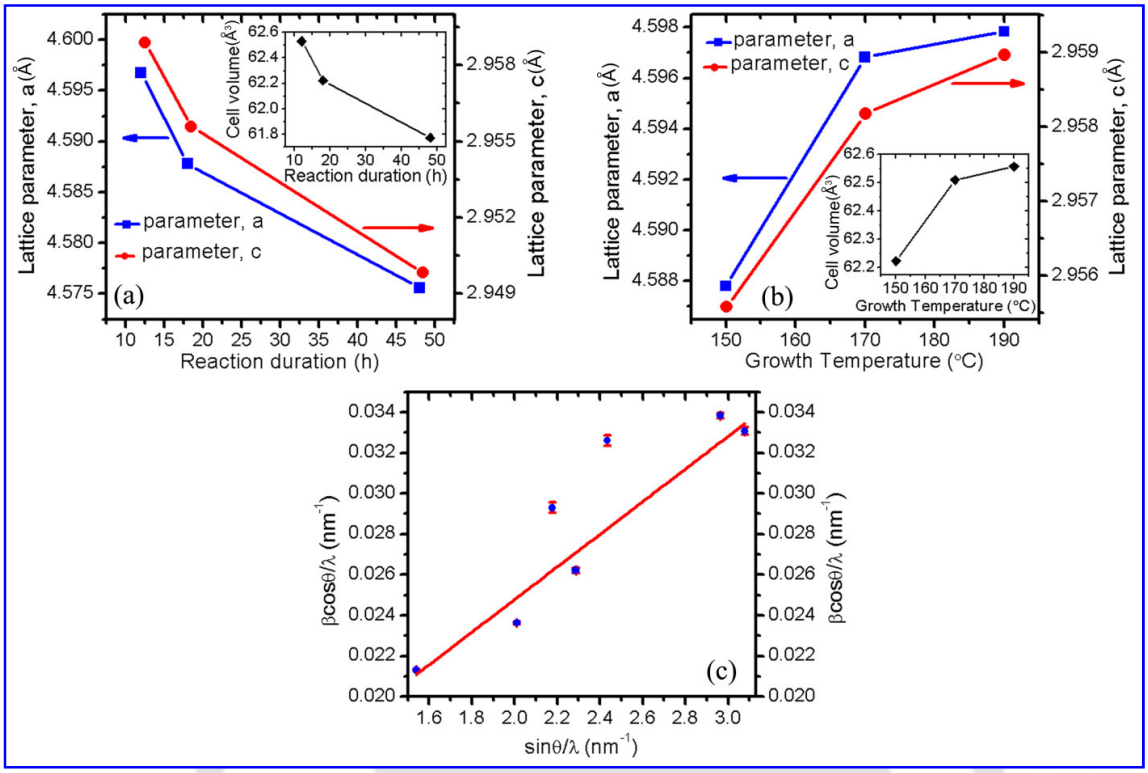

Fig. 6.2. Variation of lattice parameters *a* and *c* with: (a) reaction duration, (b) growth temperature. The inset in each case shows the corresponding change in lattice volume. (c) A plot of *(β cosθ)/λ vs (sinθ)/λ* for B18.

To isolate the contributions of strain from that of the size effect, Williamsons-Hall (W-H) method[16, 17] is used for sample B18 and we calculated the crystallite size and strain for the NS using the following equation:

$$\frac{\beta cos\,\theta}{\lambda} = \frac{1}{D} + \frac{\varepsilon sin\,\theta}{\lambda}, \qquad (6.1)$$

where β is the full width at half maximum (fwhm), θ is the diffraction angle, λ is the x-ray wavelength, D is the average crystalline size, and ε is the effective strain. The strain is calculated from the slope and the crystallite size is calculated from the inverse of the intercept of linear fit (**Fig. 6.2(c)**). The positive slope indicates tensile strain, consistent with the lattice expansion. Note that there is large scatter in data in the plot, which is indicative of the anisotropic strain in the nanocrystals.[18] Since the analysis of the anisotropy factor for TiO_2 is a complex function of elastic constants and dislocation contrast factors, and these

quantities are not known for TiO_2, accurate analysis of size and strain was not possible from such a plot. However, if we ignore the errors due to the scatter in data, a rough estimate of the average crystallite size and strain can be calculated from **Fig. 6.2(c)**. The average crystallite size and strain thus calculated was found to be 114 nm and 0.008 $\pm$0.001 from the W-H plot. The tensile strain of 0.8% is likely to be caused by the large density of Ti_i and O_v defects, as evidenced from other studies discussed below. We also used Scherrer formula to calculate the crystallite size. In all the cases, the Scherrer formula yields a lower size value as compared to the size extracted from W-H plot, as expected. Interestingly, the average crystallite sizes extracted from the W-H plot is very similar to the width/ thickness of the nanostructures obtained from the FESEM images.

Raman scattering studies: The Raman studies are employed to further confirm the phase, crystallinity and defects in the as-synthesized NS. All the peaks correspond to the characteristic Raman modes of rutile TiO_2 structure (**Fig. 6.3**). **Fig. 6.3(a)** shows the Raman modes of sample A12, A18 and A48. The three typical first order Raman modes B_{1g} (weak), most intense E_g and A_{1g} along with a second order vibrational mode E_g(SO) at ~240 cm^{-1} were observed for all samples. The most intense E_g mode is red shifted while A_{1g} mode slightly blue shifted for sample A18 and A48 compared to A12. The blue shift of A_{1g} mode may be due to the compressive strain implying a lattice contraction. The red shift of E_g and A_{1g} modes is generally due to phonon confinement effect and oxygen vacancy defects[19-21] in

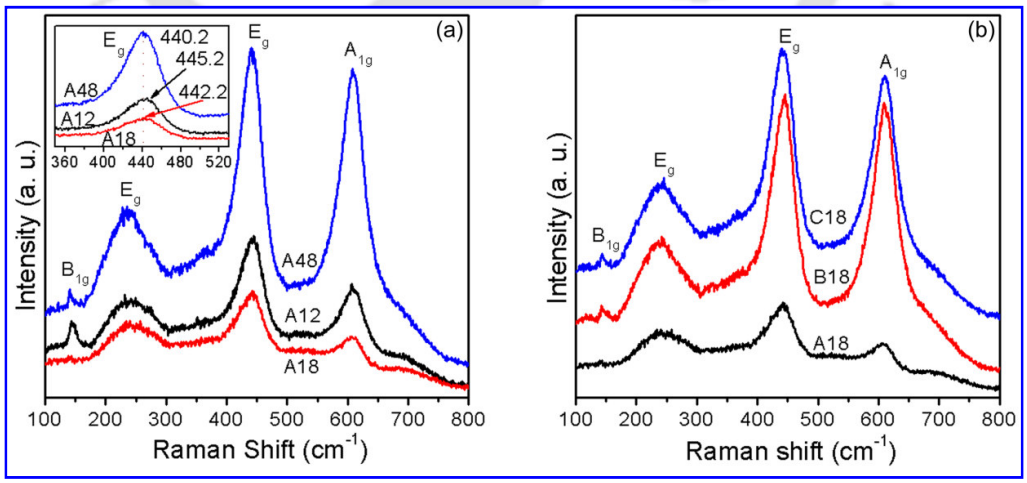

Fig. 6.3. Comparison of Raman spectra for: (a) A12, A18 and A48; (b) A18, B18 and C18. The inset in (a) shows magnified view of the most intense E_g mode.

rutile TiO_2. As the size of the NS is increased for higher reaction duration, the red shift cannot be explained by phonon confinement effect. Therefore, the red shift of E_g mode may be due to the higher concentration of defects in A18 and A48 as compared to that in A12. **Fig. 6.3(b)** shows the Raman spectra of sample A18, B18 and C18 which were grown at different growth temperatures.

6.4. FESEM and TEM studies

FESEM imaging: The morphologies of as-synthesized samples as obtained from FESEM images are shown in **Fig. 6.4**. The samples grown after different reaction durations, i.e., 12 h, 18 h and 48 h are shown in **Figs. 6.4(a)-(c)**, respectively. Sample A12 revealed NRs like morphologies, while A18 and A48 revealed tetragonal nanopillar like structures with rough surfaces on the top portion having small NRs like morphologies. The NRs of length ~320-550 nm and diameter ~26-74 nm is observed from the FESEM images for the sample A12 (**Fig. 6.4(a)**). However, sample A18 and A48 shows nanopillars with tetragonal cross section of size in the range ~109 – 280 nm and ~215 – 684 nm, respectively (**Fig. 6.4(b) and (c)**). **Figs. 4(d) and (e)** show the FESEM images of the samples grown at 170 and 190 °C, respectively. Sample B18 shows the nanopillar like morphologies, whereas C18 shows the 3D nanoflowers. The tetragonal nanopillars having square cross section of side ~390 – 684 nm for sample B18. In both samples B18 and C18, the top surface consist of small NRs like budding structures and this rough surface increases the effective surface area of the rutile TiO_2 nanostructures which may increase the surface reactivity. The high magnification image of C18 is showing 3D nanoflowers having nanopillars as petals (**Fig. 6.4(f)**). The EDX spectrum of corresponding nanoflowers is shown in the inset of **Fig. 6.4(e)**. The EDX spectrum shows only Ti and O element, indicating the phase purity of TiO_2 NS. It is interesting to note that the change in reaction durations and growth temperatures lead to the alteration of the hydrolysis rate of titanium butoxide in presence of HCl, which helped in designing various architectures from NRs to nanopillars and nanoflowers.

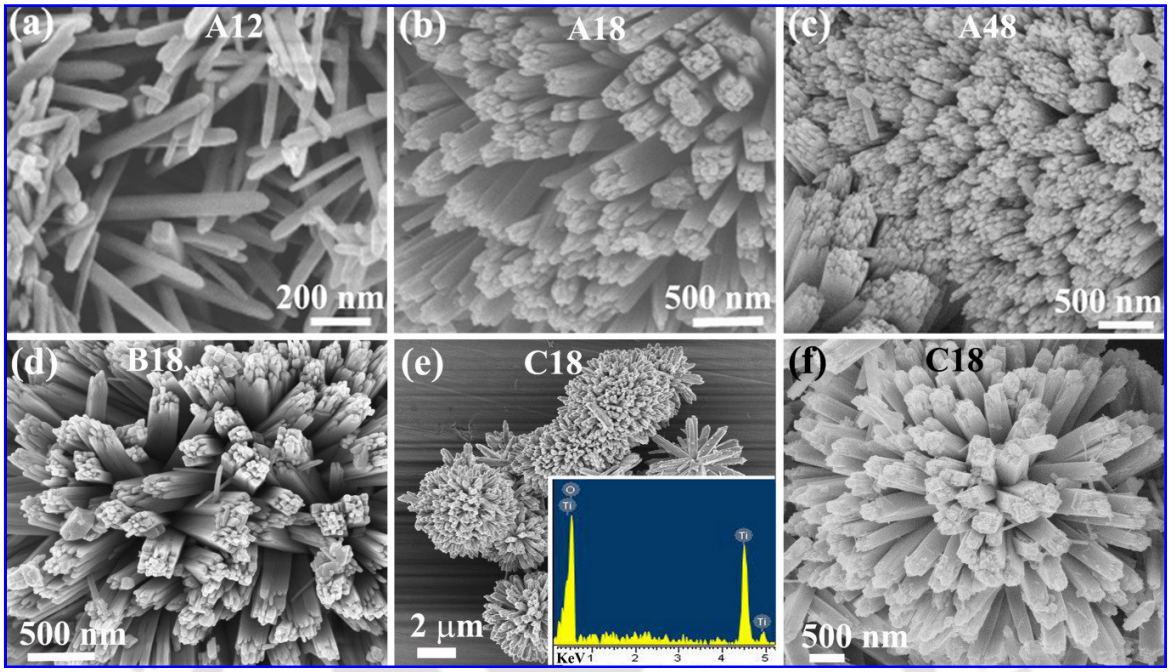

Fig. 6.4. FESEM images of the morphology of TiO_2 NS: (a) A12, (b) A18, (c) A48, (d) B18, (e) C18, (f) high magnified view of C18.The inset in (e) shows the EDX spectrum of C18 indicating Ti and O elements.

TEM imaging: TEM images of as-synthesized samples are shown in **Fig. 6.5**. TEM image of sample A12 shows NRs of width 13 nm and length 286 nm (**Fig. 6.5(a)**). The inset in **Fig. 6.5(a)** shows the SAED pattern of corresponding NRs indicating single crystalline and tetragonal nature of rutile TiO_2. The HRTEM image of A12 is shown in **Fig. 6.5(b)**. The d-spacing of 3.25 Å correspond to the (110) plane of rutile TiO_2. The observed lattice fringe demonstrates that the exposed surface of the NRs has {110} facet. **Fig. 6.5(c)** shows a single nanopillar in A18 and the corresponding SAED pattern is shown in **Fig. 6.5(d)**. The clear electron diffraction spots indicate the single crystalline and tetragonal nature of the as-grown rutile TiO_2 nanopillars. **Fig. 6.5(e)** shows the TEM image of a single NR of sample A18s and the corresponding lattice fringe is shown in **Fig. 6.5(f)**. The d-spacing of 2.33 Å corresponds to (200) plane of rutile TiO_2 structure. The lattice fringes of A18s revealed that the growth of NRs is along [200] direction.

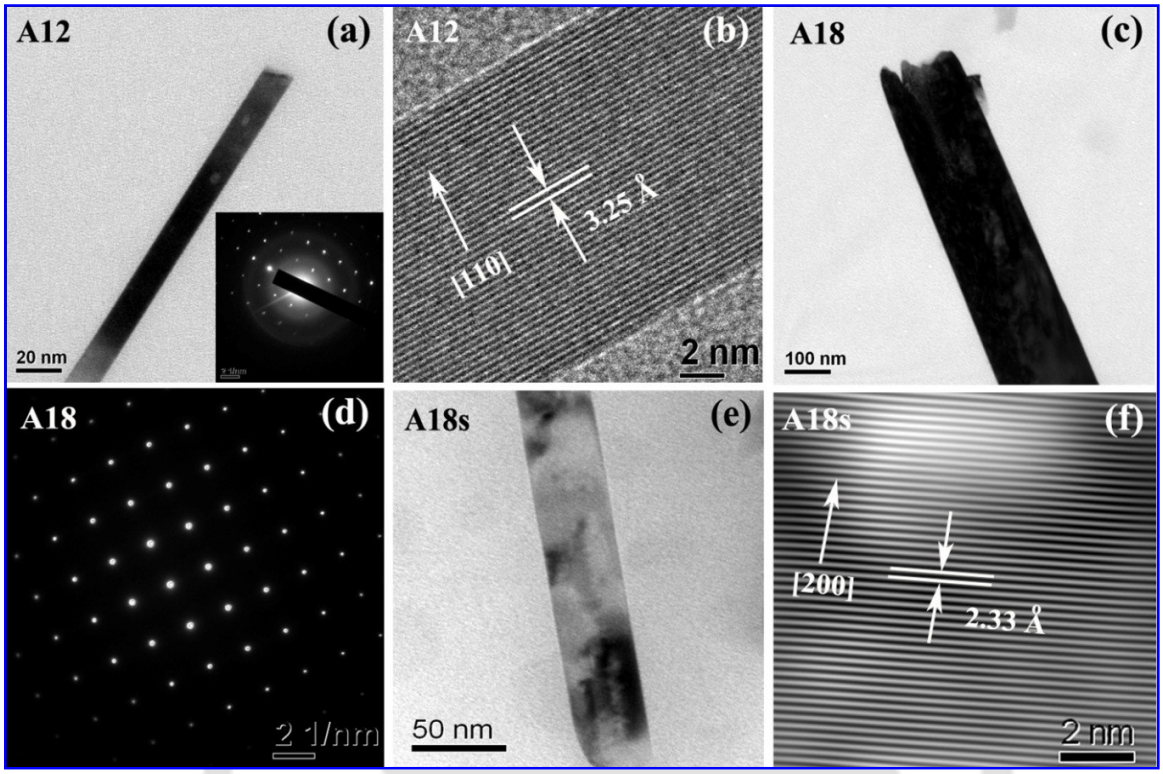

Fig. 6.5. TEM image of (a) a single nanorod in A12, inset is the corresponding SAED pattern; (b) HRTEM lattice fringe of A12; (c) a single nanopillar in A18, (d) SAED pattern showing single crystalline tetragonal rutile TiO_2 in A18, (e) a single nanorod A18s, (f) HRTEM lattice fringe of A18s.

6.5. Optical absorption studies

Light absorption characteristics of hydrothermally synthesized TiO_2 NS are shown in **Fig. 6.6**. The absorption edges of the samples show systematic blue shift with increasing reaction duration from 12 h to 18 h (**Fig. 6.6(a)**), while the absorption edges are red-shifted with increase in growth temperature (**Fig. 6.6(b)**). The Tauc's plot ($(\alpha hv)^2$ versus hv) shows a direct band gap behavior, as shown in the insets in each case. The indirect band gaps of the samples are also calculated from the linear extrapolation of $(\alpha hv)^{1/2}$ versus hv plot (Tauc's plot). Both the direct and indirect band gaps show decrease with higher growth temperatures, whereas it increased with increase in reaction durations from 12 h to 18 h (sample A12 and A18) and then decreased for 48 h reaction (sample A48) (see **Table 6.1**). The variation of band gap for samples grown under different growth conditions may have relation to the

variation in lattice constants and this may hint to the contribution of intrinsic defects in different samples. These defect states are confirmed from our PL measurements, as discussed below. **Fig. 6.6(c)** shows a comparison of absorption spectra for A18 and A18s. The sample A18s grown under stirring condition shows a red shift of absorption edge relative to that of A18, indicating a reduction in the band gap. The samples (A18s, B18, and C18) with lattice expansion show higher band gap compared to that in A18. However, band gap of A18 and A48 showing lattice contraction is also increased. Ekuma et al.[22] reported the indirect band gap (R- Γ) of 2.95 eV and direct band gap of 3.05 eV in rutile TiO_2 using *ab initio* calculation. They observed reduction in the indirect band gap (2.73 eV) by 1% lattice expansion and increased to 3.02 eV by 2% contraction of both lattice parameters, which is consistent with our results discussed above. However, we observed a reduction of band gap

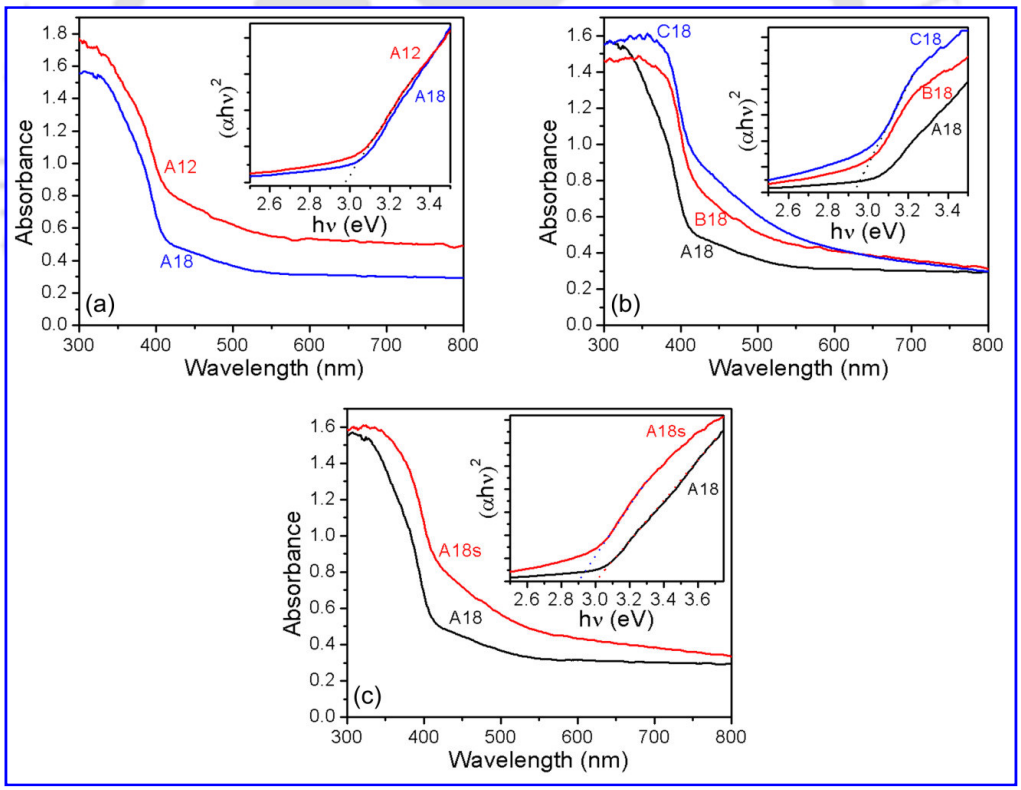

Fig. 6.6. UV-visible-NIR absorption spectra: (a) A12 and A18 grown after 12 and 18 h, respectively; (b) A18, B18 and C18 grown at 150, 170 and 190 °C, respectively; (c) A18, A18s grown without and with stirring during the growth. The inset in each case shows the $(\alpha h\nu)^2$ *vs* $h\nu$ plot indicating the direct band gap for the corresponding absorption spectrum of each sample. Band gap energy is calculated from the extrapolated line (dashed) fitted to the respective linear portions.

with lattice contraction for sample A48 compared to that in A18. It is quite likely that the increased concentration of both Ti_i and O_i defects may help in lowering the band gap in A48 compared to A18. The calculated direct and indirect band gaps for the samples grown under different growth conditions are listed in **Table 6.1**. Earlier optical absorption measurement[23, 24] and band gap calculation[25, 26] revealed that rutile TiO_2 is direct forbidden, i.e., the direct transition Γ_{3c}-Γ_{1v} is dipole forbidden,[27] while the indirect-allowed transition (M- Γ [25] or R-Γ [26] is nearly degenerate with the direct-forbidden transition. The energy separation between the direct-forbidden and indirect-allowed transition is reported to be 10-100 meV [24, 28] for bulk TiO_2 and the difference in our case is ~110-230 meV. The higher difference in our case may be due to the size and strain effects in the NS.

6.6. Photoluminescence studies

In order to understand the nature of defects and the associated localized trap states, PL studies are performed at room temperature (RT) on different samples. We observed a strong near infrared (NIR) PL emission at 1.43 eV (~867 nm) for all samples irrespective of growth conditions and a weak broad visible PL emission (see **Fig. 6.7**). Through *in-situ* PL studies presented in the previous chapter,[29] we argued that the origin of the NIR and visible PL in TiO_2 NS is Ti_i defects and O_v defects, respectively. Oxygen vacancy induced visible PL is well known in TiO_2 NS.[29-31] However, there are very few reports on the PL signature of Ti_i defects in TiO_2. **Fig. 6.7(a)** shows that the intensity of NIR PL increases with increase in the reaction duration, indicating that more Ti_i defects are formed after longer reaction durations. TiO_2(B) nanoribbons also showed similar visible and NIR PL at RT.[29] This essentially means that with increase in reaction duration, both Ti interstitial and oxygen vacancy defects are considerably increased. However, in A18 and A48, the visible band is splitted into two peaks, i.e., one broad peak centered at ~2.77 eV and another peak at 1.96 eV (~633 nm) and 1.99 eV (~623 nm) for sample A18 and A48, respectively. The new feature that evolves at lower energy side is observed for the first time and it is likely to be related to O_i^{2-} defects, whose formation mechanism is explained later.[15]

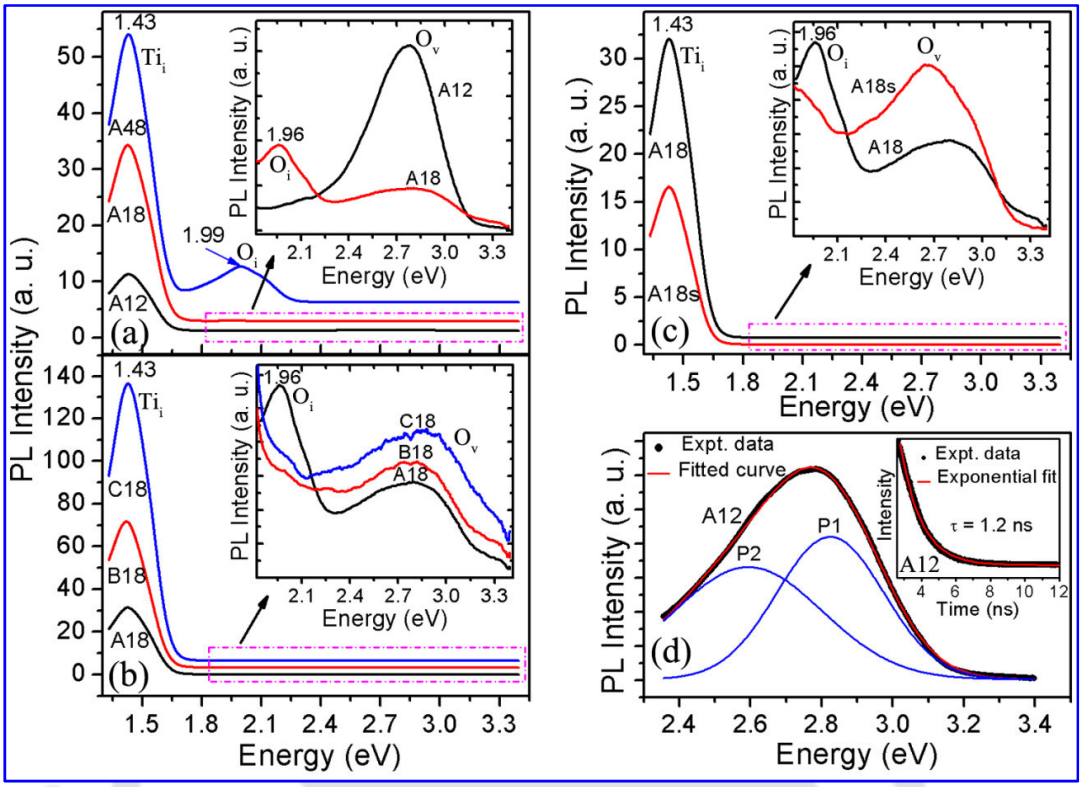

Fig. 6.7. Room temperature PL spectra for: (a) A12, A18 and A48 grown after 12, 18 and 48 h, respectively; inset shows the magnified view of PL spectra in A12 and A18 in the visible region; (b) A18, B18 and C18 grown at 150, 170 and 190 °C, respectively; (c) A18, A18s grown without and with stirring during the growth, respectively; (d) visible PL of A12 with Gaussian peak fitting, inset shows the PL decay of A18. The insets in (b) and (c) show the corresponding magnified view of the visible PL. The energy peaks responsible for oxygen vacancy, oxygen interstitial and Ti interstitial defects are indexed as O_v, O_i and Ti_i, respectively in the figure.

The effect of growth temperature on the PL is shown in **Fig. 6.7(b)**. The NIR PL increases in the order A18< B18 <C18, indicating the concentration of Ti_i defects are increased in the samples grown at higher temperature. The PL emission at 1.96 eV disappears for B18 and C18. **Fig. 6.7(c)** shows the PL spectra for the samples A18 and A18s. The NIR PL intensity is increased whereas broad visible PL is decreased for sample A18 compared to A18s. Note that red PL at 1.96 eV is not observed for A18s. The broad asymmetric visible PL emission of A12 is deconvoluted by two symmetric Gaussian peaks centered at 2.82 eV (peak P1, violet curve) and 2.59 eV (peak P2, blue curve), as shown in **Fig. 6.7(d)**. Recently, a blue PL at 2.8 eV was reported by Yamada et al.[32] in rutile TiO_2 and based on their time

resolved PL analysis, the blue PL was attributed to the localized defect induced states, instead of the band-edge delocalized states. It was argued that because only a free exciton PL is observed under low density excitation at low temperature, the initial photocarriers exist in the free band-edge state rather than the trapped states.[32] Interestingly, there has been no report of intrinsic PL in rutile TiO_2 bulk crystals at room temperature, except that due to the impurity or defects. We attributed the peaks P1 and P2 to the transition from neutral O_v and singly charged O_v (F^+) trap states, respectively, just below the conduction band to the valence band. Note that the signature of F^+ center is confirmed from ESR spectra. Upon the loss of an O atom in TiO_2 lattice, the two unpaired electrons that remains trapped in the vacancy cavity give rise to an F center. The basic assumption is that one of the electrons in F center tends to occupy the neighbouring Ti^{4+} ion and yield Ti^{3+}center and F^+center. A more detailed explanation and the evidence for $F^+$and Ti^{3+} trap states in reduced TiO_2 NS was provided in the previous chapter (*Chapter 5*).[30] However, we do not observe any signature of Ti^{3+} in our ESR data and XPS studies for samples used in this work. We believe that the Ti^{3+} ions are migrated towards the surface to interact with the atmospheric oxygen and converted to Ti^{4+} by occupying an interstitial site. The time resolved PL spectra of sample A12 monitored at 2.76 eV (450 nm) with 3.06eV (405 nm) excitation is shown in inset of **Fig. 6.7(d)**. The decay spectrum is well fitted by a single exponential decay with time constant of 1.2 ns. This is typical of PL emission from defect states in TiO_2.[32] Though there are two peaks in the steady state PL spectra (**Fig. 6.7(d)**), single exponential fit to the decay curve indicates that both the defect states have identical decay time constants. These states correspond to F and F^+ centers in TiO_2.

6.7. XPS and ESR studies

XPS studies: XPS is a unique tool to investigate the surface defects and chemical environments, because of the high sensitivity to surface. Evidence of oxygen vacancy related surface defects,[30, 33] such as Ti^{3+} or Ti^{2+} core level peaks in Ti 2p spectra are not observed in our samples (**Figs. 6.8(a) and (b)**). **Figs. 6.8(a) and (b)** show that Ti $2p_{3/2}$ and $2p_{1/2}$ core level peaks show shifting among the samples, keeping the difference between binding energy of $2p_{3/2}$ and $2p_{1/2}$ (Δp = 5.7 eV) constant. The shift in the Ti 2p peaks may be due to the

lattice distortion in rutile TiO_2 NS. The Ti $2p_{3/2}$ core level peak of A18 is observed at 457.7 eV which is attributed to Ti^{4+}. The Ti $2p_{3/2}$ peak of A18s, B18 and C18 is shifted to higher binding energy compared to A18 and this may be due to the lattice expansion (**Fig. 6.8(a)**). However, the lower binding energy of $2p_{3/2}$ core level peak of A18 as compared to A12 may be due to the lattice contraction (**Fig. 6.8(b)**). Similar shift of O 1s core level peaks are observed (**Fig. 6.8(c)**). The absence of any shoulder at higher binding energy of O 1s spectra except A12 and A18s indicates that samples A18, B18 and C18 are free of impurity bonding like hydroxyl (OH) groups and C-O bonds.[30, 34] The lower binding energy shoulder in A12 and A18s suggests the presence of OH groups in these samples, which show lattice expansion as compared to A18 and is inconsistent with the lattice contraction in anatase TiO_2 due to the surface OH group, as reported by Li et al.[2]

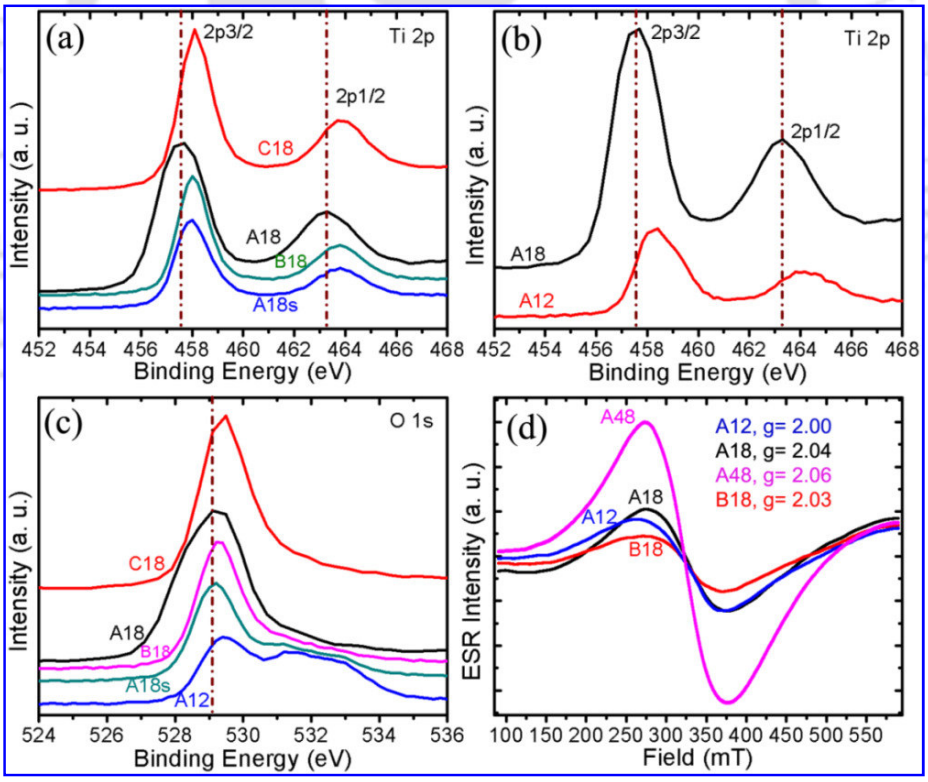

Fig. 6.8. XPS spectra: (a) Ti 2p core level spectra for A18, A18s, B18 and C18. (b) Ti 2p core level spectra for A12 and A18. Dotted vertical lines show the change in relative peak position in each case. (c) O 1s core level spectra for A12, A18, A18s, B18 and C18. Dotted vertical line shows the change in relative peak position. (d) Room temperature ESR spectra for A12, A18, A48 and B18.

ESR studies: ESR is an exceptionally useful technique in detecting the spin polarized charge state of defective TiO_2 NS. The presence of singly ionized oxygen vacancy is identified from the ESR spectra, as shown in **Fig. 6.8(d)**. The samples A12, A18, A48 and B18 show g= 2.00, 2.04, 2.06 and 2.03, respectively, which are assigned to singly ionized oxygen vacancy F^+ defects. Note that various groups observed these defects in TiO_2 from ESR studies and reported that the g-value for singly ionized oxygen vacancy is 2.00.[35-37] This implies that our samples contain oxygen vacancy related F^+ centers. These defects play a key role for the observed lattice parameter variations in rutile TiO_2 NS.

6.8. Discussion

There are several reports on the size effect of lattice parameter variation in metal oxides nanocrystals.[1-4, 6, 7] Recently, it was reported[38] that the oxygen vacancy formation by itself, without a cation radius change in CeO_2 results in a contraction of lattice parameters on the basis of molecular dynamic simulation. It was explained that upon the formation of oxygen vacancy, the cation relaxed away from the vacancy (by approximately 0.10 Å), however the anion got closer to it (by approximately 0.16 Å) and the magnitude of the significant distortion resulted in a net local contraction of the lattice around the vacancy. However, the combined effects of oxygen vacancy and associated cation radii change results in lattice expansion of CeO_2.[38] In particular, the lattice expansion and contraction of rutile and anatase TiO_2 was reported by various groups.[1-3, 6] Li et al.[2] reported that particle size reduction induces lattice contraction due to surface hydration effect in pure anatase TiO_2 nanocrystals. On the other hand, Swamy et al.[3] observed lattice expansion at reduced crystallite size in anatase TiO_2 and explained the lattice expansion in terms of increased Ti vacancy and lattice strain with decreasing crystallite size. Moreover, lattice expansion with decreasing crystallite size is reported in rutile TiO_2.[1, 6] A surface defect dipole model was proposed by Li et al.[1] to explain the lattice expansion of rutile TiO_2 nanocrystals with the reduction in size in terms of the strong interaction among the surface dipoles that produced an increased negative pressure. This is in contrast to the ionicity increase induced lattice expansion in $BaTiO_3$ proposed by Tsunekawa et al.[5] The size dependent lattice expansion of rutile TiO_2 was explained in terms of Ti vacancy abundance by Kuznetsov et al.[6] Using *ab initio* calculation,

Iddir et al.[14] predicted that for O_v, the significant displacement extended along the [110] and [001] directions of the equatorial plane encompassing the vacancy. The three Ti nearest neighbor have the largest outward displacement of 0.31 Å and the nearest O neighbor of O_v have the largest inward displacement of 0.14 Å. It was also reported[14] that for Ti_i, the major displacement occurred in the plane perpendicular to [001], the largest being observed in the plane passing through Ti_i. The two nearest neighbor Ti are pushed away from their ideal position by 0.3 Å and the closest four O atoms relax toward the Ti_i by 0.21 Å. The lattice atoms relaxed around the defects to accommodate the induced stress due to the diffusion of Ti_i through the interstitial region. Based on the above information, we discuss the atomistic origin of lattice expansion and contraction of rutile TiO_2 in terms of intrinsic defects rather than size induced lattice variations, as the size of our nanostructure is relatively large compared to those reported in the literature.[1, 6] The intrinsic defects include Ti_i, O_v and O_i in our rutile TiO_2 NS.

First, we discuss the possible mechanisms of lattice expansion in our rutile TiO_2 NS. From **Fig. 6.2(b)** and **Table 6.1**, it is seen that the lattice is expanded as the growth temperature is increased. Generally, in nanoscale regime, the lattice expansion in metal oxide nanocrystals is believed to result from complex interplay of defect chemistry and physics. For example, (i) increase in ionic radius upon the reduction of cation valence state might cause the lattice expansion, and (ii) the electrostatic repulsion between positively charged oxygen vacancy and metal cations surrounding it may also be responsible for the lattice expansion. ESR and XPS measurement on our samples do not show any signature of Ti^{3+}, which eliminates the possibility of lattice expansion due to reduction of cationic radii. However, ESR signal shows the evidence of F^+ (singly ionized oxygen vacancy) center in our samples. In our previous report and *Chapter 5*, the pathways for the formation of F^+ and Ti^{3+} trap center were explained.[30] Note that we observed Ti_i related NIR PL and $F^+$and neutral O_v related visible PL emission in our samples. The Ti-Ti and Ti-O bonds are relaxed due to the missing O atom. The nearest-neighbor Ti atoms move outward from the vacancy to strengthen the bonding with rest of the neighboring O lattice. While the next-nearest-neighboring O atoms move inward due to the absence of electrostatic repulsion by the missing O atom. It was reported[39, 40] that the local distortion due to the Ti atom displacement

depends upon the different charge state of oxygen vacancy, i.e. neutral, singly charged (+1) and doubly charged (+2) oxygen vacancy. The positive charges cause greater repulsion for Ti-Ti distance compared to neutral oxygen vacancy.[39, 40] Note that we observed singly charged oxygen vacancy (F^+) in ESR measurement and both neutral O_v and singly charged F^+ in PL measurement. So, we expect the lattice expansion in our samples to be caused by the oxygen vacancies creating $F^+$and neutral O_v defects. The electrostatic repulsion between F^+ and Ti^{3+} helps in migration of the unsaturated Ti^{3+} from the bulk towards the surface to interact with the atmospheric O_2 and form Ti^{4+}during the course of air annealing and occupying an interstitial site similar to the lattice Ti site in octahedral TiO_2 crystal system. It was reported from both experimental and theoretical analyses that Ti_i diffusion is faster in rutile TiO_2 than the O_v diffusion when annealing in O_2 atmosphere.[41-43] The lattice Ti is strongly bonded with the lattice O atoms. When the Ti^{4+} is placed in the interstitial site, the Ti atoms are relaxed outward due to the electrostatic repulsion between positively charged Ti ions. However, the lattice O atoms are slightly distorted towards the Ti_i^{4+} as they are strongly bonded to lattice Ti atoms. As a result, the net relaxation favors the expansion of lattice volume which is due to the presence of Ti_i^{4+}defects. It is noticed that the Ti_i^{4+} increases with the increase in growth temperature from the PL spectra suggesting more lattice expansion. So, the lattice expansion is observed in our samples in the order C18> B18> A18. The sample A18 has an additional PL peak at 1.96 eV compared to B18 and C18 which is related to O_i and will be discussed in the following paragraph. Our experimental results regarding the lattice expansion due to Ti_i and O_v are consistent with the theoretical prediction of Iddir et al.[14]

Secondly, we discuss the possible mechanism behind the lattice contraction in rutile TiO_2 NS. Our PL study on TiO_2 NS showed that longer the reaction duration, higher the O_v and Ti_i defects for the same growth temperature.[29] This is also reflected in the present case, as Ti_i^{4+} related PL emission is enhanced for the longer reaction duration samples. Since the oxygen vacancies are more in these samples, it is expected that the atmospheric O_2 may inject rapidly into the TiO_2 to occupy the oxygen vacancy positions during the course of air annealing at 500 °C, as a result the oxygen vacancy concentration decreased considerably after annealing, which is reflected in our PL spectra (reduction of broad visible PL in samples

A18 and A48 compared to A12). It was recently reported that adsorbed isotopic oxygen is injected into the bulk rutile TiO_2 as O_i^{2-} which underwent drift towards the surface due to space-charge layers and retarded the diffusion of interstitials, promoting the exchange with lattice oxygen.[44, 45] Presumably most of the O_v near the surface are annihilated due to diffusion of O_2 and shut down the path for further diffusing O_i and creating separate O_i^{2-} ions which facilitates creation of surface electronic bands. The PL emission at 1.96/ 1.99 eV observed in A18/A48, may be attributed to the surface electronic bands created by O_i^{2-} ions. The electrostatic attraction between the Ti_i^{4+} and O_i^{2-} is dominant over the lattice expansion due to F^+ and neutral $O_v$which results in the lattice contraction for the samples A18 and A48 compared to A12.

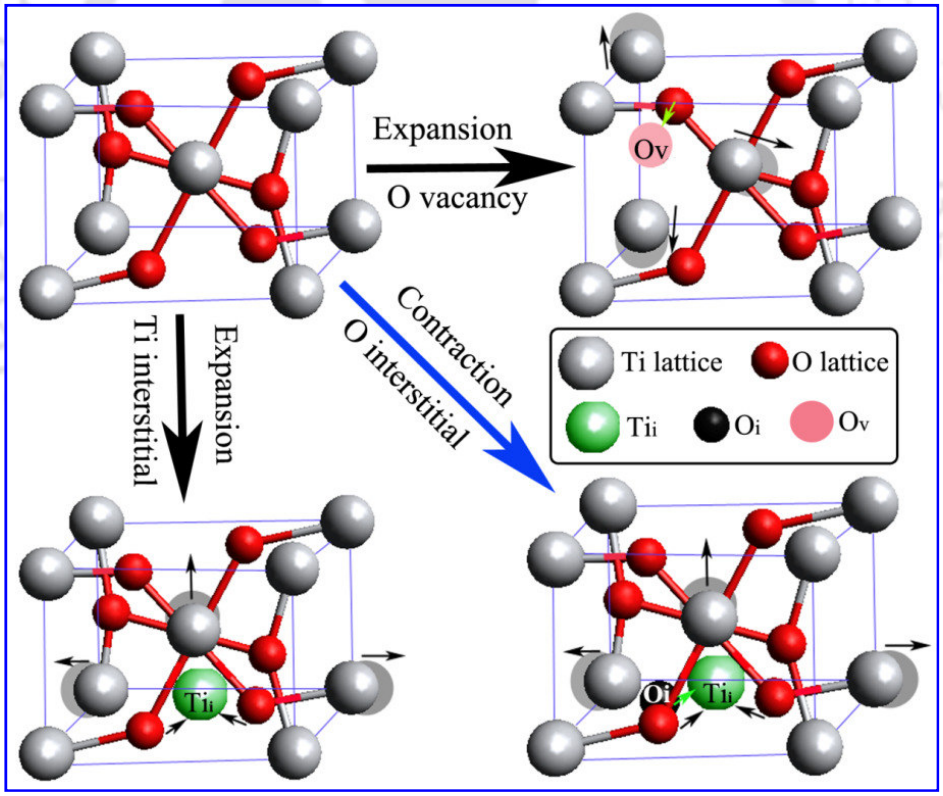

Fig. 6.9. Schematic diagram illustrating lattice expansion and lattice contraction in TiO_2 lattice due to intrinsic defects. Grey (large) balls are Ti atoms and red (small) balls are oxygen atoms. The light pink (small) ball indicates the oxygen vacancy. The green (large) and black (small) ball indicate Ti_i and O_i, repectively. The arrow shows the direction of relaxation of atoms due to O_v, Ti_i and O_i defects.

Another interesting point to be noted is that the red PL at 1.96 eV is absent for the sample B18 and C18 grown at higher growth temperature. It was shown in *Chapter 4* that for growth at higher temperature, PL due to Ti_i was much stronger than the PL due to O_v.[29] Due to lower concentration of O_v, the atmospheric O_2 interacts with Ti^{3+} and oxidized to Ti^{4+} instead of injecting into the bulk and this may be a possible reason for the absence of O_i related PL peak at 1.96 eV (1.99 eV) in B18 (C18). The lattice expansion of A18s compared to A18 can be explained on basis of higher concentration of F^+ and neutral O_v and absence of O_i^{2-}, which results in net electrostatic repulsion between F^+ and Ti cations. The lattice contraction due to surface hydroxyl group in pure anatase TiO_2[2] is inconsistent with the lattice expansion in our rutile TiO_2 samples A12 and A18s, which are associated with adsorbed surface OH group, as confirmed from XPS studies. Therefore, we strongly believe that the intrinsic defects, such as Ti_i^{4+}, F^+ and $O_i^{2-}$are primarily responsible for lattice parameter variation in our rutile TiO_2 NS. A schematic diagram illustrating the lattice expansion due to the presence of oxygen vacancy and Ti interstitial defects, whereas lattice contraction due to the electrostatic attraction between the Ti_i^{4+} and O_i^{2-} defects is shown in **Fig. 6.9**. In case of O_v mediated expansion, due to the missing O atom, the Ti-Ti and Ti-O bonds are relaxed. The nearest-neighbor Ti atoms move outward from the vacancy to strengthen the bonding with rest of the neighboring O lattice. Though the next-nearest-neighboring O atoms may move inward to fill the O_v site, the net outward movement of Ti atoms is higher than the net inward movement of O atoms. This results in lattice expansion. Lattice expansion due to Ti interstitial is more natural due to larger size of the Ti atoms and electrostatic repulsion between Ti^{4+} ions. On the other hand, lattice contraction is caused by the electrostatic attraction between Ti_i^{4+} and O_i^{2-}, as shown by the green arrow. Note that the requirement of a small size below a critical size is not imperative in this mechanism. This calls for a revisit of the earlier reported results on the size dependent lattice expansion in TiO_2 NS.

6.9. Conclusions

Rutile TiO_2 NS with NRs, nanopillars and nanoflower-like morphologies are synthesized by an acid-hydrothermal process. At higher growth temperatures, lattice expansion is observed,

while lattice contraction is observed for the samples grown with longer duration of reaction. We also observed lattice expansion for the samples grown under constant stirring during the reaction. Our studies reveal that the lattice expansion/contraction depends on the types, concentration and nature of various intrinsic defects that are created under different growth and processing conditions. These NS are highly crystalline as observed from SAED patterns and lattice fringes of HRTEM analyses. The direct and indirect band gaps of the NS grown under different growth conditions are varied from 2.90 - 3.01 eV and 2.68 - 2.86 eV, respectively. The NIR peak at 1.43 eV in PL spectra is attributed to the Ti_i^{4+} defects in rutile TiO_2 NS. This peak is enhanced with higher growth temperatures and longer reaction duration. Relative shift in Ti 2p and O 1s core level XPS spectral positions under various growth conditions hints towards lattice distortions in TiO_2 NS. Based on our experimental observations, we believe that the presence of Ti_i^{4+} and F^+ and neutral oxygen vacancy defects are mainly responsible for lattice expansion, while the electrostatic attraction between Ti_i^{4+} and O_i^{2-} defects cause the lattice contraction in rutile TiO_2 NS. The intrinsic defects induced lattice parameter variations may provide new routes to achieving novel functionalities in TiO_2 based advanced materials that can be tailored for many technological applications.

References

1. G. Li, J. Boerio-Goates, B. F. Woodfield and L. Li, Applied Physics Letters **85**, 2059-2061 (2004).

2. G. Li, L. Li, J. Boerio-Goates and B. F. Woodfield, Journal of the American Chemical Society **127**, 8659-8666 (2005).

3. V. Swamy, D. Menzies, B. C. Muddle, A. Kuznetsov, L. S. Dubrovinsky, Q. Dai and V. Dmitriev, Applied Physics Letters **88**, 243103-243103 (2006).

4. S. Deshpande, S. Patil, S. V. N. T. Kuchibhatla and S. Seal, Applied Physics Letters **87**, 133113 (2005).

5. S. Tsunekawa, K. Ishikawa, Z. Q. Li, Y. Kawazoe and A. Kasuya, Physical Review Letters **85**, 3440-3443 (2000).

6. A. Y. Kuznetsov, R. Machado, L. S. Gomes, C. A. Achete, V. Swamy, B. C. Muddle and V. Prakapenka, Applied Physics Letters **94**, 193117-193113 (2009).

7. Y. Liusai, L. Liping, Z. Minglei, F. Chaochao and L. Guangshe, Nanotechnology **24**, 305701 (2013).

8. V. R. Palkar, P. Ayyub, S. Chattopadhyay and M. Multani, Physical Review B **53**, 2167-2170 (1996).

9. H. J. Wasserman and J. S. Vermaak, Surface Science **22**, 164-172 (1970).

10. H. J. Wasserman and J. S. Vermaak, Surface Science **32**, 168-174 (1972).

11. D. K. Yu, R. Q. Zhang and S. T. Lee, Physical Review B **65**, 245417 (2002).

12. Y. Ji, L. Guo, H. Xu, J. Liu, X. Li, Y. Li, Z. Wu and P. Simon, Physica Status Solidi (a) **198**, 210-214 (2003).

13. J.-Y. Zhang, X.-Y. Wang, M. Xiao, L. Qu and X. Peng, Applied Physics Letters **81**, 2076-2078 (2002).

14. H. Iddir, S. Öğüt, P. Zapol and N. D. Browning, Physical Review B **75**, 073203 (2007).

15. B. Santara, P. K. Giri, I. Kenji and F. Minoru, Journal of Physics D: Applied Physics **47**, 215302 (2014).

16. G. K. Williamson and W. H. Hall, Acta Metallurgica **1**, 22-31 (1953).

17. S. B. Qadri, J. P. Yang, E. F. Skelton and B. R. Ratna, Applied Physics Letters **70**, 1020-1021 (1997).

18. P. K. Giri, Journal of Physics D: Applied Physics **42**, 245402 (2009).

19. S.-M. Oh and T. Ishigaki, Thin Solid Films **457**, 186-191 (2004).

20. V. Swamy, Physical Review B **77**, 195414 (2008).

21. V. Swamy, B. C. Muddle and Q. Dai, Applied Physics Letters **89**, 163118-163113 (2006).

22. C. E. Ekuma and D. Bagayoko, Japanese Journal of Applied Physics **50**, 7 (2011).

23. J. Pascual, J. Camassel and H. Mathieu, Physical Review B **18**, 5606-5614 (1978).

24. A. Amtout and R. Leonelli, Physical Review B **51**, 6842-6851 (1995).

25. R. V. Kasowski and R. H. Tait, Physical Review B **20**, 5168-5177 (1979).

26. M. A. Khan, A. Kotani and J. C. Parlebas, Journal of Physics: Condensed Matter **3**, 1763 (1991).

27. H. Mathieu, J. Pascual and J. Camassel, Physical Review B **18**, 6920-6929 (1978).

28. B. Poumellec, P. J. Durham and G. Y. Guo, Journal of Physics: Condensed Matter **3**, 8195 (1991).

29. B. Santara, P. K. Giri, K. Imakita and M. Fujii, The Journal of Physical Chemistry C **117**, 23402-23411 (2013).

30. B. Santara, P. K. Giri, K. Imakita and M. Fujii, Nanoscale **5**, 5476-5488 (2013).

31. J. Shi, J. Chen, Z. Feng, T. Chen, Y. Lian, X. Wang and C. Li, The Journal of Physical Chemistry C **111**, 693-699 (2006).

32. Y. Yamada and Y. Kanemitsu, Physical Review B **82**, 113103 (2010).

33. Q. Zhao, P. Wu, B.-L. Li, Z.-M. Lu and E.-Y. Jiang, Chinese Physics Letters **25**, 1811 (2008).

34. J. Zhuang, S. Weng, W. Dai, P. Liu and Q. Liu, The Journal of Physical Chemistry C **116**, 25354-25361 (2012).

35. M. Sterrer, E. Fischbach, T. Risse and H.-J. Freund, Physical Review Letters **94**, 186101 (2005).

36. S. V. Chong, K. Kadowaki, J. Xia and H. Idriss, Applied Physics Letters **92**, 232502-232503 (2008).

37. L. Li, G. Li, J. Xu, J. Zheng, W. Tong and W. Hu, Physical Chemistry Chemical Physics **12**, 10857-10864 (2010).

38. D. Marrocchelli, S. R. Bishop, H. L. Tuller and B. Yildiz, Advanced Functional Materials **22**, 1958-1965 (2012).

39. H.-Y. Lee, S. J. Clark and J. Robertson, Physical Review B **86**, 075209 (2012).

40. A. Janotti, J. B. Varley, P. Rinke, N. Umezawa, G. Kresse and C. G. Van de Walle, Physical Review B **81**, 085212 (2010).

41. S. Wendt, P. T. Sprunger, E. Lira, G. K. H. Madsen, Z. Li, J. Ø. Hansen, J. Matthiesen, A. Blekinge-Rasmussen, E. Lægsgaard, B. Hammer and F. Besenbacher, Science **320**, 1755-1759 (2008).

42. H. Onishi and Y. Iwasawa, Physical Review Letters **76**, 791-794 (1996).

43. R. A. Bennett, P. Stone, N. J. Price and M. Bowker, Physical Review Letters **82**, 3831-3834 (1999).

44. P. Gorai, A. G. Hollister and E. G. Seebauer, Applied Physics Letters **103**, 141601-141604 (2013).

45. A. G. Hollister, P. Gorai and E. G. Seebauer, Applied Physics Letters **102**, 231601-231605 (2013).

Chapter 7

Optical and Magnetic Properties of Fe and Cr doped TiO_2 Nanostructures

Diluted magnetic semiconductors (DMSs) are semiconductors doped with a small amount (a few atomic %) of transition metal (TM) ions that introduce local magnetic moments in the host semiconductors and thus exhibit both semiconducting and ferromagnetic properties. Particularly, the realization of room temperature ferromagnetism (RTFM) in TM doped TiO_2 is more interesting as it can be applicable for the spintronic and magneto-optic devices that can be operated at room temperature, if the ferromagnetism (FM) is indeed intrinsic. However, there are lots of controversies among the different research groups related to the issue of the origin of FM in TM doped TiO_2 nanostructures. It is being currently debated whether the FM arises due to the ferromagnetic metal cluster or secondary phases leading to an extrinsic origin or indeed an intrinsic nature of FM mediated by carriers or defects. In this chapter, we studied the structural, optical and magnetic properties of Fe and Cr doped TiO_2 one dimensional (1D) nanostructures by solvothermal and hydrothermal method, respectively. We observed tunable RTFM in our Fe and Cr doped TiO_2 nanostructures depending on the growth conditions and doping concentrations, and attempt to clarify the origin of FM with the help of structural and optical spectroscopy measurements. The development of TiO_2 nanostructures with tunable optical and magnetic properties constitutes an important step towards realizing improved magneto-optic and spintronic devices from novel TiO_2 nanostructures.

7.1. Introduction

Diluted magnetic semiconductors (DMSs), where transition metal (TM) atoms are introduced into the cationic sites of the semiconducting host lattice have been at the forefront of research interest due to the existence of both semiconducting and ferromagnetic properties. These

materials could be applicable for the possibility of use in future spintronic and magneto-optic devices,[1-3] where both spin and charge degrees of freedom can be manipulated in comparison to the conventional electronic devices where only electronic charges are considered. Therefore, intensive attention has been focused on DMS such as TM doped ZnO,[4, 5] SnO_2,[6, 7] In_2O_3[8] and TiO_2[9] due to realization of room temperature ferromagnetism (RTFM) in these systems. Among various oxide based DMS, TiO_2 has drawn extensive research interest because it is an excellent photo-catalyst for water splitting, high solubility limit of dopant magnetic ions and it possesses good optical transmission in the visible and near infrared region making it a suitable candidate for magneto-optic devices as well. However, in spite of several studies reported on TiO_2-based DMS, there is no clear agreement about the nature and origin of the observed ferromagnetism (FM) in the diluted magnetic oxide doped with few percentages of 3d cations. It is still controversial, whether the FM is indeed intrinsic which is mediated by carriers or defects inside the host semiconductor and/ or related to the purely extrinsic origin due to formation of ferromagnetic secondary phases or metallic cluster. It was suggested that the magnetic properties of DMS materials are critically dependent on fabrication, growth procedure, doping agents and processing conditions. Different synthesis methods may result in different defect concentrations, structures and surface morphologies, affecting the magnetic properties. Compared to other methods of preparation, solvothermal/ hydrothermal method is very simple, low cost, and one can easily tune the surface as well as bulk defects by controlling the growth temperature, reaction duration, and doping concentrations etc. In particular, solvothermal/ hydrothermal method is an effective method of doping, because the dopant ion precursor distributes uniformly in a high pressure reaction chamber under continuous stirring throughout the synthesis process, depending upon the solvent used, pH concentration and the solubility limit of doping agent in the mixed precursor solution.

Interestingly, RTFM have been observed in a wide range of undoped oxides such as TiO_2,[10-12] HfO_2,[13] In_2O_3,[10] SnO_2[14] and ZnO.[15] These reports help to address the controversies about the issues related to the role of defects in the ferromagnetic ordering. Some of the outstanding reports revealed no evidence of ferromagnetic ordering in Fe doped TiO_2 (Fe:TiO_2) systems.[16, 17] Using density functional theory (DFT) calculation, Chen et al.[18] proposed that O_v plays the important role in determining the FM in Fe doped rutile TiO_2.

There are several experimental reports supported the intrinsic nature of FM in Fe:TiO_2 DMS.[12, 19-21] However, Balcells et al.[16] did not observed FM in their Fe:TiO_2 nanoparticles and suggested that FM in Fe:TiO_2 system is an extrinsic effect due to either ferromagnetic secondary phases or any other impurity phases. Moreover, Kim et al.[22] reported that FM in their samples is related to the formation of secondary Fe_2O_3 phase suggesting extrinsic origin of FM. Unlike many other metals (i.e., Fe, Co, Ni), Cr itself is antiferromagnetic and their clusters/compounds (except nanocrystalline CrO_2) do not contribute to ferromagnetism. Thus, it would not induce an extrinsic ferromagnetism even if Cr clustering occurs in the Cr doped TiO_2 (Cr:TiO_2) nanostructures. Moreover, the pure phase ferromagnetic CrO_2 is difficult to synthesize[23] because it is metastable at atmospheric pressure.

At present, most of the reported FM in undoped and doped TiO_2 systems has been for thin films[24-26] and nanoparticles[27] while their undoped bulk counterparts are diamagnetic or paramagnetic. This implies that the spatial dimensionality might play an important role in the ferromagnetic ordering. Compared to thin films and nanoparticles, exploitation of 1D TiO_2 nanostructures such as nanowires, nanorods (NRs) and nanoribbons (NRbs) with high surface area make it easier to engineer high availability of defect sites for trapping electrons and may favor the ferromagnetic ordering, thus making them an ideal candidate for the realization of intrinsic enhanced RTFM. Moreover, 1D nanostructures are favored compared to nanoparticles in terms of electron transport, storage and information processing that can enhance the performance of spintronic devices at the nanoscale for practical applications. Although lots of reports on the RTFM in undoped and TM (Fe, Cr) doped TiO_2 thin films and nanoparticles are available in the literature,[19, 24, 25, 28, 29] there is little information about undoped and doped 1D nanostructures.[21, 30, 31] In our recent report[32] (which is discussed in *Chapter 5*), we observed RTFM in undoped TiO_2 NRbs and the FM was enhanced after vacuum annealing which suggested that O_v defects are the source of magnetism in undoped TiO_2. The earlier results motivated us to examine the individual and combined effect of TM doping and oxygen vacancy defects and clarify the controversial issues related to the long-range ferromagnetic ordering in TM doped TiO_2 systems. Moreover, a clear demonstration by correlating the magnetism between dopant concentration and O_v defects in the host semiconducting oxide lattice is crucial and it needs thorough investigations. Our present attempt in this study is to enhance the magnetic moments by Fe and Cr doping into the TiO_2

matrix and explore a better understanding about the origin of observed FM in doped TiO_2 1D systems.

Here, we grow Fe and Cr doped TiO_2 1D nanostructures by solvothermal/ hydrothermal method and study the effect of doping concentrations and calcination temperatures on the optical and magnetic properties. We investigate the origin of RTFM in the Fe and Cr doped TiO_2 nanostructures. The high surface area and higher concentration of surface defects, such as oxygen vacancies, expected in these nanostructures could ultimately lead to enhanced ferromagnetic ordering and strong FM even at room temperature. In *Chapter 5*, it was demonstrated that a large concentration of oxygen vacancies with high thermal stability indeed results in RTFM in undoped TiO_2 systems. Moreover, when TiO_2 is doped with low concentration of Fe and Cr, its properties are modified. For example, additional oxygen vacancy defects are expected due to the substitution of Ti^{4+} by Fe^{3+} and Cr^{3+} in TiO_2 lattice and thus, formation of Fe^{3+}-O_v and Cr^{3+}-O_v defect complexes resulting in enhanced FM in Fe and Cr doped TiO_2 nanostructures, respectively is expected compared to undoped TiO_2. However, we observed that higher concentration of Fe doping leads to decrease in FM that may be due to the Fe^{3+}-Fe^{3+} antiferromagnetic ordering in the absence of O_v in between two nearby Fe atoms. Similar behavior is observed for higher concentration of Cr doping. These results highlight that TM ion in the presence/ absence of O_v in the host TiO_2 still play a major role in deciding the DMS properties. The primary aim of this work is to figure out the precise role and impact of O_v defects and Fe and Cr dopants on the observed RTFM in our Fe:TiO_2 and Cr:TiO_2 nanostructures, which is supported by structural and optical measurements.

7.2. Growth and processing of doped TiO_2 nanostructures

Growth of Fe doped TiO_2 nanoribbons: The details of the synthesis procedure for the undoped TiO_2 NRbs were discussed in *Chapter 5*. For Fe doped samples, Fe_2O_3 (Loba Chemie) is used as precursor with appropriate quantity (0.1 at.% and 0.2 at.% of Fe) and mixed with anatase TiO_2 precursor, ground it for 10 minutes in a ceramic mortar, then mixed with the alkaline 10M NaOH mixed solvent and similar growth procedure was followed as for the undoped samples.

Table 7.1. Details of the samples synthesis, crystal structures and magnetization parameters: Crystal structure obtained from XRD studies, saturation magnetization (M_s), remanent magnetization (M_r), and Coercive field (H_c) were determined from M–H loops.

Samples name	Reaction temperature, duration, calcinations	% Fe/ Cr doping	Crystal structures	M_s (emu g^{-1})	M_r (emu g^{-1})	H_c (Oe)
A500	180 °C, 24 h, 500 °C	undoped	TiO_2(B)	0.061	0.004	0.099
B500	180 °C, 24 h, 500 °C	0.1% Fe	TiO_2(B)	0.292	0.031	0.129
B500V	B500 vac. annealed	0.1% Fe	TiO_2(B)	0.382	0.043	0.133
B700	180 °C, 24 h, 700 °C	0.1% Fe	Anatase	0.253	0.021	0.09
B900	180 °C, 24 h, 900 °C	0.1% Fe	Anatase-rutile	0.171	0.013	0.088
C500	180 °C, 24 h, 500 °C	0.2% Fe	Anatase-TiO_2(B)	0.075	0.008	0.134
D500	170 °C, 24 h, 500 °C	0.3% Cr	TiO_2(B)	0.320	…..	…..
D500V	D500 vac. annealed	0.3% Cr	TiO_2(B)	0.410	…..	…..
D700	170 °C, 24 h, 700 °C	0.3% Cr	Anatase	0.228	…..	…..
D900	170 °C, 24 h, 900 °C	0.3% Cr	Anatase-rutile	…..	…..	…..
E500	190 °C, 24 h, 500 °C	0.3% Cr	TiO_2(B)	0.276	…..	…..
F500	190 °C, 24 h, 500 °C	0.7% Cr	TiO_2(B)	0.111	…..	…..
F700	190 °C, 24 h, 700 °C	0.7% Cr	Anatase	…..	…..	…..
F900	190 °C, 24 h, 900 °C	0.7% Cr	Anatase-rutile	…..	…..	…..

For convenience of discussion here, the undoped TiO_2 NRbs samples are categorized as "A" and after calcinations at 500 °C are named as A500. The 0.1% Fe doped samples are termed as 'B' series and after calcinations at 500, 700, and 900 °C are named as B500, B700, B900, respectively. The sample B500 after vacuum annealing at 300 °C under 1.2×10^{-2} mbar

pressures for 2 h is named as B500V. Similarly 0.2% Fe doped sample is termed as C500 after calcinations at 500 °C. The details of the growth conditions and nomenclatures for different samples are shown in **Table 7.1**.

Growth of Cr doped TiO_2 nanorods/nanoribbons: Anatase TiO_2 powder, chromium nitrate nonahydrate ($Cr(NO_3)_3 \cdot 9H_2O$) were used as TiO_2 and Cr precursors, respectively. DI water was used as solvent for the synthesis of Cr doped TiO_2 nanostructures. The appropriate quantity (0.3 at% and 0.7 at% of Cr) was mixed with TiO_2 powder and ground it for 10 minutes in a ceramic mortar. The mixed powder was added in 10M NaOH (alkaline water) and stirred for 30 minutes in a conical flask. Then the solution was transferred into the Teflon-lined autoclave for hydrothermal reaction at 170 and 190 °C for 24 h. The precipitates after HCl treatment and washing with DI water were allowed for calcinations in a hot furnace at 500 – 900 °C temperatures. For the simplicity of discussion, the 0.3% Cr doped sample grown at 170 °C is named as "D" series and after calcinations at 500, 700 and 900 °C are named as D500, D700 and D900, respectively. The sample D500 after vacuum annealing at 300 °C under 1.2×10^{-2} mbar pressures for 2 h is named as D500V. The 0.3% Cr doped sample grown at 190 °C is termed as E500 after calcinations at 500 °C. Similarly 0.7% Cr doped sample grown at 190 °C is termed as F500, F700 and F900 after calcinations at 500, 700, and 900 °C, respectively. The details of the growth conditions and nomenclatures for different samples are shown in **Table 7.1**.

The results and discussion section is presented separately for Fe and Cr doped samples.

7.3. Results and discussion for Fe doped TiO_2 nanostructures

7.3.1. XRD pattern

The XRD patterns of the solvothermally synthesized undoped and Fe doped TiO_2 nanostructures after different calcinations are shown in **Fig. 7.1**. All the peaks correspond to TiO_2(B) phase for the sample A500 and B500; however, the diffraction peaks of doped sample (B500) is shifted to lower angle compared to the undoped sample (A500). The inset in **Fig. 7.1(a)** shows a enlarged view of (110) peak of TiO_2(B) phase, showing the lower angle peak shift in doped sample. This lower angle shift in doped sample provides a clue

regarding the occupation of mostly Fe^{3+} ions at the substitutional sites of Ti^{4+} in TiO_2 host lattice. Note that for a coordination number of 6 (octahedral), high spin Fe^{3+} (0.79 Å) has slightly larger ionic radii than Ti^{4+} ion (0.75 Å), so Fe^{3+} can more easily substitute Ti^{4+} in TiO_2 lattice and the corresponding lattice expansion (the lower 2θ value) is expected. Patel et al.[21] reported the incorporation of high spin Fe^{3+} and occupation of Ti^{4+} site in TiO_2 using Mössbauer spectroscopy. The inset of **Fig. 7.1(a)** shows a very broad peak with a shift in the center of peak by ~0.06° for the (110) at 24.91°. Note that the step size was 0.01° for the XRD measurement. So, we believe that the shift is meaningful and may be due to the substitution of Ti^{4+} by Fe^{3+} ion. The large concentration of oxygen vacancy in doped sample may also have some contribution for the lattice expansion, as it is reported theoretically[33, 34] that the Ti-Ti and Ti-O bonds are relaxed due to the missing O atom. The nearest-neighbor Ti atoms move outward from the vacancy to strengthen the bonding with rest of the neighboring O lattice. While the next-nearest-neighboring O atoms move slightly inward due to the absence of electrostatic repulsion by the missing O atom. The outward relaxation is more compared to inward relaxation; as a result lattice expansion is possible. We observed the mixed phase TiO_2(B)-anatase for C500 with mostly anatase phase while pure TiO_2(B) phase for B500, indicating that dopant concentrations play an important role for the formation of different phases of TiO_2. **Fig. 7.1(b)** shows the phase transformation of 0.1% Fe doped samples with different calcination temperatures. The XRD pattern of sample B700 reveals the pure anatase phase, whereas B900 reveals mixed phase anatase-rutile with mostly anatase

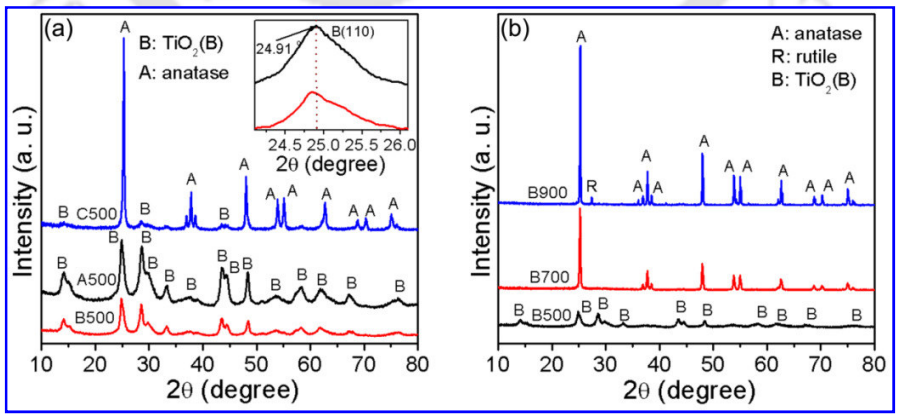

Fig. 7.1. Comparison of XRD patterns for different samples: (a) A500, B500 and C500; (b) B500, B700 and B900. The inset in (a) shows the magnified view of corresponding (110) brag peak of TiO_2(B) indicating shift in peak position for A500 and B500 samples.

structure. Note that no segregated phases such as Fe-Ti oxides ($FeTiO_3$ (JCPDS: 79-1838), Fe_2TiO_5 (JCPDS: 73-1898)), iron oxides (Fe_2O_3 (JCPDS: 79-1741), Fe_3O_4 (JCPDS: 85-1436)) and metallic clusters (JCPDS: 85-1410) are found within the XRD detection limit.

7.3.2. FESEM and TEM studies

FESEM imaging: The morphologies of the as-synthesized nanostructures observed by FESEM are shown in **Fig. 7.2**. The FESEM image of sample A500 (**Fig. 7.2(a)**) shows long and straight NRbs of TiO_2. **Figs. 7.2(b)-(d)** show the FESEM images of Fe doped samples, i.e., B500, B700 and C500, respectively. These samples show the well-defined 1D NRbs without any signature of impurity cluster, indicating that all the precursor anatase TiO_2 and Fe_2O_3 are uniformly mixed and distributed throughout the solvent and formed a uniform aqueous mixed solution and then underwent the solvothermal reaction inside the high pressure reaction chamber and formed doped 1D NRbs. The EDX spectrum of NRbs (B500) is shown in **Fig. 7.2(e)**, which shows only Ti, O and Fe elements indicating that no other contamination element is introduced into the Fe:TiO_2 nanostructures during the sample preparation.

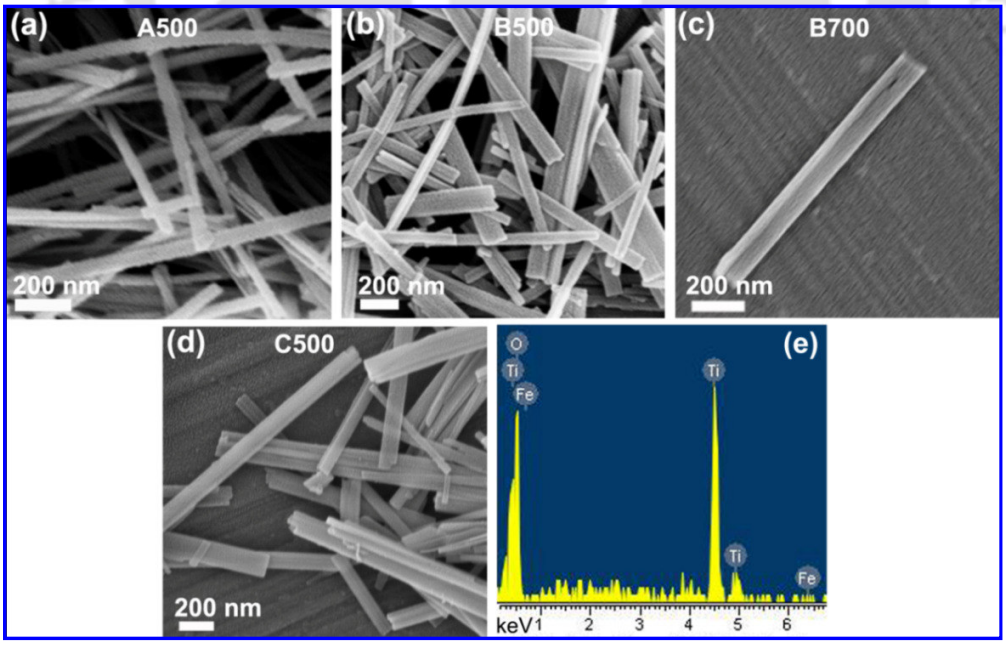

Fig. 7.2. FESEM images of the morphology of TiO_2 NRbs: (a) A500, (b) B500, (c) B700 and (d) C500; (e) the EDX spectrum of B500 indicating Ti, O and Fe elements.

TEM imaging: **Figs. 7.3(a)-(b), (c)-(d) and (e)-(f)** show the TEM images of as-grown samples A500, B500 and C500, respectively. All the samples show the complete formation of 1D NRbs morphology consistent with the FESEM images. The nanobricks like structures are attached on the surface of the NRbs making them porous like structures. Besides the surface, HRTEM image in **Fig. 7.3(e)** shows that nanobricks are also observed at the edges of the NRbs. These surface morphologies are not affected by the Fe doping, indicating that Fe is successfully incorporated into the TiO_2 crystal lattice, and thus eliminating any impurity and Fe metal clusters forming from the morphological point of view. The insets in **Figs. 7.3(a), (c) and (e)** show the SAED patterns of the corresponding NRbs. The SAED patterns demonstrate single crystalline nature and clearly indicate the monoclinic structure of TiO_2(B) phase of as-grown samples, fully consistent with the XRD results. **Fig. 7.3(b)** shows the HRTEM lattice fringe of A500 with d-spacing of 3.55 Å corresponding to (110) plane of TiO_2(B) phase. The HRTEM lattice fringe of B500 with d-spacing of 3.55 Å and 3.07 Å corresponds to (110) and (002) plane of TiO_2(B) phase, respectively (**Fig. 7.3(d)**). **Fig. 7.3(f)** shows the lattice fringe of C500 with d-spacing of 2.62 Å corresponding to (110) plane of anatase TiO_2 phase. These nanoporous NRbs with nanobricks like structures on the surface of

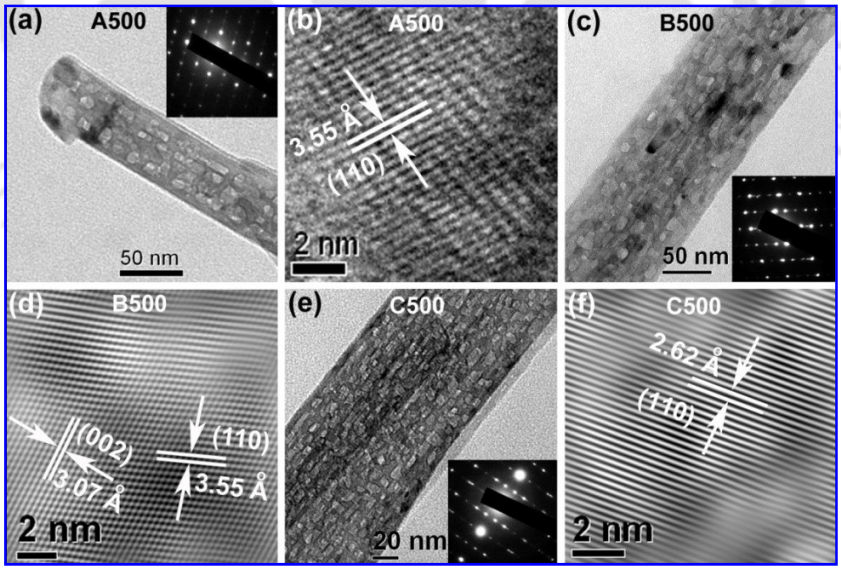

Fig 7.3. TEM image of (a) higher magnification single nanoporous NRb in A500, inset is the corresponding SAED pattern; (b) HRTEM lattice fringe of A500; (c) higher magnification single nanoporous NRb in B500, inset is the corresponding SAED pattern; (d) HRTEM lattice fringe of B500; (e) higher magnification single nanoporous NRb in C500, inset is the corresponding SAED pattern; (f) HRTEM lattice fringe of C500.

NRbs may arise due to the defects in TiO_2 and this plays a crucial role in tuning the electrical, optical and magnetic properties of the nanostructures. Note that the precursor TiO_2 powder did not show any trace of FM, despite the presence of a large concentration of oxygen vacancies as evidenced by a strong visible PL band. Thus, the surface morphology strongly influences the surface defects as a result of different surface areas and seems to be able to tune the RTFM.

7.3.3. Optical absorption studies

Light absorption characteristics of the solvothermally synthesized TiO_2 NRbs and the precursor TiO_2 ($PTiO_2$) are shown in **Fig. 7.4**. All the as-synthesized samples exhibit a red-shift of the absorption edge and considerable absorption in the visible violet region. With the increase in doping concentration, the band gap is slightly decreased (inset of **Fig. 7.4(a)**). According to the energy band structure of TiO_2, the valence band (VB) top and the conduction band (CB) bottom correspond to mainly O 2p and Ti 3d states, respectively. The optical absorption around 380 nm for precursor TiO_2 is solely due to the band-to-band (O 2p $\rightarrow$ Ti 3d) transition, while the slight red shift in Fe:TiO_2 NRbs can be explained as being mainly due to sp-d exchange interactions between the band electrons and the localized *d* electrons of the Fe^{3+} ions substituting Ti^{4+} cations. The s-d and p-d exchange interactions give rise to downward shifting of the CB edge and an upward shifting of the VB edge, leading to a band gap narrowing. The indirect band gap of all samples were determined from the linear fit to the linear portion of the $(\alpha hv)^{1/2}$ versus hv plot (insets of **Fig. 7.4**). The calculated band gap of undoped, 0.1% and 0.2% Fe doped TiO_2 NRbs are 3.22, 2.71, and 2.66 eV, respectively. The lowering of band gap energy for undoped NRbs synthesized by solvothermal method was shown in *Chapters 4, 5* and reported by us,[32, 35] which are attributed to O_v and Ti interstitial defects in TiO_2 NRbs. So, it is not straight forward to indentify the origin of the band gap narrowing in Fe:TiO_2 NRbs from the absorption spectra only. **Fig. 7.4(b)** shows the comparison of absorption spectra of B500 and B900. With increase in calcination temperature, the band gap is decreased. Note that B900 sample shows Ti interstitial defect related near infrared PL in the PL spectra (discussed below) and this defect may be responsible for the decrease in band gap.[35] The red shift in the absorption edge in the as-synthesized NRbs may be associated with oxygen vacancies.

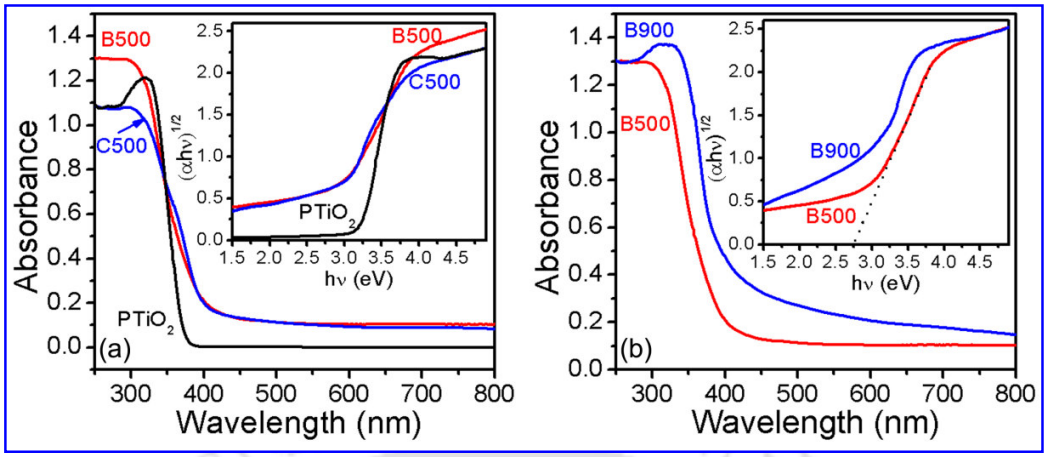

Fig. 7.4. UV-visible-NIR absorption spectra: (a) B500, C500 and precursor TiO_2; (b) B500 and B900. The inset in each case shows the $(\alpha h\nu)^{1/2}$ *vs* $h\nu$ plot indicating the indirect band gap for the corresponding absorption spectrum of each sample. Band gap energy is calculated from the extrapolated line (dashed) fitted to the respective linear portions.

7.3.4. Photoluminescence studies

In order to confirm the nature of defects in undoped and doped TiO_2, PL studies are performed. **Fig. 7.5(a)** shows the room temperature PL spectra of samples A500, B500, B900 and B500V under identical conditions of measurement. The observed broad visible PL for all samples is primarily related to self-trapped excitons and O_v related defect states in TiO_2.[32, 36] **Fig. 7.5(b)** shows the comparison of PL spectra for B500 and C500. It is observed that the intensity of visible PL decreases for sample C500, indicating less concentration of oxygen vacancy in C500 compared to B500. For a clearer understanding of the origin of the broad PL emission, the deconvolution of the peak was necessary. The broad emission peak of sample B500 is fitted properly with four Gaussian bands centered at 469.1 (peak 1), 519.2 (peak 2), 596.5 (peak 3) and 745.8 (peak 4) nm, as shown by the solid lines (blue curves) in **Fig. 7.5(c)**. According to the literature, peak 1 may be ascribed to self-trapped excitons located at TiO_6 octahedra, while peak 2 and 3 are ascribed to O_v related trap states.[36] Peak 4 is attributed to the presence of hydroxyl (OH^-) species which may form an acceptor level just above the valence band.[32] After vacuum annealing (sample B500V), the visible PL intensity

is increased, which is an indication that the visible PL may be due to the O_v related defect trap states. Upon the loss of an O atom from TiO_2 lattice, the electron pair that remains trapped in the vacancy cavity gives rise to an F center and one of the electron in the F center tends to occupy the neighboring Ti^{4+} ion and yield Ti^{3+} center and F^+ center states within the band gap of the material.[32] Further, the incorporation of Fe^{3+} into the substitutional site of Ti^{4+} creates additional oxygen vacancies for the charge neutrality in the host crystal lattice. Therefore, a large concentration of O_v is expected in our Fe doped samples compared to undoped samples and this is observed from the enhancement of visible emission for doped samples in the PL spectra. We observed that the visible PL decreased for the Fe doped sample calcined at 900 °C as compared to the sample calcined at 500 °C. This is because of the dehydration of as-grown solvothermal products and creation of oxygen vacancies at lower calcination temperatures and the molecular O_2 may not interact with the material at this stage. However, at higher observed that the visible PL decreased for the Fe doped sample calcined at 900 °C as compared to the sample calcined at 500 °C. This is because of the dehydration of as-grown solvothermal products and creation of oxygen vacancies at lower calcination temperatures and the molecular O_2 may not interact with the material at this stage. However, at higher calcination temperature (900 °C), the molecular O_2 interacts with the surface of the materials and start filling oxygen vacancies. The NIR PL observed for the samples A500 and B900 is attributed to the Ti interstitial defects in TiO_2.[35] Note that the NIR PL is not observed for B500 and B500V, indicating the absence or very low concentration of Ti interstitial defects below the detection limit. The Ti interstitial defects related NIR PL evolved with higher growth temperatures and calcination temperatures and the corresponding mechanism was explained in *Chapter 4* and our previous report.[35] So, we observed mainly Ti interstitial defects in B900, which was calcined at 900 °C. In order to gain a better understanding of broad visible PL, we performed the time-resolved PL (TRPL) measurements for B500 monitoring the emission at 550 nm with 405 nm laser excitation and the data is shown in **Fig. 7.5(d)**. The TRPL spectrum is fitted by a bi-exponential decay curve with time constant τ_1 = 0.4 ns and τ_2 = 2.2 ns. This result reveals that two defect states contributed to the emission at 550 nm, consistent with the steady state PL contribution of peak 2 and peak 3 excluding the negligible contribution from peak 4.

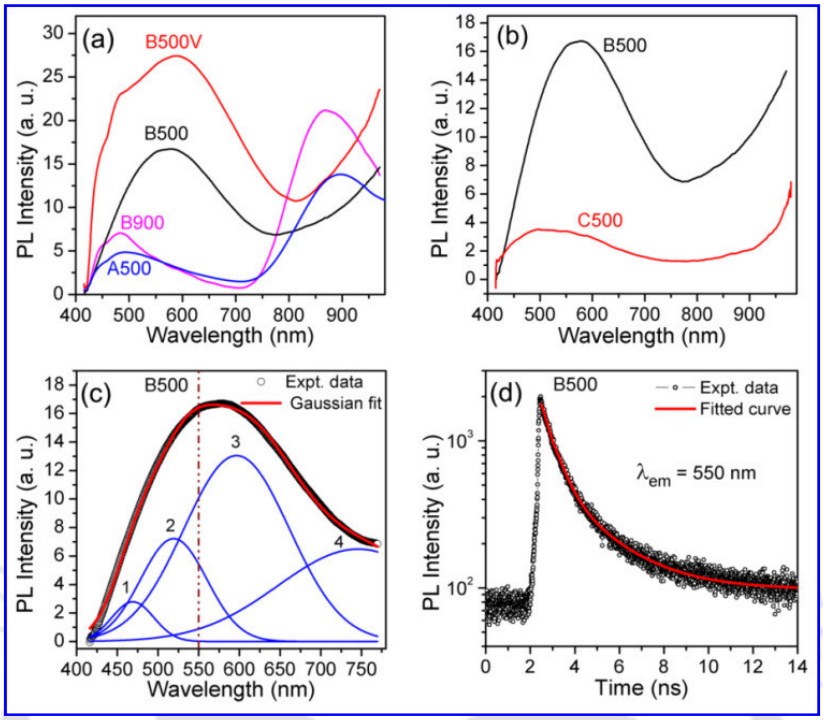

Fig. 7.5. Room temperature PL spectra for: (a) A500, B500, B900 and B500V; (b) comparison of PL of B500, C500; (c) visible PL of B500 with Gaussian peak fitting; (d) shows the PL decay of B500 with bi-exponential decay fit.

7.3.5. XPS and ESR studies

XPS studies: XPS is a unique tool to investigate surface defects and chemical environment, because of its high sensitivity to surface. A more direct evidence of O_v related surface defect states and incorporation of Fe^{3+} in TiO_2 matrix are further confirmed from XPS analyses. A comparison of the Ti 2p core level spectra for sample B500, B500V and B500, C500 are shown in **Fig. 7.6(a) and (b)**, respectively. The Ti $2p_{3/2}$ and Ti $2p_{1/2}$ core level peak positions of samples B500, B500V, C500 are at 458.2, 458.1, 458.5 eV and 464.1, 463.9, 464.4 eV, respectively indicating Ti^{4+} state. Interestingly, the Ti 2p peak slightly shifts to lower binding energy in vacuum annealed sample B500V as compared to B500, which can be attributed to large concentration of O_v in B500V.[37] The Ti 2p peaks of C500 are shifted to higher binding energy compared to B500. Further, an obvious broadening and shouldering of Ti $2p_{3/2}$ peak towards higher binding energy for sample C500 can be noted, which may be

due to the effect from large concentration of Fe^{3+} in the interstitial and/ or substitutional site in the TiO_2 crystal lattice. A lower binding energy for O 1s core level peak is observed for B500V (**Fig. 7.6(c)**), while higher binding energy is observed for C500 as compared to B500 (not shown). Note that we observed a higher binding energy shoulder in the O 1s spectra for both B500 and B500V. Such a shouldering may be attributed to the presence of O_C (oxygen bound to carbon), OH^- species (O_H) in TiO_2 nanostructures.[32, 38] In particular, the shouldering is enhanced for B500V, which implies that the O_v concentration is dramatically increased after vacuum annealing; this ultimately increases the reactivity and binds more carbon and hydrogen as impurity. Finally, the Fe 2p core level spectrum of C500 is shown in **Fig. 7.6(d)**. The Fe $2p_{3/2}$ and $2p_{1/2}$ peaks are observed at 710.7 and 724.7 eV, respectively, which are the characteristic peaks of Fe^{3+}. This is significantly different from that of the metallic Fe, whose $2p_{3/2}$ peak position is at 706.25 eV. Moreover, the broad satellite peak at around 717.5 eV is attributed to Fe^{3+} state. Thus Fe doping and corresponding Fe^{3+} states are confirmed in the doped samples.

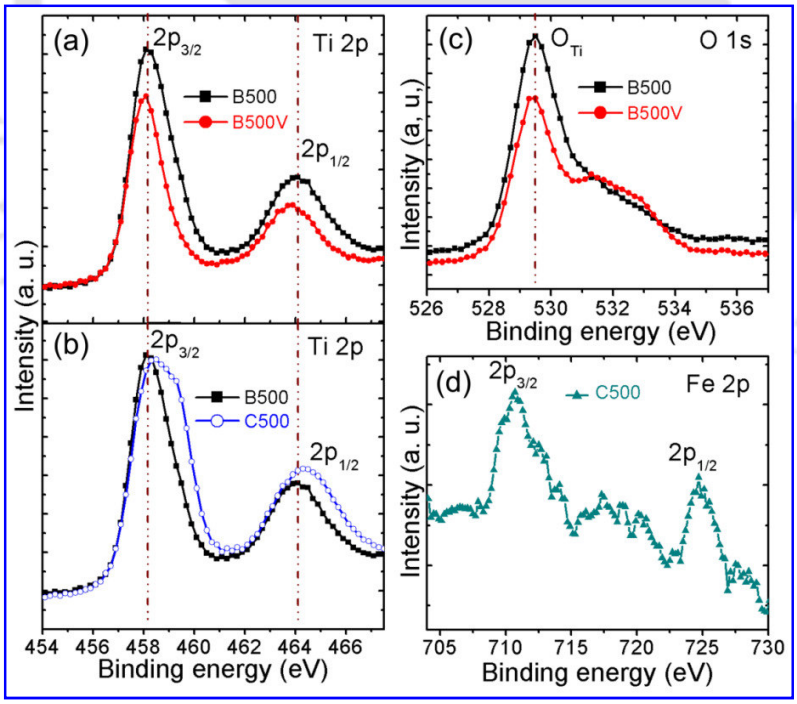

Fig. 7.6. XPS spectra: (a) Ti 2p core level spectra for B500 and B500V. (b) Ti 2p core level spectra for B500 and C500. Dotted vertical lines show the change in relative peak position in each case. (c) O 1s core level spectra for B500 and B500V. Dotted vertical line shows the change in relative peak position. (d) Fe 2p core level spectrum for C500.

ESR studies: ESR is an exceptionally powerful tool in detecting the spin polarized charge state of defective TiO_2 nanostructures. ESR spectra of Fe_2O_3, A500, B500 and C500 are shown in **Fig. 7.7(a)-(d)**, respectively. We observed the ESR signal with g values 2.00 and 1.97 for A500, B500, B700 and C500, and these signals are assigned to single ionized O_v (F^+) and Ti^{3+}, respectively.[35, 39] The ESR spectra reveal the g = 2.22 and 2.27 for B500 and C500, respectively, indicating the presence of Fe^{3+} in the TiO_2 lattice.[40] Note that the precursor Fe_2O_3 shows the ESR signal at g= 2.11 (**Fig. 7.7(a)**) and this is assigned to Fe^{3+} in Fe_2O_3, which is different from the g-value of the Fe^{3+} in B500 and C500 samples. This eliminates the existence of Fe_2O_3 type clusters in our samples. If it exists, the g-value should be at 2.16-2.00.[41] Inamdar et al.[40] reported that a broad signal with g= 2.20 corresponds to ferromagnetic resonance (FMR) and was arising due to the ferromagnetic exchange interaction between Fe^{3+} ions in Fe doped ZnO nanocrystals. Since the ESR signal is at g= 2.22 for B500 and it varies with Fe dopant concentration, this signal may be attributed to FMR signal due to the ferromagnetic exchange interaction between Fe^{3+} and F^+ ions. More interestingly, we observed ESR signal at g= 4.77 for samples A500, B500, B700 and C500 for the first time, and this signal is not observed in Fe_2O_3. Generally, ESR signal with g= 4.20 – 4.29 is reported for Fe^{3+} located in a strongly distorted rhombic environment.[40, 42] Hence, the observed g-value at 4.76 in our samples is not due to Fe species, because it is also observed in undoped sample (A500) and more intense compared to doped samples. Therefore, we assigned this signal to the Ti^{3+} in distorted octahedral environment and it may possibly have originated due to the O_v and contribute to the ferromagnetic resonance due to the orbital overlapping of $3d^1$ spin Ti^{3+} and $1s^1$ spin of F^+ within the O_v cavity in the TiO_2 NRbs. Note that the broad ESR signals of Fe doped TiO_2 NRbs consist of three overlapping signals and is clearly shown in **Fig. 7.7(c)** for B700 sample. The g-values are obtained by differentiating the observed broad 1^{st} order derivative ESR signal from all the samples. Thus, the ESR study proved very useful in identifying the Fe^{3+} in doped samples and O_v related Ti^{3+} and F^+ defects in both undoped and Fe doped samples. The Ti^{3+} defects are not observed in the XPS Ti 2p core level spectra, but observed in ESR spectra indicating that the Ti^{3+} species is present inside the bulk rather surface of NRbs[39] and this plays a very crucial role in enhancing the stability of ferromagnetic properties in TiO_2 system.

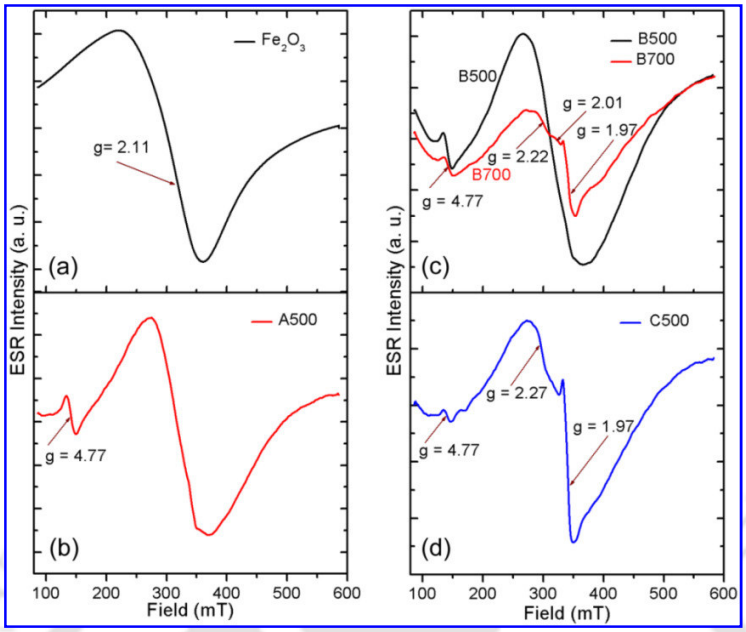

Fig. 7.7. Room temperature ESR spectra for: (a) Fe_2O_3, (b) A500, (c) B500 and B700, and (d) C500.

7.3.6. Magnetization studies

The magnetic properties of as-synthesized undoped and Fe doped samples were investigated using VSM. The field dependent magnetic (M–H) measurements are shown in **Fig. 7.8**. **Fig. 7.8(a)** shows ferromagnetic hysteresis loops for undoped sample A500. **Fig. 7.8(b)** shows the M–H loops of the 0.1% Fe doped samples. The saturation magnetization systematically decreases with increasing calcinations temperatures. This may be related to the different concentration of O_v and evolution of Ti interstitial defects. Note that the FM is enhanced by ~4.8 fold in Fe doped sample B500 compared to undoped A500 of same TiO_2(B) phase. It is well known that the structure of TiO_2 is very sensitive to oxygen content and can be easily reduced under an oxygen deficient environment. Therefore, the sample B500 was annealed at 300 °C under moderate vacuum in order to induce a higher concentration of oxygen vacancies in the sample. Interestingly, the FM is significantly increased for the vacuum annealed sample B500V as compared to B500. This clearly indicates that O_v indeed play the key role in inducing the FM in Fe doped TiO_2 system. The M-H measurement of sample C500 (0.2% Fe doped) is shown in **Fig. 7.8(c)**. It is observed that the saturation

magnetization decreases with increase in Fe doping concentration. These results underscore the active role of O_v defects and Fe dopant in the observed RTFM. Note that the observed M_s at room temperature in our undoped and Fe doped TiO_2 NRbs is more than three times and more than one order of magnitude higher than that reported for Fe and N co-doped TiO_2 nanorods[12] and other reported literatures.[31, 43] Our results provide strong indication that oxygen vacancies are directly involved in enhancing the ferromagnetic interaction. Such a strong RTFM in 0.1% Fe doped TiO_2 nanostructure may extend the development of spintronic devices which can be operated at RT. The magnetization parameters for different samples are listed in **Table 7.1**. Clearly, the 0.1% Fe doped vacuum annealed sample exhibit the highest M_s. Though PL measurement cannot provide quantitative analysis on the density of oxygen vacancies, following the discussion of *Chapter 5*,[32] we expect the oxygen vacancy density to be ~10^{16} cm^{-3} in our samples. However, more complimentary studies are requires for a better quantification of the vacancy density.

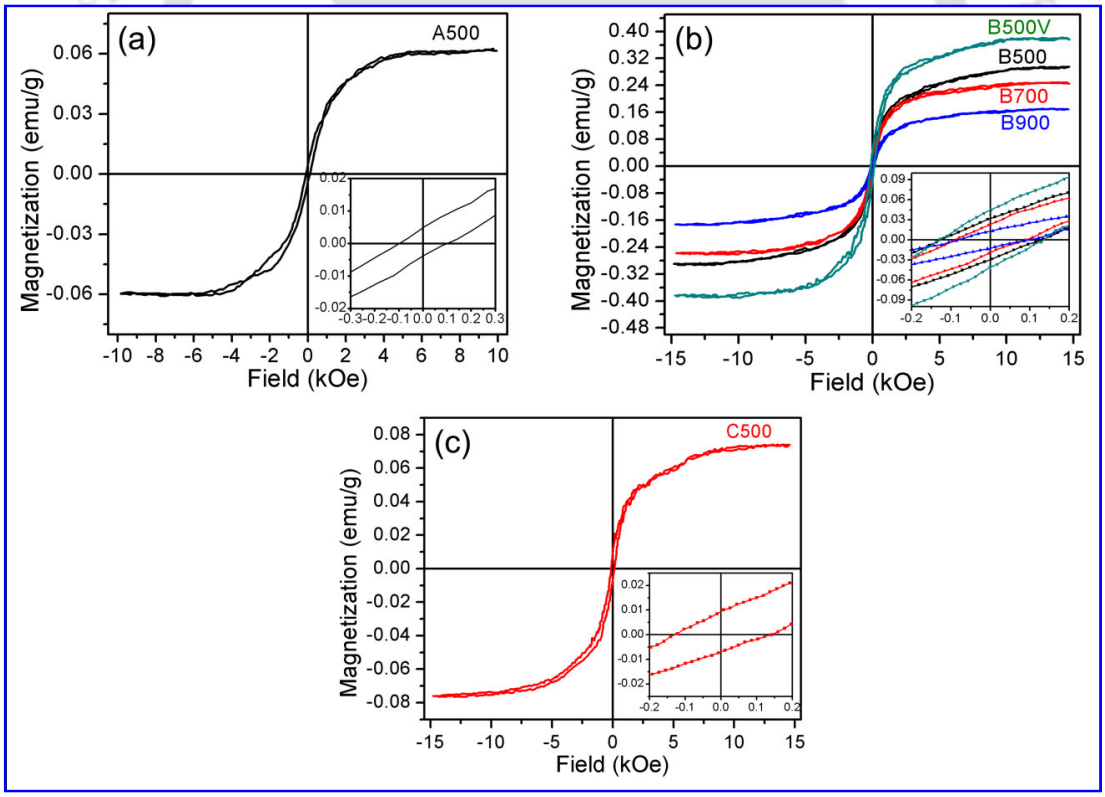

Fig. 7.8. Magnetic field versus magnetization (M–H) loop at room temperature showing hysteresis in samples: (a) A500; (b) B500, B700, B900 and B500V; (c) C500. The insets in each case show the M–H loop at low field near origin in magnified scale.

7.4. Results and discussion for Cr doped TiO_2

7.4.1. XRD pattern

The XRD patterns of Cr doped TiO_2 nanostructures are shown in **Fig. 7.9**. The 0.3% doped samples grown at 170 °C and 0.7% doped samples grown at 190 °C after different calcinations temperatures are shown in **Fig. 7.9(a) and (b)**, respectively. The sample D500 and F500 which are calcined at 500 °C show the brag peaks correspond to pure TiO_2(B) phase. All the peaks of samples D700 and F700 corresponded to pure anatase TiO_2 while the samples D900 and F900 show the mixed phases of anatase-rutile TiO_2. All the peaks of samples D500, E500 and F500 show the pure TiO_2(B) phase, indicating that TiO_2(B) phase is

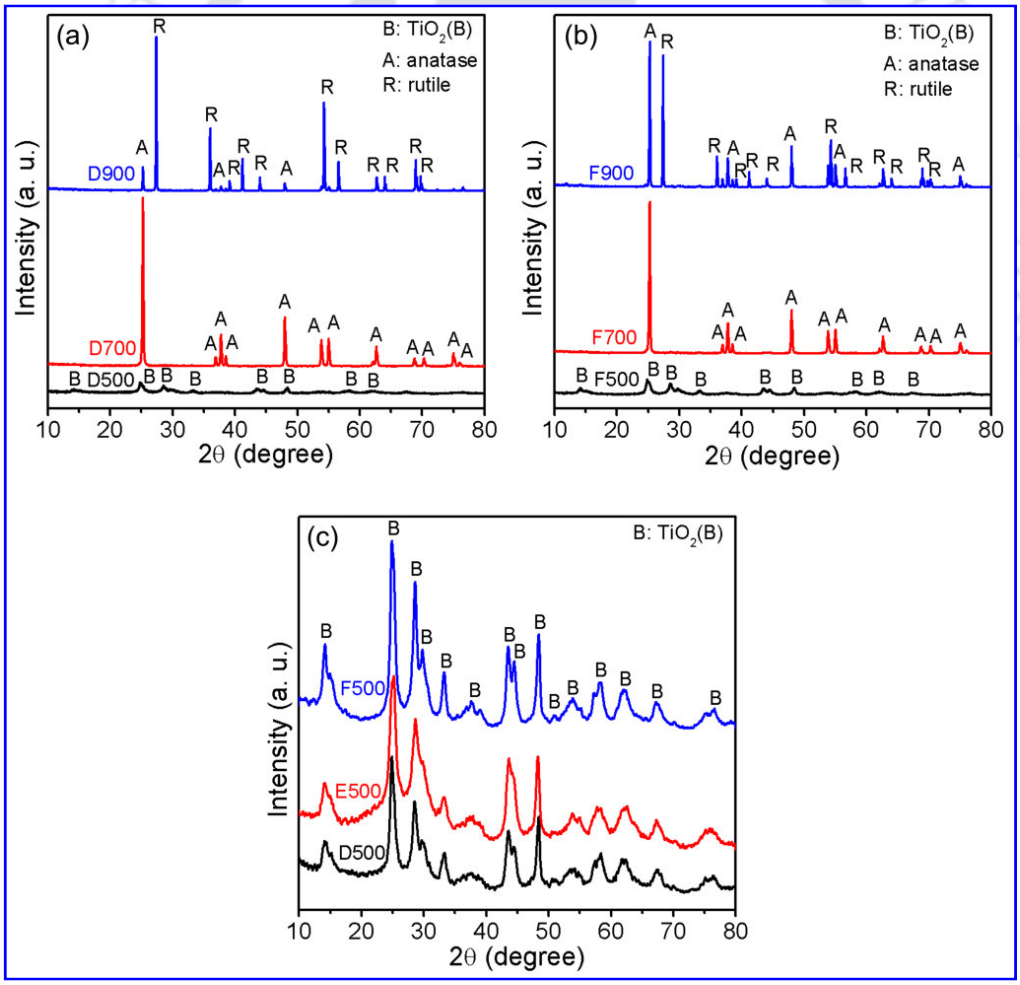

Fig. 7.9. XRD patterns of the Cr doped samples: (a) D500, D700 and D900; (b) F500, F700 and F900; (c) D500, E500 and F500.

formed after 500 °C calcinations irrespective of growth temperatures and doping concentrations (**Fig. 7.9(c)**). No signature of peaks related to Cr or Cr-oxides are observed in these Cr doped samples within the XRD detection limit, indicating the Cr may be successfully doped into the TiO_2 crystal lattice. Due to the similar ionic radii of Ti^{4+} (75 Å) and Cr^{3+} (76 Å) in 6-coordinate octahedral systems, the Cr^{3+} is more likely to occupy the regular lattice position and substituted for the Ti^{4+} cation in the TiO_2 lattice.

7.4.2. FESEM and TEM studies

FESEM imaging: The morphologies of the synthesized Cr doped samples as-studied by FESEM imaging are shown in **Fig. 7.10**. The high magnification image of a single nanorod (NR) of sample D500 is shown in **Fig. 7.10(a)**. **Fig. 7.10(b)** shows a single straight and thick nanoribbon like structure for the sample D900. The FESEM image of F500 shows the NRbs like structures co-existing with small nanorods (**Fig. 7.10(c)**). **Fig. 7.10(d)** shows the NRbs for the sample F700. These samples reveal the well-defined 1D NRs/NRbs without appearance of any additional impurity cluster, indicating that all the precursor anatase TiO_2 and $Cr(NO_3)_3{\cdot}9H_2O$ are uniformly mixed and homogeneously distributed throughout the solvent, and chromium ions are incorporated into the lattice of TiO_2 after hydrothermal treatment forming doped 1D NRs/NRbs.

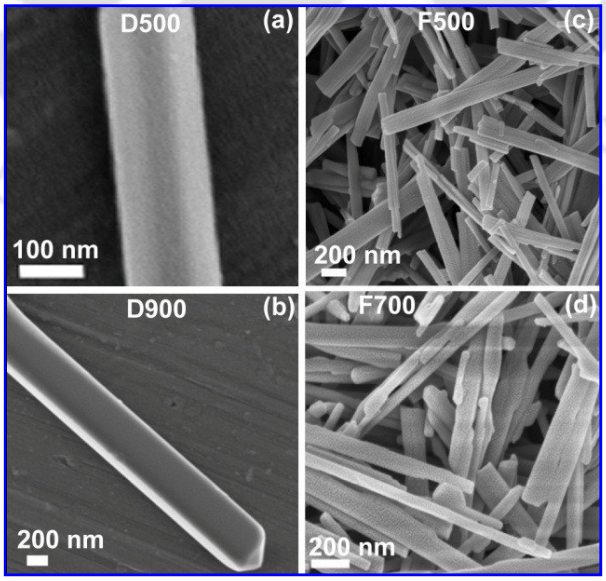

Fig. 7.10. FESEM images of Cr doped TiO_2 samples: (a) D500, (b) D900, (c) F500 and (d) F700.

TEM imaging: **Fig. 7.11** shows the TEM images of as-synthesized Cr:TiO_2 nanostructures. Sample D500 shows the NRs/NRbs with nanobricks/ nanostones like structures on the surface (**Fig. 7.11(a)**). The inset in **Fig. 7.11(a)** shows the SAED patterns of the corresponding NRs/NRbs, indicating single crystalline nature of TiO_2(B) phase. The high resolution TEM image of a single nanorod of D500 is shown in **Fig. 7.11(b)**, which shows nanobricks/ nanostones like morphologies on the surface making it a homogeneous nanoporous structures. The lattice fringe of the nanorod is shown in **Fig. 7.11(c)**. The d-spacing of 3.12 Å corresponds to (002) plane of TiO_2(B) phase. A single nanoribbon of F500 is shown in **Fig. 7.11(d)**. Nanobricks/ nanostones are formed on the surface of nanoribbon. The lattice fringe of the corresponding nanoribbon is shown in **Fig. 7.11(e)**. The d-spacing of 3.12 Å corresponds to (002) plane of TiO_2(B) phase. The SAED pattern of the nanoribbon is shown in **Fig. 7.11(f)** showing the single crystalline nature of TiO_2(B) phase. The monoclinic structure of TiO_2(B) is clearly observed in the well spotted SAED pattern. The cluster related structures is not observed in HRTEM images. Further clear SAED pattern of TiO_2(B) phase dictates that Cr is well incorporated into the TiO_2 crystal lattice.

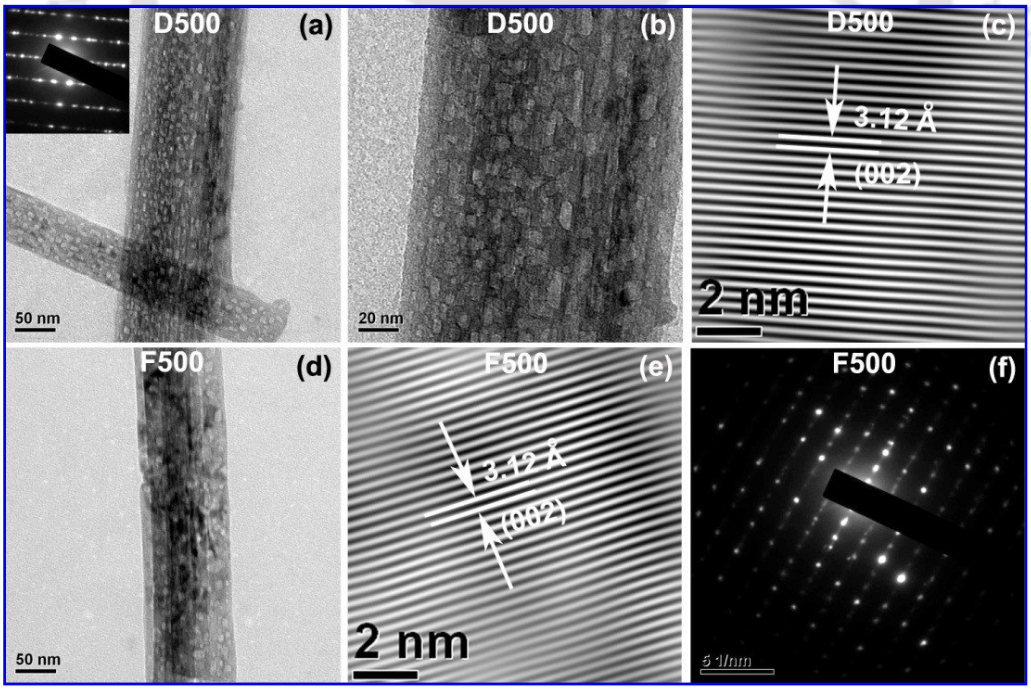

Fig. 7.11. TEM images of Cr doped TiO_2 nanorods/nanoribbons: (a) D500, inset is the corresponding SAED pattern; (b) D500, high magnification image; (c) lattice fringe of nanorod of D500; (d) F500; (e) lattice fringe of nanoribbon of F500; (f) SAED pattern of F500.

7.4.3. Optical absorption and Photoluminescence studies

Optical absorption studies: The UV-visible-NIR absorption spectra of D500, D700 and D900 along with precursor TiO_2 are shown in **Fig. 7.12(a)**. The absorption edge of Cr doped samples is red-shifted compared to the precursor TiO_2 ($PTiO_2$) nanoparticles. The red-shift in doped sample can be assigned to the charge transfer band $Cr^{3+} \rightarrow Ti^{4+}$ [44] or may be due to the oxygen vacancy.[32] The large red shift is observed for the sample D900 which is attributed to presence of large concentration of Ti interstitial defects.[35] The D900 sample shows strong Ti interstitial defects related NIR PL discussed in the following paragraph. The indirect band gaps of the Cr doped samples are shown in **Fig. 7.12(b)**. It is seen that the band gap of the doped samples are reduced as compared to the $PTiO_2$ (3.22 eV). The calculated band gaps are 2.73, 2.73 and 2.38 eV for the samples D500, D700 and D900, respectively which is very important for the visible light photocatalytic applications.

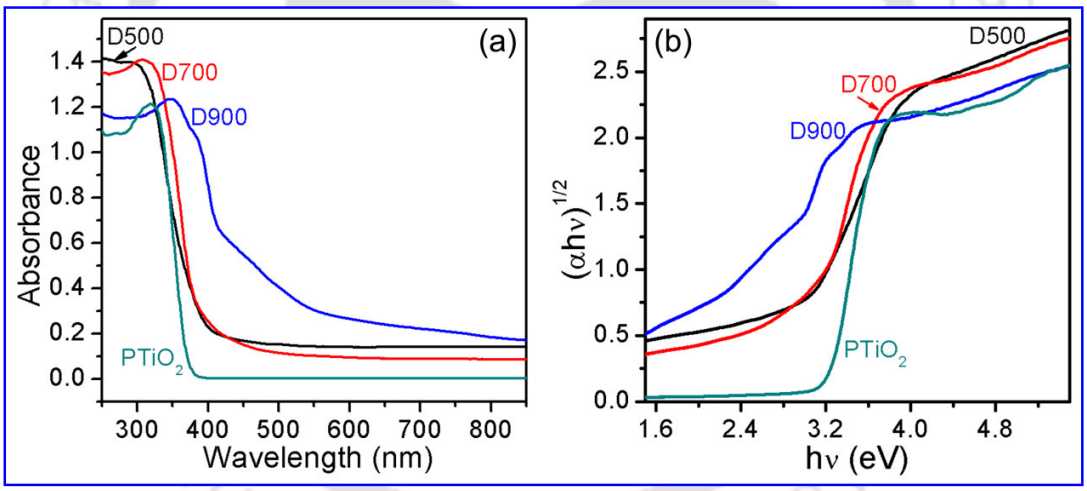

Fig. 7.12. (a) UV-visible-NIR absorption spectra of Cr doped samples D500, D700, D900 and precursor TiO_2 ($PTiO_2$), (b) $(\alpha hv)^{1/2}$ *vs hv* plot indicating the indirect band gap for the corresponding absorption spectrum of each sample.

Photoluminescence studies: **Fig. 7.13(a)** shows the room temperature PL emission spectra of 0.3% Cr doped samples grown at 170 °C after different calcinations temperatures. The broad visible PL is attributed to the oxygen related trap states emission.[32, 35] The NIR PL is related to the Ti interstitial defect related trap states emission whose evolution is discussed in

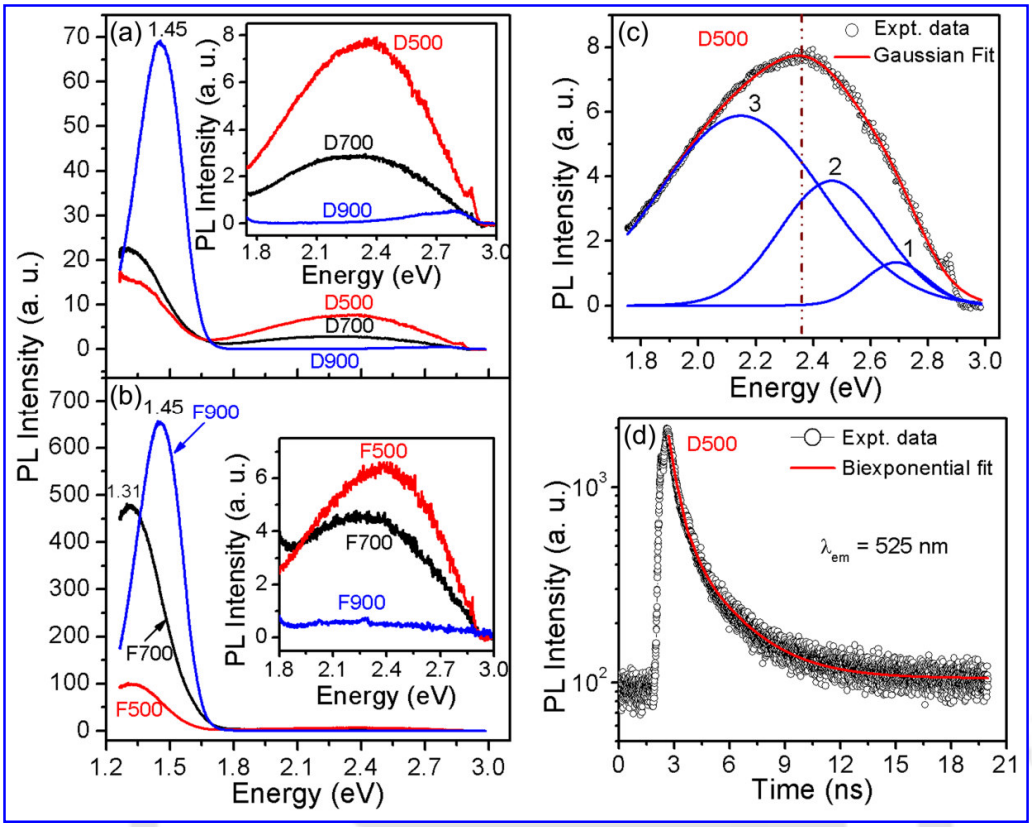

Fig. 7.13. PL spectra of Cr doped TiO_2 nanostructures: (a) D500, D700 and D900; (b) F500, F700 and F900; (c) Gaussian peak deconvolution of broad visible PL of D500; (c) PL decay spectrum of D500 monitored at 525 nm.

Chapter 4 and our previous report.[35] With increase in calcinations temperatures, the oxygen vacancy related visible PL decreases while Ti interstitial related NIR PL increases, which is consistent with the previous results for undoped TiO_2 NRbs whose origin and mechanism were discussed through an *in-situ* PL studies in *Chapter 4*. Similar response of PL is observed for the 0.7% Cr doped samples grown at 190 °C (**Fig. 7.13(b)**). These results indicate that the visible PL decreased due to reduction of oxygen vacancies during the calcinations at higher temperatures in air. Interestingly, the NIR PL is shifted to higher energy with increasing calcinations temperatures. The NIR PL at lower energy side can be attributed to the Ti^{3+} interstitial defects while the NIR PL at 1.45 eV is attributed to Ti^{4+} interstitial defect states within the band gap of Cr doped TiO_2 nanostructures.[35] Note that the observed intensity of NIR PL for the sample F900 is one order of magnitude higher

compared to that of D900; this may be due to the higher growth temperature. It seems that more interstitial defects are evolved at higher growth temperature, which was also discussed in *Chapter 4*. Cr^{3+} interstitial may also contribute to the NIR PL. In order to understand the origin of broad visible PL, we fit the spectrum of D500 with Gaussian peaks (**Fig. 7.13(c)**). The spectrum is well fitted with three Gaussian peaks. The peak 1 may be attributed to the emission from self trapped exciton while peak 2 and peak 3 are assigned to the emission from oxygen vacancy related F^+ and Ti^{3+} trap states, which was discussed in *Chapter 5*. Further we monitor the emission at 525 nm and measured the PL decay (**Fig. 7.13(d)**). The PL decay is well fitted with double exponential decay curve with time constants τ_1 = 0.3 ns and τ_2 = 2.5 ns. Thus, the emission at 525 nm is contributed by two defect states, i.e., peak 2 and 3 as shown by drawing the dotted vertical line in **Fig. 7.13(c)**. Thus the steady state PL and TRPL results are consistent.

7.4.4. XPS and ESR studies

XPS studies: The XPS measurements were carried out to obtain information about the electronic valence states of the elements in the Cr doped TiO_2 D500 sample (**Fig. 7.14(a)-(c)**). The Ti $2p_{3/2}$ and Ti $2p_{1/2}$ core level peak positions of sample D500 are at 458.0 eV and 463.7 eV, respectively which indicates that Ti is in 4+ oxidation state (**Fig. 7.14(a)**). **Fig. 7.14(b)** shows the O 1s core level spectrum of D500. The intense peak at 529.5 eV is attributed to the lattice O associated with Ti^{4+} while the asymmetric broad shouldering at higher binding energy may be due to the O attached to surface atmospheric carbon (O_C) contamination and hydroxyl group (O_H).[38, 45] The Cr 2p core level spectrum of D500 is shown in **Fig. 7.14(c)**. The asymmetric Cr $2p_{3/2}$ peak indicates the overlapping of more than one peak. So the deconvolution of the peak is necessary. The Cr $2p_{3/2}$ core level peak is deconvoluted by two Gaussian peaks centered at 577.0 and 579.7 eV. The peak at 577.0 eV is assigned to Cr^{3+} $2p_{3/2}$ state, while the peak at 579.7 eV is attributed to Cr^{6+} $2p_{3/2}$ state. Moreover, Cr $2p_{1/2}$ core level peak is observed at ~586 eV which is attributed to the Cr^{3+} state. The core level binding energy observed for the Cr $2p_{3/2}$ is different from ~574.02 eV of Cr metal or 576.3 eV of CrO_2.[46] It indicates that there is no metallic Cr or clusters on the surface of the nanostructure. These results signify that Cr has been incorporated as Cr^{3+} in the TiO_2 lattice.

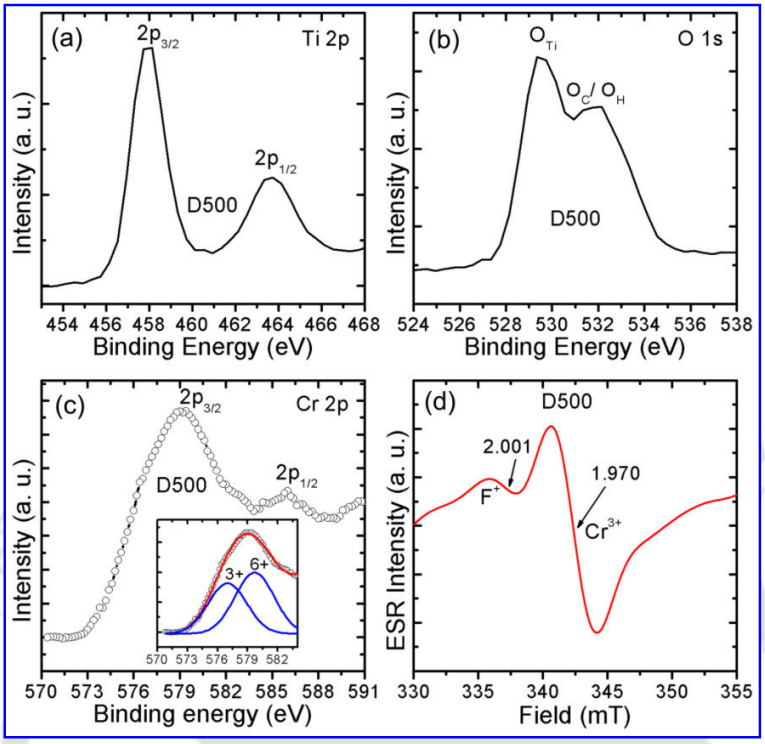

Fig. 7.14. XPS core level spectra for D500: (a) Ti 2p, (b) O 1s, (c) Cr 2p. (d) ESR spectrum of D500. The inset in (c) is the Gaussian deconvolution of Cr $2p_{3/2}$ peak, the symbols (open circles) represent the experimental data and the solid lines are the fitted curves.

ESR studies: The room temperature ESR spectrum of D500 is shown in **Fig. 7.14(d)**. We observed the ESR signal with g-values 2.001 (weak) and 1.970 (intense), and these signals are assigned to single ionized O_v (F^+) and Ti^{3+}, respectively.[35, 39] The Cr^{3+} signal is also observed at g=1.970.[47] Since no trace of Ti^{3+} is observed in XPS Ti 2p spectra and Cr^{3+} state is observed in Cr 2p spectra, we assigned this signal at g=1.970 to the Cr^{3+}. However, the presence of Ti^{3+} in the doped sample cannot be completely ruled out.

7.4.5. Magnetization studies

Room temperature magnetic measurements of the Cr doped TiO_2 nanostructures were carried out using a VSM. The field dependent magnetizations (M-H) of the doped samples are shown in **Fig. 7.15**. All the samples exhibit clear ferromagnetic hysteresis behavior with saturation magnetization. **Fig. 7.15(a)** shows the hysteresis loop of D500 and E500 which are

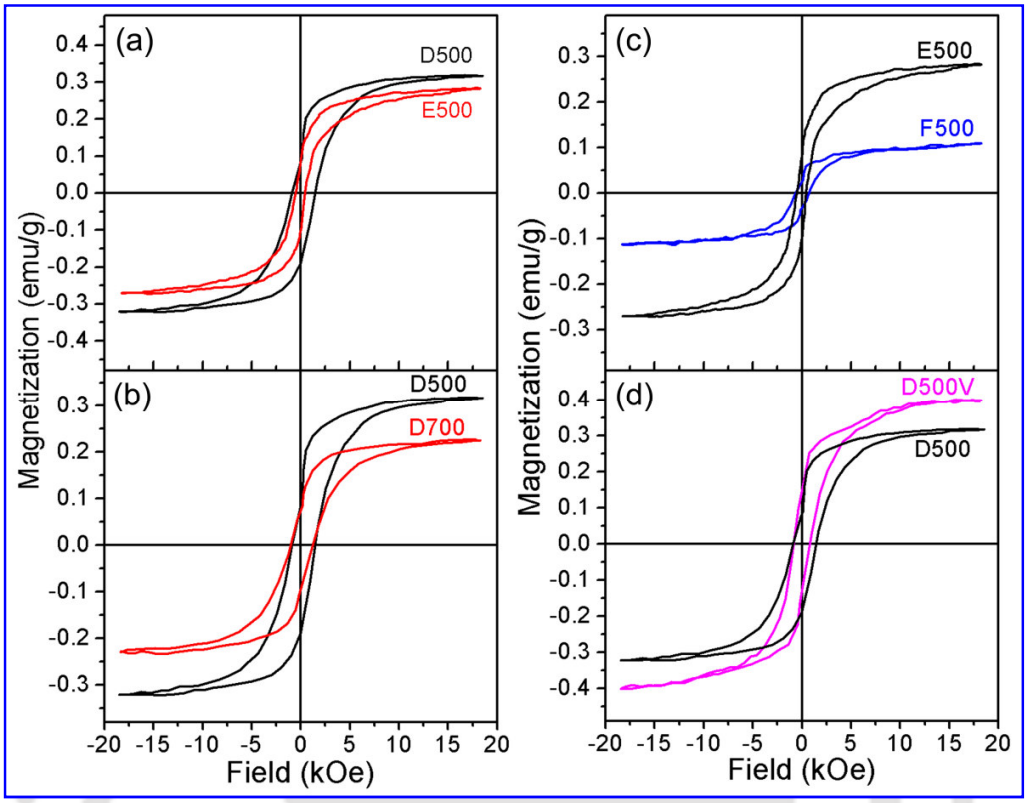

Fig. 7.15. Magnetic field versus magnetization (M–H) loop at room temperature showing comparison of hysteresis in samples: (a) D500 and E500; (b) D500 and D700; (c) E500 and F500; (d) D500 and D500V.

grown at two different reaction temperatures with same doping concentration (0.3% Cr). The saturation magnetization of E500 is less compared to D500. This may be due to different concentration of oxygen vacancy in D500 and E500. From our earlier study, we observed that the samples grown at higher temperature have comparatively lower concentration of oxygen vacancy. So, this may be a possible reason for the less magnetization in E500 as compared to D500. **Fig 7.15(b)** shows the comparison of D500 and D700, which are calcined at two different temperatures in air. The magnetic moment decreases with increase in calcinations temperature which is attributed to the lower concentration of oxygen vacancy in D700 and this is consistent with the PL spectra (**Fig. 7.13(a)**). The M-H loop of E500 and F500 are shown in **Fig. 7.15(c)**. It is observed that the sample F500 of higher doping concentration (0.7% Cr) has less magnetization as compared to 0.3% Cr doped sample

(E500). Interestingly, the magnetic moment is considerably increased after moderate vacuum annealing of sample D500, which is shown in **Fig. 7.15(d)**, suggesting that oxygen vacancy play an important role in enhancing the ferromagnetic ordering. The saturation magnetization values are provided in the **Table 7.1**. Note that we did not mentioned the coercive field (H_c) and remanent magnetization (M_r) in the **Table 7.1** for the Cr doped samples. This is because the VSM measurements for the Cr doped samples are run manually by switching the magnetic field (i.e., rotating the knob of the electromagnet power supply), not run through software control. So, the coercive field and remanent magnetization values are not accurate due to measurement limitations. However, the saturation magnetization value is unaffected and accurate. As we have measured the M-H behavior for the Fe doped samples through VSM software and run by manually and observed the H_c and M_r are less in the case of samples measured through software whereas the M_s remain almost constant. So, the observed large M-H loop area is not very accurate for the Cr doped samples, however nature of the loops remain unchanged.

7.5. Origin of ferromagnetism

Since the prediction and discovery of oxide based DMSs, there is still a lack of unique model to explain the experimental observations of ferromagnetism on a wide range of materials from a variety of synthesis methods and, the actual physical mechanism remains an open question. Despite many efforts, there is an incomplete understanding on the origin of RTFM in oxide-based DMS materials, whether it is an extrinsic effect due to direct interaction between the local moments in magnetic impurity clusters or is indeed an intrinsic property caused by exchange coupling between the spin of the carriers and the local magnetic moments. Experimental results reported by various groups are quite controversial and in particular, the underlying origin of RTFM in TiO_2 based DMSs is still debated. The possible reasons for the inconsistent results may have arisen due to the creation and distribution of different concentration of defects and/ or formation of secondary ferromagnetic phases/ metal clusters that are dependent on the growth methods and processing conditions during sample preparations. However, due to the fact that the RTFM is observed in undoped TiO_2 system, it helps to resolve the controversies partly about the issues related to the crucial role of defects in the ferromagnetic ordering in TiO_2 nanostructures.[10, 30] In our recent report[32] and

discussed in *Chapter 5*, it was demonstrated that a large concentration of O_v in TiO_2 NRbs with high thermal stability results in strong RTFM compared to those earlier reported in undoped/ doped TiO_2 systems. The electrons in F^+ center localize and may form bound magnetic polarons by ordering the Ti^{3+} ($3d^1$) electron spin neighboring the oxygen vacancies, thereby gaining exchange energy. The s-d exchange interaction between the $1s^1$ electron spin in the F^+ center, which is localized in the vicinity of $3d^1$ electron spin of Ti^{3+} ions within an orbit around oxygen vacancies favors long range FM. Note that our ESR result confirms the presence of Ti^{3+} and F^+ defect species in undoped A500 sample. The electrons in doubly occupied oxygen vacancies (F center) form $1s^2$ state, which only mediates weak antiferromagnetic exchange.[48] Thus the formation of bound magnetic polaron (BMP), which includes electrons locally trapped by oxygen vacancies, with the trapped electron in the F^+ center occupying an orbital overlapping with the unpaired electron ($3d^1$) of Ti^{3+} is proposed to explain the observed FM in our undoped TiO_2 NRbs. Here, we explore the understanding on the role of oxygen vacancies and TM (i.e., Fe and Cr) dopants towards the origin of enhanced FM in Fe/ Cr doped TiO_2 nanostructures compared to undoped TiO_2 and the mechanism of decrease in magnetization for higher doping concentration.

The mechanism of FM in Fe doped TiO_2 is rather complicated and several mechanisms have been proposed, such as double exchange and super exchange coupling,[18] RKKY[49] and coupling of BMP which is formed with a localized hole/ electron (usually induced by O_v defects) and the Fe^{3+} surrounding[50] etc. However, the dominant mechanism is still unclear, though one common feature in all these models is the vital role played by defects, carriers and/ or their coupling. From the M-H measurements, it is found that the saturation magnetization of 0.1% Fe doped sample is ~4.8 times enhanced compared to undoped sample, and the density of oxygen vacancies is simultaneously increased in doped B500 as compared to undoped A500, as confirmed from the PL analysis. Further, the magnitude of FM varies with different calcination temperatures for the same doping concentration (**Fig. 7.8(b)**). In order to understand the specific role of O_v in Fe:TiO_2, we studied the M-H behavior of vacuum annealed sample B500V and this study showed that oxygen vacancies indeed play the key role in the observed FM. Our results point to the fact that the O_v defects constitute the main ingredient to the observed FM in both undoped and Fe:TiO_2. This is quite reasonable since due to Fe^{3+} substituting in the Ti^{4+} lattice sites,

additional oxygen vacancies are expected owing to the charge neutrality in the host TiO_2 crystal. Since we observed FM in undoped system and a lower magnetic moment in 0.2% Fe doped sample as compared to 0.1% doped sample, it strongly suggest that a simple carrier mediated mechanism is not applicable to TiO_2 based DMS in this case. The O_v defects introduced in the TiO_2 host lattice during the solvothermal growth and post-growth calcinations play a significant role in the ferromagnetic ordering of 3d local spin, which are determined by the local atomic arrangement and local orbital overlapping, and control the magnitude of the ferromagnetic signal in Fe:TiO_2 nanostructures.[51]

Question may arise on how the O_v helps in the ferromagnetic ordering of Fe:TiO_2 systems. Chen et al.[18] predicted that O_v enhance the FM in Fe:TiO_2 system in two different ways, either through a shallow impurity state of a nearest neighbor Fe-O_v complex or through the capture of vacancy electrons by the Fe atoms and subsequent enhancement of the FM double exchange. Coey et al.[52] reported that an electron trapped in the O_v defect level creates an F center. The exchange interaction between neighboring magnetic ions mediated by the F center forms a BMP and the overlapping of such BMPs contributes to long-range ferromagnetic ordering in doped nanocrystals. Based on this mechanism, several authors[21, 50] reported that when the defect concentration exceeds the percolation threshold, the electron associated with the oxygen vacancies overlaps with the 3d shells of many dopant ions to yield the BMPs. The coupling between the two Fe^{3+} dopant spins through $O_v$with trapped electron (Fe^{3+}-O_v-Fe^{3+}) leads to long range ferromagnetic ordering and this is known as F center exchange coupling. However, if the one of the Fe^{3+} is far away from the O_v, then another possible source of antiferromagnetic interaction can be the existence of oxygen vacancies with two trapped electrons having $1s^2$ configuration.[48] Therefore, we believe that exchange interaction between $3d^5$ spins of Fe^{3+} and $1s^1$ spin of F^+ center is most likely responsible for the observed enhanced FM in Fe:TiO_2 systems along with the exchange interaction between $3d^1$ electron spin of Ti^{3+} and $1s^1$ spin of F^+ like in undoped systems.[51] Theoretical studies suggested that oxygen vacancies can cause an obvious change of band structure of the host oxides and makes a significant contribution to the FM. We observed that the absorption edges of as-synthesized NRbs are red shifted compared to the precursor TiO_2 powder, which may be due to sp-d exchange interactions between the band electrons and the

localized d electrons of the Fe^{3+} ions substituting Ti^{4+}cations and/ or s-d exchange interaction between the F^+ and Ti^{3+}/ Fe^{3+} and favor the observed FM.

At higher Fe concentration (0.2%), the FM is decreased. A similar feature was reported recently by Dodge et al.[7] in Fe doped SnO_2 system. Chen et al.[18] reported that the reduction of FM in large concentration of Fe^{3+} doping is possibly due to the antiferromagnetic ordering between two nearby Fe^{3+} ions in the absence of O_v by super exchange interaction. When the dopant concentration is high, the Fe^{3+} may reside into the interstitial position in host TiO_2 and most of the Fe^{3+} spins exist in the isolated paramagnetic spin system or may interact antiferromagnetically by super exchange interaction between the two neighboring Fe^{3+} ions, which is responsible for the reduction of FM signals in 0.2% Fe:TiO_2 samples. Our PL results show that concentration of oxygen vacancy is considerably lower in C500 as compared to that in B500 (**Fig. 7.5(b)**). Hence, lower oxygen vacancy is partly responsible for the lower saturation magnetization. Note that the FM decreases with the calcinations temperatures in 0.1% Fe:TiO_2 system which is just opposite to the case of undoped system. This implies that the dopant concentrations, their distribution within the host lattice and the energy level of the dopant as well as the band gap of TiO_2 host may affect the FM in Fe:TiO_2 systems. In the present case, different concentrations of overlapping of Fe^{3+}-F^+ and/ or Ti^{3+}-F^+ complexes are expected and may enhance/ reduce the overlapping of BMPs which determine the magnitude of FM.[51] The concentration of O_v is considerably lower in B900 as compared to that in B500, as confirmed from the PL spectra (**Fig. 7.5(a)**). Hence, the reduction of FM in the higher calcined sample (B900) is consistent with the above model. Another possible reason for the reduction of FM with calcinations in 0.1% Fe:TiO_2 sample is the migration of Ti^{3+} defects towards the surface to interact with atmospheric oxygen and convert to Ti^{4+} interstitial defects during the course of calcinations in air at 900 °C and this may result in the reduction of BMPs. Note that the interstitial defects related NIR PL was strong in B900 (**Fig. 7.5(a)**). Thus, the O_v mediated ferromagnetic interaction seems to be fully consistent with our results.

Unlike many other TMs, Cr itself is antiferromagnetic and so the observed FM would not induce any extrinsic ferromagnetism even if Cr clustering occurs. Moreover, all the other oxides of Cr except CrO_2 are not ferromagnetic. It was reported that the synthesis of CrO_2 is too difficult at atmospheric pressure and generally stable at high oxygen pressure.[23] Thus, Cr

doped TiO_2 is an excellent platform to investigate the nature and origin FM in DMS systems. Further, trivalent Cr^{3+} ions exhibit $3d^3$ high-spin configuration, which may induce long range ferromagnetic ordering by exchange interaction with nearby oxygen vacancy in the defective host semiconductors. We observed that with increase in calcinations temperatures in air, the FM decreases considerably. The oxygen vacancy related visible PL emission decreases with increase in calcinations due to the oxidation of samples at high temperature in air. Further the FM is enhanced in the vacuum annealed samples D500V having large concentration of oxygen vacancies compared to as-synthesized D500. So, a strong correlation between the oxygen vacancy and FM is observed. This strong correlation between the FM and the oxygen deficiency must be considered in order to understand the origin of the observed RTFM.

Therefore, it is believed that the oxygen vacancy plays an important and complimentary role in ferromagnetic ordering of $3d^3$ spins of Cr^{3+}. Note that the presence of Cr^{3+} is confirmed from our ESR and XPS analyses. Since the ionic charge of Cr^{3+} is different from that of Ti^{4+}, substitution of Cr^{3+} for Ti^{4+} generate oxygen vacancies nearby Cr^{3+} in the lattice of TiO_2 to maintain charge neutrality. However, the oxygen vacancies alone without any proper charge distribution are not adequate to establish a robust ferromagnetism in the Cr:TiO_2 nanostructures. More recently, Da Pieve et al.[53] reported that the O vacancy is a F^{++}center and the associated absence of electrons implies that the F-center exchange, usually invoked to stabilize ferromagnetism in these systems,[52, 54] cannot be active in Cr-doped TiO_2. Moreover, the O_v with two trapped electrons having $1s^2$ configuration exhibit antiferromagnetic ordering.[48] Based on a density-functional calculation, Raebiger et al.[55] showed that in Cr doped In_2O_3 the ferromagnetic Cr-Cr interaction can be tuned and even switched via electron doping. The extrinsic additional electrons doping, such as the large amount of donors induced by oxygen vacancies could provide the needed carriers to stabilize the long-range ferromagnetic ordering as Cr itself may not produce any free electrons.[55] Therefore, we believe that the partially filled Cr 3d states have to interact with the electron in F^+ center and the exchange interaction between $3d^3$ spins of Cr^{3+} and $1s^1$ spin of F^+ center is most likely responsible for the observed enhanced FM in Cr:TiO_2 system, which is similar to the Fe:TiO_2 systems discussed above. Note that the presence of F^+ center in doped sample D500 is confirmed from our ESR spectrum (**Fig. 7.14(d)**).

We observed that the FM drops when the Cr concentration is increased to 0.7% (sample F500) shown in **Fig. 7.15(c)**. A similar decrease in magnetization is observed by Choudhury et al.[29] for higher doping concentration of Cr in TiO_2. As we increase the doping of Cr^{3+}, some of the Cr^{3+} may reside in the interstitial site in the host TiO_2 or to the surface or grain boundary regions. All of the added Cr^{3+} may not be associated with an oxygen vacancy and these Cr^{3+} ions may bind with oxygen ions by $Cr^{3+} - O^{2-} - Cr^{3+}$ bonds or may be associated with another Cr^{3+} ion.[29] The decrease of magnetization may be expected due to $Cr^{3+} - O - Cr^{3+}$ super exchange interaction or due to the Cr^{3+}- Cr^{3+} interaction in the absence of oxygen vacancy which lead to antiparallel alignment of the spins. For observing ferromagnetism there should be exchange interaction of the $3d^3$ spins of Cr^{3+} ions via oxygen vacancies and for that purpose the dopant ions and defects should be situated close by. If the Cr^{3+} ions are isolated or formed coupled pairs without any oxygen vacancies, antiferromagnetic interaction will take place and ultimately result in the effective reduction of magnetization, which is observed for higher concentration Cr:TiO_2 nanostructures in our case. Similar results are also observed in our Fe:TiO_2 system for higher concentration of Fe, as discussed above.

The only possibility of extrinsic FM in Cr:TiO_2 may be expected from the CrO_2 as all other form of Cr oxide and Cr metal cluster itself are not ferromagnetic. So, the question arises whether the observed RTFM in our Cr:TiO_2 nanostructures is intrinsic or due to the solely presence of CrO_2 phase. If the ferromagnetism is due to CrO_2 phase, then the magnetization is expected to be increasing with increasing Cr concentration. However, in our samples we did not observe steady rise in magnetization for higher doping concentration. This result suggests that the observed RTFM is intrinsic in nature.

7.6. Conclusions

We successfully synthesized the undoped and Fe doped TiO_2 NRbs by a low temperature solvothermal method and Cr doped TiO_2 NRs/NRbs by a hydrothermal method. We investigated the origin of RTFM in these novel systems using several experimental tools. Our studies revealed strong correlation of O_v and RTFM in both Fe and Cr doped TiO_2 nanostructures. The enhanced FM after vacuum annealing for both Fe and Cr doped samples

compared to the as-prepared samples indicates that O_v play a major role in the observed FM in TM doped TiO_2 systems. By comparing the O_v related visible emission from PL spectra and saturation magnetization from M-H loops, we found that O_v is mainly responsible in dictating the magnitude of FM in different samples. Since we observed the FM in undoped TiO_2 NRbs and there was no signature of impurity from XRD and HRTEM studies in Fe:TiO_2 samples, the controversy related to the Fe metal cluster and other secondary phases towards the FM in our Fe:TiO_2 system is eliminated. The ~4.8 fold enhanced saturation magnetization in 0.1% Fe:TiO_2 compared to undoped TiO_2 indicates that Fe^{3+} also play an important role in ferromagnetic ordering in the presence of O_v in Fe:TiO_2 systems. The FM decreases with increase in Fe or Cr dopant concentration, which is attributed to the antiferromagnetic ordering caused by the super exchange interaction between two neighboring Fe^{3+} or Cr^{3+} ions in the absence of O_v in Fe doped and Cr doped samples, respectively. The observed RTFM is explained on the basis of BMPs whose formation is due to the s-d exchange interaction between Ti^{3+}-F^{+}, Fe^{3+}-F^{+} and Cr^{3+}-F^{+} in the vicinity of O_v and the overlapping of more BMPs result in enhanced FM. An optimal concentration of Fe or Cr doped into the substitutional site of Ti^{4+} and the creation of nearby O_v are the primary requirement for the enhanced FM in Fe:TiO_2 or Cr:TiO_2 nanostructures, respectively. On the basis of our experimental findings, we conclude that both O_v and Fe or Cr dopants and their charge distribution within the TiO_2 lattice play the pivotal role in increasing the ferromagnetic ordering and enhancement of FM in the doped TiO_2 nanostructures. These findings not only help to gain better insight into the defect engineering of RTFM in undoped and Fe doped TiO_2 or Cr doped TiO_2, but also constitute an important step for the development of practical nanospintronic devices which can be operated at room temperature.

References

1. H. Ohno, Science **281**, 951 (1998).
2. S. A. Wolf, D. D. Awschalom, R. A. Buhrman, J. M. Daughton, S. V. Molnar, M. L. Roukes, A. Y. Chtchelkanova and D. M. Treger, Science **294**, 1488 (2001).

3. Y. Matsumoto, M. Murakami, T. Shono, T. Hasegawa, T. Fukumura, M. Kawasaki, P. Ahmet, T. Chikyow, S. Koshihara and H. Koinuma, Science **291**, 854 (2001).
4. B. Pal and P. K. Giri, Journal of Applied Physics **108**, 084322 (2010).
5. B. Ghosh, M. Sardar and S. Banerjee, Journal of Physics D: Applied Physics **46**, 135001 (2013).
6. X. Liu, J. Iqbal, Z. Wu, B. He and R. Yu, The Journal of Physical Chemistry C **114**, 4790-4796 (2010).
7. K. Dodge, J. Chess, J. Eixenberger, G. Alanko, C. B. Hanna and A. Punnoose, Journal of Applied Physics **113**, 17B504 (2013).
8. G. Z. Xing, J. B. Yi, D. D. Wang, L. Liao, T. Yu, Z. X. Shen, C. H. A. Huan, T. C. Sum, J. Ding and T. Wu, Physical Review B **79**, 174406 (2009).
9. B. Santara, B. Pal and P. K. Giri, Journal of Applied Physics **110**, 114322 (2011).
10. N. H. Hong, J. Sakai, N. Poirot and V. Brizé, Physical Review B **73**, 132404 (2006).
11. K. Bapna, R. J. Choudhary, S. K. Pandey, D. M. Phase, S. K. Sharma and M. Knobel, Applied Physics Letters **99**, 112502 (2011).
12. H. Wang, J. Wei, R. Xiong and J. Shi, Journal of Magnetism and Magnetic Materials **324**, 2057-2061 (2012).
13. M. Venkatesan, C. B. Fitzgerald and J. M. D. Coey, Nature **430**, 630 (2004).
14. N. H. Hong, N. Poirot and J. Sakai, Physical Review B **77**, 033205 (2008).
15. X. Xu, C. Xu, J. Dai, J. Hu, F. Li and S. Zhang, The Journal of Physical Chemistry C **116**, 8813-8818 (2012).
16. L. Balcells, C. Frontera, F. Sandiumenge, A. Roig, B. Martínez, J. Kouam and C. Monty, Applied Physics Letters **89**, 122501 (2006).
17. C. E. Rodríguez-Torres, A. F. Cabrera, L. A. Errico, C. Adán, F. G. Requejo, M. Weissmann and S. J. Stewart, Journal of Physics: Condensed Matter **20**, 135210 (2008).
18. J. Chen, P. Rulis, L. Ouyang, S. Satpathy and W. Y. Ching, Physical Review B **74**, 235207 (2006).
19. Q. H. Li, L. Wei, Y. R. Xie, F. Jiang, T. Zhou, G. X. Hu, J. Jiao, Y. X. Chen, G. L. Liu, S. S. Yan and L. M. Mei, Journal of Alloys and Compounds **574**, 67-70 (2013).

20. H. J. Meng, D. L. Hou, L. Y. Jia, X. J. Ye, H. J. Zhou and X. L. Li, Journal of Applied Physics **102**, 073905 (2007).
21. S. K. S. Patel, S. Kurian and N. S. Gajbhiye, AIP Advances **2**, 012107 (2012).
22. Y. J. Kim, S. Thevuthasan, T. Droubay, A. S. Lea, C. M. Wang, V. Shutthanandan, S. A. Chambers, R. P. Sears, B. Taylor and B. Sinkovic, Applied Physics Letters **84**, 3531-3533 (2004).
23. L. Ranno, A. Barry and J. M. D. Coey, Journal of Applied Physics **81**, 5774-5776 (1997).
24. A. K. Rumaiz, B. Ali, A. Ceylan, M. Boggs, T. Beebe and S. Ismat Shah, Solid State Communications **144**, 334-338 (2007).
25. K. Dongyoo, H. Jisang, P. Young Ran and K. Kwang Joo, Journal of Physics: Condensed Matter **21**, 195405 (2009).
26. P. Mohanty, N. C. Mishra, R. J. Choudhary, A. Banerjee, T. Shripathi, N. P. Lalla, S. Annapoorni and R. Chandana, Journal of Physics D: Applied Physics **45**, 325301 (2012).
27. A. Sundaresan and C. N. R. Rao, Nano Today **4**, 96-106 (2009).
28. T. C. Kaspar, T. Droubay, V. Shutthanandan, S. M. Heald, C. M. Wang, D. E. McCready, S. Thevuthasan, J. D. Bryan, D. R. Gamelin, A. J. Kellock, M. F. Toney, X. Hong, C. H. Ahn and S. A. Chambers, Physical Review B **73**, 155327 (2006).
29. B. Choudhury and A. Choudhury, Materials Science and Engineering: B **178**, 794-800 (2013).
30. N. Hoa and D. Huyen, Journal of Materials Science: Materials in Electronics **24**, 793-798 (2013).
31. S. K. S. Patel and N. S. Gajbhiye, Journal of Magnetism and Magnetic Materials **330**, 21-24 (2013).
32. B. Santara, P. K. Giri, K. Imakita and M. Fujii, Nanoscale **5**, 5476-5488 (2013).
33. H.-Y. Lee, S. J. Clark and J. Robertson, Physical Review B **86**, 075209 (2012).
34. S. Na-Phattalung, M. F. Smith, K. Kim, M.-H. Du, S.-H. Wei, S. B. Zhang and S. Limpijumnong, Physical Review B **73**, 125205 (2006).
35. B. Santara, P. K. Giri, K. Imakita and M. Fujii, The Journal of Physical Chemistry C **117**, 23402-23411 (2013).

36. J. Shi, J. Chen, Z. Feng, T. Chen, Y. Lian, X. Wang and C. Li, The Journal of Physical Chemistry C **111**, 693-699 (2006).

37. S. Sharma, S. Chaudhary, S. C. Kashyap and S. K. Sharma, Journal of Applied Physics **109**, 083905 (2011).

38. J. Zhuang, S. Weng, W. Dai, P. Liu and Q. Liu, The Journal of Physical Chemistry C **116**, 25354-25361 (2012).

39. F. Zuo, L. Wang, T. Wu, Z. Zhang, D. Borchardt and P. Feng, Journal of the American Chemical Society **132**, 11856-11857 (2010).

40. D. Y. Inamdar, A. K. Pathak, I. Dubenko, N. Ali and S. Mahamuni, The Journal of Physical Chemistry C **115**, 23671-23676 (2011).

41. G. Pecchi, P. Reyes, T. López, R. Gómez, A. Moreno, J. L. G. Fierro and A. Martínez-Arias, Journal of Sol-Gel Science and Technology **27**, 205-214 (2003).

42. K. Duerr, J. Olah, R. Davydov, M. Kleimann, J. Li, N. Lang, R. Puchta, E. Hubner, T. Drewello, J. N. Harvey, N. Jux and I. Ivanovic-Burmazovic, Dalton Transactions **39**, 2049-2056 (2010).

43. S. K. S. Patel and N. S. Gajbhiye, Solid State Communications **151**, 1500-1503 (2011).

44. J. Zhu, Z. Deng, F. Chen, J. Zhang, H. Chen, M. Anpo, J. Huang and L. Zhang, Applied Catalysis B: Environmental **62**, 329-335 (2006).

45. J. C. Yu, J. Yu, H. Y. Tang and L. Zhang, Journal of Materials Chemistry **12**, 81-85 (2002).

46. I. Ikemoto, K. Ishii, S. Kinoshita, H. Kuroda, M. A. Alario Franco and J. M. Thomas, Journal of Solid State Chemistry **17**, 425-430 (1976).

47. I. S. Pentegov and E. A. Konstantinova, Physica Status Solidi (c) **8**, 1954-1956 (2011).

48. J. M. D. Coey, M. Venkatesan and C. B. Fitzgerald, Nature Materials **4**, 173-179 (2005).

49. Z. Wang, W. Wang, J. Tang, L. D. Tung, L. Spinu and W. Zhou, Applied Physics Letters **83**, 518-520 (2003).

50. K. Griffin Roberts, M. Varela, S. Rashkeev, S. T. Pantelides, S. J. Pennycook and K. M. Krishnan, Physical Review B **78**, 014409 (2008).

51. B. Santara, P. K. Giri, S. Dhara, K. Imakita and M. Fujii, Journal of Physics D: Applied Physics **47**, 235304 (2014).

52. J. M. D. Coey, A. P. Douvalis, C. B. Fitzgerald and M. Venkatesan, Applied Physics Letters **84**, 1332-1334 (2004).

53. F. Da Pieve, S. Di Matteo, T. Rangel, M. Giantomassi, D. Lamoen, G. M. Rignanese and X. Gonze, Physical Review Letters **110**, 136402 (2013).

54. J. Osterwalder, T. Droubay, T. Kaspar, J. Williams, C. M. Wang and S. A. Chambers, Thin Solid Films **484**, 289-298 (2005).

55. H. Raebiger, S. Lany and A. Zunger, Physical Review Letters **101**, 027203 (2008).

Chapter 8

High Temperature Ferromagnetism in Co doped TiO_2 Nanoparticles Grown by a Ball Milling Method

The first report on room temperature ferromagnetism (RTFM) in Co-doped TiO_2 (Co:TiO_2) by Matsumoto et al.[1] has stimulated great interest in the search for diluted magnetic semiconductor (DMS) materials and a number of studies have been carried-out to investigate whether the ferromagnetism (FM) is carrier-mediated or not. However, the issue related to the origin of FM still remains a subject of intense debate. It has proved to be difficult to determine whether the observed FM is an intrinsic effect due solely to the substitution of Co on the Ti sites or an extrinsic effect due to the presence of clustered metallic Co and/ or formation of secondary ferromagnetic phases in Co:TiO_2 systems. Several important tools such as anomalous Hall effect (AHE),[2, 3] x-ray photoelectron spectroscopy (XPS),[4, 5] x-ray magnetic circular dichroism (XMCD)[6, 7] have been applied to the Co:TiO_2 system to identify the exact origin of FM. The reported literatures are controversial and the mystery of the origin of FM is still remains an open question. Recently, advances in the spintronic technology have exploited considerable interest in TiO_2-based diluted magnetic semiconductors (DMSs) with Curie temperature (T_C) well above room temperature for the device applications. In this chapter, we report on the high temperature FM in Co:TiO_2 nanoparticles (NPs) grown by a ball milling method, which is different from the methods discussed in the previous chapters. We investigated the structural and optical properties of as-grown NPs to identify the nature and contribution of defects, which are responsible for the observed FM at and above room temperature.

8.1. Introduction

In the recent decades, intensive attention has been focused on diluted magnetic semiconductor (DMS) such as transition metals doped ZnO,[8, 9] SnO_2[10] and TiO_2[11] due to realization of room temperature ferromagnetism (RTFM) in these systems. Among these DMS, Co doped TiO_2 (Co:TiO_2) has been considered as one of the promising candidate owing to its excellent transparency, stability, high n-type carrier mobility, and low cost. A key component to exploiting TiO_2 based DMS is the realization of intrinsic FM with Curie temperature (T_C) well above room temperature (RT) for the development of future spintronic devices that can be operated at and above RT. However, the reported results are controversial. Numerous studies have reported that the magnetism is sensitive to the preparation conditions and doping agents. For example, Li et al.[12] synthesized Co:TiO_2 nanopowders via Ar/O_2 RF thermal plasma oxidizing mists of liquid precursors containing titanium tetra-*n*-butoxide and cobalt (II) nitrate. They determined that the solubility of Co^{2+} in the TiO_2 lattice was around 2 atomic%, above which $CoTiO_3$ and Co_2TiO_4 impurity phases are formed. Huang et al.[4] reported synthesis of 5 atomic% Co doped TiO_2 nanotube arrays by a sol–gel template method without any evidence of metallic Co or formation of any secondary phases. The thin films of Co doped TiO_2 were prepared by laser molecular beam epitaxy on TiO_2-buffered sapphire substrates by Quilty et al.[13] with varying Co concentration, i.e., 1%, 5% and 10%. They demonstrated that Co^{2+} was successfully incorporated into the TiO_2 matrix using XPS studies. Up to now, most studies reported on Co:TiO_2 have been made primarily by thin film method, such as sputtering,[14, 15] pulsed laser deposition,[16-18] molecular beam epitaxy,[19, 20] and chemical vapor deposition.[21, 22] Very little studies have been done on doped TiO_2 nanoparticles (NPs) that are freestanding and do not involve any chemical method for preparation.

The Co doped TiO_2-based DMS has been widely discussed and highly debated about the nature and origin of the observed FM, leading to confusion whether the true DMS exist in Co:TiO_2 systems. Some reports suggested segregation and the formation of Co clusters as the origin of FM signal,[5, 6] while the others results strongly support the intrinsic nature of FM mediated by carriers or defects.[11, 23, 24] Toyosaki et al.[2] found a correlation between anomalous Hall effect (AHE) and magneto optical dichroism measurements and suggested carriers enhanced ferromagnetism in Co:TiO_2 films. However, Shinde et al.[3] suggested that

observing an AHE is not a robust test for confirming carrier mediated ferromagnetism, because the co-occurrence of superparamagnetic Co clusters and the AHE is possible in Co-doped TiO_2 films. Kim et al.[6] investigated the origin of ferromagnetism in Co-doped anatase TiO_2 thin films with x-ray absorption spectroscopy (XAS) and XMCD at the Co $L_{2,3}$ edges. They observed that the Co $L_{2,3}$ edge XAS spectrum becomes identical to that of Co metal, suggesting that Co metal clusters are the cause for FM. On the other hand, Mamiya et al.[7] reported multiplet features characteristic of Co^{2+} in Co $L_{2,3}$ edges XMCD spectra of Co doped rutile TiO_2, suggesting that Co^{2+} ions, and not metallic Co, contribute to FM. Quilty et al.[13] suggested a strong hybridization between carriers in the Ti 3d t_{2g} band and the t_{2g} states of a high spin Co^{2+} ion in rutile Co:TiO_2 films. By using XPS technique, they showed that Co^{2+} is with high-spin state in which an unoccupied t_{2g} state is expected to hybridize with the Ti 3d t_{2g} orbital, permitting direct t_{2g}-t_{2g} hopping. Such direct hopping should enhance the exchange coupling between the Co ions, increasing the magnetic moment. Further, they did not observe any Co metal related core-level spectrum in the XPS measurements and reported an intrinsic RTFM in Co:TiO_2 thin films up to 10% Co doping.

The above controversial results among research groups suggest that the magnetic properties of Co doped TiO_2-based DMSs are critically dependent on fabrication and growth conditions. Here, we grow Co doped TiO_2 NPs by using a mechanical ball milling process and it proves to be an effective and simple technique to grow transition metal doped oxide semiconductors that exhibit high temperature FM. The observed magnetization and its temperature dependence are discussed with reference to the role of defects and doping concentration in the TiO_2 sublattice.[25] The focus of the present work is to bring further insight about the origin of the FM observed in the Co:TiO_2 system by studying the role of oxygen vacancies in TiO_2.

8.2. Synthesis of Co doped TiO_2 nanoparticles

The starting materials are commercial TiO_2 powder (purity 99%, Merck) and cobalt (Co) powder (99.5%, Loba Chemie). 3 wt% and 8 wt% Co powders are mixed with the required amount of TiO_2 powder. After mixing, the powders are ground for 10 minutes using a ceramic mortar and milled in a mechanical planetary ball-milling machine (Retsch, PM 100) at 350 rpm for duration of 5 h in a contamination-free zirconium dioxide (zirconia) vial under

atmospheric pressure and temperature. Zirconium dioxide balls of diameter 5 mm are used in this experiment. The ball to powder mixture weight ratio was taken as 10:1. Post-growth annealing was done for the Co doped samples at 300 °C for 2 h in air.

8.3. Structural and morphological studies

XRD patterns: The XRD patterns of undoped and Co doped TiO_2 NPs are shown in **Fig. 8.1**. All the diffraction peaks corresponded to the tetragonal anatase phase of TiO_2. Regardless of the concentration of the substituted Co into TiO_2 crystal lattice, there was no signature of Co metal clustered or any secondary phases such as Co-oxides phases and Co-Ti composites, which indicates that Co cations successfully occupy Ti cations sites in the anatase TiO_2 lattice. Interestingly, a very slow scan comparison of (101) peaks for undoped and doped samples are shown in the inset of **Fig. 8.1**, which indicates a slight down shift of the peak in doped samples.

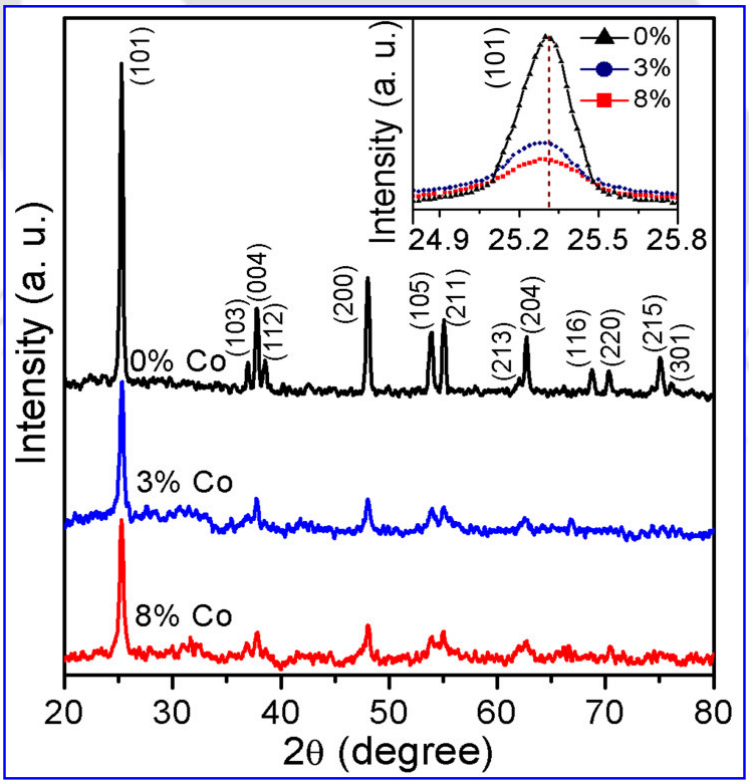

Fig. 8.1. XRD patterns of undoped, 3% and 8% Co doped TiO_2 NPs. The inset shows the magnified view of the comparison of the (101) peak for undoped and doped TiO_2 NPs.

In addition, the doped samples show lowering of peak intensity and increase in full width at half maximum of XRD patterns. A corresponding expansion of the lattice parameter is expected, because the ionic radius of dopant Co^{2+} ions (0.79 Å) was larger than that of host Ti^{4+} ions (0.75 Å) for the same coordination type, i.e., 6-coordinate octahedral. Compared to undoped TiO_2, the NPs size of doped samples is reduced considerably during milling. The average crystallite size of undoped and Co:TiO_2 NPs, determined from the XRD pattern using Scherrer's equation[26] was obtained as ~81 and 35–40 nm, respectively. Note that the existence of very small amount of Co clusters cannot be excluded since they are hardly detectable by standard XRD measurement.

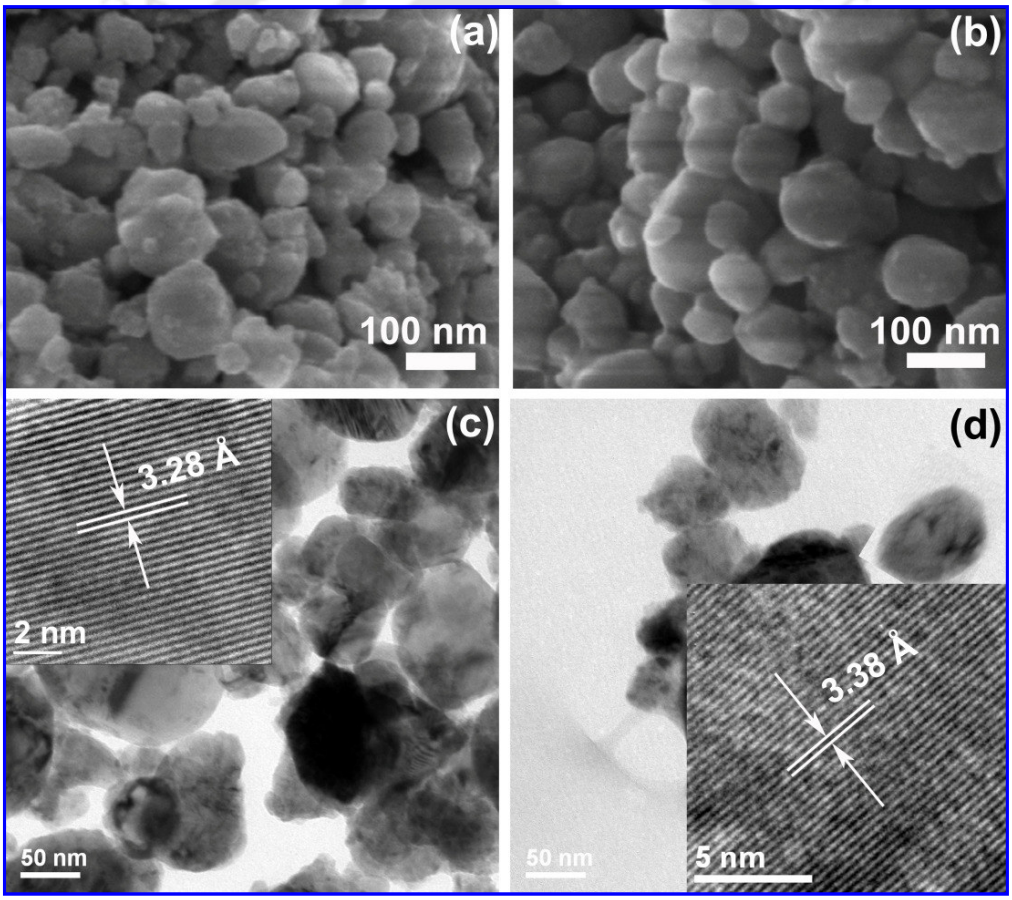

Fig. 8.2. FESEM images of the morphology of the Co doped TiO_2 NPs: (a) 3% doped, (b) 8% doped. TEM images of the doped TiO_2 NPs: (c) 3% Co doped, (d) 8% Co doped. The inset in (c) and (d) show corresponding HRTEM lattice images.

FESEM imaging: The morphologies of 3% and 8% Co doped NPs as obtained by FESEM and TEM are shown in **Figs. 8.2(a)**, **(b)** and **Figs. 8.2(c)**, **(d)**, respectively, which reveal that the as-grown NPs were almost spherical in size with average particle size in the range of 35–50 nm. The HRTEM study was further applied to analyze the lattice fringes for the doped samples, which are presented in the inset of **Figs. 8.2(c) and (d)**. The clear lattice fringes were obtained, implying that the as-grown samples are highly crystalline. The d-spacing of the crystal plane is calculated as 3.28 Å and 3.38 Å for 3% and 8% doped samples, respectively. Note the increase in d-spacing for 8% Co doped samples from that of the 3% doped samples. This again confirms that Co atoms are indeed incorporated in the TiO_2 crystal lattice.

8.4. Raman scattering studies

Raman scattering is one of the most effective tools for the study of crystallinity, crystalline phases and defects structure associated with the materials. The change of Raman spectra was related to non-stoichiometry and phonon confinement effect[27-30] in nanostructured materials. Oxygen deficiency within the material, however, strongly affects the Raman spectrum by producing shifting and broadening of some spectral peaks. The Co:TiO_2 NPs were characterized by micro-Raman spectroscopy and the result is shown in **Fig. 8.3**. All the Raman peaks of as-grown Co:TiO_2 NPs are similar with the tetragonal anatase TiO_2 phase. However, the most intense $E_g(1)$ Raman mode at 142 cm^{-1} shows the maximum blue-shift, while $E_g(3)$ Raman mode at 638 cm^{-1} is red-shifted in doped samples as compared to undoped TiO_2. Moreover, all the observed peaks for doped samples broaden and decrease in intensity with respect to undoped samples. Further the peak intensities decrease with the increase in Co concentration, indicating that the crystalline quality of NPs is very sensitive to the substitution of Co into the TiO_2 crystal lattice. The dramatic change of the main $E_g(1)$ Raman mode was interpreted by different competing mechanism such as the non-stoichiometry due to oxygen vacancies or disorder induced defects and phonon confinement effects.[30-32] The crystalline size in the nanoscale range may affect the frequency shifting and broadening of Raman peaks due to the phonon confinement. This was reported for small sized TiO_2 NPs by various authors.[31, 32] Zhang et al.[30] analyzed the phonon confinement effect both experimentally and theoretically and suggested that along with the phonon

confinement, oxygen vacancies play an important role for frequency shifting as well as broadening of Raman modes. To compare the phonon confinement, we also measured Raman spectrum of undoped TiO_2 5 h milled NPs having nearly similar crystallite size. In our case,

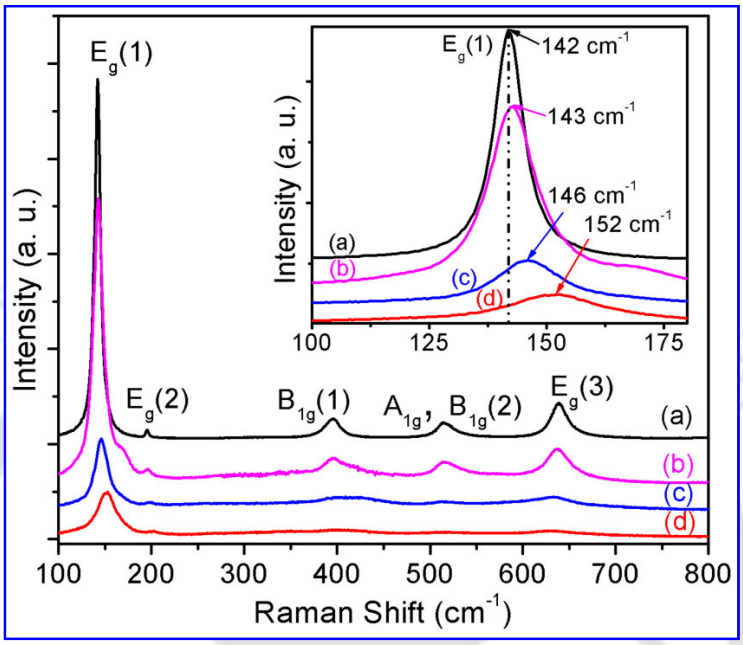

Fig. 8.3. Raman spectra for the undoped and Co doped TiO_2 NPs: (a) undoped before milling, (b) undoped after milling, (c) 3% Co doped and (d) 8% Co doped 5 h milled NPs. The inset shows the magnified view of relative changes in the $E_g(1)$ mode with doping concentrations.

there is a small blue-shift of $E_g(1)$ Raman mode for undoped TiO_2 5 h milled NPs which may be due to phonon confinement and/or defects, but considerable large blue-shift for 5 h milled Co:TiO_2 NPs is attributed to the existence of high defect density and lattice distortion caused by the incorporation of Co into TiO_2 lattice.[25] The red-shift of $E_g(3)$ Raman mode in doped samples is due to the tensile strain associated with Co doping in TiO_2. This is consistent with the XRD analysis. Huang et al.[4] reported a similar red-shift for Co doped TiO_2 nanotubes. Thus, the introduction of Co into the TiO_2 lattice largely affects the Raman modes. The absence of characteristic vibrational modes of any cobalt-oxides[33] in the Raman spectra of doped samples indicates that Co may be occupying the substitutional sites in the host TiO_2 lattice.

8.5. Optical absorption, Photoluminescence and XPS studies

UV-visible absorption studies: Many research groups have confirmed incorporation of Co into the TiO_2 lattice using a wide variety of optical methods such as x-ray photoelectron spectroscopy[24] and optical absorption spectroscopy.[34, 35] Evidence for Co substitution in the TiO_2 can be further confirmed from the UV-visible absorption spectra. Compared to undoped TiO_2, the band gaps of Co doped samples are shifted to lower energy, as shown in **Fig. 8.4**. The red-shift of absorption spectra with insertion of Co into TiO_2 has already been reported in Co doped TiO_2 thin films as well as the other transition metal doped oxide materials.[36-38] According to the energy band structure of TiO_2, the valence band (VB) top and the conduction band (CB) bottom correspond to mainly O 2p and Ti 3d states, respectively. The

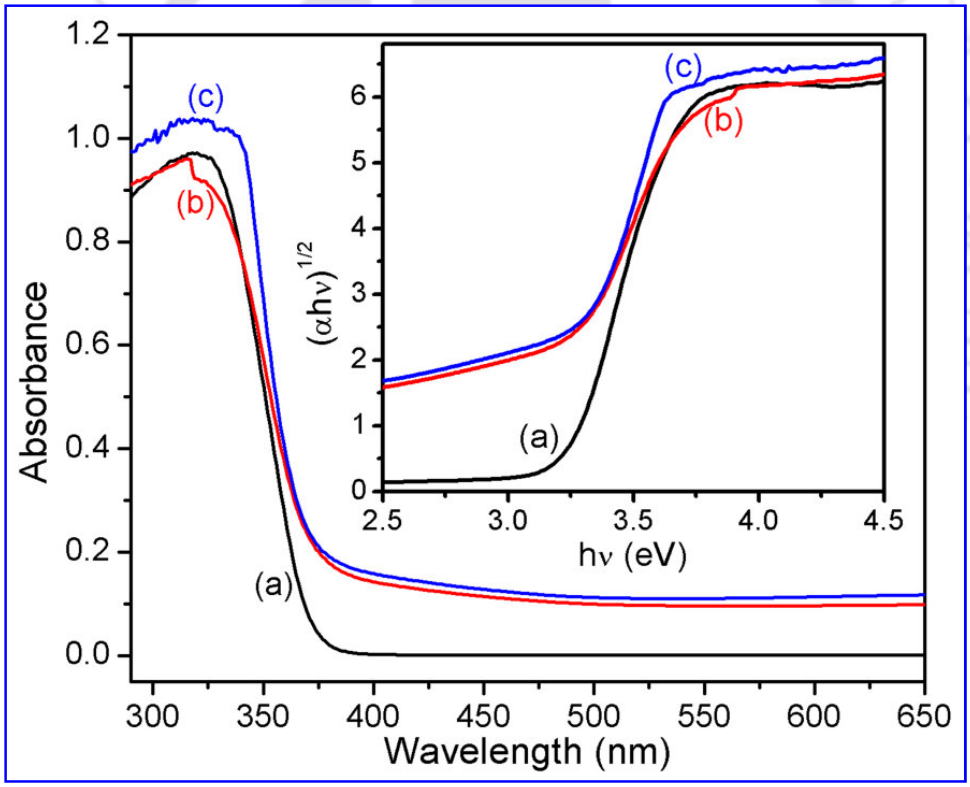

Fig. 8.4. UV-visible absorption spectra of undoped and Co doped TiO_2 NPs: (a) undoped, (b) 3% Co and (c) 8% Co doped. The inset shows the $(\alpha h\nu)^{1/2}$ *vs* $h\nu$ plot indicating reduction of band gap for doped NPs.

optical absorption around 380 nm for undoped TiO_2 is solely band-to-band (O 2p → Ti 3d) transition, while the slight red-shift in Co:TiO_2 NPs can be explained as being mainly due to sp-d exchange interactions between the band electrons and the localized d electrons of the Co^{2+} ions substituting Ti^{4+} cations. The s-d and p-d exchange interactions give rise to downward shifting of the CB edge and an upward shifting of the VB edge, leading to a band gap narrowing. The indirect band gap of all samples were determined from the linear fit to the linear portion of the $(\alpha hv)^{1/2}$ *versus* hv curves to $(\alpha hv)^{1/2} = 0$ [39] as shown in the inset of **Fig. 8.4**. The calculated band gap of undoped, 3% and 8% Co doped TiO_2 NPs are 3.22, 3.06, and 3.05 eV, respectively. The lowering in band gap energy for doped samples strongly indicates that Co cations have been successfully incorporated into the TiO_2 crystal lattice.

Photoluminescence studies: Room temperature photoluminescence measurements were carried out on the Co doped samples to understand the nature of defects in TiO_2 NPs. The photoluminescence spectra of 3%, 8% Co doped and 8% Co doped air annealed samples are shown in **Fig. 8.5**. All the samples show broad visible PL centered at ~465 nm. The visible PL is attributed to self trapped excitons and oxygen vacancy related trap states, which are discussed in the previous chapters. Note that the enhancement in intensity of the visible PL is

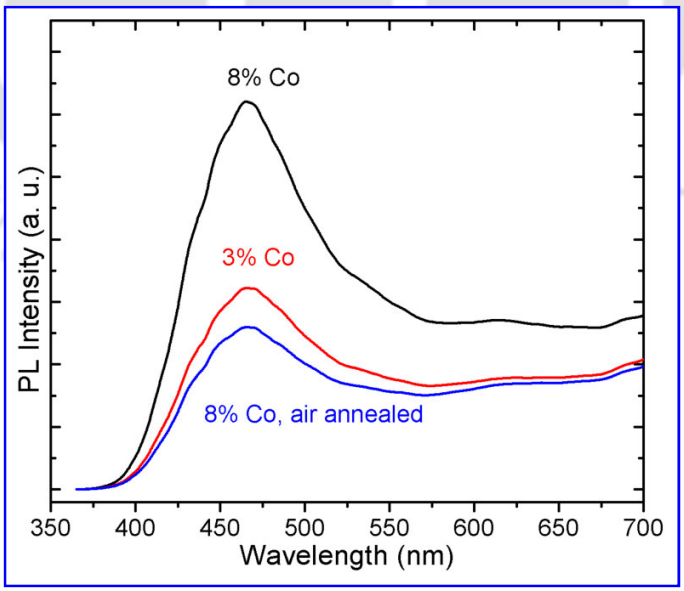

Fig. 8.5. Visible PL spectra of 3%, 8% Co doped and annealed 8% Co doped TiO_2 NPs.

observed in 8% doped sample as compared to 3% doped samples, which indicates higher concentration of oxygen vacancies in 8% doped sample. When a large number of Co^{2+} cations occupy the substitutional sites of Ti^{4+}, additional oxygen vacancies are expected owing to charge neutrality in the host TiO_2 crystals. We observed larger magnetic moment in 8% doped sample as compared to 3% doped sample, which is discussed later. So, our PL results confirm the presence of oxygen vacancies in Co doped TiO_2 NPs. Further the visible PL of 8% doped sample is reduced after air annealing, indicating the decrease in concentration of oxygen vacancies. This is consistent with the decrease in magnetic moment in the air annealed sample. Hence, the oxygen vacancy mediated FM is quite likely in our samples.

XPS studies: Ti 2p and O 1s core level spectra of the undoped and 3% doped samples are shown in **Fig. 8.6(a) and (b)**, respectively. The Ti $2p_{3/2}$ and $2p_{1/2}$ peaks at 457.7 and 463.5 eV, respectively for undoped sample correspond to Ti is in 4+ oxidation state. Both Ti 2p and O1s peaks are slightly shifted to a higher binding energy for the doped sample compared to undoped sample, which may be due to lattice distortion caused by the incorporation of Co^{2+} into the TiO_2 crystal lattice. This implies that chemical state of TiO_2 is little influenced by the Co^{2+} substitution for Ti^{4+}. Similar higher binding energy shift in Cr^{3+} doped TiO_2 nanorods has been reported[40] due to Cr^{3+} substitution for Ti^{4+}. The formation of neighboring oxygen vacancies due to Co^{2+} substitution for Ti^{4+} for the charge neutrality may also affect the shifting to the higher binding energy in the doped sample.[41] The O 1s spectra show a peak at 529.2 eV for undoped sample, which is attributed to lattice oxygen (O_{Ti}) associated with TiO_2 crystal lattice. The shoulder at higher binding energy may be related to surface hydroxyl species (O_H) and oxygen bonded to atmospheric carbon (O_C) on the sample surface.[42, 43] In order to evaluate the electronic valence state of Co in Co:TiO_2 NPs, we measured the Co 2p core level spectra which are shown in the inset of **Fig. 8.6(b)**. The Co 2p core level spectrum of 3% Co doped sample exhibits a main peak at 780.5 eV, accompanied with a weak satellite peak at around 785.5eV. The peak at 780.5 eV is attributed to the Co^{2+} $2p_{3/2}$ and there is no sign of Co metal related peak is observed in doped samples whose peak position is at around 778 eV. This eliminates the presence of metallic Co cluster.[4, 13] The

satellite peak at 785.5 eV further supports the presence of Co^{2+} ions in the Co:TiO_2 samples.[4, 13]

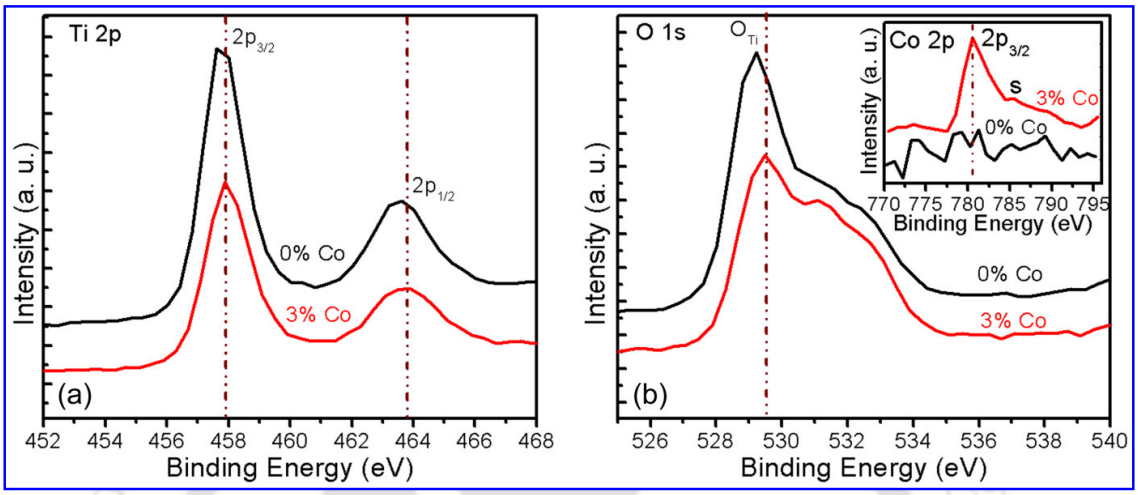

Fig. 8.6. XPS spectra: (a) Ti 2p core level spectra and (b) O 1s core level spectra of 0% and 3% Co doped NPs. The inset in (b) shows the Co 2p core level spectra of 0% and 3% Co doped NPs, '**s**' denotes the satellite peak.

8.6. Magnetization studies

Field-dependent magnetization (M-H curve): The magnetic properties of the Co:TiO_2 NPs were investigated using VSM. We observed distinct ferromagnetic behavior at room temperature in the doped samples only. Despite the presence of intrinsic oxygen vacancy defects in undoped TiO_2 NPs, no trace of FM was observed in the undoped precursor and milled TiO_2 samples that were first tested under similar conditions using the VSM. This confirms that intrinsic defects alone in TiO_2 NPs cannot account for the observed FM in the doped NPs. **Fig. 8.7** shows the magnetic hysteresis (M-H) loops for 3% and 8% doped NPs, measured at 300 K. The saturation magnetizations (M_s) of 3% and 8% doped samples are 2.79 and 7.39 emu/g with a coercive field (H_c) 253 and 259 Oe, respectively. Post growth annealing of both 3% and 8% doped samples in air ambient at 300 °C for 2 h affects the magnetization. The saturation magnetization of post-growth annealed samples is found to be decreased considerably which might be due to reduction of oxygen vacancy concentration when annealed in oxygen-rich environment. This observation strongly suggests that oxygen

vacancies play a dominant role in the observed FM. A similar observation was reported by Lin et al.[24] and they proposed that the decrease of magnetization could be explained in terms of a direct ferromagnetic coupling being weaker between two neighboring Co^{2+} ions via electrons trapped nearby the oxygen vacancies.

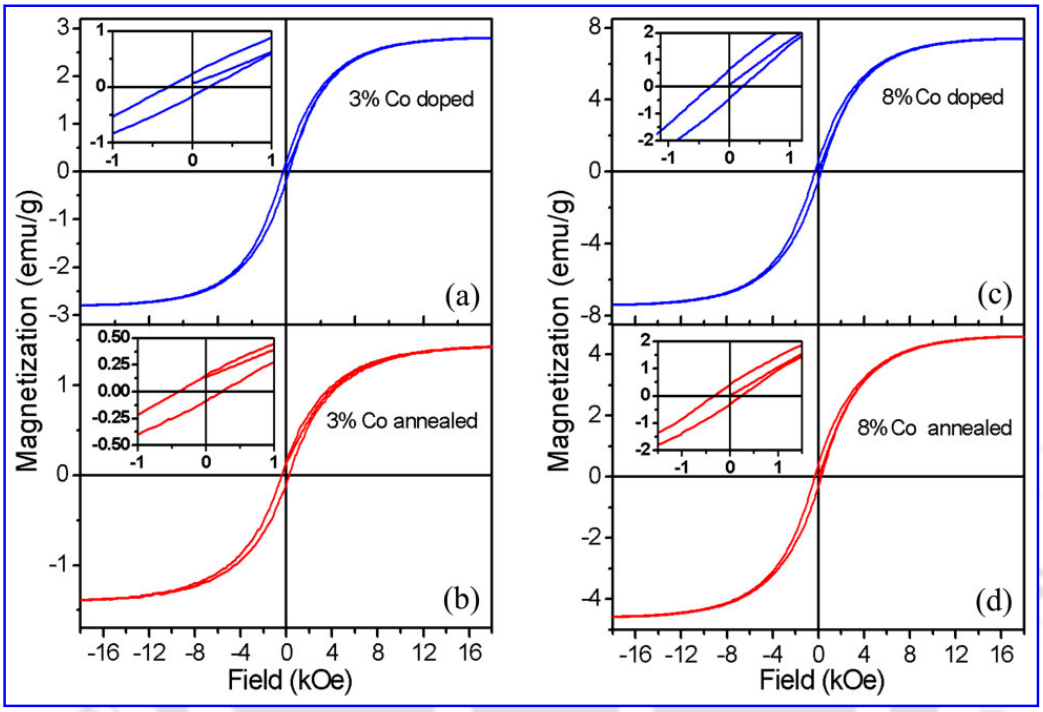

Fig. 8.7. Room temperature M-H loop of Co doped TiO_2 NPs: (a) 3% Co and (b) 3% Co doped air-annealed NPs; (c) 8% Co and (d) 8% Co doped air-annealed NPs. The insets in each case show the M-H loop at low field near origin in magnified scale.

Temperature-dependent magnetization (M-T curve): It is well known that for use in a wide range of applications without temperature control, the ferromagnet should have a T_C enough above RT (300 K). **Fig. 8.8** shows the temperature dependent magnetization of 3% and 8% doped NPs in the temperature range 300 to 900 K. Since the effect of high temperature VSM measurement in atmospheric condition is equivalent to the post annealing of as-grown samples in air that can destroy the ferromagnetic coupling, we have performed the high temperature measurement in nitrogen atmosphere. From the differential plot of the M-T curve, we obtained the T_C as ~793 K for 3% doped NPs and ~811 K for 8% NPs, which implies that the FM is not due to the Co metal (T_C >1300 K).[25] Interestingly, the gradual

increase in magnetization from 300 K to around 500 K is observed in the M-T curves for both 3% and 8% doped NPs. This study reveals that the oxygen vacancies are increased during heating process in nitrogen atmosphere and these defects play a crucial role in the observed FM. Note that defect mediated bound magnetic polaron (BMP) model has been invoked to explain room temperature FM. Due to increased vacancy concentration, more BMPs are available, which include electrons locally trapped by the oxygen vacancy, giving rise to gradual increase in magnetization. The thermal fluctuations of the localized spins may have comparatively less effect in this temperature range. Very recently, Tian et al.[44] reported nearly temperature-independent saturation magnetization up to 600 K strongly favoring the BMP model. The strength of exchange interaction is strong in magnetic semiconductor in the nanoscale where the mean distance between the localized spins is small which may enhance the thermal stability. We believe that our results provide important experimental input to stimulate further theoretical work in this regard to pinpoint the exact mechanism. As seen from the M-T curve, at higher temperature (>750 K) the curve shows a sharp drop in magnetization with temperature for 3% doped sample. The M-H measurement of the post M-T measurement shows almost paramagnetic nature for the 8% Co doped sample shown in the

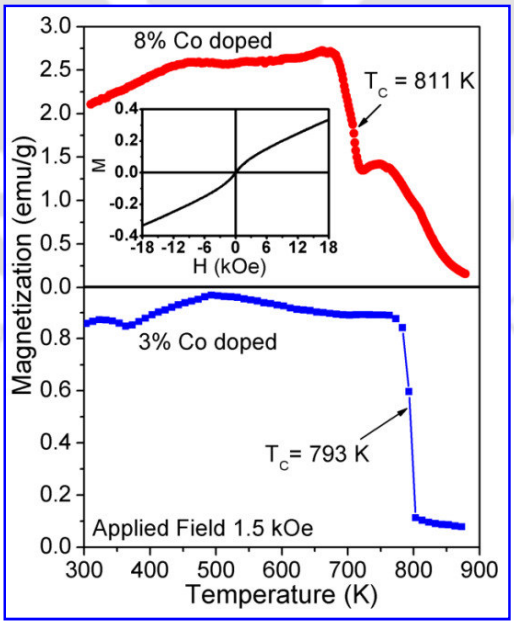

Fig. 8.8. Temperature dependent (M-T) curve of 3% and 8% Co doped TiO_2 NPs, showing high transition temperature in K. The inset shows the field versus magnetization (M-H) characteristic of 8% Co doped sample after post M-T measurement, indicating almost paramagnetic nature.

inset of **Fig. 8.8**. This magnetic transition suggests that high-temperature process causes a rapid destruction of ferromagnetic coupling as expected. Note that compared to the 3% doped sample, 8% doped sample did not exhibit any sharp transition at higher temperature. The absence of a sharp ferromagnetic to paramagnetic transition in M-T curve for higher doped (8% Co) TiO_2 NPs may be because of possible antiferromagnetic interaction due to the reduction in average interatomic distance of doped Co ions. Thus, 3% doped NPs is found to yield optimum result for the observed high temperature FM.

8.7. Origin of ferromagnetism

The realization of true intrinsic Co doped TiO_2 DMSs and the associated mechanisms, if the DMS really exists, are not clearly understood till date. The wide variety of growth processes under ambient conditions and several experimental tools were employed to find out the exact origin of observed RTFM in Co:TiO_2 based DMS. However, wide debate is still continuing on the validity of the existence of intrinsic Co:TiO_2 DMSs, leading to a confusion among the researchers. In particular, the origin of observed FM in Co:TiO_2 NPs could be possibly arise due to the intrinsic properties of the doped NPs, extended defects in TiO_2 NPs, formation of Co clusters or Co-related secondary phases. The metallic Co or any Co-oxides phases can be ruled out as there is no signature of any secondary phases other than the anatase TiO_2 observed in XRD and Raman results and absence of core level peak of Co metal in XPS spectrum. Undoped TiO_2 that were milled under identical conditions does not exhibit any measurable magnetization. Hence, intrinsic defects or trace impurity alone cannot make the observed high magnetic moment in the Co:TiO_2 NPs. On the other hand, annealing studies show that oxygen vacancies indeed play a significant role in the observed FM. Thus, Co along with the defects essentially plays the key role to the observed FM here. Several features like band gap narrowing, shifting, and broadening of some of the Raman modes and XPS studies strongly support the incorporation of Co^{2+} into the TiO_2 lattice. The oxygen vacancy defects are confirmed from PL studies. Therefore, FM is expected to arise from the intrinsic exchange interaction of magnetic moments mediated by defects in doped NPs.

Recently, several theoretical models have been proposed that the FM is strongly dependent on the creation and distribution of oxygen vacancies in the Co doped TiO_2 system. However, the exact mechanism of intrinsic FM is still under active debate. According to the

literature, magnetic cations, carriers, and defects can make up BMP that may be responsible for the RTFM. In addition to the magnetic doping effect, oxygen vacancy (O_v) defects have been suggested to play an important role in the magnetic origin for oxide DMS.[45] Though the high concentrations of oxygen vacancies are present in the precursor TiO_2 NPs, no FM is observed, indicating that simple oxygen vacancies cannot be responsible for the ferromagnetic ordering. However, there are lots of reports on the RTFM in undoped TiO_2 and the FM was enhanced after vacuum annealing or annealing in reduce atmosphere, claiming that the O_v plays the key role for the ferromagnetic ordering. We also observed RTFM in undoped TiO_2 nanoribbon grown by a different technique, which is discussed in the *Chapter 5*. We explained the s-d exchange interaction between $3d^1$ electron spin of Ti^{3+} and $1s^1$ spin of F^+ (singly ionized oxygen vacancy) are responsible for the FM. There are three kinds of O_v species such as O_v with doubly occupied electrons (F center, associated with two electrons), singly ionized O_v (F^+ center, associated with one electron) and doubly ionized O_v (F^{++} center, no electron at all). Coey et at.[46] reported that O_v with two electrons (F center) form $1s^2$ state, which mediate weak antiferromagnetic exchange. More recently, Da Pieve et al.[47] reported that the O vacancy with a F^{++} center and the associated absence of electrons implies that the F-center exchange cannot be active in their Cr-doped TiO_2 system. Moreover, isolated Ti^{3+} cations (created due to the O_v, as the two electrons left behind due to absence of an O atom may interact with neighboring Ti^{4+} ions and create two Ti^{3+} ions or one Ti^{3+} and F^+) are paramagnetic species and do not contribute to FM without any exchange interaction. So, particular charge creation and redistribution of O_v, and their interactions with the $3d^1$ spin of Ti^{3+} in case of undoped TiO_2 or unpaired 3d electron of TM cations in TM doped TiO_2 nanostructures are the primary requirement for the ferromagnetic ordering. The electrons in the F^+-centre localize and may form BMPs by ordering the Co^{2+} ($3d^5$) electron spin neighboring the oxygen vacancies, thereby gaining exchange energy. The s-d exchange interaction between the $1s^1$ electron spin in the F^+-centre, which is localized in the vicinity of the $3d^5$ electron spin of Co^{2+} ions within an orbit around the oxygen vacancies, favors long-range FM. The exchange interaction between $3d^5$ electron spin of Co^{2+} cation and $1s^1$ spin of F^+ may be responsible for the observed FM in Co:TiO_2 NPs in our case.

Theoretical studies suggest that O_v can cause an obvious change of the band structure of host oxides and makes a significant contribution to the FM.[46, 48] We observed that the

absorption edges of as-grown NPs are red shifted compared to the precursor TiO_2 powder, which may be due to sp-d exchange interactions between the band electrons and the localized d-electrons of the Co^{2+} ions substituting Ti^{4+} cations and/ or the s-d exchange interaction between F^+ and Co^{2+}, and favor the observed FM. The formation of BMP, which include electrons locally trapped by oxygen vacancy, with the trapped electron occupying an orbital overlapping with the *d* shells of TM neighbors, has also been proposed to explain the origin of FM.[46] When the oxygen content of the unit cell is increased, ferromagnetism is suppressed. We notice that post growth annealing in air at 300 °C shows the decrease in M_s owing to decease in O-vacancies that may reduce the BMP. This seems to support the percolation model of BMP developed by Kaminski and Das Sarma[49] and specifically extended to magnetically doped oxides by Coey et al.[46] Our systematic study shows that oxygen-vacancy defect constituted BMP are one of the promising candidate to account for the RTFM observed in this system. Within the BMP model, the greater density of oxygen vacancy (O_v) and more doping help to produce more BMP which yields a greater overall volume occupied by BMP, leading to the overlap of BMP and enhancing FM. This evolution is observed in our case, increase of magnetization with the Co concentration indicating that the FM in our samples may be due to percolation of BMP.

To understand the suitability of the BMP model quantitatively, the most widely accepted theory, we attempted to fit the observed M versus H data to the BMP model by following McCabe et al.[50] According to the BMP model, the measured magnetization can be fitted to the relation

$$M = M_0 L(x) + \chi_m H \qquad (8.1)$$

where the first term is from BMP contribution and the second term is due to paramagnetic matrix contribution. Here $M_0 = Nm_s$, N is the number of BMP involved and m_s is the effective spontaneous moment per BMP. $L(x) = coth(x) - 1/x$ is the Langevin function with $x = m_{eff}H/k_BT$, where m_{eff} is the true spontaneous moment per BMP, and at higher temperature it can be approximated to $m_s = m_{eff}$. We have analyzed the M-H curve by using Eq. (8.1). The parameters M_0, m_{eff}, and χ_m are variable in the fitting process. The experimental data along with fitted data are shown in **Fig. 8.9** for the 3% and 8% Co doped TiO_2 samples at 300 K. We notice that the fitted data closely follows the experimental data

and the fitted parameters are tabulated in **Table 8.1**. The total BMP magnetization M_0 values are found to be in the order of 3–9 emu/g. The M_0 value is found to increase with increase in doping concentration. The paramagnetic susceptibility χ_m is found to be of the order of 10^{-5} cgs unit and its value marginally changes with doping. The spontaneous moment per BMP, m_{eff} is found to be in the order of 10^{-17} emu. By assuming $m_s = m_{eff}$, we have estimated the concentration of BMP, which was found to be in the order of 10^{18} cm^{-3} (see **Table 8.1**). BMP model actually cannot account for the high temperature FM observed here.

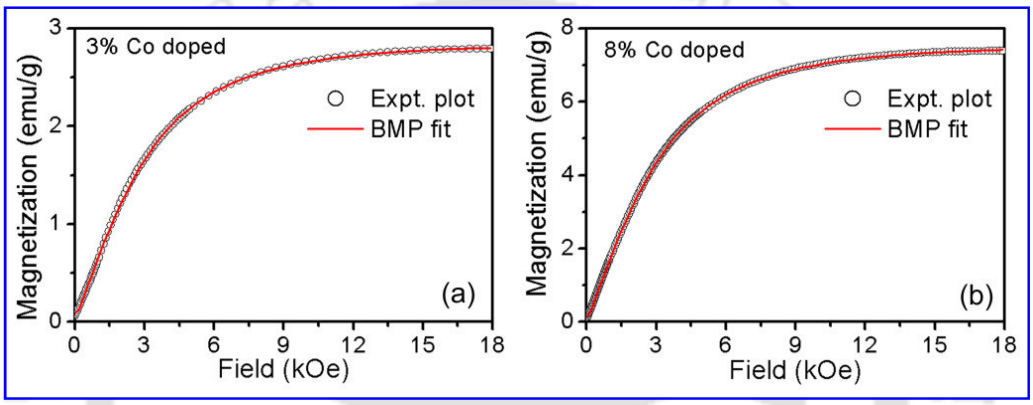

Fig. 8.9. Initial portion of M-H curve fitted with BMP model (Eq. 8.1): (a) 3% and (b) 8% Co doped NPs. Symbols are for experimental data and the solid line is a fit with BMP model. Extracted parameters are listed in **Table 8.1**.

Table 8.1. Magnetization parameters for 3% and 8% Co doped TiO_2 NPs: saturation magnetization (M_s), coercive field (H_c), and remanent magnetization (M_r) were determined from M-H loops, transition curie temperature (T_C) was determined from differentiated M-T curve; M_0 , m_{eff}, χ_m and N were evaluated from fitting of the M-H curve with BMP model.

Co doping concentration	M_s (emu/g)	M_r (emu/g)	H_c (Oe)	T_C (K)	M_0 (emu/g)	$m_{eff} \times 10^{-17}$ (emu)	$\chi_m \times 10^{-6}$ (cgs)	$N \times 10^{18}$ (cm^{-3})
3%	2.79	0.21	253	793	3.31	2.56	1.16	0.504
8%	7.39	0.54	259	811	8.73	2.53	2.91	1.311
3% annealed	1.42	0.12	324	.....	.....	.....	.....	.....
8% annealed	4.58	0.37	282	.....	.....	.....	.....	.....

Extended defects such as dislocation and grain boundary may contribute to the observed FM, as reported recently.[51, 52] In the ball milled NPs, lattice strain is usually caused by dislocations that develop during milling process. Usually this dislocation density first goes up with milling time and then it reduces with further milling accompanied by particle size reduction. Thus, it is quite likely that strain/dislocations may have reasonable contributions to the observed high temperature FM. Note that dislocations usually have high thermal stability and low temperature annealing does not destroy the FM. Nevertheless, more studies are required to pinpoint the exact mechanism of high temperature FM.

8.8. Conclusions

We investigated the origin of ferromagnetism at and above room temperature in Co doped TiO_2 NPs using a variety of experimental tools. XRD analysis confirms the absence of any secondary phases other than the anatase TiO_2 structure. Micro-Raman studies show the defect related shifting and broadening of $E_g(1)$ and $E_g(3)$ Raman modes due to incorporation of Co into the TiO_2 crystal lattice. The red-shift of UV-visible absorption spectra for doped samples indicates that Co is successfully doped into TiO_2 lattice. PL studies confirm the presence of oxygen vacancy defects in the doped NPs. XPS results revealed that the Co is in 2+ oxidation state suggesting Co^{2+} is successfully incorporated into the TiO_2. From these observations, we expect that the FM behavior of as-grown NPs is due to the exchange interaction between $1s^1$ electron of F^+ center and $3d^5$ electron of Co^{2+}, not being caused by metallic Co or any other Co-oxides. We conclude that both Co dopant and nearby O_v and their charge distribution within the TiO_2 lattice play the pivotal role in increasing the FM ordering and enhancement of FM in Co:TiO_2 NPs. Moreover, extended defects may help to stabilize FM at high temperature. Thus Co:TiO_2 NPs were found to exhibit effective high T_C ferromagnetism and it is an important step for the development of practical commercial devices.

References

1. Y. Matsumoto, M. Murakami, T. Shono, T. Hasegawa, T. Fukumura, M. Kawasaki, P. Ahmet, T. Chikyow, S.-y. Koshihara and H. Koinuma, Science **291**, 854-856 (2001).
2. H. Toyosaki, T. Fukumura, Y. Yamada and M. Kawasaki, Applied Physics Letters **86**, 182503 (2005).
3. S. R. Shinde, S. B. Ogale, J. S. Higgins, H. Zheng, A. J. Millis, V. N. Kulkarni, R. Ramesh, R. L. Greene and T. Venkatesan, Physical Review Letters **92**, 166601 (2004).
4. C. Huang, X. Liu, Y. Liu and Y. Wang, Chemical Physics Letters **432**, 468-472 (2006).
5. J. Xu, S. Shi, L. Li, X. Zhang, Y. Wang, X. Chen, J. Wang, L. Lv, F. Zhang and W. Zhong, Journal of Applied Physics **107**, 053910 (2010).
6. J. Y. Kim, J. H. Park, B. G. Park, H. J. Noh, S. J. Oh, J. S. Yang, D. H. Kim, S. D. Bu, T. W. Noh, H. J. Lin, H. H. Hsieh and C. T. Chen, Physical Review Letters **90**, 017401 (2003).
7. K. Mamiya, T. Koide, A. Fujimori, H. Tokano, H. Manaka, A. Tanaka, H. Toyosaki, T. Fukumura and M. Kawasaki, Applied Physics Letters **89**, 062506 (2006).
8. K. Ueda, H. Tabata and T. Kawai, Applied Physics Letters **79**, 988-990 (2001).
9. B. Pal and P. K. Giri, Journal of Applied Physics **108**, 084322 (2010).
10. X. Liu, J. Iqbal, Z. Wu, B. He and R. Yu, The Journal of Physical Chemistry C **114**, 4790-4796 (2010).
11. R. K. Singhal, A. Samariya, S. Kumar, Y. T. Xing, D. C. Jain, S. N. Dolia, U. P. Deshpande, T. Shripathi and E. B. Saitovitch, Journal of Applied Physics **107**, 113916 (2010).
12. J.-G. Li, R. Büchel, M. Isobe, T. Mori and T. Ishigaki, The Journal of Physical Chemistry C **113**, 8009-8015 (2009).
13. J. W. Quilty, A. Shibata, J. Y. Son, K. Takubo, T. Mizokawa, H. Toyosaki, T. Fukumura and M. Kawasaki, Physical Review Letters **96**, 027202 (2006).
14. W. K. Park, R. J. Ortega-Hertogs, J. S. Moodera, A. Punnoose and M. S. Seehra, Journal of Applied Physics **91**, 8093-8095 (2002).

15. X. F. Yao, T. J. Zhou, Y. X. Gai, T. C. Chong and J. P. Wang, Journal of Applied Physics **95**, 7375-7377 (2004).
16. S. R. Shinde, S. B. Ogale, S. Das Sarma, J. R. Simpson, H. D. Drew, S. E. Lofland, C. Lanci, J. P. Buban, N. D. Browning, V. N. Kulkarni, J. Higgins, R. P. Sharma, R. L. Greene and T. Venkatesan, Physical Review B **67**, 115211 (2003).
17. Y. Yamada, H. Toyosaki, A. Tsukazaki, T. Fukumura, K. Tamura, Y. Segawa, K. Nakajima, T. Aoyama, T. Chikyow, T. Hasegawa, H. Koinuma and M. Kawasaki, Journal of Applied Physics **96**, 5097-5102 (2004).
18. D. H. Kim, J. S. Yang, Y. S. Kim, T. W. Noh, S. D. Bu, S. I. Baik, Y. W. Kim, Y. D. Park, S. J. Pearton, J. Y. Kim, J. H. Park, H. J. Lin, C. T. Chen and Y. J. Song, Physical Review B **71**, 014440 (2005).
19. Y. Matsumoto, M. Murakami, T. Hasegawa, T. Fukumura, M. Kawasaki, P. Ahmet, K. Nakajima, T. Chikyow and H. Koinuma, Applied Surface Science **189**, 344-348 (2002).
20. S. A. Chambers, S. M. Heald and T. Droubay, Physical Review B **67**, 100401 (2003).
21. N.-J. Seong, S.-G. Yoon and C.-R. Cho, Applied Physics Letters **81**, 4209-4211 (2002).
22. S. A. Chambers, Materials Today **5**, 34-39 (2002).
23. K. Griffin Roberts, M. Varela, S. Rashkeev, S. T. Pantelides, S. J. Pennycook and K. M. Krishnan, Physical Review B **78**, 014409 (2008).
24. Y. B. Lin, Y. M. Yang, B. Zhuang, S. L. Huang, L. P. Wu, Z. G. Huang, F. M. Zhang and Y. W. Du, Journal of Physics D: Applied Physics **41**, 195007 (2008).
25. B. Santara, B. Pal and P. K. Giri, Journal of Applied Physics **110**, 114322 (2011).
26. K. Ishikawa, K. Yoshikawa and N. Okada, Physical Review B **37**, 5852-5855 (1988).
27. J. C. Parker and R. W. Siegel, Applied Physics Letters **57**, 943-945 (1990).
28. D. Bersani, P. P. Lottici and X.-Z. Ding, Applied Physics Letters **72**, 73-75 (1998).
29. W. Ma, Z. Lu and M. Zhang, Applied Physics A **66**, 621-627 (1998).
30. W. F. Zhang, Y. L. He, M. S. Zhang, Z. Yin and Q. Chen, Journal of Physics D: Applied Physics **33**, 912 (2000).
31. H. C. Choi, Y. M. Jung and S. B. Kim, Vibrational Spectroscopy **37**, 33-38 (2005).

32. L. Li-Hong, S. Cheng-Min, C. Xi-Ping, L. Wu-Ming and G. Hong-Jun, Journal of Physics: Condensed Matter **16**, 267 (2004).
33. D. Gallant, M. Pézolet and S. Simard, The Journal of Physical Chemistry B **110**, 6871-6880 (2006).
34. X. W. Wang, X. P. Gao, G. R. Li, L. Gao, T. Y. Yan and H. Y. Zhu, Applied Physics Letters **91**, 143102 (2007).
35. K. Das, S. N. Sharma, M. Kumar and S. K. De, The Journal of Physical Chemistry C **113**, 14783-14792 (2009).
36. M. Subramanian, S. Vijayalakshmi, S. Venkataraj and R. Jayavel, Thin Solid Films **516**, 3776-3782 (2008).
37. Y. Cong, J. Zhang, F. Chen, M. Anpo and D. He, The Journal of Physical Chemistry C **111**, 10618-10623 (2007).
38. F. Gracia, J. P. Holgado, A. Caballero and A. R. Gonzalez-Elipe, The Journal of Physical Chemistry B **108**, 17466-17476 (2004).
39. A. P. Singh, S. Kumari, R. Shrivastav, S. Dass and V. R. Satsangi, International Journal of Hydrogen Energy **33**, 5363-5368 (2008).
40. H. Zhu, J. Tao and X. Dong, The Journal of Physical Chemistry C **114**, 2873-2879 (2010).
41. M. Xing, J. Zhang, F. Chen and B. Tian, Chemical Communications **47**, 4947-4949 (2011).
42. J. Zhuang, S. Weng, W. Dai, P. Liu and Q. Liu, The Journal of Physical Chemistry C **116**, 25354-25361 (2012).
43. J. C. Yu, J. Yu, H. Y. Tang and L. Zhang, Journal of Materials Chemistry **12**, 81-85 (2002).
44. Y. Tian, Y. Li, M. He, I. A. Putra, H. Peng, B. Yao, S. A. Cheong and T. Wu, Applied Physics Letters **98**, 162503 (2011).
45. H. S. Hsu, J. C. A. Huang, Y. H. Huang, Y. F. Liao, M. Z. Lin, C. H. Lee, J. F. Lee, S. F. Chen, L. Y. Lai and C. P. Liu, Applied Physics Letters **88**, 242507 (2006).
46. J. M. D. Coey, M. Venkatesan and C. B. Fitzgerald, Nature Materials **4**, 173-179 (2005).

47. F. Da Pieve, S. Di Matteo, T. Rangel, M. Giantomassi, D. Lamoen, G. M. Rignanese and X. Gonze, Physical Review Letters **110**, 136402 (2013).

48. J. E. Jaffe, T. C. Droubay and S. A. Chambers, Journal of Applied Physics **97**, 73908 (2005).

49. A. Kaminski and S. Das Sarma, Physical Review Letters **88**, 247202 (2002).

50. G. H. McCabe, T. Fries, M. T. Liu, Y. Shapira, L. R. Ram-Mohan, R. Kershaw, A. Wold, C. Fau, M. Averous and E. J. McNiff, Physical Review B **56**, 6673-6680 (1997).

51. H. S. Hsu, J. C. A. Huang, S. F. Chen and C. P. Liu, Applied Physics Letters **90**, 102506 (2007).

52. R. Podila, W. Queen, A. Nath, J. T. Arantes, A. L. Schoenhalz, A. Fazzio, G. M. Dalpian, J. He, S. J. Hwu, M. J. Skove and A. M. Rao, Nano Letters **10**, 1383-1386 (2010).

Chapter 9

Summary and Outlooks

The highlights of the major contributions of the thesis and important conclusions of the work are presented in this chapter. New findings on the controlled growth and formation mechanism of different one dimensional (1D) nanostructures, identification of intrinsic defects in undoped TiO_2 nanostructures, tunable optical and magnetic properties of undoped and doped TiO_2 nanostructures are summarized. Open questions and scope for future studies are also presented.

9.1. Summary and conclusions

In this thesis work, we have described the controlled growth and elucidated the formation mechanism of 1D TiO_2 nanostructures with different morphologies grown by solvothermal method under constant stirring throughout the reaction using various solvents and growth temperatures (*Chapter 3*). We have studied the presence of intrinsic defects such as oxygen vacancy (O_v) and Ti interstitial (Ti_i) defects, and their evolutions in the as-prepared undoped TiO_2 nanoribbons (NRbs) depending upon the growth temperatures, reaction durations and calcinations. We discussed the Ti_i defects induced extended visible absorption and near infrared (NIR) photoluminescence (PL) from undoped TiO_2 NRbs and identified it for the first time experimentally through an *in-situ* PL studies (*Chapter 4*). We explained lattice expansion and contraction in undoped rutile TiO_2 nanostructures on the basis of electrostatic force of attraction/ repulsion caused by the native defects and detected experimentally for the first time (*Chapter 6*). We observed room temperature ferromagnetism in undoped TiO_2 NRbs and direct evidence of oxygen vacancy induced room temperature ferromagnetism (RTFM) was demonstrated for the first time and quantitatively analyzed using bound magnetic polaron (BMP) model (*Chapter 5*). We have investigated the origin of the RTFM in our Fe and Cr doped TiO_2 1D nanostructures through various structural and optical characterization tools and were able to clarify the controversial issue related to the TiO_2

based diluted magnetic semiconductors (DMSs) to reasonable extent (*Chapter 7*). We observed high temperature ferromagnetism in Co doped TiO_2 nanoparticles (NPs) grown by a contamination free ball milling method. We studied the structural, optical and magnetic (field-dependent, M-H and temperature-dependent, M-T) properties of the Co doped TiO_2 NPs and explained the possible origin of high temperature FM in our samples (*Chapter 8*).

The major contributions and new findings of the present thesis can be summarized as follows:

A. Critical growth parameters for morphology controlled growth of TiO_2 nanostructures

The effect of co-solvents and temperatures on the synthesis of TiO_2 1D nanostructures with different morphologies such as nanotubes (NTs), nanorods (NRs), nanowires (NWs) and nanoribbons (NRbs) have been studied systematically with varying growth temperatures and solvents. At an early stage of growth (i.e., at 130 °C), rolling of nanosheets and partially developed nanotubes, splitted nanosheets and thicker nanosheets are formed in case of alkaline DI water, ethanol co-solvent and ethylene glycol co-solvent, respectively. At 155 °C, the mixed nanotubes and nanorods are grown in case of DI water solvent, while small nanorods and nanorods with larger size are formed for the ethylene glycol and ethanol co-solvent, respectively. Complete formation of NRs and nanoporous NRbs are obtained for DI water solvent and ethylene glycol co-solvent, respectively, while mixed NRs and NWs are formed in case of ethanol co-solvent at higher growth temperature (180 °C). Thus, it is observed that solvent and growth temperatures are the two important parameters for the different shape and size evolutions of TiO_2 1D nanostructures from the successive transformations of precursor TiO_2 NPs $\rightarrow$ nanosheets $\rightarrow$ NTs/ NRs/ NWs/ NRbs. The possible reason for the formation of wide varieties of morphologies may be due to the polarity and coordinating ability of different solvents that have a strong effect on the solubility, reactivity and diffusion behavior of the reactants depending on the reaction temperatures, thus ultimately influencing the structure and morphological features of the resulting products. The stirring also play an important role for the uniform mixture formation

throughout the reaction. It accelerates the reaction, splitting of the nanosheets and prevent the agglomeration or bundling of NTs/ NRs/ NRbs. From this study, it is concluded that solvent, growth temperatures and stirring are the key factors for controlling the different shape and size evolution of TiO_2 nanostructures.

B. Identification of native defects responsible for extended visible light absorption, and visible and NIR PL emission from undoped TiO_2 NRbs

We have identified the defects such as O_v, Ti_i and O interstitial (O_i) defects in undoped TiO_2 NRbs through optical studies. We have demonstrated that the visible and NIR PL are due to O_v and Ti_i defects, respectively, in TiO_2 through PL measurements under various ambient conditions including *in-situ* PL studies under ultra high vacuum and in air environments for the first time. It has been observed that with higher growth temperatures and calcinations temperatures, the Ti_i defects are more pronounced. The oxygen vacancy concentration decreases due to oxidation of the materials with increase in calcination temperature in air atmosphere while the O_v concentration increases after vacuum annealing and, these are confirmed from the decrease/ increase of O_v related visible PL peak intensities. We demonstrated the Ti_i defects induced extended visible absorption, which is very important towards photocatalytic applications of TiO_2 nanostructures. The highly porous TiO_2 NRbs developed in this work accompanied by identification of the defects responsible for strong visible absorption and NIR PL emission is considered as an important milestone for engineering the efficient visible light photocatalytic and photovoltaic applications of undoped TiO_2-based materials.

C. Microscopic origin of lattice expansion/ contraction in rutile TiO_2 nanostructures

We have demonstrated the lattice expansion and contraction in rutile TiO_2 nanostructures due to native defects such as O_v, Ti_i and O_i defects for first time experimentally following the theoretical predictions, contrary to the frequently experimentally reported size-induced lattice parameter variation. When the Ti^{4+} is placed in the interstitial site, the Ti atoms are relaxed outward due to the electrostatic repulsion between positively charged Ti ions. However, the lattice O atoms are slightly distorted towards the Ti_i^{4+} as they are strongly bonded to lattice

Ti atoms. As a result, the net relaxation favors the expansion of the lattice volume which is due to the presence of Ti_i^{4+} defects. In the case of O_v-mediated expansion, due to the missing O atom, the Ti–Ti and Ti–O bonds are relaxed. The nearest-neighbor Ti atoms move outward from the vacancy to strengthen the bonding with the rest of the neighboring O lattice. Though the next-nearest-neighboring O atoms may move inward to fill the O_v site, the net outward movement of Ti atoms is higher than the net inward movement of O atoms. This results in lattice expansion. Based on our experimental observations, we argued that the presence of Ti_i^{4+} and $F^+$and neutral oxygen vacancy defects are mainly responsible for lattice expansion, while the electrostatic attraction between Ti_i^{4+} and O_i^{2-}defects cause the lattice contraction in rutile TiO_2 nanostructures.

D. Oxygen vacancy mediated ferromagnetism in undoped and transition metal (Fe, Cr, Co) doped TiO_2 nanostructures

We observed room temperature ferromagnetism in undoped and transition metal (Fe, Cr and Co) doped TiO_2 nanostructures, and investigated the origin of ferromagnetism (FM) in these undoped and doped TiO_2 materials using various structural, optical and magnetic characterization tools. We have demonstrated that the introduction of defects such as oxygen vacancy by solvothermal/ hydrothermal growth methods and post-growth vacuum annealing in undoped and doped TiO_2 systems, or those introduced for local charge balance due to valence differences between the dopant and the host in doped TiO_2 nanostructures strongly influence the magnetization results because they can contribute to the magnetization through their role in the exchange mechanism with the dopant cations. A simple oxygen vacancy cannot contribute to the FM in TiO_2 systems. The oxygen vacancy with appropriate charge redistribution and their orbital overlapping/ exchange interaction with the nearby unpaired 3d electron of Ti^{3+} in case of undoped TiO_2 and/ or unpaired 3d electrons of dopant with proper charge distribution and occupation inside the host lattice in case of transition metal (TM) dopant play the pivotal role for the ferromagnetic ordering and observed of RTFM. We argued that the electrons in F^+ center localize and may form bound magnetic polarons (BMPs) by ordering the Ti^{3+} ($3d^1$) electron spin neighboring the oxygen vacancies, thereby gaining exchange energy. The s-d exchange interaction between the $1s^1$ electron spin in the F^+ center which is localized in the vicinity of $3d^1$ electron spin of Ti^{3+} ions within an orbit

around oxygen vacancies favors long range FM in undoped TiO_2 NRbs. Thus the formation of BMP, which includes electrons locally trapped by oxygen vacancies, with the trapped electron in the F^+ center occupying an orbital overlapping with the unpaired electron ($3d^1$) of Ti^{3+} is proposed to explain the observed FM in our samples. Similarly, we believed that exchange interaction between $3d^5$ spins of Fe^{3+} and $1s^1$ spin of F^+ center, $3d^3$ electron spin of Cr^{3+} and $1s^1$ spin of F^+ center, and $3d^5$ electron spin of Co^{2+} and $1s^1$ spin of F^+ center are most likely responsible for the observed enhanced FM in Fe:TiO_2, Cr:TiO_2 and Co:TiO_2 systems, respectively. Note that these defects states and dopant ions were confirmed from the ESR, XPS and PL spectroscopy studies. Moreover, the observed high temperature FM well above room temperature can be partly attributed to the extended defects such as structural/ morphological defects and strain/ dislocations. However, more studies are required to pinpoint the exact mechanism of high temperature FM. The present work suggests that not only the magnetic dopants themselves but also the defects are important to understand ferromagnetism of the TiO_2-based DMS nanostructures.

We believe that the comprehensive study presented in this thesis on the controlled growth and tunable optical and magnetic properties of TiO_2 nanostructures through intrinsic defects and doping would further promote TiO_2-based research and development efforts to tackle the environmental and energy challenges which we are currently being faced by the humanity. The results discussed in this thesis provide a strong evidence for intrinsic ferromagnetism in the TiO_2 nanostructures and reveal deep underlying physics on the origin of the room temperature ferromagnetism, and will contribute to the development of spintronic and magneto-optic devices which can be operated at and above room temperature. Finally the future prospects of the defect engineering of TiO_2 nanostructures research for the possible improvement of the optical and magnetic properties, their understandings and related applications are mentioned in the following section.

9.2. Scope for further works on TiO_2 nanostructures

We have studied the formation mechanism of TiO_2 nanostructure with different morphologies grown by solvothermal method. The growth mechanism can be explored further and understood better by *in-situ* hydrothermal/ solvothermal process. It has been

demonstrated that the O_v and Ti_i defect induced extended visible response of TiO_2 may be advantageous for a wide range of photocatalytic applications which can be used with solar light instead of using costly and hazardous UV light. However, further efforts are still needed in this area to rationally engineer the defects in TiO_2 in such a way that enhancement of charge (electron-hole) separation, especially interfacial electron transfer mediated by O_v, Ti_i defects related trap states and/ or other structural defects, which is very important for a good photocatalyst, aiming to tune its properties in a desired manner for advancing environmental and energy-related applications. Regarding the TiO_2-based DMS materials, a large number of conflicting results have pointed toward both intrinsic and extrinsic origin for FM during the last decade leading to confusions among the researchers for the realization of practical spintronic devices. The reason for these controversial issues can be attributed to intrinsic and extrinsic nature of FM that depends mainly on the fabrication/ growth processes of the materials and the sensitive characterization tools to pin point the origin of the observed FM. The controversy is partly related to lack of understanding of origin of intrinsic FM. Here we try to resolve the problem of understanding the origin of intrinsic FM with the help of several spectroscopy characterization tools. However, still a unified theoretical model and further efforts are required to explain the intrinsic FM. Moreover, more sophisticated and sensitive characterization tools should be employed to determine the exact origin of FM whether of intrinsic or extrinsic nature. Thus, based on the results presented in this thesis, further studies on TiO_2 nanostructures can be in the following directions:

1. Growth mechanism can be explored further by *in-situ* time dependant reaction studies of hydrothermal products.
2. Oxygen vacancy concentration could be tuned in undoped TiO_2 by introducing inert gases into the reaction chamber during the reaction or by post-growth annealing under controlled environment.
3. Our undoped TiO_2 nanoribbons with extended visible absorption are highly promising for the highly efficient visible light photocatalytic applications. Photocatalytic degradation studies should be performed on such TiO_2 nanoribbons.

4. *In-situ* doping of N and H should be possible by the respective gas feeding into the autoclave during the reaction, which may provide better optical, electrical and magnetic properties, and can be more efficient for the related applications.
5. We demonstrated the native defects induced lattice expansion and contraction in undoped rutile TiO_2 nanostructures. This calls for a revisit of the earlier results on the size dependent lattice expansion in TiO_2 nanostructures.
6. More sophisticated characterization techniques such as synchrotron based x-ray absorption spectroscopy (XAS) and x-ray circular magnetic dichroism (XMCD) may be employed to investigate the extrinsic or intrinsic nature of FM in the TiO_2 nanostructures. These techniques have their strengths in providing element specific information on the electronic and magnetic properties of materials.
7. Transition metal doped TiO_2 1D nanostructures should be grown on suitable substrates for specific applications such as spintronic and magneto-optic devices.
8. More accurate theoretical models are needed for a quantitative understanding of both RTFM and high temperature FM in metal oxide semiconductors.
9. Despite great academic research interest, it is not clear whether defect induced ferromagnetic states could be stabilized under device processing conditions and could actually be utilized as it is very sensitive to oxygen atmosphere. So, there must be some coating/ passivation needed on the surface of the device which helps to prevent direct contact with the atmosphere.
10. TiO_2 based hybrid structures such as graphene-TiO_2 nanostructures can be studied for energy applications.